

# **INCREASING STABILITY OF MICROBUBBLES UNDER ULTRASOUND**

**A Thesis Submitted to  
the Graduate School of Engineering and Sciences of  
İzmir Institute of Technology  
in Partial Fulfillment of the Requirements for the Degree of**

**DOCTOR OF PHILOSOPHY**

**in Bioengineering**

**by  
İlyas Umur AYZ**

**December 2019  
İZMİR**

We approve the thesis of İlyas Umur AYAZ

**Examining Committee Members:**

  
\_\_\_\_\_  
**Prof. Dr. Ekrem ÖZDEMİR**

Department of Chemical Engineering, Izmir Institute of Technology

  
\_\_\_\_\_  
**Prof. Dr. Mehmet POLAT**

Department of Chemical Engineering, Izmir Institute of Technology

  
\_\_\_\_\_  
**Prof. Dr. Osman YILMAZ**

Department of Laboratory Animal Science, Dokuz Eylul University

  
\_\_\_\_\_  
**Prof. Dr. Zekiye Sultan ALTUN**

Department of Basic Oncology, Dokuz Eylul University

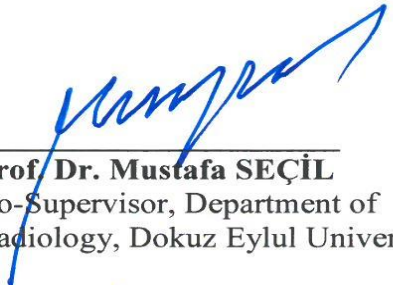
  
\_\_\_\_\_  
**Assist. Prof. Dr. Mehmet Zübeyir ÜNLÜ**

Department of Electrical and Electronics Engineering, Izmir Institute of Technology

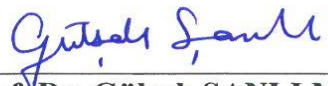
**December 17, 2019**

  
\_\_\_\_\_  
**Prof. Dr. Ekrem ÖZDEMİR**

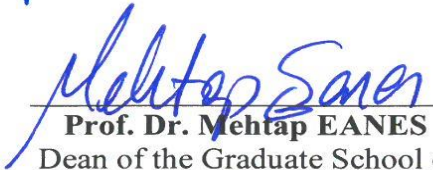
Supervisor, Department of Chemical Engineering,  
Izmir Institute of Technology

  
\_\_\_\_\_  
**Prof. Dr. Mustafa SEÇİL**

Co-Supervisor, Department of  
Radiology, Dokuz Eylul University

  
\_\_\_\_\_  
**Prof. Dr. Gülşah ŞANLI MOHAMED**

Head of the Biotechnology  
and Bioengineering Graduate Program

  
\_\_\_\_\_  
**Prof. Dr. Mehtap EANES**

Dean of the Graduate School of  
Engineering and Sciences

## ACKNOWLEDGMENTS

First and foremost I would like to express my sincere gratitude to my supervisor Prof. Ekrem Özdemir for his guidance, encouragement, and endless support throughout my PhD. This work would not be possible without him. I would also like to thank my co-supervisor Prof. Mustafa Seçil for his support and guidance. I am grateful to Dr. Sevgi Kılıç Özdemir for her invaluable support and scientific guidance over the course of the work. She has always been generous with her time in answering my questions. A huge debt of thanks is owed to M.D. Mustafa Barış who I worked together in the TÜBİTAK projects. I am grateful to him whom I learned a lot from throughout my experimental work with the ultrasound imaging system. The *in-vivo* experiments of my research was carried out in collaboration with Prof. Osman Yılmaz. I am grateful to him for the opportunity to work in his lab and for his support. His guidance and technical expertise has proved invaluable. I would also like to thank Prof. Şule Alkan, Prof. Safiye Aktaş, and Prof. Zekiye Altun at Dokuz Eylül University for their collaborations and valuable discussions; and Dr. Murat Özmen for the biochemical analysis in the TÜBİTAK projects. I am immensely grateful to Prof. Mehmet Polat for his valuable suggestions and support throughout this research. Furthermore, my thanks go to friends and colleagues at Izmir Institute of Technology and at Dokuz Eylül University, especially my group mates, Gülşah Kürkcü, Sema Coşkun, Hatice Güven, Meryem Çalışır, and Melek Aydın. I would also like to gratefully acknowledge TÜBİTAK for the financial support of this PhD through the project numbers of 113M270 and 213M668.

My special thanks go to my parents for their constant support and encouragements in every step of my way. The last but not the least, my sincere appreciation goes to my beloved wife, Gizem. She has always shown her patience and love for me through difficult times.

# ABSTRACT

## INCREASING STABILITY OF MICROBUBBLES UNDER ULTRASOUND

Microbubbles are used as effective contrast agents in ultrasound imaging. However, low stability of the microbubbles limits their use for prolonged period of time in medical applications. The aim of this dissertation is to increase the stability of microbubbles under ultrasound. The stability and acoustic response of microbubbles were investigated under ultrasound as a function of their shell composition. Microbubbles were fabricated using combinations of phospholipid (DSPC) and an emulsifier (PEG<sub>40</sub>St) in different molar ratios. It was found that adding the emulsifier decreased the microbubble stability under ultrasound; however, the echogenicity of microbubbles was shown to increase with increasing emulsifier content. A method was developed to estimate the concentration of microbubbles with ultrasound. Hydrostatic pressure studies showed that the microbubbles recovered their spherical structures at low pressure pulses, in contrast, disappeared in a very short time at high pressure pulses. B-mode ultrasound intensity of microbubbles was investigated at different ultrasound powers under Doppler ultrasonography, and for the first time, a model was developed to relate the intensity to effective bubble concentration. We calculated acoustic energy thresholds and explained a possible mechanism for the destruction of microbubbles under ultrasound. The effect of shell loadings on the acoustic response and stability of microbubbles were investigated under ultrasound. It was found that both the echogenicity and stability of microbubbles increased with increasing mass of the loadings on microbubble shell. *In-vivo* studies showed that the acoustic performance of in-house made microbubbles was comparable to that of commercial standard Vevo MicroMarker<sup>®</sup> contrast agents.

# ÖZET

## MİKROKÖPÜKÇÜKLERİN ULTRASON ALTINDA STABİLİTELERİNİN ARTTIRILMASI

Mikroköpükçükler, ultrason görüntülemeye etkili kontrast ajanları olarak kullanılmaktadır. Mikroköpükçüklerin stabilitesinin düşük olması, tıbbi uygulamalarda uzun süre kullanımlarını sınırlamaktadır. Bu tezin amacı, ultrason altında mikroköpükçüklerin stabilitesini artırmaktır. Mikroköpükçükler, farklı molar oranlarda fosfolipid (DSPC) ve emülsifiyer (PEG<sub>40</sub>St) karışımları kullanılarak üretildi. Farklı formülasyonlarda üretilen mikroköpükçüklerin stabilitesi ve akustik yanıtı, ultrason altında incelendi. Mikroköpükçüğün yüzeyini oluşturan zarın yapısındaki emülsifiyer içeriğinin artmasıyla ultrason altında mikroköpükçüklerin stabilitesinin azaldığı, artan emülsifiyer içeriği ile birlikte mikroköpükçüklerin ekojenitesinin arttığı bulundu. Ultrason ile mikroköpükçük konsantrasyonunu tahmin etmek için yeni bir yöntem geliştirildi. Hidrostatik basınç çalışmaları, mikroköpükçüklerin düşük basınç pulslarında küresel yapılarını geri kazandıklarını, aksine, yüksek basınç pulslarında çok kısa sürede ortadan kaybolduğunu gösterdi. Mikroköpükçüklerin B-mod ultrason intensitesi, Doppler ultrasonografi altında farklı ultrason güçlerinde araştırıldı ve ilk kez, ultrason intensitesini etkin mikroköpükçük konsantrasyonuyla ilişkilendirmek için bir model geliştirildi. Ultrason altında mikroköpükçük yıkımı için akustik enerji eşikleri hesaplandı ve olası bir yıkım mekanizması açıklandı. Mikroköpükçük zarı üzerine eklenen farklı kütleli yüklemelerin mikroköpükçüklerin akustik yanıtı ve stabilitesi üzerindeki etkisi ultrason altında incelendi. Mikroköpükçüklerin ekojenitesinin ve stabilitesinin, yüklemelerin kütesinin artmasıyla arttığı bulundu. *In-vivo* çalışmalar, laboratuvarında geliştirilen mikroköpükçüklerin akustik performansının ticari MicroMarker® kontrast maddelerinininkiyle karşılaştırılabilir olduğunu gösterdi.

# TABLE OF CONTENTS

LIST OF FIGURES .....	xi
LIST OF TABLES .....	xx
CHAPTER 1 .....	1
1.1. Overview .....	1
1.2. Motivation.....	3
1.3. Objectives .....	5
CHAPTER 2 .....	7
2.1. Ultrasound.....	7
2.1.1. Basic Definition .....	7
2.1.2. Ultrasound Imaging.....	10
2.2. Ultrasound Contrast Agents .....	11
2.3. Microbubble Generation .....	17
2.4. Stability of Microbubbles .....	19
2.4.1. Static Diffusion .....	19
2.4.2. Rectified Diffusion.....	21
2.4.3. Stability from Surface Coating.....	22
2.5. Acoustic Properties of Microbubbles.....	23
2.6. Shell Effects on Acoustic Performance and Stability of Microbubbles under Ultrasound Activation.....	28
2.7. Microbubbles for Targeted Drug Delivery .....	32
CHAPTER 3 .....	34
3.1. Preparation of Microbubbles.....	34
3.2. Determination of the Size and Concentration of Microbubbles .....	35
3.3. <i>In-vitro</i> Characterization of Microbubbles under Ultrasound Activation.....	36
3.3.1. Determination of the Focus Zone.....	36
3.3.2. Characterization of the Ultrasonic Echoscope .....	37

3.3.3. Characterization of Microbubbles in the A-scan mode and B-mode of the Ultrasonic Echoscope .....	38
3.4. Stability of Microbubbles under Ultrasound Excitation through the Peristaltic Pump .....	40
3.5. <i>In-vitro</i> Stability of Microbubbles with Different Shell Compositions under Ultrasound Excitation .....	41
3.6. Optical Characterization of Microbubbles under Ultrasound Activation with High-Speed Imaging .....	42
3.7. Stability of Microbubbles under Doppler Ultrasonography at Different Ultrasound Powers .....	43
3.8. Investigation of <i>In-vitro</i> Echogenicity of Microbubbles with Different Shell Compositions .....	45
3.9. Measuring Acoustic Response of Loaded Microbubbles under Ultrasound Excitation via the Bolus Injection .....	47
3.9.1. Preparation of Biotinylated Microbubbles .....	48
3.9.2. Preparation and Characterization of Liposomes .....	48
3.9.3. The Assay of Doxorubicin Loading into Liposomes .....	49
3.9.4. Production of Targeted DOX-Loaded Microbubbles .....	49
3.10. Investigation of the Stability of Loaded Microbubbles under Ultrasound Excitation .....	51
3.11. Investigation of the Microbubble Shell Composition .....	51
3.11.1. NMR Measurements .....	51
3.11.2. Determination of the Amounts of Microbubble Shell Components and Subphase Components .....	52
3.12. Stability of Microbubbles under Hydrostatic Pressure .....	52
3.13. <i>In-vivo</i> Studies .....	53
3.13.1. <i>In-vivo</i> Toxicity of Microbubbles .....	53
3.13.1. Diagnostic Dose Study for the Rats .....	56
3.13.2. Comparison of Microbubbles with the Commercial Standard Vevo MicroMarker <sup>®</sup> Contrast Agents .....	57
3.13.3. Echogenicity Study in Rat Kidney Model .....	57
3.13.4. Toxic Dose Study for the Rats .....	58
3.13.5. Toxic Dose Study for the Rabbits .....	58

CHAPTER 4 .....	60
4.1. Optimization Study for the Microbubble Concentration and Size	
Measurements with the Coulter Counter Multisizer .....	60
4.2. Investigation of the Microbubble Shell Composition .....	64
4.3. The Amount of Microbubble Shell and Subphase in the Microbubble	
Suspension .....	70
4.4. <i>In-vitro</i> Characterization of Microbubbles under Ultrasound	
Activation .....	71
4.4.1. Determination of Focus Zones .....	71
4.4.2. Characterization of the Ultrasonic Echoscope .....	72
4.4.3. Characterization of Microbubbles under Ultrasound Excitation...	73
4.4.4. Calibration Study for Microbubbles in the A-scan Mode and in	
the B-mode .....	74
4.4.5. Characterization of Microbubbles at Different Transmitter	
Powers and Different Transducer Frequencies .....	78
4.5. Investigation of the Stability of Microbubbles under Ultrasound	
Excitation through the Peristaltic Pump .....	83
4.5.1. Investigation of Shear Effect on Microbubbles under	
Ultrasound Excitation .....	84
4.5.2. Effect of Ultrasound Power and Transmitter Frequency on the	
Stability of Microbubbles .....	85
4.6. Investigation of the Stability of Microbubbles with Different Shell	
Compositions under Ultrasound Activation .....	87
4.6.1. Calibration Study for Microbubbles.....	87
4.6.2. Stability of Microbubbles at Different Transducer Frequencies...	89
4.6.3. Stability Test for the Microbubbles with Different Shell	
Compositions under Ultrasound Excitation .....	90
4.7. Characterization of the Oscillation of Microbubbles under	
Ultrasound Activation with High-Speed Imaging .....	95
4.8. Stability of Microbubbles under Hydrostatic Pressure .....	99
4.9. Effect of Ultrasound Power on the Stability of Microbubbles .....	106
4.9.1. Stability of Microbubbles under Doppler Ultrasonography.....	107
4.9.2. Model for Calculating the Acoustic Energy Thresholds.....	109

4.10. Investigation of the Echogenicities of Microbubbles with Different Shell Compositions .....	115
4.10.1. Developing Concentration Estimation Method for the Bolus Injection Technique .....	116
4.10.2. Estimation of Microbubble Concentration by Bolus Injection Method .....	119
4.10.3. Echogenicities of Microbubbles with Different Shell Compositions.....	126
4.11. Investigation of the Echogenicity of Microbubbles Loaded with Different Masses .....	128
4.12. Stability of Loaded Microbubbles under Ultrasound Activation.....	131
4.13. Characterization of Microbubbles in the Doppler Flow Phantom ....	135
4.14. <i>In-Vivo</i> Studies with Microbubbles .....	136
4.14.1. Determination of Diagnostic Microbubble Dose for the Rats ..	137
4.14.2. Comparison of 5:5 Microbubbles with the Commercial Standard Vevo MicroMarker <sup>®</sup> .....	148
4.14.3. Toxicity Studies .....	151
4.14.3.1. Biochemistry and Complete Blood Count (CBC) Results in Toxicities of Microbubbles .....	151
4.14.3.2. Pathology Results .....	156
4.14.3.2.1. Microbubble-1 (RAT – 5E+08 #/ml).....	156
4.14.3.2.2. Microbubble-2 (RAT – 5E+08 #/ml).....	156
4.14.3.2.3. Microbubble-3 (RAT – 2.5E+08 #/ml).....	157
4.14.3.2.4. Microbubble-4 (RAT – 5E+08 #/ml).....	157
4.14.3.2.5. Microbubble-5 (RAT – 5E+08 #/ml).....	158
4.14.3.2.6. Microbubble-6 (RAT - 2.5E+08 #/ml).....	159
4.14.3.2.7. Microbubble-7 (RAT - 2.5E+08 #/ml).....	159
4.14.3.2.8. Microbubble-8 (RAT - 2.5E+08 #/ml).....	160
4.14.3.2.9. Microbubble-9 (RAT – 3.2E+09 #/ml).....	160
4.14.3.2.10. Microbubble-10 (RABBIT – 3.2E+09 #/ml).....	161

4.14.3.2.11. Microbubble-11	
(RABBIT – 3.2E+09 #/ml).....	161
4.14.3.2.12. Microbubble-12	
(RABBIT – 3.2E+09 #/ml).....	162
4.14.3.2.13. Microbubble-13	
(RABBIT – 3.2E+09 #/ml).....	162
4.14.3.2.14. Microbubble-14	
(RABBIT – 3.2E+09 #/ml).....	163
4.14.3.2.15. Vevo MicroMarker <sup>®</sup> -15	
(RAT – 5E+08 #/ml).....	163
4.14.3.2.16. Vevo MicroMarker <sup>®</sup> -16	
(RAT – 5E+08 #/ml).....	164
CHAPTER 5 .....	165
5.1. Contributions.....	165
5.2. Future Work .....	167
REFERENCES .....	168

# LIST OF FIGURES

<b><u>Figure</u></b>	<b><u>Page</u></b>
Figure 2.1. The simplest description of ultrasound as linked sine waves at low or high frequencies (A. Sofferma 2012).....	8
Figure 2.2. Images of tumor in the thigh of a rabbit before (a) and after (b) the injection of ultrasound contrast agents. The tumor becomes extremely bright relative to the surrounding tissue when the microbubbles injected (Schutt, Klein et al. 2003). .....	11
Figure 2.3. A typical microbubble with various coating monolayers (Sirsi and Borden 2009).....	12
Figure 2.4. Schematic representation of the acoustic behavior of lipid and polymer microbubbles with increasing amplitude of ultrasound (Hernot and Klibanov 2008). .....	13
Figure 2.5. Schematic representation of the microbubble formation mechanism (Kwan and Borden 2012).....	19
Figure 2.6. Enhanced drug extravasation at high mechanical index through inertial cavitation (Sirsi and Borden 2014). .....	24
Figure 2.7. Non-spherical vibrations of the insonified microbubbles (de Jong, Emmer et al. 2009).....	28
Figure 3.1. Schematic representation of experimental set-up for the determination of focus zones of the probes.....	37
Figure 3.2. Schematic illustration of the experimental set-up for the characterization of the ultrasonic echoscope. ....	38
Figure 3.3. Characterization of microbubbles under ultrasound excitation.....	39
Figure 3.4. Experimental set-up to investigate the stability of microbubbles at different shear rates, different output powers and different frequencies under ultrasound.....	40
Figure 3.5. Experimental set-up for the investigation of the <i>in-vitro</i> stability of microbubbles under ultrasound activation. ....	42
Figure 3.6. Experimental set up. ....	43
Figure 3.7. RIOs created in the acoustic window and in the out of focal zone within a freeze-captured B-mode image in the flow phantom. ....	45

<b><u>Figure</u></b>	<b><u>Page</u></b>
Figure 3.8. The Vevo 2100 ultrasonographic system, 3-D transducer positioning platform and the experimental animal stabilization panel. ....	46
Figure 3.9. (a) ATS Laboratories Model VP-3 three vein training phantom (b) ATS Laboratories Model 525 peripheral vascular doppler flow phantom. ....	46
Figure 3.10. Schematic representation of acoustic testing set up. ....	47
Figure 3.11. Experimental set-up for measuring the acoustic response of loaded microbubbles in the B-mode. ....	47
Figure 3.12. Bright-field (a) and fluorescent (b) images of Lipo-DOX loaded microbubbles. Red color on the surface of microbubbles depicts the DOX loaded liposomes. ....	50
Figure 3.13. Hydrostatic constant pressure system. 1. PBS, 2. Pump, 3. Pressure regulator, 4. One-way pressure valve, 5. Cell view, 6. Microscopy, 7. Camera, 8. Computer. ....	53
Figure 3.14. Rat metabolism cage. ....	55
Figure 3.15. Three-dimensional positioning system and abdominal evaluation in rats. ....	57
Figure 4.1. (a) Image of the 5:5 microbubble population after production, (b) size distribution of the microbubble suspension. ....	60
Figure 4.2. Calculated microbubble concentration versus measured microbubble concentration at different dilutions and different sample volumes. ....	62
Figure 4.3. Microbubble concentrations measured at different sample volumes for different dilutions. ....	62
Figure 4.4. Mean diameters of the microbubble suspensions versus microbubble concentrations measured at different sample volumes for different dilutions. ....	63
Figure 4.5. Chemical structure and <sup>1</sup> H NMR spectra of (a) DSPC and (b) PEG <sub>40</sub> St. Arrows show the proton chemical shifts at certain ppm values. ....	64
Figure 4.6. <sup>1</sup> H NMR spectra of pure DSPC and pure PEG <sub>40</sub> St on the same graph. ....	66
Figure 4.7. <sup>1</sup> H NMR spectra of DSPC/PEG <sub>40</sub> St mixtures at molar ratios of 9:1, 7:3, 4:6 and 2:8. ....	66
Figure 4.8. <sup>1</sup> H NMR calibration curve. ....	68

<b><u>Figure</u></b>	<b><u>Page</u></b>
Figure 4.9. <sup>1</sup> H NMR spectra of microbubble shells (a) and subphases (b) at different PEG <sub>40</sub> St contents from 10% to 80%. .....	69
Figure 4.10. Molar percentage of PEG <sub>40</sub> St in the shells of DSPC/PEG <sub>40</sub> St-coated microbubbles as a function of PEG <sub>40</sub> St content in the DSPC/PEG <sub>40</sub> St mixture prior to microbubble formation. The line is theoretical result of equivalent shell and mixture fractions. ....	70
Figure 4.11. Percentages of microbubble shells and subphases in the microbubble suspensions as a function of PEG <sub>40</sub> St content in the mixtures. ....	71
Figure 4.12. Focus zones for different probe frequencies. ....	72
Figure 4.13. (a) Amplitude profile of the plastic tube containing PBS. (b) Peak amplitudes of PBS and front wall of the tube for different receiver gain powers at a 10 dB of output power and the ratios. (c) Maximum amplitude values for PBS.....	73
Figure 4.14. (a) Characterization of microbubbles in the A-scan mode under ultrasound, (b) imaging the air, buffer solution and microbubbles in the B-mode.....	74
Figure 4.15. Amplitude profile of microbubbles at different concentrations within a plastic tube in the A-scan mode. ....	75
Figure 4.16. Amplitude change as a function of microbubble concentration and the change of the signal reflected from the tube wall in the A-scan mode and the B-mode. ....	77
Figure 4.17. Amplitude profiles of microbubbles within a plastic tube at different concentrations for (a) 1 MHz, (b) 2 MHz and (c) 4 MHz in the A-scan mode.....	78
Figure 4.18. (a) Change in amplitude of ultrasonic echo versus microbubble concentration for different transducer frequencies at the transmitter power of 10 dB in the A-scan mode, (b) linear relationship between the logarithm of microbubble concentration and the amplitude for different transducer frequencies.....	79
Figure 4.19. Amplitude profiles of microbubbles of different concentrations within a plastic tube at different transmitter powers, (a) 10 dB, (b) 20 dB, (c) 30 dB, for the 1 MHz probe in the A-scan mode. ....	80
Figure 4.20. Change in amplitude with respect to microbubble concentration at different transmitter powers for the 1 MHz probe in the A-scan mode. ....	80

<b><u>Figure</u></b>	<b><u>Page</u></b>
Figure 4.21. Amplitude profiles of microbubbles of different concentrations within a plastic tube at different transmitter powers, (a) 10 dB, (b) 20 dB, (c) 30 dB, for the 2 MHz probe in the A-scan mode.....	81
Figure 4.22. Change in amplitude with respect to microbubble concentration at different transmitter powers for the 2 MHz probe in the A-scan mode. (a) Normalized amplitude vs. concentration for different transmitter powers, (b) linear relationship between the logarithm of microbubble concentration and the amplitude of ultrasonic echo for different transmitter powers.....	82
Figure 4.23. Amplitude profiles of microbubbles of different microbubbles within a plastic tube at different transmitter powers, (a) 0 dB, (b) 10 dB, (c) 20 dB, (d) 30 dB, for the 4 MHz probe in the A-scan mode.....	82
Figure 4.24. Change in amplitude with respect to microbubble concentration at different transmitter powers for the 4 MHz probe in the A-scan mode. (a) Normalized amplitude vs. concentration for different transmitter powers, (b) linear relationship between the logarithm of microbubble concentration and the amplitude of ultrasonic echo for different transmitter powers.....	83
Figure 4.25. The effect of shear rate on the stability of microbubbles under ultrasound activation. ....	84
Figure 4.26. The effect of different transducer frequencies on the stability of microbubbles.....	85
Figure 4.27. Effect of different dBs on stability. ....	86
Figure 4.28. Photo indicating that the peristaltic pump rotating parts used in the experiment crushed the microbubbles. White arrow shows the remaining lipid aggregates from the destroyed microbubbles. ....	86
Figure 4.29. a) The peak signals reflected from the rear wall of the container at different microbubble concentrations, (b) calibration graph for microbubble concentration.....	88
Figure 4.30. Microbubble calibration graphs at different frequencies, (a) concentration values vs. amplitude values, (b) concentration values vs. attenuation values.....	89
Figure 4.31. Stability of microbubbles at different probe frequencies in terms of concentration and attenuation. ....	90
Figure 4.32. Stability of microbubbles with different shell compositions under ultrasound activation with respect to concentration and attenuation. ....	91

<b><u>Figure</u></b>	<b><u>Page</u></b>
Figure 4.33. The change of volume-weighted size distribution with time for microbubbles at DSPC/PEG <sub>40</sub> St molar ratios of (a) 9:1, (b) 8:2, (c) 7:3, (d) 6:4, and (e) 5:5 under ultrasound excitation.....	93
Figure 4.34. The mean diameter changes with time for microbubbles at DSPC/PEG <sub>40</sub> St molar ratios of 9:1, 8:2, 7:3, 6:4, 5:5 under high-power ultrasound excitation. ....	94
Figure 4.35. Lifetime of microbubbles as a function of PEG concentration at high ultrasound powers. ....	95
Figure 4.36. Video image recorded with “Ultra High Speed Camera System” at the University of Pittsburgh Medical Center (UPMC). ....	96
Figure 4.37. Sequence of 8 image frames of two selected microbubbles, MB-1 and MB-2, under ultrasound excitation. ....	96
Figure 4.38. Sequence of 7 image frames of a single microbubble (MB-3) with an initial diameter of 4.2 $\mu\text{m}$ under ultrasound excitation.....	97
Figure 4.39. Sequence of 8 image frames of a single microbubble (MB-4) with an initial diameter of 2.9 $\mu\text{m}$ under ultrasound excitation.....	98
Figure 4.40. Normalized diameter-time curves for four selected microbubbles. ....	99
Figure 4.41. (a) Microscope images of changes in the sizes of bare bubbles with pressure, (b) changes in the sizes of bare bubbles at different pressures. ....	100
Figure 4.42. Change in the size of bare bubbles with time by increasing and decreasing pressure gradually. ....	101
Figure 4.43. Change in the dimensions of bare bubbles in different initial sizes with different pressures over time.....	102
Figure 4.44. Behavior of lipid microbubbles under pressure. ....	102
Figure 4.45. Behavior of 5:5 air-filled microbubbles at a pressure of 0.11 bar.....	103
Figure 4.46. Behavior of lipid microbubbles under the pressure of 0.19 bar; (a) pressure, (b) the change in the number and size of the microbubbles over time, and (c) the light, fluorescence, and the merged microscope images of the microbubbles. ....	104
Figure 4.47. The behavior of microbubbles in short-term pressure pulses; (a) change in pressure, (b) change in the number and size of microbubbles over time, and (c) light, fluorescence, and merged microscope images of microbubbles.....	105

<b><u>Figure</u></b>	<b><u>Page</u></b>
Figure 4.48. B-mode images of microbubbles in the tubing of flow phantom at certain time intervals for the 20% and 100% transmit powers. ....	107
Figure 4.49. Time-intensity curves for ROI1 (a) and ROI2 (b) at different transmit powers. ....	109
Figure 4.50. Schematic representation illustrating the possible physical mechanisms for the destruction of microbubbles under insonification. ....	110
Figure 4.51. The initial slopes for the first order equation. ....	112
Figure 4.52. $\ln(k\alpha)$ versus $P_A$ . Slope of the curve gives $1/E_T$ . ....	112
Figure 4.53. Different slopes taken for the $n^{\text{th}}$ order equation. ....	113
Figure 4.54. Intercept/slope versus $P_A$ . Slope of the curve gives $1/E_T$ . ....	114
Figure 4.55. Decay constants plotted against $P_A$ . ....	115
Figure 4.56. Development of the estimation method for the bolus injection technique. (a) The model setup and (b) the resulting experimental TIC. ....	116
Figure 4.57. (a) TICs obtained with Vevo2100 in different bolus injection volumes, (b) TICs obtained for bolus injection at different flow rates, (c) TICs obtained for bolus injection at different concentrations, (d) TICs obtained for bolus injection in different microbubble compositions. The curves shown by straight lines are model equation curves. ....	121
Figure 4.58. Evaluation of the AUC and MTT parameters obtained with the bolus injection for (a) different bolus injection volumes, (b) different flow rates, (c) different concentrations, and (d) different microbubble compositions. ....	122
Figure 4.59. Evaluation of (a) AUC and (b) MTT values for all measured parameters. ....	122
Figure 4.60. Different bolus volumes for different concentrations of 9:1 microbubbles and AUC values for different flow rates. ....	123
Figure 4.61. (a) The slope values obtained for the 9:1 microbubbles at different concentrations and (b) the slope value measured for the same microbubble. ....	124

<b><u>Figure</u></b>	<b><u>Page</u></b>
Figure 4.62. (a) The measured microbubble concentration versus the microbubble concentration calculated by the ultrasound method, (b) the measured microbubble concentration and the calculated microbubble concentration as a function of PEG <sub>40</sub> St, and (c) the microbubble concentrations calculated by the AUC obtained for the ultrasound contrast agent microbubbles prepared in different formulations. ....	125
Figure 4.63. The logarithm of the microbubble concentration is linearly proportional to the AUC. ....	126
Figure 4.64. Echogenicity of microbubbles with different shell compositions. ....	127
Figure 4.65. B-mode image of the inside of the tube filled with buffer solution as microbubbles pass through the tube after injected. ....	128
Figure 4.66. Time-intensity curves fitted to the model equation at different microbubble concentrations for different types of microbubbles: (a) bare MB, (b) MB-Biotin, (c) MB-Avidin, (d) MB-LipoDOX, and (e) Targeted MB. ....	129
Figure 4.67. AUC-Concentration curves for the loaded microbubbles. ....	130
Figure 4.68. Echogenicity of microbubbles loaded with different masses. ....	131
Figure 4.69. Change of amplitudes of acoustic signals reflected from the rear wall of the cuvette with respect to time. ....	132
Figure 4.70. Change in concentration and attenuation over time for the unloaded microbubble and microbubbles loaded with different mass under ultrasound excitation. ....	133
Figure 4.71. Stability of microbubbles with increasing loadings under ultrasound excitation. ....	135
Figure 4.72. In the time-echogenicity curve, echogenicity was significantly increased in ROIs after the microbubble injection. ....	137
Figure 4.73. Change in the contrast mean power at different ROIs with time after bolus injection of microbubbles at different concentrations through the tail vein under ultrasound: (a) 1E+08 #/ml, (b) 1E+08 #/ml, (c) 1E+09 #/ml, (d) 1E+07 #/ml, (e) 5E+08 #/ml, and (f) 2.5E+08 #/ml. ....	139
Figure 4.74. Echogenicity of microbubbles at different concentrations. Concentration of 2.5E+08 #/ml gives the highest peak enhancement for the VCI. ....	139

<b><u>Figure</u></b>	<b><u>Page</u></b>
Figure 4.75. Change in the contrast mean power at different ROIs with time after single bolus injection of microbubbles at different concentrations through the tail vein under ultrasound: (a) 1E+08 #/ml, (b) 5E+08 #/ml, (c) 2.5E+08 #/ml and (d) 2.5E+08 #/ml. ....	140
Figure 4.76. Echo power of microbubbles at different concentrations. Concentration of 5E+08 #/ml gives the highest peak enhancement for the VCI. ....	141
Figure 4.77. Change in the contrast mean power at different ROIs with time at different bolus injection volumes: (a) 0.03 ml, (b) 0.05 ml, (c) 0.1 ml and (d) 0.15 ml. ....	141
Figure 4.78. Echo power of microbubbles at different bolus volumes in a multiple injection. 0.15 ml bolus volume gives the highest peak enhancement for all regions. ....	142
Figure 4.79. Change in the contrast mean power at different ROIs with time at different microbubble concentrations: (a) 8.5E+06 #/ml, (b) 1.7E+07 #/ml, (c) 1.7E+08 #/ml, (d) 2E+08 #/ml, (e) 5E+08 #/ml and (f) 1.7E+09 #/ml. ....	143
Figure 4.80. ROIs placed at the level of the cortex of the kidney parenchyma were monitored. Contrast signal was measured in 2 ROIs, drawn in the anterior cortex and the posterior cortex of rat kidney. ....	144
Figure 4.81. Change in the contrast mean power at the anterior and posterior cortex with time at different bolus injection volumes: (a) 0.01 ml, (b) 0.03 ml, (c) 0.06 ml, (d) 0.08 ml, (e) 0.1 ml, (f) 0.15 ml and (g) 0.23 ml. ....	145
Figure 4.82. Peak enhancement at different bolus volumes in the anterior and posterior cortex regions. 0.23 ml bolus volume gives the highest peak enhancement for the two regions. ....	146
Figure 4.83. Change in the contrast mean power at the anterior and posterior cortex with time at different concentrations: (a) 1.9E+07 #/ml, (b) 1E+08 #/ml, (c) 2.5E+08 #/ml, (d) 5E+08 #/ml, (e) 8E+08 #/ml and (f) 1E+09 #/ml. ....	147
Figure 4.84. Peak enhancements at different microbubble concentrations in the posterior cortex region. 2.5E+08 #/ml gives the highest peak enhancement for the posterior cortex. ....	147
Figure 4.85. Change in the contrast mean power in different ROIs with time for the commercial contrast agent and the 5:5 microbubbles. (a), (b) and (c) represent the commercial standard. (d), (e), (f) and (g) represent the 5:5 microbubbles. ....	148

<b><u>Figure</u></b>	<b><u>Page</u></b>
Figure 4.86. Peak enhancements in ROIs of the rat liver after single bolus injection of Vevo MicroMarker® contrast agents and 5:5 microbubbles. ....	150
Figure 4.87. Echogenicities of 5:5 microbubbles and Vevo MicroMarker® contrast agents in the rat kidney model. ....	150

## LIST OF TABLES

<b><u>Table</u></b>	<b><u>Page</u></b>
Table 2.1. Ultrasound contrast agent microbubbles approved for clinical use or under development (Alzaraa, Gravante et al. 2012).....	16
Table 3.1. The transmit powers and the corresponded acoustic energies.....	44
Table 4.1. Proton chemical shifts of DSPC and PEG <sub>40</sub> St.....	65
Table 4.2. Biochemical values for rats. ....	152
Table 4.3. CBC values for rats.....	153
Table 4.4. Rabbit Biochemistry Values.....	154
Table 4.5. Rabbit CBC Values.....	155

# CHAPTER 1

## INTRODUCTION

### 1.1. Overview

Ultrasound is frequently used as a medical imaging method due to its non-invasiveness, low cost and portability (Hernot and Klibanov 2008). It is a real-time modality compared to computed tomography (CT) and magnetic resonance imaging (MRI) (Overvelde, Garbin et al. 2010). Also, it is much safer than many other imaging methods since it does not use any form of ionizing radiation. However, it has a lower image quality compared with other imaging modalities (Tinkov, Bekeredjian et al. 2009). In some cases, background signals from the surrounding medium of the region of interest (ROI) reduce the image resolution, and a clear image therefore cannot be obtained. Imaging with ultrasound is based on the reflection of the transmitted sound wave at tissue interfaces, where the acoustic impedance mismatch occurs owing to inhomogeneities in the tissue. Unlike tissue, blood cells are poor ultrasound scatterers, resulting in a low contrast echo (Overvelde, Garbin et al. 2010). It is important to develop new and useful methods to improve the image quality for the accurate diagnosis. One of these methods can be the use of effective microbubbles as ultrasound contrast agents to improve the image quality while performing ultrasound (Schutt, Klein et al. 2003).

Microbubbles as ultrasound contrast agents are used in medical imaging and can be a carrier for targeted drug delivery. They are generally produced as a result of encapsulation of micron-sized gas bubbles dispersed in a physiological fluid with a phospholipid layer. Microbubbles should be stabilized in order to be used in molecular imaging and as drug-loaded carriers for therapeutic applications. Microbubbles consist of an inert gas such as perfluorocarbons (PFCs) and a stabilizing surfactant shell (Sirsi and Borden 2009, Kwan and Borden 2012). It has been shown that the choice of gas is of importance in improving the stability of microbubbles. The gas core of the microbubbles should be insoluble or partly less soluble in the physiological fluid for microbubble stability (Schutt, Klein et al. 2003, Gerber, Krafft et al. 2006). However, the shell needs to be redesigned for the increased acoustic response or “echogenicity”

while maintaining a high degree of stability whether in oscillation or at rest (Kilic and Bolukcu 2018).

The shell of a microbubble may be composed of proteins, polymers, lipids or surfactants (Hernot and Klibanov 2008, Sirsi and Borden 2009). Microbubbles coated with protein and polymer shells have been shown to demonstrate gas loss due to sonic cracking on the shell when pulsed by ultrasound. Also, previous studies showed that the protein shelled microbubbles have a tendency to adhere to vascular sites (Borden, Kruse et al. 2005, Hernot and Klibanov 2008, Sirsi and Borden 2009). On the other hand, lipid shell encapsulating microbubbles have been demonstrated to be highly echogenic owing to their flexible shells resulting from weak intra-lipid interactions (Klibanov, Hughes et al. 2002, Kim, Kim et al. 2004, Unger, Porter et al. 2004, Lozano and Longo 2009, Tinkov, Bekeredjian et al. 2009). Phospholipids alone form liposomes consisting of bilayers (Kilic and Bolukcu 2018), therefore additional components, emulsifiers, are needed to form the monolayer structure of the microbubble shell (Israelachvili, Mitchell et al. 1976, Kozlov, Lichtenberg et al. 1997). In microbubble formulations, different emulsifiers are used such as DSPE-PEG2000, DSPE-PEG5000, Tween-40, or Polyoxyethylene-40-stearate (PEG<sub>40</sub>St). PEG<sub>40</sub>St is commonly used as an emulsifying agent in the production of lipid-coated microbubbles (Borden and Longo 2002, Pu, Longo et al. 2005, Pu, Borden et al. 2006, Feshitan, Chen et al. 2009, Kwan and Borden 2010, Swanson, Mohan et al. 2010). The main function of the emulsifier is to increase the microbubble yield and stabilization. The PEG chains inhibit coalescence during microbubble generation. Additionally, they reduce non-specific adsorption of blood plasma proteins (Allen, Dos Santos et al. 2002, Immordino, Dosio et al. 2006). They also aid in the chemical modification of microbubble surfaces for biomedical applications (Kwan and Borden 2012).

Microbubbles are administered to the systemic circulation during ultrasound imaging to improve the image resolution by creating contrast with respect to the surrounding tissues. Thus, it is possible to make an earlier and a clear diagnosis of as many diseases as possible (Moriyasu and Itoh 2009). Furthermore, if these agents are targeted with antibodies or ligands sensitive to a particular intravascular disease receptor, real-time targeted imaging can be achieved through the attachment of microbubbles to the examined tissue (Dayton and Ferrara 2002, Villanueva, Lu et al. 2007). In addition, targeted agents can be used for the transfer of local substances by

loading them with drugs, genes, enzymes, DNA, etc. for therapeutic applications (Wang, Wu et al. 2009). Moreover, ultrasonography, together with these agents, creates temporary pores in the cell wall, termed sonoporation, making it easier to take up the biological molecules such as drugs, genes, DNA into cells (van Wamel, Kooiman et al. 2006).

Microbubbles oscillate rapidly contracting and expanding in response to pressure changes when exposed to an ultrasound field. Microbubbles enhance the backscattered acoustic signal, both due to a large impedance mismatch between the bubbles and the surrounding tissue, and their volumetric oscillations owing to their high compressibility. Additionally, the range of resonance frequencies for bubbles with diameters between 1 and 10  $\mu\text{m}$  is approximately 2–10 MHz which corresponds to the frequencies typically used in diagnostic ultrasound imaging. Thus, microbubbles are several thousand times more “echogenic” than normal body tissues (Mohamedi 2014). As a result of these oscillations, the microbubbles emit a secondary sound wave which includes harmonics of the insonation frequency. Thus, the reflections will contain contributions from both microbubbles and their surrounding tissue. The signal reflected from tissue is mostly linear, whereas those emitted by the microbubbles are non-linear. The signal from microbubbles can therefore be distinguished by separating the harmonic content from the signal (Azmin 2016). This further feature of microbubble behaviour can be used advantageously for diagnostics (Kwan and Borden 2012). The use of microbubbles for advanced purposes is possible through the design and fabrication of stable and robust microbubbles.

## **1.2. Motivation**

It is clear that the use of microbubbles is very promising in both diagnostic and therapeutic applications. In the literature, the number of clinical trials pointing to the activity of ultrasound contrast agents in molecular diagnosis and imaging is increasing day by day. However, only a limited number of studies have been performed on product design. The studies in the literature are mostly conducted to understand the performance of a commercially available microbubble in ultrasound applications. The main drawback of using microbubbles in ultrasound imaging is that they are unstable for extended period of time. Microbubble stability becomes more crucial in applications

such as imaging low blood flow areas, where the contrast might occur up to several minutes. Also, in targeted imaging, only a small portion of microbubbles can accumulate at the region of interest. Usage of contrast agents in imaging should have a minimum dose. This requires the high echogenicity and also high stability of the microbubbles under ultrasound. The minimum dose also reduces the cost of administration. Microbubbles are not routinely used in clinical practice due to their limited half-life. Hence, multiple injection of the contrast agent is required during imaging. It is therefore important to engineer more stable microbubbles which exhibit highly acoustic response in oscillation.

Microbubbles constantly undergo instability by a variety of mechanisms. Microbubbles' size may change during ultrasound exposure through rectified diffusion, variation of the gas core temperature, and alteration in shell composition. Such alteration to physical characteristics of a microbubble changes its acoustic response which may lower its efficacy (Azmin 2016). It has been shown that the degree of oscillation and stability of the echogenic gas core under ultrasound excitation are strongly influenced by shell composition and microstructure (Dejong, Hoff et al. 1992, Hoff, Sontum et al. 1996, Chomas, Dayton et al. 2001, Leong-Poi, Song et al. 2002, Borden, Kruse et al. 2005, Wrenn, Mleczko et al. 2009, Dicker, Mleczko et al. 2010, Wrenn, Dicker et al. 2012, Dicker, Mleczko et al. 2013, Guo, Li et al. 2013). The phosphocholine containing saturated acyl chains and the emulsifier are generally used at molar ratios of 9:1 in the formation of microbubbles (Borden and Longo 2002, Borden, Pu et al. 2005, Feshitan, Chen et al. 2009, Kwan and Borden 2010, Mulvana, Stride et al. 2010, Chen and Borden 2011, Kwan and Borden 2012, Garg, Thomas et al. 2013), and it is also assumed that the surface composition is the same as the composition of the lipid mixture (Borden, Martinez et al. 2006). To the best of our knowledge, however, studies about the effect of the microbubble shell composition at higher PEG<sub>40</sub>St contents on the acoustic response and stability of microbubbles under ultrasound activation are limited in the current literature (Hosny, Mohamedi et al. 2013).

In ultrasound-mediated drug delivery, using microbubbles alone is not a rational approach for an efficient therapeutic delivery due to their thin shells limiting the drug-carrying capacity. One of the approaches for the targeted delivery is to bind the drug-loaded nanoparticles (e.g., liposomes) to the shell of microbubbles via biotin-streptavidin linkages. The force acting on any mass on the microbubble shell

corresponds to the mass carried on the shell, according to the Newton's second law,  $\vec{F} = m \times \vec{a}$  (Chaline, Jimenez et al. 2015). If the lipids forming the shell structure of the microbubbles are in an even distribution, microbubbles will tend to oscillate spherically. However, the presence of molecules, such as liposomes or other ligands bound to microbubbles, in different molecular weights on the microbubble coatings can lead to an imbalance in the shell structure during oscillation, thus non-spherical dimensional changes occur at high ultrasonic pulses (de Jong, Emmer et al. 2009). The loadings on the surface of a microbubble shell may have significant impact on the microbubble in oscillation. Yet, the effect of the nanoparticle loadings on the acoustic response and stability of microbubbles in the acoustic field has not been extensively studied (Luan, Faez et al. 2012, Escoffre, Mannaris et al. 2013, McLaughlan, Ingram et al. 2013, Mohamedi, Rademeyer et al. 2013). Therefore, acoustic behaviour and stability of loaded microbubbles under ultrasound excitation needs to be characterized for the optimal use in clinical research.

### 1.3. Objectives

The main aim of this thesis is to increase the stability of microbubbles under ultrasound activation. For this purpose, microbubbles were fabricated by using phospholipid and emulsifier in varying compositions, and their acoustic response and stability were investigated in the acoustic field. The specific objectives were:

- To understand the role of shell composition on the *in-vitro* stability of microbubbles under ultrasound excitation.
- To develop concentration estimation method for the bolus injection technique.
- To investigate the *in-vitro* echogenicity of microbubbles with different shell compositions.
- To investigate the acoustic response of loaded microbubbles.
- To investigate the stability of loaded microbubbles under ultrasound excitation.
- To investigate the stability of microbubbles at different ultrasound powers under insonification.
- To formulate a model describing the effect of acoustic energy upon the oscillation behavior of microbubbles.

- To investigate the *in vivo* acoustic performance of in-house made microbubbles comparing to that of commercial standard Vevo MicroMarker® contrast agents.
- To investigate the *in-vivo* toxicity of in-house made microbubbles.

## CHAPTER 2

### LITERATURE REVIEW

#### 2.1. Ultrasound

##### 2.1.1. Basic Definition

Sound is produced by the vibration of objects. The sound wave from a source hits an object and reflects back and reaches its source again. The sound waves reaching its source is called echo. Sound waves travel easily through fluid medium and poorly through air (A. Sofferman 2012). Unlike electromagnetic waves, sound cannot be transmitted in vacuum. Sound waves can only propagate in a material medium. Hence, acoustic properties of the sound waves (e.g., wave velocity, attenuation, etc.) strongly depend on the properties of the medium (e.g., structure, elasticity, density, etc.) in which the waves pass through (Azhari 2010). Sound is transmitted as sequential sine waves in the medium (Figure 2.1). The height of each pulse represents its amplitude. The wave amplitude is typically expressed in terms of pressure,  $p$ . The frequency,  $f$ , termed the number of cycles per one second, is related to the wavelength,  $\lambda_w$ , and the wave velocity  $c = \lambda_w \times f$  (Azmin 2016). The frequency is generally described in Hertz (Hz). Ultrasound is defined as the mechanical pressure waves propagating within a matter medium at frequencies beyond the auditory range which is normally 20 Hz to 20 kHz (Hauff, Reinhardt et al. 2008).

In solids, ultrasound may be transmitted as both longitudinal waves in which the particles move in the same direction as the propagation, and transverse waves (or shear waves) in which the particles move in a plane perpendicular to the propagation direction. In fluids and in the majority of soft tissues, however, the waves are mainly longitudinal (Wilhjelm, Andreas Illum et al. 2013).

The speed of sound waves in any medium is constant regardless of its frequency, wavelength, and direction. When the wave passes through the material medium, a pressure gradient is formed. Acoustic impedance is defined as the ratio of the acoustic pressure to the propagation velocity.

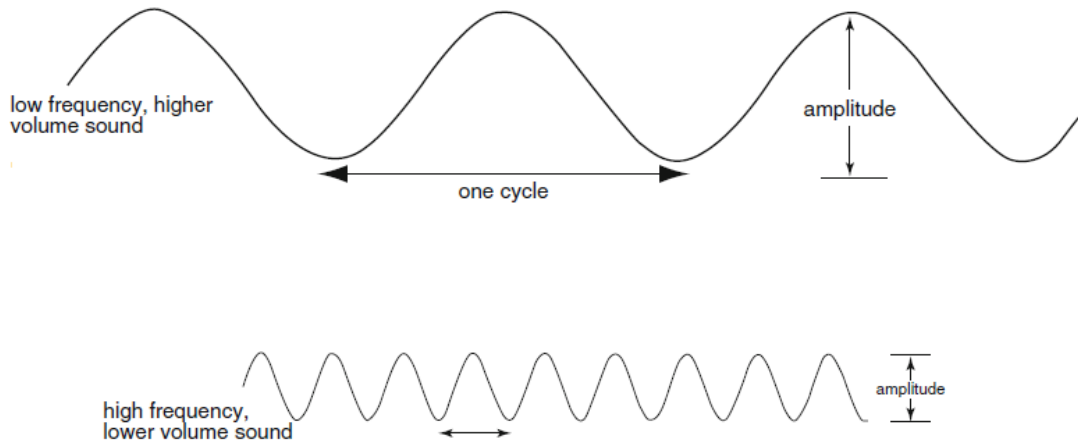


Figure 2.1. The simplest description of ultrasound as linked sine waves at low or high frequencies (A. Sofferman 2012).

The acoustic impedance at a particular frequency indicates how much acoustic pressure is produced by a given oscillation at that frequency. The acoustic impedance,  $z$ , is the result of the product of the sound velocity and density of the medium in which the sound propagates,  $z = \rho \times c$  (Wilhjelm, AndreasIllum et al. 2013). The velocity of a sound wave changes when it moves to another medium while propagating at a certain velocity. At the interface, there is no exact match between the energy of the sound wave and the medium through which it passes, causing this wave to be reflected. The intensity of the reflected and transmitted sound waves between the two mediums are shown by following equations with different acoustic impedance values (Kane, Donaldson et al. 2009):

$$\frac{I_{refl}}{I_{total}} = \frac{(z_1 - z_2)^2}{(z_1 + z_2)^2} \quad (2.1)$$

$$\frac{I_{trans}}{I_{total}} = 100\% - \frac{I_{refl}}{I_{total}} \quad (2.2)$$

where  $I_{total}$  is the total intensity of the sound wave,  $I_{refl}$  is the intensity of the reflected sound wave (echo), and  $I_{trans}$  is the intensity of the transmitted sound wave. Therefore, differences in acoustic impedance are the factors that cause sound reflection. The greater the differences in acoustic impedance, the greater the intensity of the echo. Even

if two mediums are different but have the same acoustic impedance, then no echo will occur.

Attenuation is defined as the loss of intensity (or energy) of the propagating wave with the wave traveling distance in a homogeneous medium. This phenomenon can be the result of reflection, refraction, scattering or absorption (Wilhelm, Andreas Illum et al. 2013). If dependence on frequency is neglected, the decrease in amplitude versus distance can be approximated by

$$p(x) = p_0 e^{-\alpha x} \quad (2.3)$$

where  $p_0$  is the wave pressure at some reference point in space,  $p(x)$  is the wave pressure at distance  $x$  from that reference point, and  $\alpha$  is the attenuation coefficient.  $\alpha$  depends on the medium through which the wave propagates and is approximately proportional with frequency. Eq. (2.3) can also be written in terms of intensity which is measured in  $W/cm^2$ . Intensity is proportional to the square of the pressure:  $I = p^2/z$ . Thus, one can use the following equation:

$$I(x) = I_0 e^{-2\alpha x} \quad (2.4)$$

where  $I_0$  is the intensity of the pressure wave at some reference point in space and  $I(x)$  is the intensity at distance  $x$  from that reference point. We can write the Eq. (2.4) in the following form:

$$\frac{I(x)}{I_0} = e^{-2\alpha x} \quad (2.5)$$

The intensity ratio is measured in decibel units,

$$db = 10 \log_{10} \frac{I_2}{I_1} \quad (2.6)$$

where  $I_1$  and  $I_2$  are two values measured at two defined points.

### 2.1.2. Ultrasound Imaging

In ultrasonography, ultrasonic sound waves that produce imaging are generated in pulses. The ultrasound wave can be both transmitted and detected by a piezoelectric transducer. The piezoelectric transducer can convert electrical signals (voltage) into mechanical waves, i.e., transmitting ultrasound, and *vice versa* (Hauff, Reinhardt et al. 2008). Piezoelectric crystals within the transducer undergo a shape change through elongating and shortening in response to the voltage. In ultrasound devices, ceramic discs are used as a transducer protector. The head of the transducer is called a probe. In an ultrasound system, a scanner called echoscope transmits short voltage pulses similar to ultrasound pulses used in medical imaging to the transducer. The transducer converts the voltage pulses into ultrasound pulses and emits them in the medium and then detects the returning echoes as the receiver. The echoscope records the time required for each pulse and then converts the speed of sound to the distance from the object reflecting the echo. The amplitude or A-mode signal is generated by plotting the time versus the intensity of the echo.

In the B-scan technique, the amplitude of the echo and the time taken between transmitting and receiving the sound wave are calculated and the echo is coded in different brightness (gray scale) with regard to the wave intensity (amplitude) value. This information is used to construct two-dimensional image by multiple ultrasound beams, arranged successively in one plane (Hauff, Reinhardt et al. 2008).

The spatial resolution in the image firstly depends on the wavelength of the ultrasound pulse in both the axial and lateral directions. The higher the frequency, the better the resolution, but the lower the penetration depth at which the image is required since the degree of attenuation also depends upon the ultrasound frequency. The attenuation coefficient is approximately proportional to the square of the ultrasound frequency in most of the soft tissues. Hence, in medical imaging, low frequencies are used corresponding to wavelengths in soft tissue of ~0.1-1 mm and depths of ~5-20 cm. High frequencies are used for the superficial body structures such as musculoskeletal imaging.

## 2.2. Ultrasound Contrast Agents

Today, ultrasonography is one of the main diagnostic imaging modalities used in medicine. Ultrasonography has been increasingly used for the imaging of body organs and for the diagnosis of diseases. It has no known side-effect compared to other imaging modalities such as magnetic resonance (MR), computed tomography (CT), angiography etc. In ultrasonography, ultrasound images are created as a result of the reflection of the sound waves from the transducer. However, in some cases, background signals from the surrounding tissues and the signals from the tissues with nearly the same acoustic impedance can reduce the sensitivity of the method and thus a clear image could not be obtained for the accurate diagnosis (Klibanov 2002). This may make diagnosis difficult and/or may lead to misdiagnosis. Ultrasound contrast agents can be used to improve the quality and resolution of ultrasound images. Contrast agents injected into systematic circulation during imaging create contrast by increasing the scattering and reflection of ultrasonic waves at different frequencies than that of the acoustic signals reflected from the surrounding tissues, as seen in Figure 2.2 (Schutt, Klein et al. 2003, Hernot and Klibanov 2008).

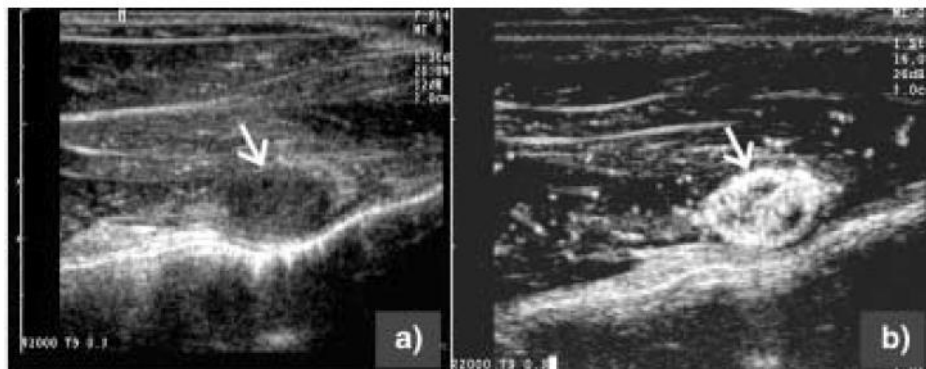


Figure 2.2. Images of tumor in the thigh of a rabbit before (a) and after (b) the injection of ultrasound contrast agents. The tumor becomes extremely bright relative to the surrounding tissue when the microbubbles injected (Schutt, Klein et al. 2003).

Microbubbles are ultrasound contrast agents which are typically defined as gas particles of 1-10  $\mu\text{m}$  in diameter encapsulated with a monolayer (Figure 2.3) (Sirsi and Borden 2009). In the late of 1960's, the use of ultrasound contrast agent microbubbles

was first introduced in echocardiography by Gramiak and Shah (Gramiak and Shah 1968), which was a serendipitous discovery. The improvement in image quality with free air bubbles obtained by well shaking the saline solution and injecting it into the body, scattering of ultrasound by air bubbles, thus increasing the image resolution were the first steps taken in this field (Nanda, Shah et al. 1976). Subsequently, other studies using different contrast agents such as Renografin, indocyanine green dye, and dextrose have been performed, and they demonstrated similar effects. However, these formulations could not remain stable enough in the body, since they were unable to pass through the pulmonary capillaries, dissolved vary rapidly and were removed by filtration in the lungs (Meltzer, Sartorius et al. 1981). Injecting gas bubbles into the body by encapsulating them into amphiphilic lipids, polymers, or a denatured protein-based monolayer (shell) has been proposed as a solution for the effective use of ultrasound contrast agents. According to the Epstein-Plesset theory (Epstein and Plesset 1950), this monolayer both reduces the gas-liquid surface tension and resists the diffusion of gas into the liquid, hence, improving the half-life of the microbubbles. Encapsulation also improves persistence against microbubble coalescence, and it gives a more standard size distribution. Since then, contrast agents consisting of different gas or gas mixtures such as air, nitrogen, oxygen, SF<sub>6</sub>, and fluorinated hydrocarbon gases, including C<sub>3</sub>F<sub>8</sub>, C<sub>4</sub>F<sub>10</sub> and C<sub>5</sub>F<sub>12</sub>, and different monolayer material combinations have been designed and performed *in-vivo* and *in-vitro*.

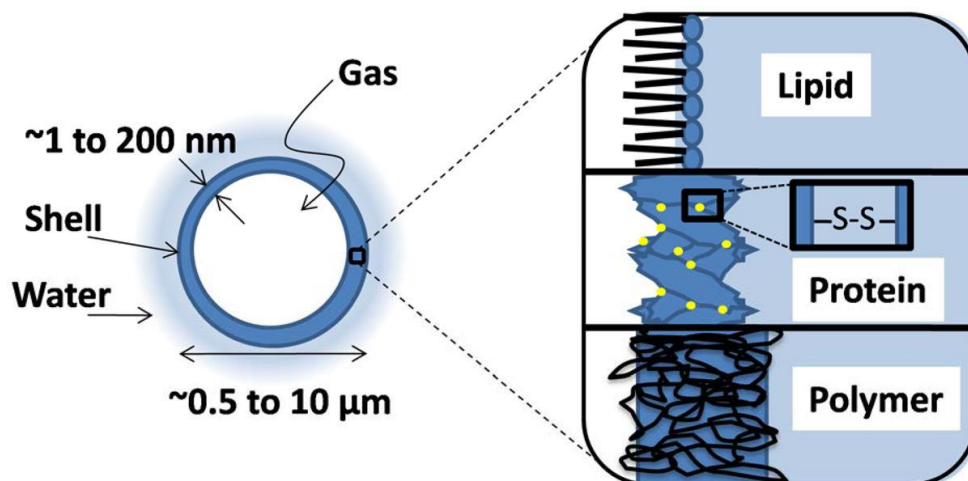


Figure 2.3. A typical microbubble with various coating monolayers (Sirsi and Borden 2009).

Amphiphilic lipids, denatured proteins, or polymers can be used as stabilizing agents for the encapsulation of the gas core. However, in studies with denatured protein-based or polymeric microbubbles, the sonic cracking occurred in their shells which are not elastic due to its rigidity and thus the gas was quickly separated from the microbubble shell by diffusion (Chomas, Dayton et al. 2001, Leong-Poi, Song et al. 2002, Bloch, Wan et al. 2004). In addition, since the polymers and proteins are not sufficiently elastic, it has been concluded that the microbubbles coated with polymers and proteins are less echogenic. However, since the lipid molecules form flexible layer around the gas core, lipid-based microbubbles are found to be more echogenic due to their increased resonating ability under ultrasound excitation (Figure 2.4). In addition, lipid-based microbubbles can freely circulate in the bloodstream without attaching to the endothelial cells. This may be advantageous for the *in-vivo* applications. They can also more likely decrease the adverse immune response in the body compared with the protein coated microbubbles, if these phospholipid coated agents are emulsified with polyethylene glycol (PEG) (Stride and Edirisinghe 2008, Lentacker, De Smedt et al. 2009). Moreover, it is easier to target lipid-based microbubbles for use in drug, gene, and DNA transfer by marking them with ligands or antibodies specific to a particular disease receptor (Borden, Pu et al. 2004).

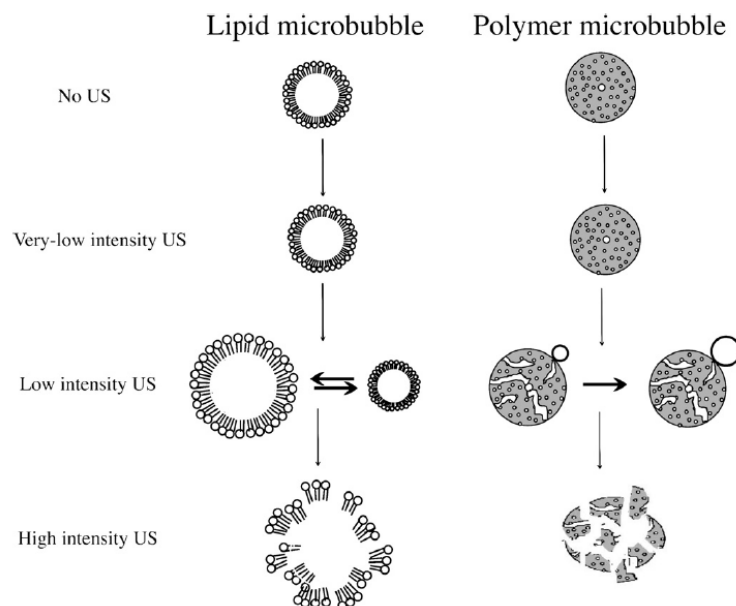


Figure 2.4. Schematic representation of the acoustic behavior of lipid and polymer microbubbles with increasing amplitude of ultrasound (Hernot and Klivanov 2008).

Contrast agents should have a long-term stability and flexibility for maximum acoustic signaling in order to be used effectively in molecular diagnosis and imaging, and even in the transfer of local substances such as drugs, DNA and genes (Schutt, Klein et al. 2003, Ferrara, Pollard et al. 2007, de Jong, Emmer et al. 2009). Yet, it is not known exactly what mechanisms cause the contrast agents to be disappeared after being injected into the blood. It has hypothesized that the gas dissolves into the blood (Kabalnov, Bradley et al. 1998, Kabalnov, Klein et al. 1998). There are mainly two approaches in the design of stable, robust microbubbles: one is to use gases with low solubility, and the other is to redesign a cohesive layer with high attractive forces (Kilic and Bolukcu 2018). The solubility of air in water is higher than that of perfluorocarbons. It is therefore expected that the microbubbles filled with inert low-soluble gases such as perfluorocarbons may persist in the bloodstream for a longer period of time. As a matter of fact, this has been observed in experimental studies (Schutt, Klein et al. 2003). The first generation of encapsulated microbubbles, e.g. Albunex<sup>®</sup>, was fabricated from air-filled human albumin (Kasprzak and Ten Cate 1998). Optison<sup>®</sup> contrast agents, which was a second generation of microbubbles, were filled with octafluoropropane gas, and they improved the half-life of microbubbles (Correas, Bridal et al. 2001, Mayer and Grayburn 2001).

Microbubbles are used in many areas (Tinkov, Bekeredjian et al. 2009, Suzuki, Oda et al. 2011). It has been reported that microbubbles are used in oxygen (Borden and Longo 2004, Swanson, Mohan et al. 2010), Nitric Oxide (NO) (Postema, Bouakaz et al. 2006), and drug/gene/DNA transfer (Borden, Caskey et al. 2007, Ferrara, Pollard et al. 2007, Suzuki, Oda et al. 2011). Microbubbles are actively used for drug/gene/DNA loading into cells by sonoporation (Kudo, Okada et al. 2009). In the sonoporation method, microbubbles near the cell membrane or adsorbed to the surface are shown to increase the transport due to the jetting formation under ultrasound excitation (Kudo, Okada et al. 2009, Qin, Caskey et al. 2009, Wang, Wilson et al. 2013, Yu, Lin et al. 2015).

There are a vast number of studies in the literature pointing to the advantages of using microbubbles under ultrasound activation. Development of microbubbles is mainly carried out by companies in US and Europe for commercial purposes today. Most of the clinical trials reported in the literature use microbubbles that are commercially developed or under development (Table 2.1). In a review article,

information about the properties and usages of contrast agents that are commercially developed or under development were summarized (Mayer and Grayburn 2001). It was shown that stabilities of the developed microbubbles were very low. For example, a FDA-approved Definity<sup>®</sup>, commercially available on the market, consists of homogenized lipid solution with a headspace containing octafluoropropane gas. Prior to the bolus injection, the solution is agitated with a high-speed device used in dental applications to form microbubbles. Only 5 minutes of imaging could be performed with a bolus injection of Definity<sup>®</sup> microbubbles for the imaging of the left ventricle of the heart (Williams, Hudson et al. 2011). In case of another FDA-approved contrast agent, Optison<sup>®</sup>, octafluoropropane gas was stabilized with denatured human serum albumin, where the shell was in matrix form and contained covalent linkages. Optison<sup>®</sup> microbubbles adhered to the cell walls in blood vessels and had a half-life of 31-78 seconds (Mayer and Grayburn 2001). Moreover, their echogenicities were quite low due to the covalent bonds in the shell monolayer (De Jong et al., 2009). The contrast agent, SonoVue<sup>®</sup>, approved for use in Europe, is suitable for the imaging of the left part of the heart. SonoVue<sup>®</sup> microbubbles in the form of powder were obtained by freeze-drying of the lipid solution, mainly composed of palmitic acid, DSPC and DPPG, and then filled with sulfur hexafluoride gas and stored in special small vials. SonoVue<sup>®</sup> microbubbles were re-suspended in a pharmaceutically acceptable liquid prior to administration to the patient for the imaging. SonoVue<sup>®</sup> had a half-life of 7 minutes for females and 5 minutes for males (Mayer and Grayburn 2001).

In a study by Mulvana et al. (Mulvana, Stride et al. 2011), the effect of temperature on the acoustic behavior of SonoVue<sup>®</sup> microbubbles was investigated. SonoVue<sup>®</sup> microbubbles maintained their spherical shapes during insonation at room temperature within 25 milliseconds; however, at body temperatures the shell structure of microbubbles was disrupted or even collapsed. Another contrast agent, Imagent<sup>®</sup>, under development consists of lipid-based microbubbles containing perfluorohexane/air mixture. Imagent<sup>®</sup> microbubbles were known to be capable of imaging with an average of 2.6 minutes in the heart ventricle chambers.

Villanueva et al. (Kilic, Lu et al. 2005, Villanueva, Lu et al. 2007) examined the *in-vivo* pharmacokinetic behavior of microbubbles containing the decafluorocarbon gas (n-C<sub>4</sub>F<sub>10</sub>) prepared in different formulations through intra-vital microscopy. The pharmacokinetic behavior of the microbubbles and their echogenicity under ultrasound

excitation differed from each other and it was concluded that the composition of the shell monolayer significantly affected the properties of the microbubbles. In these studies, FDA-approved Definity<sup>®</sup> and Optison<sup>®</sup> microbubbles were compared with in-house microbubbles, and it was found that the non-commercial microbubbles were found to have superior performance over Definity<sup>®</sup> and Optison<sup>®</sup> microbubbles in both echogenicity and half-life (Kilic, Lu et al. 2005, Villanueva, Lu et al. 2007).

Table 2.1. Ultrasound contrast agent microbubbles approved for clinical use or under development (Alzaraa, Gravante et al. 2012).

Microbubble	Company	Shell	Gas	Size, $\mu\text{m}$	Charge	Storage	Preparation	Approval
Albunex	Mallinckrodt, Inc (St Louis, MO)	Albumin	Air	—	—	—	—	—
Cardiosphere/Bisphere	Point Biomedical, Corp (San Carlos, CA)	Poly lactide/albumin	Nitrogen	4.0	Slight negative	—	Reconstitute with 2 mL H <sub>2</sub> O per vial and dilute with 150 mL distilled water	No
AI-700	Acusphere, Inc (Lexington, MA)	Poly-L-lactide co glycolide	Perfluorocarbon	2	Negative	—	Reconstitute with water	No
Optison	Molecular Biosystems, Inc (San Diego, CA)	Albumin N-acetyltryptophan, Caprylic acid	Octafluoropropane	2–4.5	Slightly negative	Refrigerate 2°C–8°C	Hand agitate	United States/Europe
Definity	Bristol-Myers Squibb Medical Imaging, Inc (New York, NY)	Lipids: DPPA, DPPC, MPEG5000 DPPE/surfactant	Octafluoropropane	1.1–3.3	Negative	Refrigerate 2°C–8°C	Activate through Vialmix agitation	United States
Imagent/Imavist	Imcor Pharmaceuticals, Inc (San Diego, CA)	Lipid: DMPC/surfactant	Perfluorohexane/nitrogen	6.0	Neutral	Room temperature 15°C–30°C	Reconstitute with 10 mL water	United States
Sonovue	Bracco Diagnostics (Princeton, NJ)	Lipids: Macrogol 4000, DSPC, DPPG, Palmitic acid	Sulfurhexafluoride	2–3	Negative	No special storage conditions required	Reconstitute with 5 mL saline	Europe
Levovist	Shering AG (Berlin, Germany)	Galactose/palmitic acid	Air	2–4	Negative	Room temperature 15°C–30°C	Reconstitute with 5–17 mL water	Europe/Japan
Sonazoid	GE Healthcare (Piscataway, NJ)	Lipid	Perfluorobutane	2.4–3.6	Negative	—	Reconstitute with 2 mL water	No
Sonovist	Shering AG (Berlin, Germany)	Cyanoacrylate (polymer shell)	Air	1–2	—	—	—	No
Echovist	Shering AG (Berlin, Germany)	D-galactose	Air	—	—	<30°C	Reconstitute with water	Europe
BR14	Bracco diagnostic (Princeton, NJ)	Lipid	Perfluorobutane	2.5–3.0	Negative	—	—	—
EchoGen	Sonus pharmaceuticals (Bothell, WA)	—	Dodecafluoropentane	—	Negative	Refrigerate 2°C–8°C	—	—

In previous studies, it was suggested that the parameters affecting the *in-vivo* stability of microbubbles were gas diffusion, mechanical degradation of the microbubble shell structure under ultrasound excitation, and removal of the microbubbles by the reticuloendothelial system, including the macrophages of liver and spleen. In a study by MorAvi et al. (MorAvi, Robinson et al. 1997), it was observed that the stability of Albunex<sup>®</sup> microbubbles decreased with both increasing temperature and acoustic effect. It was also found that microbubbles containing perfluorocarbon gas with

the same shell material as Alburnex<sup>®</sup> were less affected by temperature and acoustic effects.

Borden et al. performed a vast number of studies on microbubbles prepared in the form of a suspension of phospholipids containing choline in different hydrocarbon lengths and a fatty acid conjugated with polyethylene oxide as emulsifier (Borden and Longo 2002, Borden and Longo 2002, Borden, Pu et al. 2003, Borden, Dayton et al. 2004, Borden, Pu et al. 2004, Borden, Kruse et al. 2005, Borden, Pu et al. 2005, Borden, Martinez et al. 2006). In these studies, the phase behaviors of the shell structure which mainly formed microbubbles were investigated. There were limited studies on the behavior of these microbubbles under ultrasound excitation (Borden, Martinez et al. 2006). Cox et al. studied the behavior of the saturation degree of the hydrocarbon chain at the tail of the phospholipids under ultrasound excitation (Cox and Thomas 2010). In general, the degree of saturation in the phospholipid hydrocarbon chain did not significantly affect the size of the insonified microbubbles at initial sizes of 10 microns and above, however in the sizes of 2-10 microns, microbubbles composed of phospholipids containing unsaturated bonds in the hydrocarbon chain rapidly decreased in size.

### **2.3. Microbubble Generation**

There are several methods for creating lipid-coated microbubbles. The microbubble shell assembly process can mainly include either mechanical disruption of the gas-liquid interface or injection of a gas stream that is induced to break up into a bubble sequence. Each method has its own advantages and disadvantages. Mechanical disruption techniques such as sonication and high-speed homogenization (Hilman, Hoffmann et al. 1984) are readily available and economical and produce large quantities of microbubbles (typically  $\sim 10^9$  microbubbles per milliliter in a few seconds), but they create polydisperse size suspensions. Gas injection methods produce microbubbles in a monodispersed population, but these methods are not cost effective and have a high processing time and manufacture much lower yields (typically  $\sim 10^6$  microbubbles per milliliter over several hours). Today, the economy and quality of microbubble production are enhanced through advances in both methods (Talu, Hettiarachchi et al. 2008, Ferrara, Borden et al. 2009).

Sonication is the most widely used method for microbubble fabrication. In this technique, using high intensity ultrasound, a gas is dispersed in a suspension of a desired coating material (Feinstein, Shah et al. 1984, Unger, Porter et al. 2004, Stride and Edirisinghe 2008). During the formation of the phospholipid microbubbles by sonication, gas bubbles are generated by cavitation in the liquid using a tip sonicator at the air/liquid interface. Phospholipids, which are in the form of multilayer and/or bilayer vesicles (liposomes) in the liquid, form the microbubbles by condensing around the gas bubbles in the liquid. Because of the surface tension at the gas-liquid interface, the phospholipids separate from the vesicles and adsorb to the surface of the gas bubbles. It is postulated that the phospholipid adsorption continues until the equilibrium surface tension at the gas surface is 25 mN/m (Borden 2009, Kwan and Borden 2012). On the other hand, after the phospholipid molecules adsorb onto the surface, the gas inside the microbubbles dissolves under the Laplace pressure and the dissolution continues until the intermolecular distances between the lipids reach to a certain equilibrium value. Hydrophobic and van der Waals forces become more dominant as the molecules come together and molecules are oriented to minimize the surface tension. It is known that the use of low water-soluble perfluorocarbons instead of air when producing microbubbles increases the lipid adsorption and thus the stability of the microbubbles (Szijarto, Rossi et al. 2012). The microbubbles produced with more hydrophobic gases compared to air are smaller in size (Szijarto, Rossi et al. 2012). The size distribution and concentration of the resulting bubble population depend upon the pulse regime, power, frequency of the sonic waves and the processing time (Feinstein, Keller et al. 1989, Zhou, Cavalieri et al. 2011).

The microbubble formation mechanism was illustrated by Kwan and Borden (Figure 2.5) (Kwan and Borden 2012). Molecules on the surface of microbubbles are considered to form solid-like condensed and fluid-like expanded phases by phase separation during the microbubble formation (Kim, Costello et al. 2003, Borden, Martinez et al. 2006, Borden 2009, Lozano and Longo 2009, Kwan and Borden 2012, Schutt, Ibsen et al. 2014).

Emulsifier molecules with a much larger head group compared to phospholipids are considered to be in the expanded phase, exhibiting resistance to lipid condensation. Although it appears that this may adversely affect the microbubble stabilization, emulsifier molecules are required for microbubble formation. Studies showed that

phospholipids did not form microbubbles on their own (Borden, Dayton et al. 2004, Abou-Saleh, Swain et al. 2014). When phospholipids were dispersed in aqueous phase on their own, they became the thermodynamically stable liposomes (Kozlov, Lichtenberg et al. 1997). Liposomes are the spherical form of bilayer structures formed by the phospholipid molecules in the aqueous phase. Microbubbles are spherical structures formed by adsorption as a monolayer at the gas-liquid interface. They are in foam-like structures because the density of the gas is much lower than that of the liquid. Phospholipids serve as a barrier at the gas-liquid interface to prevent gas diffusion. Hence, the gas bubble surface must be completely surrounded by the molecules in order to minimize the surface tension at the gas-liquid interface, thereby increasing the stabilization of the microbubbles.

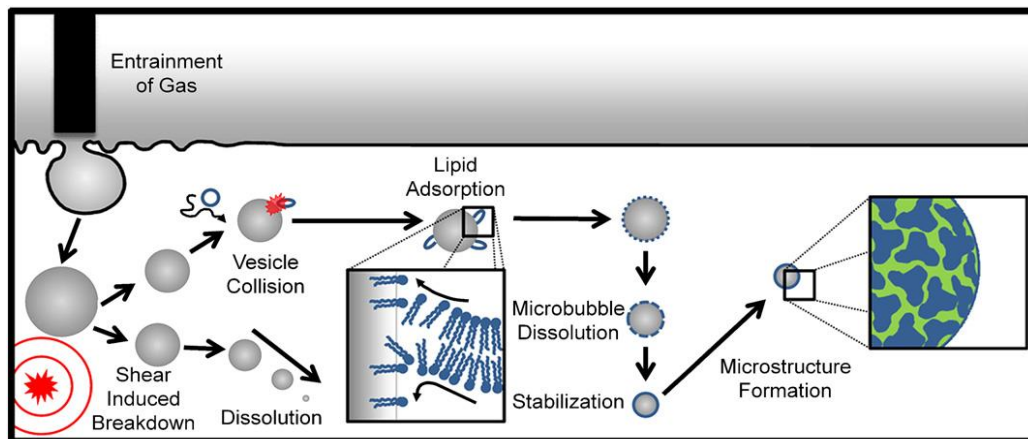


Figure 2.5. Schematic representation of the microbubble formation mechanism (Kwan and Borden 2012).

## 2.4. Stability of Microbubbles

### 2.4.1. Static Diffusion

A microbubble suspension is thermodynamically unstable since the free energy of the system is minimized in case of entirely separation of the gas phase from the liquid medium (Kwan and Borden 2012). The gas/liquid interfacial tension which imposes pressure on the microbubble surface and the gas concentration gradient between the microbubble surface and the bulk medium are the factors leading to a finite

stability of microbubbles (Azmin 2016). The effects of capillarity must be considered to understand the dissolution behavior of microbubbles (Kwan and Borden 2012). The surface energy can be shown as a Laplace capillary pressure ( $P_L$ ) inside the spherical gas bubble suspended in an infinite volume of liquid and is expressed as:

$$P_L = \frac{2\sigma}{R} \quad (2.7)$$

where  $\sigma$  is the surface tension and  $R$  is the radius of the microbubble. The liquid pressure can change by an external oscillating pressure field, leading to alteration of the gas pressure inside the bubble. According to Henry's Law which applies at the gas/liquid interface, the local concentration of dissolved gas in the liquid next to the bubble wall is increased by the Laplace pressure. Gas dissolution occurs due to a concentration gradient between the microbubble surface and the surrounding medium. For an uncoated microbubble in a liquid of infinite volume at constant temperature and pressure, Epstein and Plesset (Epstein and Plesset 1950) derived the following equation to predict the rate of change of microbubble size, neglecting convection and transients in the concentration gradient:

$$\frac{dR}{dt} = -DK_HBT \frac{1 - f + \frac{2M_w\sigma}{\rho BTR}}{1 + \frac{4M_w\sigma}{3\rho BTR}} \left(\frac{1}{R}\right) \quad (2.8)$$

where  $D$  is the diffusivity of the gas,  $f$  is the gas saturation fraction of the surrounding medium,  $\rho$  is the density of the suspension medium,  $t$  is time,  $K_H$  is the Henry's constant for the gas,  $B$  is the ideal gas constant,  $T$  is the temperature, and  $M_w$  is the molecular weight of the gas. The Epstein–Plesset equation (Eq. (2.8)) shows that the microbubbles can be stable in such a condition either the medium is fully gas-saturated ( $f = 1$ ) or the apparent surface tension is very low ( $\sigma \rightarrow 0$ ). The latter greatly depends upon the microbubble shell structure, which typically contains a phospholipid and an emulsifying agent (Klibanov 1999, Klibanov 2002, Kwan and Borden 2012). Whether the liquid in which the microbubbles are suspended is saturated in terms of gas solubility, the presence of other gases dissolved in the medium, temperature, etc., affect the stability of microbubbles (Borden and Longo 2001, Borden and Longo 2002, Borden, Pu et al.

2003, Borden, Pu et al. 2004, Shen, Powell et al. 2008). The dissolution kinetics of coated microbubbles in an unsaturated liquid was investigated by Borden et al. (Borden and Longo 2002) and the following equation was derived for the change in microbubble size:

$$-\frac{dR}{dt} = \frac{H}{\frac{R}{D_w} + R_{shell}} \left( \frac{1 + \frac{2\sigma}{P_a R} - f}{1 + \frac{4\sigma}{3P_a R}} \right) \quad (2.9)$$

where  $H$  is the Ostwald coefficient for the gas solubility in the aqueous phase,  $P_a$  is the ambient pressure, and  $R_{shell}$  is the mass transfer resistance of the microbubble shell to gas permeation. In general, microbubble size decreases in the liquids where the gas solubility decreases, and the microbubbles undergo dissolution and disappear in the medium. The shrinkage in microbubble size continues to accelerate in time (Borden and Longo 2002). This is because the shell resistance of microbubbles decreases as the microbubble size decreases (Shen, Powell et al. 2008). In other words, as the size of the microbubbles decreases during the dissolution, the microbubble dissolution rate increases over time as the microbubble shell resistance to dissolution decreases. The resistance of microbubbles to gas transport has been shown to be increased by the acyl chain length in the shell structure, these microbubbles therefore are more stable (Borden and Longo 2002, Lozano and Longo 2009).

## 2.4.2. Rectified Diffusion

Gas bubbles have been observed to grow slowly during insonation due to an average flow of mass into the bubble over time through a process known as rectified diffusion (Crum 1984). While a stationary free gas bubble will eventually dissolve in liquids that are not over-saturated with gas, with the presence of an applied acoustic field, bubbles start to oscillate, and these oscillations can cause them to increase in size because of two mechanisms underlying this process: the area effect and the shell effect. In the area effect, although gas diffusion occurs in both directions across the bubble surface due to the varying pressure gradient, more gas diffuses into the bubble during expansion than will diffuse outwards into the liquid during compression. This is because the surface area of the bubble will be smaller during contraction than during expansion

(Stride and Coussios 2010). In the shell effect, a spherical shell of liquid surrounding the bubble is considered. Since the diffusion rate of gas in a liquid is proportional to the gradient of the concentration of dissolved gas, the local concentration of gas in the liquid near the bubble wall will be higher during bubble expansion than during contraction. This again enhances inwards diffusion (Crum 1984).

Whether or not a bubble undergoes rectified diffusion depends on its initial size, the wave frequency, the acoustic pressure, and the solubility and the concentration of dissolved gas. For free gas bubbles, approximate thresholds for rectified diffusion have been determined and reported elsewhere (Crum 1984, Church 1988). However, the observation of bubble growth in the presence of coated bubbles has been attributed to other reasons (Kwan and Borden 2010). It seems that this is still an area of some controversy (Azmin 2016).

### **2.4.3. Stability from Surface Coating**

Addition of a coating material can considerably change the durability of a microbubble. Fyrrillas and Szeri have investigated the effect of an adsorbed surfactant layer upon gas diffusion for insonating microbubbles (Fyrrillas and Szeri 1995). They found that a soluble surfactant could either enhance or inhibit bubble growth by rectified diffusion, depending on the acoustic exposure parameters. This was in agreement with the experimental findings by Crum (Crum 1984). The concentration of molecules adsorbed on the microbubble surface can also have a significant effect upon vibrations of microbubbles, which presumably cause alteration in bubble behaviour over time which have been observed in experiments (Guidi, Vos et al. 2009).

Experimental evidence suggest that the surfactant molecules may be detached from the monolayer shell through a process known as lipid shedding during oscillation (Borden, Kruse et al. 2005). O'Brien et al. derived theoretical models for this phenomena and investigated the effect of the lipid shedding mechanism upon size and acoustic responses of microbubbles (O'Brien, Ovenden et al. 2011). Morris et al. studied dynamic behaviour of lung surfactant and they suggested different regions where surfactant shedding occurs (Morris, Ingenito et al. 2001). They hypothesized that lipid shedding occurs when the maximum surfactant concentration limit is exceeded at large amplitudes of oscillation and microbubbles then reach steady state after a number of

pulses. Alteration in microstructure of the bubble or decrease in amplitude of oscillation may be the reasons of this phenomenon since the microbubble size is not its resonant size at steady-state (Azmin 2016).

## **2.5. Acoustic Properties of Microbubbles**

Acoustic response of a microbubble to an ultrasonic wave depends on various factors such as shell composition, size and concentration of the microbubble, physiochemical properties of the coating material and the properties of the surrounding medium. Environmental parameters such as frequency and pressure amplitude or acoustic power of the ultrasound field can also affect the acoustic response. Acoustic power is defined as mechanical index (MI) in echocardiography to give the operator information about the magnitude of energy administered to a patient examination (Sen, Tufekcioglu et al. 2015). MI is proportional to the peak-negative pressure of the excitation pulse at a certain frequency,  $MI = P_r / \sqrt{f_c}$  (Yeh and Su 2008). Here,  $P_r$  is the ultrasonic pressure defined as 0.3 dB/cm/MHz, and  $f_c$  is the center frequency. At very low acoustic powers ( $MI < 0.05-0.1$ ), the microbubbles undergo symmetrical oscillations that are primarily linear (Hernot and Klibanov 2008). In this case, ultrasound scattering is generated with a frequency equal to the transmitted frequency (linear backscatter). At a slightly higher MI of 0.1 to 0.3, the bubble expands more than it contracts, thus leading to non-linear oscillations. The frequency at which the amplitude of oscillation is maximized becomes dependent on pressure. This phenomenon is referred to as stable or non-inertial cavitation. The backscatter contains not only the frequency of the incident acoustic field but also a variety of frequencies (harmonics, sub-harmonics and ultra-harmonics) which considerably improves the bubble-to-tissue backscatter signal ratio in the harmonic imaging techniques (Burns, Powers et al. 1994, Vannan, Burns et al. 1998). At even higher acoustic powers ( $MI > 0.3-0.6$ ), the microbubbles undergo forced expansion and compression, and their oscillations become chaotic. Violent collapse of microbubbles occurs and a shock wave is released. Eventually bubbles often undergo complete fragmentation giving smaller bubbles. This process is referred to as inertial or transient cavitation. For example, microbubbles exposed to an ultrasonic propagation of approximate 25 pulses at 2.25 MHz were fragmented into daughter bubbles with about 1.5  $\mu\text{m}$ -2.5  $\mu\text{m}$  in size (Borden,

Kruse et al. 2005, Cox and Thomas 2010, Tang, Mulvana et al. 2011). Cavitation is an important phenomenon which can be used in drug delivery in the presence of microbubbles. Oscillations of microbubbles in an acoustic field can encourage physiological changes that enhance extravasation of drugs into target cells and tissues (Sirsi and Borden 2014). This can be achieved by increased permeability of the cell membrane through violent collapse of the microbubbles (inertial cavitation) or mechanical agitation of a stably oscillating microbubble (stable cavitation) near the boundary of the cell or vessel wall. This event may facilitate the drug uptake (Figure 2.6).

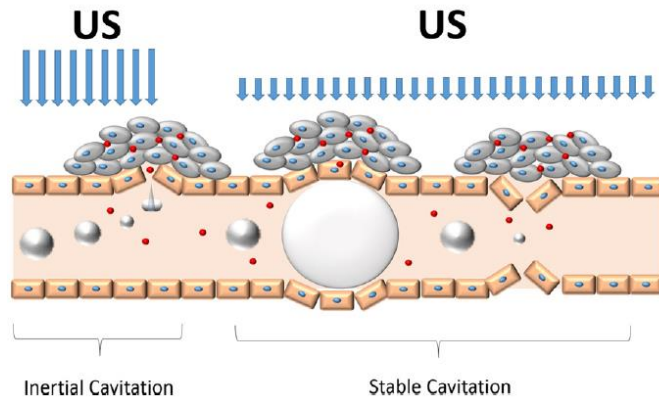


Figure 2.6. Enhanced drug extravasation at high mechanical index through inertial cavitation (Sirsi and Borden 2014).

Thus far, fundamental dynamic equations for nonlinear oscillations of free and coated gas bubbles and their modified versions were derived by several investigators. The model developed by Rayleigh-Plesset (Rayleigh 1917, Plesset 1949) provides the theoretical basis for the nonlinear vibration of microbubbles. Their model was developed with subsequent works and the resulting equation, commonly called Rayleigh-Plesset-Noltingk-Neppiras-Poritsky (RPNNP), is given as

$$\rho_l \left( R\ddot{R} + \frac{3}{2}\dot{R}^2 \right) = \left( p_0 + \frac{2\sigma}{R_0} \right) \left( \frac{R}{R_0} \right)^{-3\kappa} \left( 1 - \frac{3\kappa}{c} \dot{R} \right) - \frac{2\sigma}{R} - \frac{4\mu\dot{R}}{R} - p_0 - P_{ac}(t) \quad (2.10)$$

where  $R_0$  is the initial bubble radius,  $\dot{R}$  and  $\ddot{R}$  are the velocity and acceleration of the bubble wall, respectively,  $\rho_l$  is the density of the liquid,  $\mu$  is viscosity of the surrounding

liquid,  $p_0$  is the ambient pressure,  $P_{ac}(t)$  is the applied acoustic field,  $\kappa$  is the polytropic gas exponent, and  $c$  is the speed of sound. In this model, the bubble is considered spherical, and is suspended in an infinite body of liquid. It is assumed that the liquid is incompressible and that its viscosity is constant (de Jong, Emmer et al. 2009, Azmin 2016).

Ultrasound contrast agent microbubbles are encapsulated bubbles, and therefore the effect of encapsulation must be taken into account to describe their dynamic behaviour in an acoustic field. The shell itself increases both the resonance frequency of the microbubble due to its stiffness and damping due to its viscosity (de Jong, Emmer et al. 2009, Doinikov, Haac et al. 2009). De Jong et al. modeled the dynamic oscillations of encapsulated microbubbles for the first time in 1992 (Dejong, Hoff et al. 1992). Experimentally determined elasticity and friction parameters were incorporated to the RPNNP equation by a subsequent work (Dejong and Hoff 1993). For phospholipid-coated bubbles, the model was modified by substantial experimental results based on various investigators' studies, resulting in (Marmottant, van der Meer et al. 2005, de Jong, Emmer et al. 2009, Qin, Caskey et al. 2009, Tu, Guan et al. 2009, Overvelde, Garbin et al. 2010, Sijl, Overvelde et al. 2011, Helfield, Chen et al. 2016):

$$\rho_l \left( R\ddot{R} + \frac{3}{2}\dot{R}^2 \right) = \left( p_0 + \frac{2\sigma(R_0)}{R_0} \right) \left( \frac{R}{R_0} \right)^{-3\kappa} \left( 1 - \frac{3\kappa}{c} \dot{R} \right) - \frac{2\sigma(R)}{R} - \frac{4\mu\dot{R}}{R} - \frac{4\kappa_s\dot{R}}{R^2} - p_0 - P_{ac}(t) \quad (2.11)$$

where  $\kappa_s$  is the surface dilatational viscosity, and  $\sigma(R)$  is the effective surface tension. The extra viscosity term,  $4\kappa_s/R^2$ , is included for the microbubble shell in the RPNNP equation and this coating parameter results in oscillation damping of the microbubble (de Jong, Emmer et al. 2009, Tu, Guan et al. 2009, Sijl, Overvelde et al. 2011). In the Eq. (2.11), the surface tension ( $\sigma$ ) depends on the microbubble radius. There are three regimes for the effective surface tension at the bubble wall: elastic, buckled and ruptured (Marmottant, van der Meer et al. 2005). In the buckled regime,  $\sigma(R)$  is zero where the shell buckles for radii below the buckling radius  $R_{\text{buckling}}$ . The lower limit is  $R_{\text{buckling}}$ , and the upper limit,  $R_{\text{break-up}}$ , is fixed by the maximum surface tension,  $\sigma_{\text{break-up}}$ , before rupture of the shell. In the elastic state, the shell has an elastic oscillation in a

narrow range of  $R_{\text{buckling}}$  and  $R_{\text{break-up}}$ . In the ruptured state, the shell ruptures at  $\sigma_{\text{break-up}}$  when the radius is equal to or greater than  $R_{\text{ruptured}}$ , and  $\sigma(R)$  saturates at the surface tension of water,  $\sigma_{\text{water}}$ , due to exposing of the bare gas to the liquid directly. In this model, the oscillation of bubbles is limited to small acoustic amplitudes where radius is linear with the pressure and the surface tension is constant. However, at large pressure amplitudes microbubbles will give original nonlinear responses (de Jong, Emmer et al. 2009).

Both the viscosity and the elastic modulus of microbubbles increase with the microbubble size, as shown experimentally in previous reports (Tu, Guan et al. 2009, Parrales, Fernandez et al. 2014). Larger microbubbles can perform more flexible oscillations under ultrasound excitation. However, when their size rises above the critical size, they undergo fragmentation leading to smaller daughter microbubbles (Qin, Caskey et al. 2009). It was also reported that the microbubbles in smaller sizes are more rigid and show less oscillations in the acoustic field because they are less elastic and have lower viscosity.

The intensity of ultrasound scattered by nonresonant microbubbles which are much smaller than the wavelength of the ultrasound radiation is given by (Ophir and Parker 1989, Dejong, Tencate et al. 1991, Vanliew and Burkard 1995, MorAvi, Robinson et al. 1997, Villarraga, Foley et al. 1997, Kabalnov, Klein et al. 1998, Klibanov 2002, Schutt, Klein et al. 2003)

$$\frac{I}{I_0} \sim \frac{1}{9} n V \frac{k^4 r^6 (\gamma_c + \gamma_d \cos\theta)^2}{d^2} \quad (2.12)$$

where  $I$  is the scattered intensity,  $I_0$  is the incident intensity,  $n$  is the number density of scattering particles,  $V$  is the scattering volume,  $k$  is the wave number,  $r$  is the radius of the particle,  $\gamma_c$  is the compressibility term,  $\gamma_d$  is the density term,  $\theta$  is the scattering angle equal to  $180^\circ$  for backscattering and  $d$  is the distance from scatterers. Acoustic response of a microbubble to ultrasound excitation is strongly influenced by its initial size (Stride and Edirisinghe 2008). As can be seen from Eq. (2.12), the intensity of scattering by microbubbles is proportional to the sixth power of the radius of the bubble; hence, the bubbles with larger size have better scattering intensity. Considering that the size of a microbubble can reach up to four times its initial size under ultrasound

excitation (May, Allen et al. 2002, Qin, Caskey et al. 2009), it is seen that the backscattered intensity of the microbubble will increase exponentially. However, bubble size is a critical parameter that must be controlled between set limits for *in vivo* applications. Bubbles larger than 6–8  $\mu\text{m}$  are trapped in the lung capillaries. Therefore, the current accepted sizes are in the range of 1–7  $\mu\text{m}$ , preferably around 3  $\mu\text{m}$  (Schutt, Klein et al. 2003).

Scattering cross-section of a microbubble in a liquid can be expressed as

$$\sigma_s = \frac{4\pi r^2}{\left[\left(\frac{f_r}{f}\right)^2 - 1\right]^2 + \delta^2} \quad (2.13)$$

where  $\sigma_s$  is the scattering cross-section,  $r$  is the radius of the bubble,  $f_r$  is the resonance frequency,  $f$  is the frequency of applied ultrasound field, and  $\delta$  is the total damping (de Jong, Hoff et al. 1992). As can be seen from the Eq. (2.13), the factors affecting the ultrasound intensities of the microbubbles are the resonance frequency of the microbubbles and the damping coefficient due to their flexible structures. The resonance frequencies of microbubbles are dependent on their sizes. In order for a microbubble to oscillate at the applied frequency, the size must be above a certain value. Due to the flexible structure of microbubbles, the damping coefficient is inversely related to the scattering cross-section. The scattering cross-section of a microbubble is less than that of a free air bubble. In other words, the backscattered intensity of a free air bubble is higher than that of a microbubble at the same size due to the damping effect.

The oscillation of an insonified microbubble at the frequency of 1 MHz is defined as  $10^6$  pulses per second. For each pulse, the microbubble is expected to expand and shrink in size. Therefore, expansion-compression motion of the microbubble during oscillation is very fast. For example, the velocity and the acceleration of a lipid in the microbubble shell at 2.4 MHz was calculated as about 700 m/s and  $1.2 \cdot 10^{12}$  m/s<sup>2</sup>, respectively (Chomas, Dayton et al. 2000). Modified Rayleigh–Plesset models assume that the bubbles oscillate spherically. However, it has shown that oscillating bubbles may show various non-spherical shapes at high ultrasonic pulses (Figure 2.7) (Dollet, Van Der Meer et al. 2008, de Jong, Emmer et al. 2009). Non-spherical bubble shapes can occur due to imbalance in the shell structure through various mechanisms such as

the presence of molecules with different molecular weights in the shell, intermolecular aggregation, inhomogeneous distribution of the phases in the shell and possible phase changes during microbubble dissolution. Consequently, these non-spherical shape changes lead to fragmentation of microbubbles thus resulting in daughter microbubbles (Chomas, Dayton et al. 2000, May, Allen et al. 2002, Stride and Saffari 2003, Borden, Kruse et al. 2005)..

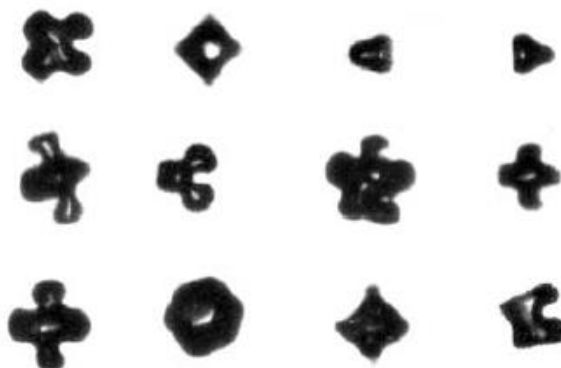


Figure 2.7. Non-spherical vibrations of the insonified microbubbles (de Jong, Emmer et al. 2009).

## **2.6. Shell Effects on Acoustic Performance and Stability of Microbubbles under Ultrasound Activation**

Various factors, such as shell composition (lipid/emulsifier ratio), lipid acyl length, the emulsifier type, and molecular weight of the emulsifier, can greatly affect the oscillation behaviour and stability of the insonified microbubbles. The influence of the composition and structural properties of the phospholipid microbubble coating upon microbubble oscillation and stability in an acoustic field was examined in a limited number of studies.

The emulsifier PEG molecules in the microbubble monolayer shell may be in the brush or mushroom regimes (Wrenn, Dicker et al. 2012, Dicker, Mleczko et al. 2013, Abou-Saleh, Swain et al. 2014). It has been reported that as the amount of PEGylated lipid, i.e. DSPE-PEG2000, molecules on the surface increases, the PEG chains will be more likely to be in the brush regime (Wrenn, Dicker et al. 2012, Abou-Saleh, Swain et al. 2014). Wrenn et al. (Wrenn, Dicker et al. 2012) investigated the influence of PEG in

terms of its regime, molecular weight and mole fraction, on microbubble inertial cavitation. Their findings confirmed that when the ratio of DSPE-PEG2000 was low, the molecules were in the mushroom regime. In this case, ultrasound did not make a significant difference in the disruption of microbubbles. When the mole fraction of DSPE-PEG2000 was increased, the molecules returned to their brush form. In this case, as the amount of PEG was increased, there was an increase in the stability of the insonified microbubbles. It was also found that PEG molecules were in the brush regime due to high concentration of DSPE-PEG2000. When the molecular weight was increased, i.e. longer PEG chains were used, the stability of the microbubbles was seen to decrease under ultrasound excitation.

Abou-Saleh et al. (Abou-Saleh, Swain et al. 2014) examined the effect of PEGylation on the microbubble properties, i.e., the production yield and stability of microbubbles produced on a microfluidic flow focusing device with different DSPE-PEG2000 concentrations ranging from 0 to 35 mol %. They found that the highest microbubble concentration was produced at 5% PEG and then a slight decrease was seen in PEG ratios up to 35%. Maximum lifetime of microbubbles occurred at 5% DSPE-PEG2000, and their stability decreased at higher PEG amounts. They also reported that the stiffness of the microbubbles as a function of external loads increased with the PEG amount.

Hosny et al. employed fluorescence lifetime imaging microscopy to study the viscosity of microbubble coatings composed of DSPC and PEG<sub>40</sub>St using a fluorescent dye termed “molecular motor” (Hosny, Mohamedi et al. 2013). They found that the surface viscosities of the microbubbles produced by the sonication method were higher than that of the microbubbles produced by the microfluidic method. It was suggested that this result was consistent with superior stability of sonicated microbubbles compared to microbubbles produced by the microfluidic method. Another finding was that viscosity was significantly decreased with increasing PEG<sub>40</sub>St ratio ranging from 9:1 to 5:5 in the microbubble shell. It was also found that the backscattered acoustic signal decreased as the PEG content was increased. This was attributed to the reduction in the measured viscosity. However, this reasoning was not rational. Lower viscosity dictates a higher fluidity. Damping of the microbubble oscillation decreases with increasing fluidity. Therefore, the measured acoustic response was expected to be increased when the PEG ratio was increased.

Brussler et al. investigated the effect of increasing PEG<sub>40</sub>St concentrations on the ultrasound contrast enhancement for the nanoscaled ultrasound contrast agents formulated with different lipids *in vitro* (Brussler, Marxer et al. 2014). The lipid formulations composed of DSPC and PEG<sub>40</sub>St were prepared with different molar ratios ranging from 99:1 to 90:10. The highest echogenicity for the ultrasound contrast agents formulated with DSPC/PEG<sub>40</sub>St and DPPC/PEG<sub>40</sub>St mixtures was seen at 4 mol% and 8 mol%, respectively. The echogenicity decreased at higher PEG contents for the DSPC/PEG<sub>40</sub>St formulation. It was suggested that a mushroom-brush transition of the PEG<sub>40</sub>St resulted in an increased acoustic response. They hypothesized that the PEG-chains in the brush regime were less coiled than in the mushroom regime, thus better interaction with ultrasound. Increased contrast enhancement at lower PEG<sub>40</sub>St molar ratio for the DSPC/PEG<sub>40</sub>St formulation compared to DPPC/PEG<sub>40</sub>St formulation was explained with earlier transition, which was attributed to longer acyl chains of DSPC leading to a tighter packing of the lipid bilayer. They also suggested that the loss of echogenicity at higher PEG contents was due to immiscibility of DSPC and PEG<sub>40</sub>St, which was observed as a domain formation of the PEG<sub>40</sub>St in the DSPC/PEG<sub>40</sub>St mixture.

Klibanov et al. (Klibanov, Hughes et al. 2002) studied the contrast agent microbubble destruction in the ultrasound field. This study utilized a commercial contrast agent, protein-coated Optison<sup>®</sup>, and a phospholipid shell microbubble (MP1950). They investigated the fate of the microbubble shell during and after ultrasound exposure. They found that the Optison<sup>®</sup> shells stayed mostly as a sheetlike structure after the gas loss from the bubbles was completed, whereas the lipid shell of MP1950 microbubbles turned into smaller particulates which were shed into the surrounding aqueous medium. They also suggested that these shell residuals were most likely lipid bilayers or micelles.

Dicker et al. (Dicker, Mleczko et al. 2010) examined the microbubble cavitation threshold as a function of the molecular weight and molar ratio of DSPE-PEG2000 (ranging from 1 to 10 mol %). They found that higher peak negative pressure was needed to cavitate microbubbles as the mole fraction of PEG increased, which was observed at all PEG molecular weights. Additionally, the cavitation threshold decreased slightly as the molecular weight of PEG was increased. The results indicated that the threshold pressure is largely sensitive changes in a certain range between 4 and 8 mol%

PEG. It was reported that the PEGylated lipid transitions from the mushroom regime to the brush regime occurred at around 4 mol-% PEG, and that 8 mol-% corresponded to the saturation limit for PEG in PEG-lipid membranes. They suggested that the shell stiffness may account for this cavitation threshold change as the PEG mole fraction increases. It was demonstrated that the bubble stability increased with increasing shell viscosity.

Wu and Tong examined the possible physical mechanisms of instability of microbubbles experimentally in an acoustic field (Wu and Tong 1998). They have shown experimentally that the insonified microbubbles may undergo three major changes at room temperature: 1. Air is diffused out from the microbubble through a structural alteration of the microbubble coating; 2. Bubble clusters may occur due to attractive forces among the adjacent microbubbles in acoustic field; 3. Significant microbubbles may undergo destruction in several minutes' ultrasonic propagation.

Borden et al. (Borden, Kruse et al. 2005) investigated the effects of monolayer shell physiochemical properties on the stability of lipid microbubbles. They altered the shell cohesiveness of microbubbles by varying phospholipid and emulsifier composition. Their results showed that lipid composition significantly influenced the acoustic dissolution rate, tendency for fragmentation, and mechanism of excess lipid shedding. Increasing shell cohesiveness (e.g., increasing phospholipid acyl-chain length) reduced the acoustic dissolution rate and fragmentation tendency of microbubbles. Also, it was demonstrated that decreasing shell cohesiveness resulted in micron-sized or smaller particles of excess lipid material that was ejected either spontaneously or on the next pulse. In contrast, more cohesive shells led to the buildup of shell-associated lipid strands and several micron-sized globular aggregates, which indicated a significant increase in total shell surface area and lability.

Mleczko et al. (Mleczko, Dicker et al. 2012) examined the effect of shell chemistry upon the destruction threshold of microbubbles. They found that the threshold pressure for the destruction of contrast agents decreased with increasing DSPE-PEG2000 concentration ranging from 2.5 mol% to 10 mol%. Their studies also indicated that there was a linear relationship between shell elasticity and viscosity and DSPE-PEG2000 concentration.

Guo et al. (Guo, Li et al. 2013) investigated the inertial cavitation thresholds and shell properties of two commercialized contrast agents, albumin-coated KangRun<sup>®</sup>

microbubbles and lipid-coated SonoVue<sup>®</sup> microbubbles. The experimental results demonstrated that the shell interfacial tension and dilatational viscosity estimated for KangRun<sup>®</sup> are greater than those of SonoVue<sup>®</sup>. They suggested that this might account for the higher inertial cavitation threshold for KangRun<sup>®</sup>.

Wrenn et al. studied the effect of microbubble lipid shell chemistry in cavitation thresholds (Wrenn, Mleczko et al. 2009). They have revealed that the amount and molecular weight of PEG affect bubble propensity to inertial cavitation. It was found that increasing PEG fraction in the range 0.5-3 mol% increased the inertial cavitation of microbubbles, in case of PEG6000. Above 3 mol%, no appreciable change occurred in the percentage of bubbles destroyed due to inertial cavitation. They have suggested that the inertial cavitation threshold is strongly related to the shell stiffness and the resonance frequency of the microbubble. They have reported that for microbubbles with a resonance frequency less than the primary driving transducer frequency, an increase in the resonance frequency due to increased shell stiffness (e.g., addition of PEG) makes the microbubbles more prone to destruction at the primary frequency.

Segers et al. studied the impact of repeated acoustic insonations on the physicochemical monolayer properties (Segers, De Rond et al. 2016). They produced monodispersed microbubbles coated with DPPC:DPPE-PEG5000 in a microfluidic flow-focusing device. Their results showed that the shell stiffness of microbubbles gradually increased with increasing number of insonations owing to the loss of emulsifier lipopolymer molecules.

Owen et al. (Owen, Kamila et al. 2018) compared the backscatter acoustic intensity of 9:1 DSPC microbubbles with PEG-40-stearate and 9:1 DSPC microbubbles with DSPE-PEG(2000), and they reported that there was no significant difference in acoustic intensity between the two microbubble formulations.

## **2.7. Microbubbles for Targeted Drug Delivery**

In recent years, ultrasound-mediated drug delivery has drawn great attention owing to its clinical potential for oncology and cardiovascular applications (Luan, Faez et al. 2012). Contrast agent microbubbles can be used in different ways for the drug delivery under ultrasound. The oscillations of microbubbles coadministered into the bloodstream can markedly improve the drug transfer efficiency. Microbubbles can also

be loaded with drug before administration, and subsequently the drug is released in the region of interest through ultrasonic propagation (Tinkov, Winter et al. 2010). However, microbubbles themselves have a low drug loading capacity. In order to increase the drug payload and to facilitate the transport of hydrophobic, hydrophilic and amphipathic drugs, liposomes are useful drug loading vehicles composed of a lipid bilayer shell. Monodisperse liposomes can be fabricated with a 100 nm in diameter to enhance the uptake of the drug into cells (Sharma and Sharma 1997, Kheirrolomoom, Dayton et al. 2007, Bohmer, Klibanov et al. 2009). Recently, liposome-loaded microbubbles have been designed by attaching liposomes to the microbubble shell via avidin-biotin conjugation (Kheirrolomoom, Dayton et al. 2007). One of the advantages of using microbubbles as drug delivery systems, compared to other delivery systems, is that they can be targeted. Although drugs can be encapsulated in systems such as liposomes, micelles, nanoparticles, these systems are more difficult to be targeted with antibodies/ligands since they are nano-sized. Hence, liposome-loaded microbubbles can be used advantageously in the targeted drug delivery combining the acoustical properties of the microbubbles and the fusogenicity of the liposomes (Luan, Faez et al. 2012).

## CHAPTER 3

### EXPERIMENTAL

#### 3.1. Preparation of Microbubbles

DSPC as a phospholipid and PEG<sub>40</sub>St as an emulsifier were used to produce microbubbles. Briefly, DSPC and PEG<sub>40</sub>St were mixed to a total amount of 40  $\mu$ mol at different molar ratios. These mixtures were then dissolved in chloroform. Chloroform was allowed to evaporate under nitrogen gas followed by several hours under vacuum to form a powder film. A 4 ml of mixture containing phosphate buffered solution (PBS) and propylene glycol (PG) (4:1 by volume) were added to the lipid/emulsifier film, and this mixture was hydrated for 2 hours in a water bath, above the main phase transition temperature of the phospholipid ( $\sim$ 55°C for DSPC) at 60°C. Microbubbles were prepared by the sonication method. The lipid suspension was sonicated using an ultrasonic sonicator (Misonix S4000) operating at a power of 50 W at the air–water interface continuously for about 15 s to generate microbubbles while the PFB gas was introduced by flowing it over the surface of the lipid suspension. The microbubble suspension was then placed in an ice bath for cooling for 10 min. 4 ml of PBS was added to the microbubble suspension. Centrifugation was performed at 1200 rpm for 2 minutes to remove the excess lipid and vesicles. Thus, all microbubbles could be collected from the suspension into a cake. In order to improve the total yield, the microbubbles in the supernatant were re-suspended in PBS after the second centrifugation of the remaining suspension (infranatant). All resulting microbubble cakes were re-suspended in PBS:PG solution (4:1 by volume). Microbubble suspensions were then placed in 1.5 ml crimp vials (Thermo Scientific), and the vials were sealed with screw cap. The air headspace of each vial was filled with the PFB gas. The microbubble suspensions were then kept at +4°C in the refrigerator overnight before usage.

### 3.2. Determination of the Size and Concentration of Microbubbles

Concentration and size distribution of microbubble suspensions were measured using the Coulter Counter apparatus (Coulter Multisizer™ 4, Beckman Coulter, Fullerton, CA). 25 ml vials and a 30- $\mu\text{m}$  aperture (size range of 0.6–18  $\mu\text{m}$ ) were used for the measurements. 10  $\mu\text{L}$  samples of microbubble suspensions were diluted into the vial containing filtrated isotonic electrolyte solution and analyzed to measure the number of particles and the particle size distribution in the microbubble suspension. Prior to microbubble size and concentration measurements for *in vitro* and *in vivo* experiments, an optimization study was performed to determine the measurement sensitivity of the apparatus for the microbubbles. The theoretical microbubble concentration values estimated from the dilution factors was compared with the empirical microbubble concentration values measured by the apparatus. It was also aimed to find out how much volume of microbubble suspension we should add into the electrolyte solution in the vial for an accurate measurement.

In the optimization study, first, the standard process method was created in the Multisizer 4 program. Here, 3 different values were entered into the system in order to determine the concentration of microbubbles within the sample: volume of the electrolyte in the vial, the analytical volume (the volume of liquid through the hole of the aperture), and volume of the sample to be placed in the electrolyte-filled vial. Microbubble suspensions with different concentrations were prepared by making dilutions in different ratios (1/10, 1/100, 1/1000, 1/10000 and 1/100000) from the stock microbubble suspension. Different volumes of samples (10, 30, 70, 150, 300 and 500  $\mu\text{l}$ ) were also prepared from each of the prepared microbubble suspensions at different concentrations. The analytical volume and the volume of electrolyte solution were kept constant at 75  $\mu\text{l}$  and 20 ml for each measurement, respectively. The analytical volume naturally also affects the measuring time. Since the microbubbles tend to rise due to buoyancy in a stagnant liquid, the measurement should be completed as soon as possible to prevent flotation-induced error. For this, a low analytical volume was selected in the control mode (75  $\mu\text{l}$ ). Accordingly, the measurements took approximately 20 seconds. This period of time was assumed not to affect the measurement. In addition, the sample was added to the electrolyte solution, followed by turning the vial upside down 3 times in a manner that would not damage the

microbubbles to ensure complete mixing prior to measurement. All measurements were repeated three times. Microbubble suspensions with different concentrations were also analyzed for both number- and volume-weighted size distributions.

### **3.3. *In-vitro* Characterization of Microbubbles under Ultrasound Activation**

In this study, microbubbles produced in our lab was characterized under ultrasound through the ultrasonic echoscope GAMPT-Scan. For this purpose, calibration studies were performed at different transmitter output powers for different transducer frequencies to assess quantitatively the microbubble concentration in the A-scan mode and B-mode of the ultrasound system. It was also aimed to determine the limiting concentration to eliminate the attenuation for accurate measurements.

#### **3.3.1. Determination of the Focus Zone**

The sound field intensities of three ultrasonic probes of different frequencies (1 MHz, 2 MHz and 4 MHz) were measured along the acoustic axis. The near field lengths (focus zone) of the probes were determined from the measuring curves. Figure 3.1 illustrates the experimental set-up for the determination of the focus zone. The ultrasonic echoscope had adjustable receiver and transmitter powers. The transmission output power was controllable in a range from 0-30 dB in steps of 10 dB. For the receiver amplification (gain) the range was from 0-35dB with steps of 5 dB. The ultrasonic probe was connected to the water reservoir with the ultrasonic gel and the hydrophone was placed in the water reservoir. The ultrasonic echoscope had two modes: reflection and transmission. In reflection mode the signal amplitude was first adjusted to a maximum while the distance between hydrophone and probe was maximised. Then, the transmission mode was switched on and the amplitude response was measured along the sound axis by moving the hydrophone holder. The depth scale in the software was used to measure the position of the hydrophone. The receiver gain power and the transmitter output power was set at 20 dB and 10 dB, respectively.

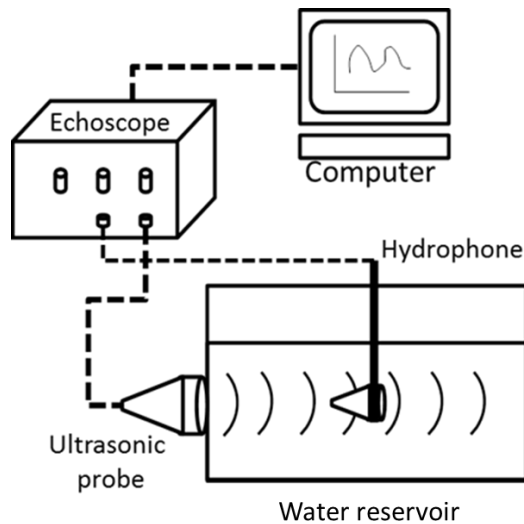


Figure 3.1. Schematic representation of experimental set-up for the determination of focus zones of the probes.

### 3.3.2. Characterization of the Ultrasonic Echoscope

The ultrasonic echoscope has adjustable receiver and transmitter powers. The transmission output power is controllable in a range from 0-30 dB in steps of 10 dB. For the receiver amplification (gain) the range is from 0-35dB with steps of 5 dB. In the experimental set-up, exposure of microbubbles to ultrasound at different powers can be adjusted with output dBs at the transmitter. The gain dBs at the receiver amplifier are used to adjust the amplitude of the reflected sound from the system in volts (V).

Characterization of the ultrasonic echoscope was conducted at different receiver gain powers and different transmitter output powers (Figure 3.2). For this purpose, a reservoir filled with deionized water and a plastic tube placed in the water reservoir were used. In the first assays, a 2 MHz ultrasonic probe was coupled by a coupling gel to the reservoir. Using the focus zone information previously obtained for the probes, the focus zone was chosen to be the region where the amplitude was maximum between the tube and the probe. By selecting the reflection mode on the echoscope, amplitudes of the sound waves reflected from the tube were recorded through a computer. In the experiment, characterization of the echoscope was conducted while the tube was filled with the buffer solution injected with a syringe.

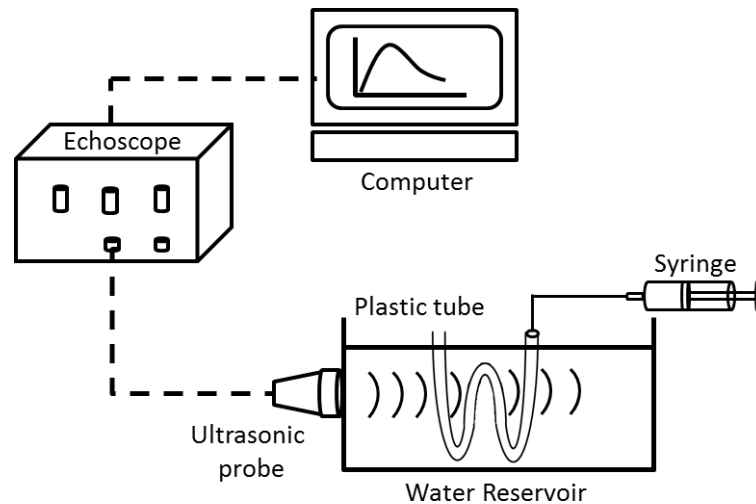


Figure 3.2. Schematic illustration of the experimental set-up for the characterization of the ultrasonic echoscope.

### 3.3.3. Characterization of Microbubbles in the A-scan mode and B-mode of the Ultrasonic Echoscope

In the ultrasonic echoscope, there were two display modes: A(mplitude)-scan and B(rightness)-mode. In the A-scan mode, amplitude values (V) were plotted with respect to distance (mm) between the sample and the probe. B-mode shows reflected echo signals in gray scale (brightness mode). In order to characterize the microbubbles under ultrasound, an experimental set-up was designed (Figure 3.3). The ultrasonic probe was coupled by a coupling gel to the reservoir. The probe frequency was 2 MHz and the transmitter output power was set at 10 dB. A plastic tube with a diameter of 2 mm was placed in the reservoir at a distance of 100 mm which is the focus zone of 2 MHz probe. First the peak amplitude value and the B-mode image were recorded in the A-scan mode and B-mode, respectively, when there was air (no buffer solution) in the tube. Secondly, PBS was injected into the tube via a syringe, and its peak amplitude value and B-mode image were recorded again. Thirdly, microbubbles were injected into the region of interest where microbubbles were exposed to ultrasonic propagation. Peak amplitude value of microbubbles in the A-scan mode and its B-mode image were also recorded.

For the calibration study of microbubbles in the A-scan mode and B-mode, experimental set-up shown in Figure 3.3 was used. After production of microbubbles,

the stock solution concentration of microbubbles was determined through the Coulter counter apparatus. Thereafter, stock solution was diluted to different concentrations. Each diluted solution was injected into the system, and the peak amplitude value and the mean gray-scale pixel intensity of each microbubble solution were determined in the A-scan mode and B-mode, respectively. The probe frequency was 2 MHz. The receiver gain power and the transmitter out power was set at 15 dB and 10 dB, respectively. In this calibration study, it was aimed to investigate the relationship between the concentration of microbubbles and the amplitudes of ultrasonic echoes from microbubbles.

Calibration study of microbubbles under ultrasound was also performed for different ultrasound powers and different probe frequencies. The experimental set-up shown in Figure 3.3 was used for this purpose. In the first experiment, stock solution of microbubbles was diluted to different concentrations. Each diluted solution was injected into the system, and the peak amplitude value of each microbubble solution was determined in the A-scan mode for different transmitter powers (0 dB, 10 dB, 20 dB and 30 dB). Probe frequency was set at 2 MHz for all assays. In the second experiment, the transmitter output power was set at 10 dB and the same assays were conducted for different probe frequencies (1 MHz, 2 MHz and 4 MHz). Finally, concentration graphs were generated against normalized amplitude values.

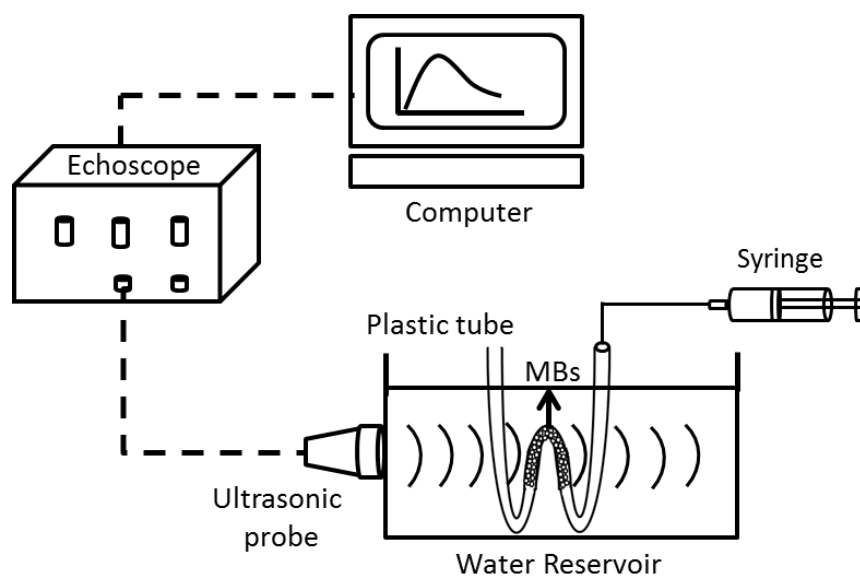


Figure 3.3. Characterization of microbubbles under ultrasound excitation.

### 3.4. Stability of Microbubbles under Ultrasound Excitation through the Peristaltic Pump

The stability of microbubbles was tested in continuous flow with a recirculation through a peristaltic pump under ultrasound. For this purpose, an experimental set-up was designed (Figure 3.4). In the first experiment, it was aimed to investigate the change in concentration of microbubbles and the amplitude in continuous flow with time at different output powers, different frequencies and different flow rates. Following the operation of the ultrasound system, sample solution in the container was drawback by the pump and the microbubbles was transferred to the region of ultrasound. Recirculation was completed after the microbubble solution is transferred into sample container. The amplitude values of the sound wave reflected from the tube obtained in each assay were recorded on the computer. Before each assay, the PBS containing no microbubbles was passed through the system and was used as a reference measurement for the subsequent normalization processes, and the background amplitude values obtained in the echoscope were recorded.

In order to determine the effect of shear rate on the stability of microbubbles, peristaltic pump was operated at different flow rates. Probe frequency was set at 2 MHz and the gain power was set at 10 dB. The backscatter intensity for each sample solution was obtained at certain intervals in A-mode.

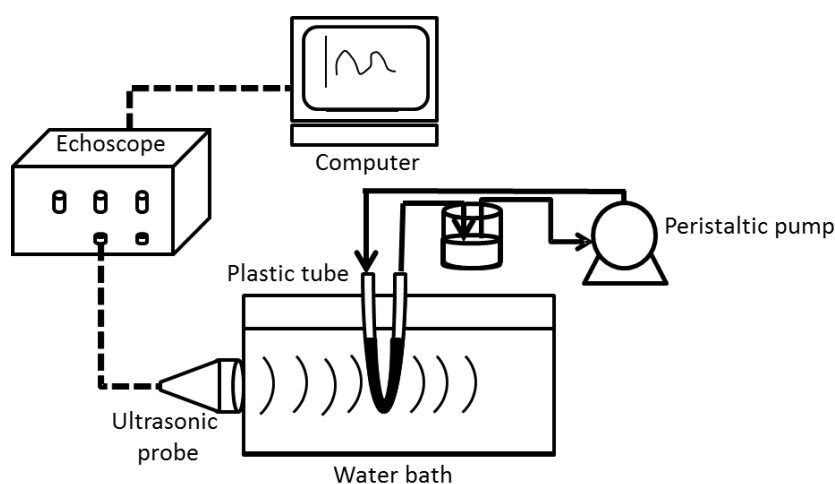


Figure 3.4. Experimental set-up to investigate the stability of microbubbles at different shear rates, different output powers and different frequencies under ultrasound.

### 3.5. *In-vitro* Stability of Microbubbles with Different Shell Compositions under Ultrasound Excitation

An experimental set-up was designed to analyze the *in-vitro* stability of microbubbles with different shell compositions (Figure 3.5). A 20 ml sample container positioned in the focus zone of the ultrasonic probe was placed in the water bath. Microbubble solution was added into the container and the sample solution was homogenized with a magnetic stirrer. Afterwards, ultrasonic propagation was performed and the backscatter intensities of the sound waves reflected from the back wall of the container were determined at certain intervals during the continuous mixing. Concentration of the microbubble solution was also measured through the Coulter counter apparatus (Coulter Multisizer™ 4, Beckman Coulter, Fullerton, CA). The energy loss in sound waves in the presence of microbubbles is called attenuation. If there was PBS with no microbubble in the container, then the sound waves could pass through the container and arrive the back wall of the container. These waves could reflect from the back wall and return to the receiver. However, if microbubble solution was added into the container, some of the sound waves could not pass through the container in the presence of microbubbles; hence there would be energy loss and the amplitude decreased as well. The attenuation is given by (Frinking and de Jong 1998),

$$\frac{I_{atten}(\omega)}{I_{ref}(\omega)} = e^{-\mu_e(\omega)d} \quad (3.1)$$

where  $I_{ref}$  is the reference measurement which is the response from the back wall of the container filled with PBS,  $I_{atten}$  is the response from the back wall after the microbubbles are added into the container,  $\mu_e$  is the extinction (attenuation) coefficient at angular frequency ( $\omega$ ), and  $d$  is the distance travelled through the bubble container. The stability of microbubbles was determined by estimating the attenuation coefficient value in the given Eq. (3.1).

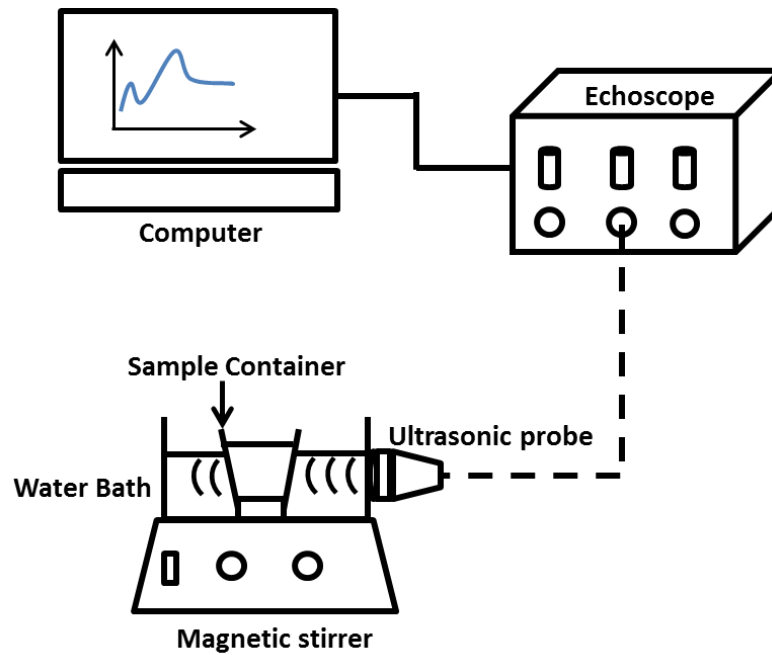


Figure 3.5. Experimental set-up for the investigation of the *in-vitro* stability of microbubbles under ultrasound activation.

### 3.6. Optical Characterization of Microbubbles under Ultrasound Activation with High-Speed Imaging

Optical visualization of microbubbles under ultrasound activation was performed with an ultra-high-speed imaging system (UPMC Cam) found in Dr. Flordeliza Villanueva's laboratory at the University of Pittsburgh-Medical School to acquire movies of oscillating microbubbles. Single bubbles could be observed by the fast-framing camera system which was capable of capturing sequences of 128 image frames at a speed of 5 million frames per second (Mfps). In the ultra-high-speed imaging system, lipid-based microbubbles were placed in a capillary tube. At a frequency of 1 MHz ( $10^6$  oscillations in a second), ultrasonic propagation was performed to oscillate the microbubbles. At this time, the local pressure was set at 0.5 MPa through the experimental setup. The video recording speed was set at  $5 \cdot 10^6$  fps, and then the video recording was performed. A new video was created at 16 fps, including 16 images in a second. Using the obtained video images, the changes in size during the oscillations of the microbubbles were determined using the ImageJ program.

### 3.7. Stability of Microbubbles under Doppler Ultrasonography at Different Ultrasound Powers

An experimental set up was designed to measure the *in vitro* stability of ultrasound contrast agents under ultrasound activation with varying acoustic powers in the power Doppler mode (Figure 3.6). The experimental set up consisted of a flow phantom, an ultrasound imaging system (VisualSonics Vevo2100), a syringe for the bubble injection, an ultrasonic probe, and two valves. The 12.5 MHz transducer was placed on the flow phantom and the microbubbles in a bolus volume of 30  $\mu\text{l}$  were injected into the vessel. Subsequently, the inlet and the outlet valves were closed, so that the microbubbles could be exposed to ultrasonic propagation in a stagnant medium where there was no flow. As the microbubble suspension passed through the acoustic region in the flow phantom, the ultrasonic propagation was carried out within a certain period of time.

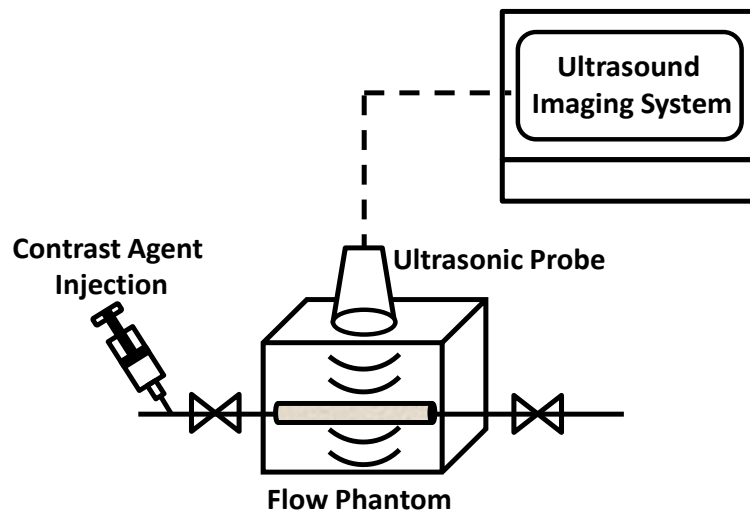


Figure 3.6. Experimental set up.

Microbubbles were exposed to ultrasonic propagation at different acoustic powers ( $P_A$ ) in percent (1%, 5%, 20%, 40%, 60%, 80%, 90% and 100%) for about 25 seconds. The acoustic power in the ultrasound system shows the amplitude of the pulse pressure of the ultrasonic wave. It has shown that there is linearity between the transmit power and the acoustic energy elsewhere (Sboros, Moran et al. 2000). 100% transmit output power corresponds to an acoustic energy of 29  $\text{mW}/\text{cm}^2$  according to power

Doppler operation settings of the imaging system. Therefore, the transmit powers could be converted to the acoustic intensities (Table 3.1). However, the applied acoustic pressure could not be estimated due to lack of information on the relationship between acoustic power and peak negative pressure.

Table 3.1. The transmit powers and the corresponded acoustic energies.

Power, %	Acoustic Energy, mW/cm <sup>2</sup>
1	0.29
5	1.45
20	5.8
40	11.6
60	17.4
80	23.2
90	26.1
100	29

The acquired videos of microbubbles exposed to ultrasound were converted to images in the order of seconds. In order to obtain the B-mode intensities of microbubbles at each acoustic power, a region of interest (ROI1) was created in the acoustic window on the B-mode image, as seen in Figure 3.7. A second region of interest (ROI2) in the same size was also created whether there was an intensity change with the ultrasound effect in the out of focal zone. For the images acquired from the recorded videos, the mean pixel intensity values within the ROIs were quantified by the ImageJ program. As seen in the figure, there is an inhomogeneous distribution of microbubbles in the vessel tube following injection. By creating a wide ROI on the image, we could acquire a mean intensity value within the acoustic window, thus eliminating the difference in intensities at different depths. Time-intensity curves were created for each acoustic power plotting the intensity against time.

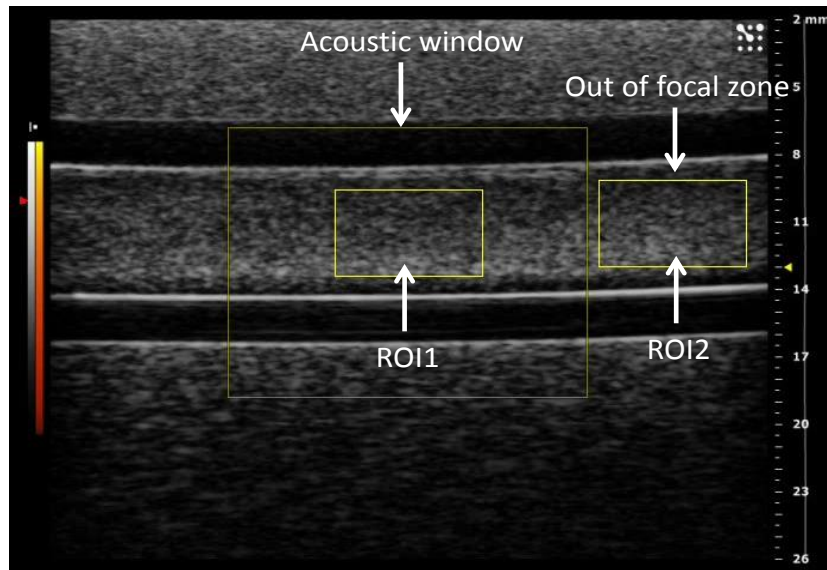


Figure 3.7. RIOs created in the acoustic window and in the out of focal zone within a freeze-captured B-mode image in the flow phantom.

### 3.8. Investigation of *In-vitro* Echogenicity of Microbubbles with Different Shell Compositions

Microbubbles formed in varying phospholipid and emulsifier compositions were investigated under ultrasound excitation to determine their echogenicities. VisualSonics Vevo 2100 high frequency, high resolution ultrasound system (Fujifilm VisualSonics, Inc., Toronto, Canada) was used as the imaging modality (Figure 3.8). The device has a panel comprising sensors capable of monitoring heart rhythm and respiratory functions and providing constant temperature, a sonic probe, a lifting and stabilization platform capable of adjusting the probe in the X-Y-Z plane, and a constant voltage unit. The measurements were performed with a MS 200 (9-18 MHz) high frequency probe. Two phantom models, namely the three vein training ultrasound phantom (ATS Laboratories, Inc. A CIRS Company, Norfolk, VA USA) and the peripheral vascular Doppler flow ultrasound phantom (ATS Laboratories Model 525), were used in the experimental set-up (Figure 3.9).

The experimental setup shown in Figure 3.10 was used to determine the echogenicities of ultrasound contrast agents. The ultrasound probe was placed on the flow phantom, and ultrasound contrast agents were injected into the fluid with a constant flow through a centrifugal pump.



Figure 3.8. The Vevo 2100 ultrasonographic system, 3-D transducer positioning platform and the experimental animal stabilization panel.

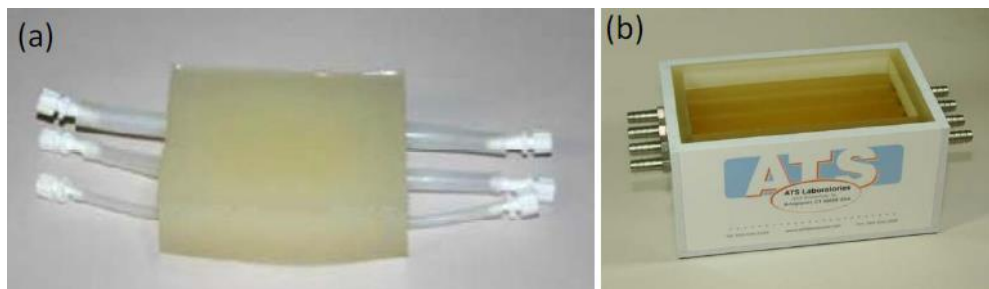


Figure 3.9. (a) ATS Laboratories Model VP-3 three vein training phantom (b) ATS Laboratories Model 525 peripheral vascular doppler flow phantom.

As the ultrasound contrast agent microbubbles were dispersed in the tube, the backscattered ultrasonic signals were recorded in the B-mode. The effluent was then collected in a collection chamber. The *in-vitro* experiment was performed to evaluate the behavior of microbubbles at different flow rates, concentrations and volumes. For this purpose, microbubbles with PEG<sub>40</sub>St ratios ranging from 10% to 90% were used in the experiment. Injections were conducted in volumes ranging from 10 to 60  $\mu\text{l}$ , with a majority of 40  $\mu\text{l}$ . In addition, different concentrations of contrast agents with PEG ratios ranging from 10% to 90% were applied at  $10^5$ ,  $10^6$ ,  $10^7$ ,  $10^8$  #/ml. Injections varying at flow rates from 1080 rpm to 4000 rpm were also performed. In each injection series, one variable was changed and the other variables were kept constant.

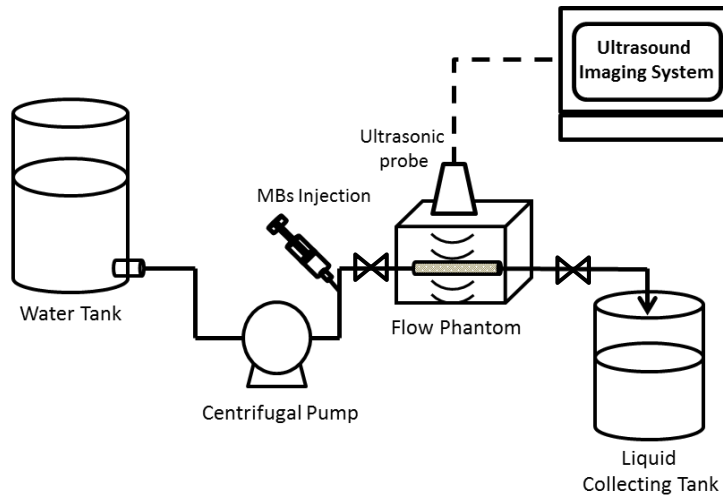


Figure 3.10. Schematic representation of acoustic testing set up.

### 3.9. Measuring Acoustic Response of Loaded Microbubbles under Ultrasound Excitation via the Bolus Injection

An experimental set-up was established to quantify the B-mode image intensities of unloaded and loaded microbubble populations at different concentrations (Figure 3.11).

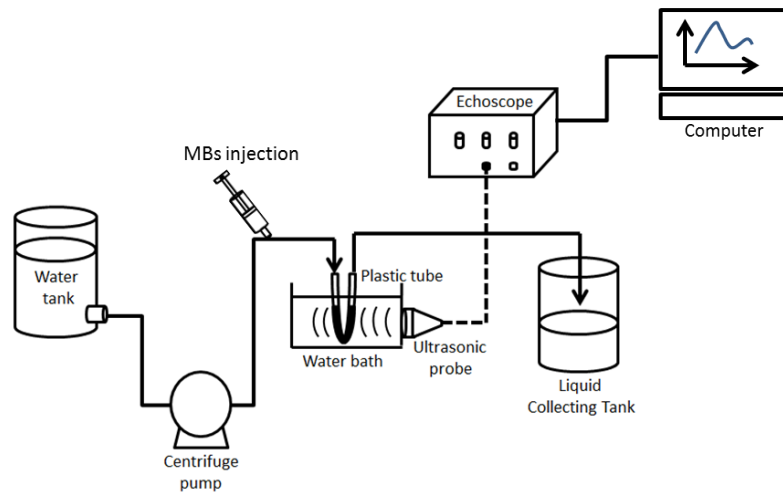


Figure 3.11. Experimental set-up for measuring the acoustic response of loaded microbubbles in the B-mode.

An ultrasonic probe (2 MHz) attached to the echoscope was coupled with the lateral surface of the water bath. A plastic tube with a diameter of 2 mm was positioned

at the focal region of the transducer in the water reservoir and the microbubbles were injected in a bolus volume of 100  $\mu$ l into the liquid flowing at a constant speed through a centrifugal pump. After the injection, the microbubbles were dispersed through the tube and the images were recorded in the B-mode within a certain period of time. In all experiments, the ultrasound output power was adjusted to 10 dB and the flow rate of the liquid in the tube was set at 0.7 l/min. For each microbubble type, bolus injections were performed at different microbubble concentrations. The images obtained from the B-mode of the echoscope were analyzed in the ImageJ program to quantify the grey scale intensities and the SigmaPlot program was used to obtain the curve fittings with the indicator dilution model.

### **3.9.1. Preparation of Biotinylated Microbubbles**

Loaded microbubbles were prepared with different loadings on the microbubble shells. The loading on the microbubble surface was increased step by step through the formation of targeted microbubbles. In this process, the first produced microbubbles were biotinylated microbubbles.

DSPC, PEG<sub>40</sub>St, and biotinylated distearoyl glycerol phosphoethanolamine-polyethylene glycol (DSPE-PEG<sub>2000</sub>-Biotin) were used to produce biotinylated microbubbles through the same procedure described in the “3.1. Preparation of Microbubbles” section.

### **3.9.2. Preparation and Characterization of Liposomes**

DSPC, cholesterol and DSPE-PEG<sub>2000</sub> were mixed in a glass vial at the specified ratios to prepare the liposomes. The DSPE-PEG<sub>2000</sub> amount in the formulation was kept constant at 5 mole%. The total amount of DSPC was adjusted to be 20  $\mu$ mole when cholesterol molar ratios were changed. DSPE-PEG<sub>2000</sub>-Biotin was added at varying molar ratios to the formulation to form the biotinylated liposome. Total molar percentage of DSPE-PEG<sub>2000</sub> and DSPE-PEG<sub>2000</sub>-Biotin was kept constant at 5 mole%. The powdery materials were dissolved in chloroform to obtain a homogeneous mixture of materials that would form the liposome structure. Chloroform was allowed to evaporate through the nitrogen gas stream, and then the mixture was dried under the

vacuum to obtain a thin lipid film in the vial. Ammonium sulphate buffer solution ((NH<sub>4</sub>)<sub>2</sub>SO<sub>4</sub>, 250 mM, pH 5.4) was added onto the lipid film, and the mixture was placed in a shaking water bath at 65°C and subjected to hydration for 1 hour. Lipids were kept for at least 30-60 minutes above the T<sub>m</sub> of DSPC for liposomes to be stable (ElBayoumi, Torchilin et al. 2010, Monteiro, Martins et al. 2014, Freeman 2017). Since the multilamellar vesicles (MLV) formed after hydration showed a wide size distribution, the solution was extruded from the polycarbonate membrane with homogeneous porosity to obtain the liposomes in the desired size and homogeneous distribution. Homogeneous distribution is also an important parameter for the drug design. Size analysis of the liposomes produced after the extrusion process was performed through the dynamic light scattering (DLS) method (Zetasizer Nano ZS90, Malvern).

### **3.9.3. The Assay of Doxorubicin Loading into Liposomes**

Doxorubicin (DOX), an anticancer substance, was loaded into liposomes via the active loading method. The active loading method was accomplished by means of an ion gradient. For this purpose, the liposomes were dialyzed with 0.9% NaCl solution or phosphate buffered solution to form a pH gradient with an inner pH of 5.5 and an outer pH of 7.2. Then, at different concentrations, the DOX solution was incubated for 4 hours at 65°C by mixing with liposomes. In order to separate free DOX molecules from DOX-loaded liposomes (Lipo-DOX), dialysis membrane method was applied. Dialysis membrane (RC tubing) (MWCO: 10 kD, Spectra/Por<sup>®</sup> 6) was used for the dialysis.

### **3.9.4. Production of Targeted DOX-Loaded Microbubbles**

DOX containing liposomes (Lipo-DOX) were conjugated with microbubbles through the avidin-biotin bridge to prepare drug-loaded microbubbles. The previously prepared biotinylated microbubbles were incubated with streptavidin dissolved in PBS for about 10 minutes. Streptavidin was conjugated with biotin on the microbubbles through incubation. After incubation, the avidin-bound biotinylated microbubbles were centrifuged at 1000 rpm for 1 minute. Hence, the unbound free avidins in the medium were removed. The avidin-bound microbubbles suspended in the medium were re-

suspended in PBS. Lipo-DOX, previously produced, was then added into the suspension containing avidin-bound microbubbles and incubated for 10 minutes. The free portion of streptavidin on the microbubbles and the biotin on the liposomes were thus conjugated. Lipo-DOX loaded microbubbles produced were centrifuged at 1000 rpm for 1 minute. Therefore, the free unbound Lipo-DOX in the medium was removed. Figure 3.12 illustrates the bright-field and fluorescent images of Lipo-DOX loaded microbubbles in the fluorescence microscope. Lipo-DOX loaded microbubbles suspended in the medium were re-suspended in PBS. Then streptavidin dissolved in PBS was added to the suspension of Lipo-DOX loaded microbubble. Incubation was performed for 10 minutes and the biotin molecules that were not bound on Lipo-DOX and the avidin molecules added into the medium were conjugated. The newly formed complex was centrifuged at 1000 rpm for 1 minute to remove unbound avidin in free form. The microbubbles suspended in the medium were re-suspended in PBS. Finally, the protein material, dissolved in distilled water, called epidermal growth factor (EGF) was added to this complex suspension in order to obtain targeted microbubbles. 10-minute incubation was carried out so that the conjugation occurred by binding EGF to the avidins on the Lipo-DOX. The microbubble solution was centrifuged at 1000 rpm for 1 minute to remove free unbound EGF molecules from the medium. The microbubbles suspended in the medium were re-suspended in PBS and stored in the refrigerator at +4°C. Thus, the targeted microbubbles were synthesized. The size and concentration analyzes of the targeted drug loaded microbubbles were determined through the Coulter Counter.

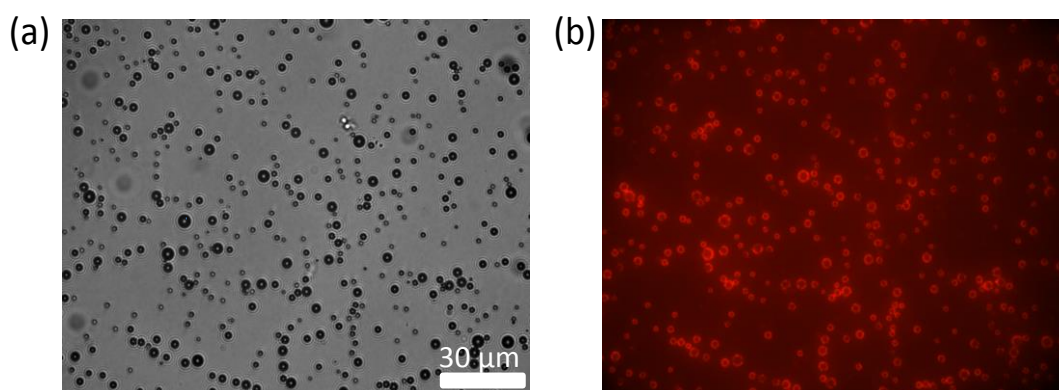


Figure 3.12. Bright-field (a) and fluorescent (b) images of Lipo-DOX loaded microbubbles. Red color on the surface of microbubbles depicts the DOX loaded liposomes.

### **3.10. Investigation of the Stability of Loaded Microbubbles under Ultrasound Excitation**

The stability of loaded microbubbles was examined in terms of attenuation coefficient and concentration change. An experimental set up was developed to examine the stability of microbubbles loaded with different masses under ultrasound activation (Figure 3.5). Here, a cuvette of 20 ml was placed in the water bath and was fixed on the bottom of the water bath. A magnetic stirrer was placed under the water bath to distribute the microbubbles in the buffer solution homogeneously. The 4 MHz ultrasound probe attached to the echoscope was coupled with the lateral surface of the water bath so that the inside of cuvette was in the focal region of the probe. The distance between the cuvette and the probe was about 14.4 cm. Initial concentrations of the different types of microbubble populations were measured through the Coulter Counter before starting the experiment. Accordingly, the initial concentration of the microbubble populations was diluted to  $1\text{E}+07$  #/ml in all assays. Thus, the initial concentration was the same for all microbubble types. 17 ml of PBS was first added into the cuvette and the amplitude of the peak signal produced by the sound wave reflected from the rear wall of the cuvette was measured in the A-mode while there were no microbubbles inside. The microbubble population was then added into the cuvette, and both the amplitude of the peak signal and the microbubble concentration were measured in every 5-10 minutes at a maximum ultrasound output power of 30 dB.

### **3.11. Investigation of the Microbubble Shell Composition**

#### **3.11.1. NMR Measurements**

$^1\text{H}$  NMR measurements were performed to investigate the microbubble shell composition. The molar ratio of PEG<sub>40</sub>St to DSPC in the microbubble shell was determined as a function of the PEG<sub>40</sub>St concentration in the DSPC/PEG<sub>40</sub>St mixture prior to microbubble formation. For the standard calibration, DSPC/PEG<sub>40</sub>St mixtures were prepared at molar ratios of 9:1, 7:3, 4:6 and 2:8. Predetermined amounts for pure DSPC, pure PEG<sub>40</sub>St, and their binary mixtures were weighed into the vials and dissolved in deuterated chloroform ( $\text{CDCl}_3$ ) resulting a concentration of 16.66 mg/ml.

Ultrapure water was used instead of phosphate buffered solution for the suspension medium of microbubbles. For the  $^1\text{H}$  NMR measurements of the microbubble shell, DSPC/PEG<sub>40</sub>St mixtures were prepared at molar ratios from 9:1 to 2:8 compositions. Following microbubble formation as described previously, 5 ml of ultrapure water at +4°C was added to each microbubble suspension. All suspensions were then centrifuged at 1200 rpm for 1 min 30 seconds. The microbubbles in the supernatant and the subphases of the suspensions were collected in separate vials. Microbubbles were burst dissolving in chloroform, thus resulting in the shell components. The shell components and the subphases were allowed to dry at 50°C overnight. The shell components and the subphase components were then lyophilized overnight to obtain a dry powder film and dissolved in CdCl<sub>3</sub> for analysis.

Peak areas were determined by using the integration feature in the MestreNova NMR software. A known molar ratio of PEG<sub>40</sub>St to DSPC was plotted as a function of the ratio of the PEG peak to the N(CH<sub>3</sub>)<sub>3</sub> peak of DSPC. This calibration, along with peak integral ratios, was used to determine the molar percentage of PEG<sub>40</sub>St in the samples.

### **3.11.2. Determination of the Amounts of Microbubble Shell Components and Subphase Components**

Before the preparation of microbubbles at different compositions, the tare of vials were determined for each composition. Microbubble suspensions were prepared from the DSPC/PEG<sub>40</sub>St mixtures at molar ratios of 9:1, 7:3, 5:5 and 3:7. Following microbubble formation, the shell components and the subphase components were obtained as described previously. The vials containing shell components and subphase components were weighed. The difference between the weight of the vials containing samples and the tare of vials gave the total amounts of the microbubble shell and the subphase.

### **3.12. Stability of Microbubbles under Hydrostatic Pressure**

A hydrostatic constant pressure system was designed in order to investigate the dimensional changes of microbubbles under hydrostatic pressure and possible changes

in the surface morphology as well (Figure 3.13). In this system, there were a pump, a pressure regulator, pressure sensors to measure the pressure values, a one-way pressure valve to keep the pressure at the desired level, and a cell view. Cell view consisted of coverslips placed between two acrylic plates. First, all the pipes in the system were filled with PBS, and then microbubbles were placed onto this coverslip via injection. At different pressure levels, microbubbles were imaged via camera under light and fluorescence microscopy.

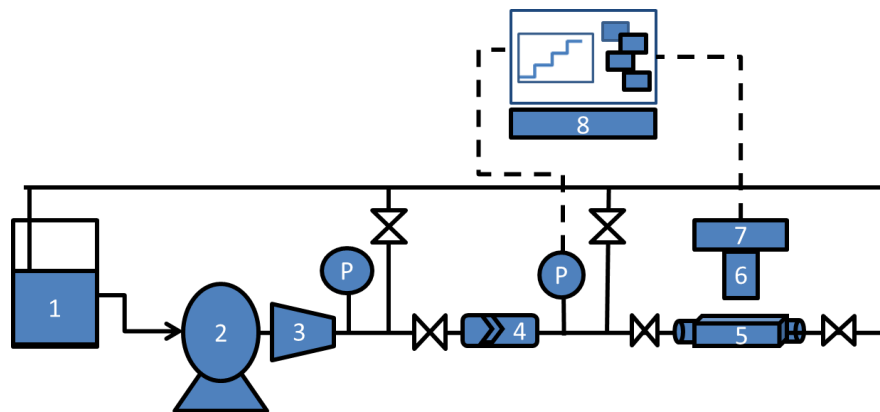


Figure 3.13. Hydrostatic constant pressure system. 1. PBS, 2. Pump, 3. Pressure regulator, 4. One-way pressure valve, 5. Cell view, 6. Microscopy, 7. Camera, 8. Computer.

### 3.13. *In-vivo* Studies

#### 3.13.1. *In-vivo* Toxicity of Microbubbles

In this study, the *in vivo* toxicity of microbubbles was investigated in rat and rabbit animal models. First, injection was performed in a single rat. The VisualSonics Vevo® 2100 high-resolution ultrasound imaging system was equipped with an animal tray for the stabilization and monitoring of the rat. The rat was anesthetized with ketamine hydrochloride and xylazine at a certain ratio. There was no need for the maintenance of anesthesia. The rat was stabilized in the large animal tray. Needle catheterization was performed through the tail vein. The MS 200 probe, placed at the upper abdomen level, was fixed by positioning the inferior vena cava (VCI), abdominal aorta and vena portae in the same section. It was applied at a microbubble concentration

of about  $1E+08$  #/ml via the tail vein of the rat at an injection volume of 0.1 ml. Ultrasonography images were recorded, simultaneously. The images were processed and evaluated with the Vevo CQ software program which was prepared for the data evaluation. Region of interests (ROIs) placed in the VCI, aorta and vena portae were plotted as time-echogenicity curves using the Vevo CQ software.

Male Wistar Albino Hannover rats weighing 200-400 g and male New Zealand rabbits weighing 2-3 kg were used for the *in-vivo* experiments. The animals were obtained from the Experimental Animals Unit of the Multidisciplinary Laboratory of Dokuz Eylül University Faculty of Medicine. During the study, the animals were housed in the standard rat and rabbit cages at the same laboratory, and the lighting was performed for 12 hours-night/12 hours-day. Food and water were met as *ad libitum*. The experimental studies were approved by Experimental Animals Local Ethics Committee of the Multidisciplinary Laboratory of Dokuz Eylül University, and the animals were cared and fed in accordance with the rules determined by the Local Ethics Committee.

Rats were grouped to not more than 4 animals in each cage two days before starting the experiment to acclimate them to their new environment, and they were labeled with the tail marking method. Rabbits' ears were marked with colored pencils and two rabbits were housed in each cage.

Basal blood and urine samples were taken before ultrasonographic imaging of the animals. The animals were anesthetized with intraperitoneal injection of a combination of Ketamine/Xylazine 80-100/5-10 mg/kg. It was observed that ketamine/xylazine caused vasoconstriction and in some cases anesthesia was applied with ether. 2 ml of blood was taken from each tail under anesthesia and sent to biochemistry laboratory. Following the blood collection process, the animals awakened due to the effect of anesthesia were taken to the metabolism cages shown in Figure 3.14 in order to measure the amount of water and feed they consumed and the amount of urine and feces they consumed, and were held there for 24 hours. The feed, the amount of water and the feces and urine of the animals were checked and measured. At the end of 24 hours, the urine of the animals was collected and sent to the biochemistry laboratory for analysis.

The animals were anesthetized with intramuscular injection of a combination of Ketamine/Xylazine 35/5 mg/kg, and 4 ml of blood was taken from each animal under

anesthesia and sent to biochemistry laboratory for biochemical analysis and hemogram tests. Urine and fecal measurements were not performed in rabbits.



Figure 3.14. Rat metabolism cage.

Imaging by ultrasonography was performed in two different ways: liver and kidney imaging. Rats were anesthetized with intraperitoneal injection of a combination of Ketamine/Xylazine 80-100/5-10 mg/kg. The hairs on the region of interest were cleaned with depilatory cream (Nair, Church & Dwight Co. Inc.-Princeton) to display the liver in the supine position or the left kidney in the prone position, depending on the region to be examined. The tail vein was then catheterized. The animal was laid and fixed in the supine position for the liver and in the prone position for kidney imaging on the tray where the ultrasound imaging would be performed. A rectal probe was then inserted into the animal. For the ultrasound imaging, physiological serum, in-house made microbubbles, and the Vevo MicroMarker<sup>®</sup> contrast agents were used as injectables.

After the ultrasound imaging was completed, each animal was injected with 2 ml of saline and allowed to awake in a separate cage. After the effect of anesthesia passed, the animals were taken back to the metabolism cages, and the amounts of water and feed consumption and the amounts of urine and feces were observed in the metabolism cage for 24 hours. Urine was collected from the animals kept in the metabolism cage for 24 hours. Animals were sacrificed using high dose anesthetic and blood was taken from

the vena cava caudalis for biochemical and hemogram parameters. Then, kidneys, lobus hepatis sinister of the liver, right lung lobes and brain organs were taken and sent to pathology laboratory.

Creatinine and urea values were measured in urine samples. The biochemical parameters measured in blood samples were creatinine, urea, alanine aminotransferase (ALT), aspartate aminotransferase (AST), alkaline phosphatase (ALP), albumin, and direct, indirect and total bilirubin. Hemogram parameters measured in blood included red blood cell count (RBC), hemoglobin, hematocrit, mean red blood cell volume (MCV), mean red blood cell hemoglobin concentration (MCHC), red blood cell distribution width (RDW), platelet, mean platelet volume (MPV), PCT, white blood cell (leukocyte), neutrophils, lymphocytes, monocytes, basophils and eosinophils.

### **3.13.1. Diagnostic Dose Study for the Rats**

In this study, the diagnostic dose was investigated for the 5:5 microbubbles in the rat animal models. Seven experimental rats were included in the study. The rats were fixed to the animal tray. Respiratory and heart rate could be displayed on the ultrasound screen with the sensors in the animal tray. Respiration and heart rhythm were recorded simultaneously during image recording. For the body temperature measurement of the rat, a rectal probe was used. Body temperature such as respiratory and heart rhythm, was also monitored on the ultrasonography screen via the probe, and the images were recorded. Catheterization was performed with a 27G needle through the tail vein of the rat, which was prepared and stabilized as described previously. Because a rat vein could not be opened, it was excluded from the experiment. The MS 200 probe placed at the upper abdomen level was fixed in the same section in such a way that the VCI, abdominal aorta and vena portae were visible. Three-dimensional positioning system, which was the component of high resolution ultrasound device, was used in Vevo2100 model animal experiments shown in Figure 3.15 for positioning and fixing. The microbubbles were applied at an injection volume of 50  $\mu$ l at different concentrations. Simultaneously, ultrasonography images were recorded. In each injection, image recording was performed for 20 minutes. Images were evaluated with the Vevo CQ software program. Microbubble distribution in the vessels was plotted as a

time-echogenicity curve using the Vevo CQ software with ROIs placed in the VCI, aorta and vena portae.

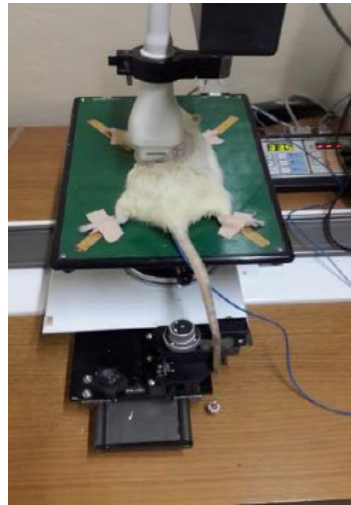


Figure 3.15. Three-dimensional positioning system and abdominal evaluation in rats.

### **3.13.2. Comparison of Microbubbles with the Commercial Standard Vevo MicroMarker<sup>®</sup> Contrast Agents**

The second experimental group was used to compare the microbubbles with the Vevo MicroMarker<sup>®</sup> contrast agents in terms of acoustic response. For this purpose, a total of 10 rat test groups were prepared, including 4 rats with microbubbles, 3 rats with the Vevo MicroMarker<sup>®</sup> contrast agents, and 3 rats with sham. Vevo MicroMarker<sup>®</sup> is a commercial microbubble formulation developed for experimental animals. For this experimental group, the steps of basal metabolism cage process, anesthesia, drug administration, follow-up metabolism cage, sacrifice and pathological evaluation were repeated.

### **3.13.3. Echogenicity Study in Rat Kidney Model**

The application of kidney model was performed on 2 pilot rats. In this experimental model, the rat was anesthetized and stabilized in the ovarian position in the large animal tray. For the left kidney view, hairs of the back and left side of the rat

were removed using a depilatory cream. The ultrasound probe was positioned in this area. All other data recording steps and preparations were performed as described in the previous experimental setup. For this experimental group, the steps of follow-up metabolism cage, sacrifice and pathological evaluation were repeated. A diagnostic dose study and comparison with the Vevo MicroMarker<sup>®</sup> contrast agents were performed on 13 rats in the kidney model experimental group. In this group, 2 rats were excluded from the experiment. Vevo MicroMarker<sup>®</sup> contrast agents at a concentration of 5E+08 #/ml were administered to 3 rats, 5:5 microbubbles at a concentration of 2.5E+08 #/ml were administered to 4 rats, and 5:5 microbubbles at a concentration of 5E+08 #/ml were administered to 4 rats. All injection volumes were 0.15 ml. One rat from 2.5E+08 #/ml and 5E+08 #/ml injection groups was excluded due to the tail problem. As a result, there were 3 injections in each group. Echogenicity increase could be monitored visually in all these injections. All injections were measured by the Vevo CQ and manual methods.

#### **3.13.4. Toxic Dose Study for the Rats**

The experiment was performed with a total of 16 rats out of 12 in the injection group and 4 in the sham. The rats were prepared as described in previous experiments and visualized with the same data recording steps. In this imaging, attenuation occurred with the high dose given. Following the injection, the rats were taken to the metabolism cage for acute toxic effects. The rats were followed for 14 days for the late toxic effects and were sacrificed at the end of this process and the organ samples were then examined for the pathological evaluation.

#### **3.13.5. Toxic Dose Study for the Rabbits**

In the rabbit experiments, firstly, 2 pilot rabbits were studied. In order to evaluate the toxic dose in a larger model than the rat, 6 rabbits were injected with a high dose of microbubbles. After removal of hairs in the abdominal regions of the rabbits, ultrasonographic evaluation was performed with a 3-dimensional positioning system. In this experiment, the purpose of the ultrasonographic evaluation was to ensure that the contrast agents reached the system and produced attenuation in a way suggesting that

they were in a high dose. As a result of this experiment, rabbits were sacrificed for 24 hours, and the tissues of the rabbits were examined for the pathological evaluation.

# CHAPTER 4

## RESULTS AND DISCUSSION

### 4.1. Optimization Study for the Microbubble Concentration and Size Measurements with the Coulter Counter Multisizer

Optimization study was performed to determine the measurement sensitivity of the Coulter Counter apparatus for the microbubbles in terms of concentration and size. Different concentrations and different volumes of microbubble suspensions were analyzed to compare the theoretical data with the empirical data.

Figure 4.1 shows the image of perfluorobutane-filled 5:5 microbubble population taken by the light microscopy and size distribution of the microbubble suspension determined through the Coulter Counter. The concentration and mean size of the stock suspension of microbubbles were measured to be  $3.42\text{E}+09$  #/ml and  $\sim 3$   $\mu\text{m}$ , respectively.

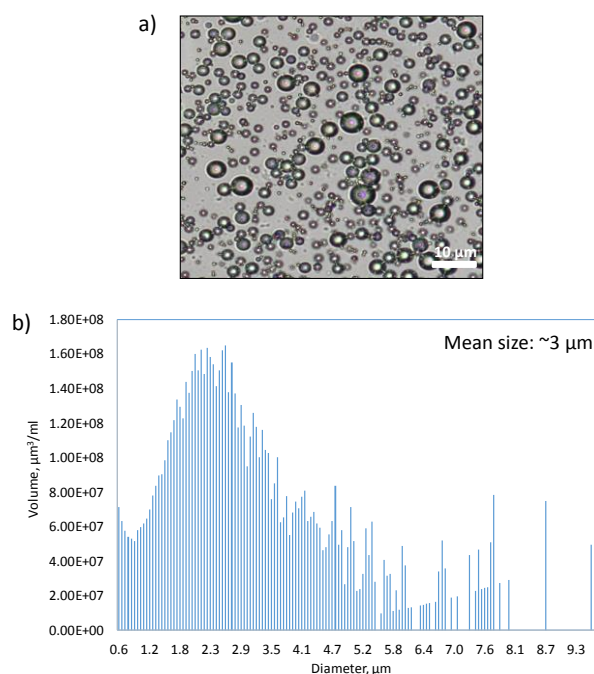


Figure 4.1. (a) Image of the 5:5 microbubble population after production, (b) size distribution of the microbubble suspension.

A 2.5 ml sample was then withdrawn from the stock solution, and its concentration and mean diameter were measured. When higher volumes of samples were taken from the stock solution, the device could not measure the concentration of these samples. This is most likely due to blockage of the aperture hole with the high number of particles. Measurement could not be performed for the samples taken in volumes of 150 ml and above from the 1/10 diluted suspension because of the high number of particles as well. Therefore, the data obtained for the 10, 30 and 70 ml sample volumes of the 1/10 diluted suspension was evaluated. At higher dilutions, higher sample volumes could be analyzed. Figure 4.2 illustrates the calculated microbubble concentration versus measured microbubble concentration at different dilutions and different sample volumes. As can be seen in the figure, the measured and calculated values at the 1/10 and 1/100 dilutions were almost correlated to each other, whereas the measured concentration did not change below the microbubble concentration of  $1\text{E}+06$  #/ml at higher dilutions. The linearity was not seen at dilutions higher than 1/1000. At the same time, as the dilution factor increased, more fluctuations in concentrations measured in different sample volumes were observed. This might be attributed to the concentration of particles within the isotonic electrolyte solution used as the medium. The relatively high particle concentration of the isotonic solution affected our measurements. The particle concentration of the isotonic solution decreased to about  $1\text{E}+06$  #/ml at low sample volumes, while to about  $1\text{E}+05$  #/ml at high sample volumes. Thus, at a dilution of 1/1000, the concentration of the microbubbles corresponded to the particle concentration of the isotonic solution, so that an accurate result could be obtained since the measured value did not correspond to the calculated value. However, when the maximum sample volume was used at a dilution of 1/1000, a more accurate measurement could be performed since the particle concentration of the isotonic solution dropped to about  $1\text{E}+05$  #/ml, and as a result, the measured value corresponded to the calculated value. At dilutions higher than 1/1000, accurate measurements could not be performed even at the maximum sample volume.

Figure 4.3 shows the microbubble concentrations measured at different sample volumes for different dilutions. As can be seen in the figure, the concentration values measured in different sample volumes were the same at low dilutions, whereas fluctuations were observed in the measured concentration values since the measurement sensitivity of the Coulter Counter apparatus decreased at higher dilutions.

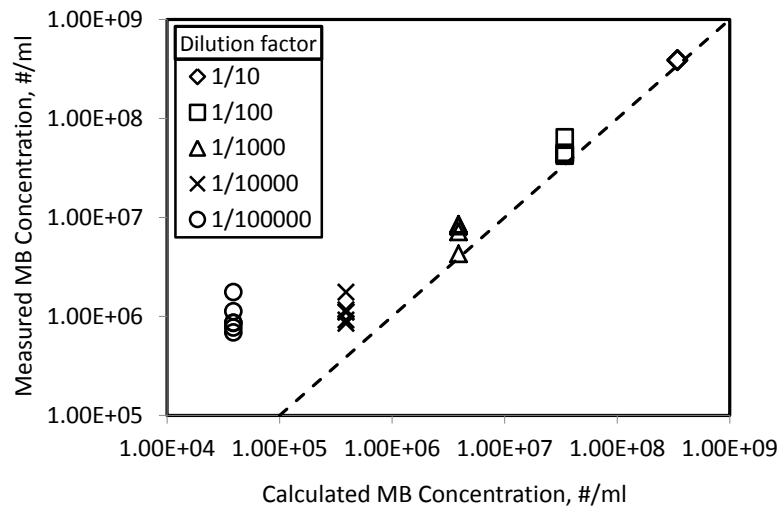


Figure 4.2. Calculated microbubble concentration versus measured microbubble concentration at different dilutions and different sample volumes.

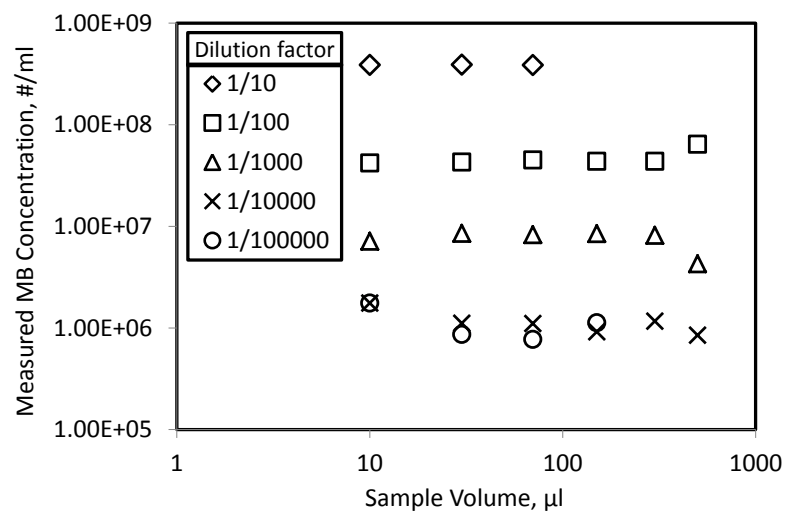


Figure 4.3. Microbubble concentrations measured at different sample volumes for different dilutions.

Figure 4.4 shows mean diameters of the microbubble suspensions versus microbubble concentrations measured at different sample volumes for different dilutions. The mean diameter of the microbubbles in the stock solution was measured to be  $\sim 2.75 \mu\text{m}$ . As shown in the figure, the mean diameter did not change significantly with varying sample volumes at low dilutions (above  $1\text{E}+07 \text{ #/ml}$ ). As a result, the mean diameter of microbubble suspensions at concentrations above  $1\text{E}+07 \text{ #/ml}$  was almost the same as in the stock solution. At lower concentrations, the mean diameter of

the microbubble suspensions did not yield the same results in different sample volumes. As seen in the figure, there was a fluctuation in the mean microbubble diameter values at higher dilutions. This might be attributed to a reduced measurement accuracy of the apparatus at very low concentrations. At very low concentrations, bubble stability decreased and the smaller bubbles more rapidly underwent destruction than the larger bubbles. Therefore, the mean diameter of the microbubble suspension could increase due to disappearance of smaller bubbles. As a result of this, the apparatus might have measured higher values. In addition, concentration and diameter values of microbubbles with a size greater than 10  $\mu\text{m}$  were not taken into account. This is because we could not ensure whether the microbubbles with a size greater than 10  $\mu\text{m}$  were either single or fused microbubbles since the possibility of the microbubbles to coalesce as they pass through the aperture hole led to the formation of larger microbubbles. It has been also reported in the literature that the size distribution of the microbubbles is 1-10  $\mu\text{m}$ . Therefore, this range was chosen.

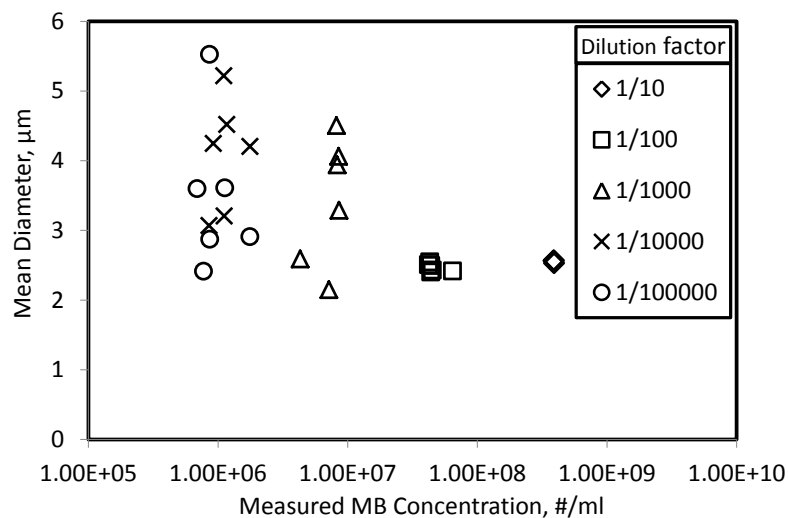


Figure 4.4. Mean diameters of the microbubble suspensions versus microbubble concentrations measured at different sample volumes for different dilutions.

As a conclusion, it is necessary to minimize the background signal from the isotonic solution itself. If the concentration of the particles in the isotonic solution could be minimized (e.g., filtration), the apparatus can give us the accurate data even at very low microbubble concentrations.

## 4.2. Investigation of the Microbubble Shell Composition

$^1\text{H}$  NMR experiments were performed to investigate the microbubble shell composition. Chemical structure of pure shell components and their binary mixtures were examined to obtain a standard calibration curve. Figure 4.5 illustrates the  $^1\text{H}$  NMR spectra and the chemical structure of DSPC and PEG<sub>40</sub>St. The proton peak assignments for DSPC and PEG<sub>40</sub>St were made using literature references (Ali and Bittman 1988, Curcio, Blanco-Fernandez et al. 2015) and are also summarized in Table 4.1.  $^1\text{H}$  NMR spectrum of DSPC showed a signal at 1.35-1.0 ppm assigned to  $(\text{CH}_2)_{14}$  protons (56 H) of the acyl chains. However, PEG<sub>40</sub>St also showed a signal at 1.30-1.15 ppm assigned to  $\text{CH}_2$  protons (32 H) of stearic moiety. These two peaks overlapped, as can be seen in Figure 4.5.

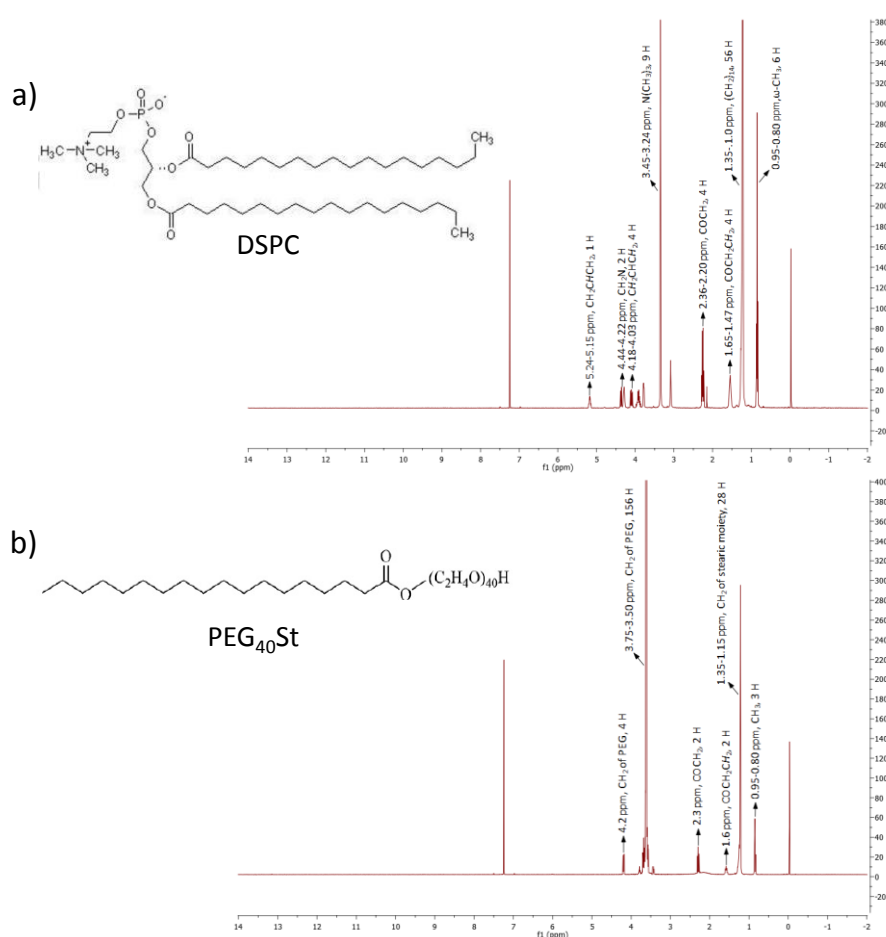


Figure 4.5. Chemical structure and  $^1\text{H}$  NMR spectra of (a) DSPC and (b) PEG<sub>40</sub>St. Arrows show the proton chemical shifts at certain ppm values.

Table 4.1. Proton chemical shifts of DSPC and PEG<sub>40</sub>St.

Proton chemical shift of DSPC	$\delta$ , ppm	Experimental DSPC Peaks		Proton chemical shift of PEG <sub>40</sub> St	$\delta$ , ppm	Experimental PEG <sub>40</sub> St Peaks
CH <sub>2</sub> CHCH <sub>2</sub> , 1 H	5.30-5.18	5.24-5.15				
CH <sub>2</sub> OP, 2 H	4.62-4.42			OH, 1 H	4.95	
CH <sub>2</sub> N, 2 H	4.40-4.25	4.44-4.22		CH <sub>2</sub> protons of PEG, 4 H	4.3-4	4.2
CH <sub>2</sub> CHCH <sub>2</sub> , 4 H	4.18-3.98	4.18-4.03				
N(CH <sub>3</sub> ) <sub>3</sub> , 9 H	3.40	3.45-3.24		CH <sub>2</sub> protons of PEG, 156 H	3.6	3.75-3.50
COCH <sub>2</sub> , 4 H	2.38-2.20	2.36-2.20		COCH <sub>2</sub> , 2 H	2.3	2.3
COCH <sub>2</sub> CH <sub>2</sub> , 4 H	1.65-1.50	1.65-1.47		COCH <sub>2</sub> CH <sub>2</sub> , 2 H	1.6	1.6
(CH <sub>2</sub> ) <sub>14</sub> , 56 H	1.38-1.0	1.35-1.10		CH <sub>2</sub> protons of stearic moiety, 28 H	1.3-1.1	1.35-1.15
$\omega$ -CH <sub>3</sub> , 6 H	0.92-0.80	0.95-0.80		CH <sub>3</sub> protons of stearic moiety, 3 H	0.9	0.95-0.80

The peaks belonging to only DSPC and only PEG<sub>40</sub>St were found to be 3.45-3.24 ppm and 3.75-3.50 ppm, respectively. Figure 4.6 illustrates the <sup>1</sup>H NMR spectra of pure DSPC and pure PEG<sub>40</sub>St on the same graph. Separate peaks for each component are clearly seen from the figure. Signals at 3.45-3.24 ppm and 3.75-3.50 ppm are assigned to N(CH<sub>3</sub>)<sub>3</sub> protons (9 H) of DSPC and CH<sub>2</sub> protons (156 H) of PEG<sub>40</sub>St, respectively.

Figure 4.7 shows the <sup>1</sup>H NMR spectra of DSPC/PEG<sub>40</sub>St mixtures at molar ratios of 9:1, 7:3, 4:6 and 2:8. Signals at 3.45-3.24 ppm and 3.75-3.50 ppm both contain the DSPC and PEG<sub>40</sub>St protons. The inner graph illustrates the selected signals at 3.45-3.24 ppm and 3.75-3.50 ppm for the standard calibration.

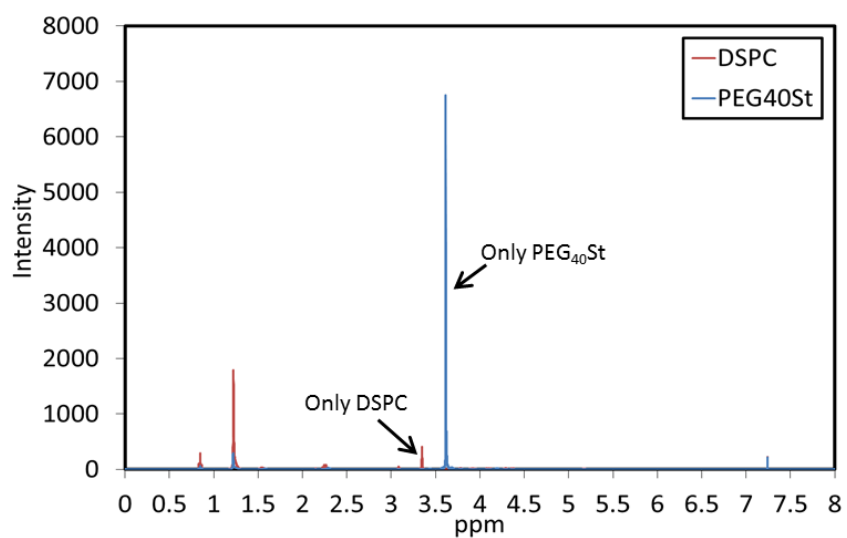


Figure 4.6.  $^1\text{H}$  NMR spectra of pure DSPC and pure PEG<sub>40</sub>St on the same graph.

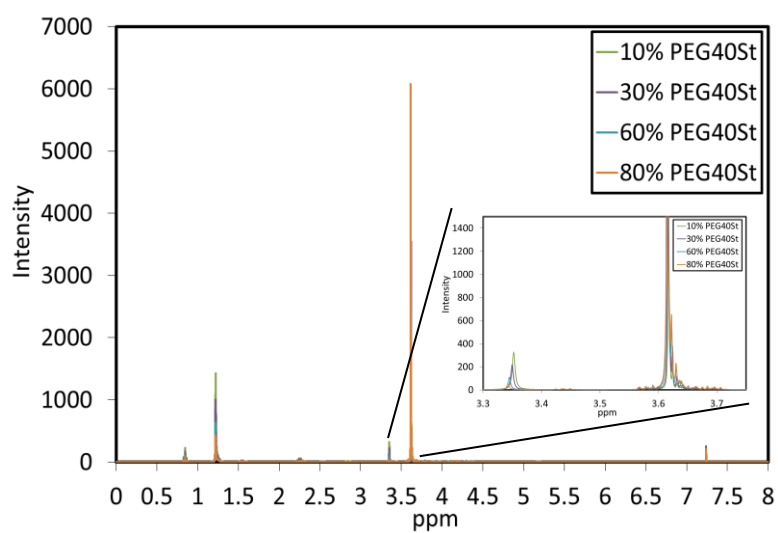


Figure 4.7.  $^1\text{H}$  NMR spectra of DSPC/PEG<sub>40</sub>St mixtures at molar ratios of 9:1, 7:3, 4:6 and 2:8.

A mathematical relationship was derived for the quantification of microbubble shell composition and the subphase of microbubble suspension, as follows:

$$N_1 = X_1 \cdot N \quad (4.1)$$

$$N_2 = X_2 \cdot N \quad (4.2)$$

where  $N$  is the mole of DSPC/PEG<sub>40</sub>St mixture,  $N_1$  is the mole of PEG<sub>40</sub>St,  $N_2$  is the mole of DSPC,  $X_1$  is the mole fraction of PEG<sub>40</sub>St, and  $X_2$  is the mole fraction of DSPC. Here, the sum of  $X_1$  and  $X_2$  is 1. Moles of protons for each component can be written as:

$$N_{H_1} = n_1 \cdot N_1 \quad (4.3)$$

$$N_{H_2} = n_2 \cdot N_2 \quad (4.4)$$

where  $N_{H_1}$  is the moles of protons of the signal assigned to CH<sub>2</sub> protons of PEG,  $N_{H_2}$  is the moles of protons of the signal assigned to N(CH<sub>3</sub>)<sub>3</sub> protons of DSPC,  $n_1$  is the proton number of the signal assigned to CH<sub>2</sub> protons of PEG (156 H), and  $n_2$  is the proton number of the signal assigned to N(CH<sub>3</sub>)<sub>3</sub> protons of DSPC (9 H). If we divide the moles of CH<sub>2</sub> protons to that of N(CH<sub>3</sub>)<sub>3</sub> protons,

$$\frac{N_{H_1}}{N_{H_2}} = \frac{n_1 \cdot X_1 \cdot N}{n_2 \cdot X_2 \cdot N} \quad (4.5)$$

If the moles of protons is proportional to the peak area, (4.5) becomes:

$$\frac{A_1}{A_2} = \left(\frac{n_1}{n_2}\right) \frac{X_1}{1 - X_1} \quad (4.6)$$

where  $A_1$  is the peak area of CH<sub>2</sub> protons of PEG,  $A_2$  is the peak area of N(CH<sub>3</sub>)<sub>3</sub> protons of DSPC. Eq. (4.6) gives the standard calibration curve by plotting the peak area ratio of CH<sub>2</sub> protons of PEG (3.62 ppm) to that of the N(CH<sub>3</sub>)<sub>3</sub> protons of DSPC (3.34 ppm) against known PEG<sub>40</sub>St/DSPC molar ratios.  $n_1/n_2$  gives the value of 17.33. Figure 4.8 shows the <sup>1</sup>H NMR calibration curve. There is a linear relationship between the peak area ratios and the molar ratios. This linearity made the calibration accurate for the quantification of shell composition. The slope of the curve is 15.47, and this value is approximately the same as the actual value (17.33).

<sup>1</sup>H NMR analysis of microbubble shell compositions and the subphases of the microbubble suspensions were performed after obtaining the standard calibration equation.

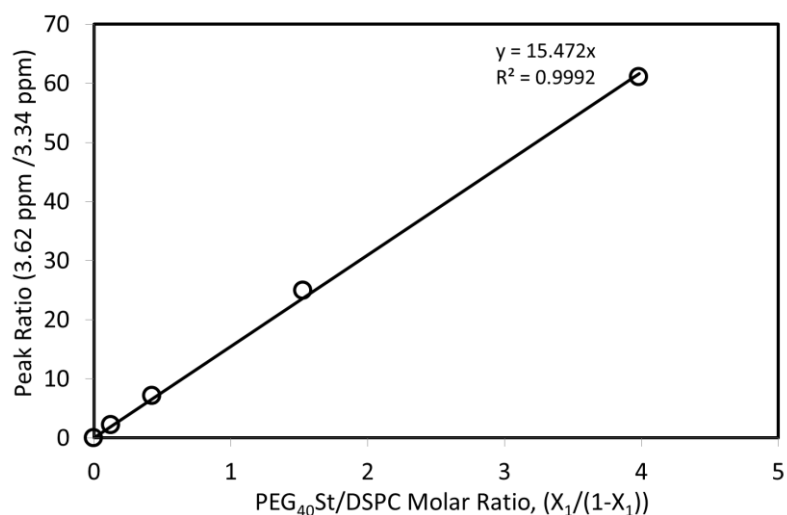


Figure 4.8. <sup>1</sup>H NMR calibration curve.

Figure 4.9 shows the <sup>1</sup>H NMR spectra of microbubble shells and subphases at different PEG<sub>40</sub>St contents from 10% to 80%. The inner graphs illustrate the selected signals at 3.45-3.24 ppm and 3.75-3.50 ppm for the quantification of shell and subphase compositions.

Using the calibration curve, the PEG<sub>40</sub>St/DSPC molar ratios ( $X_1/(1-X_1)$ ) in both microbubble shells and subphases at different PEG<sub>40</sub>St percentages of 9:1 to 2:8 were calculated. The PEG<sub>40</sub>St percentages in the microbubble shells and the subphases were then estimated from the calculated molar ratios. Figure 4.10 shows the PEG<sub>40</sub>St percentages in the microbubble shells and in the subphases with respect to PEG<sub>40</sub>St content in the DSPC/PEG<sub>40</sub>St mixture prior to microbubble formation. It was found that the PEG ratio in the microbubble shells (data points) was lower to that of the initial DSPC/PEG<sub>40</sub>St mixture prior to microbubble formation (dashed line). However, it is expected that the PEG mole fraction in a microbubble monolayer is higher than that of the starting lipid mixture due to the strong affinity of shorter species for the monolayer (Dan 1994, Wrenn, Dicker et al. 2012). This phenomenon also depends on the PEG regimes, known as the “mushroom” and the “brush” (Degennes 1987, Kenworthy, Hristova et al. 1995, Kenworthy, Simon et al. 1995, Wrenn, Dicker et al. 2012). These two regimes depend on the PEG chain density as a function of PEG mole fraction and molecular weight. The PEG<sub>40</sub>St ratio in the microbubble shell did not reach more than 50% even if the PEG<sub>40</sub>St ratio in the mixture was increased up to 80% indicating that much of the PEG<sub>40</sub>St in the initial mixture did not incorporate into the microbubble

shell monolayer at higher PEG<sub>40</sub>St contents. Borden et al. reported that the microbubble shell composition was approximately equivalent to that of the initial premicrobubble suspension up to 20% emulsifier contents. However, the emulsifier they used was a double-chained lipopolymer, DSPE-PEG2000, not our single-chained PEG<sub>40</sub>St. Therefore, the behavior of PEG<sub>40</sub>St could not be equated with the behavior of the PEG-lipids. Figure 4.10 shows that there is a good correlation between the PEG<sub>40</sub>St content of the subphases and that in the mixture indicating that the PEG ratio in the subphase is almost equal to that of the initial DSPC/PEG<sub>40</sub>St mixture. These findings were of importance to interpret the experimental results of the echogenicity and stability studies in acoustic field.

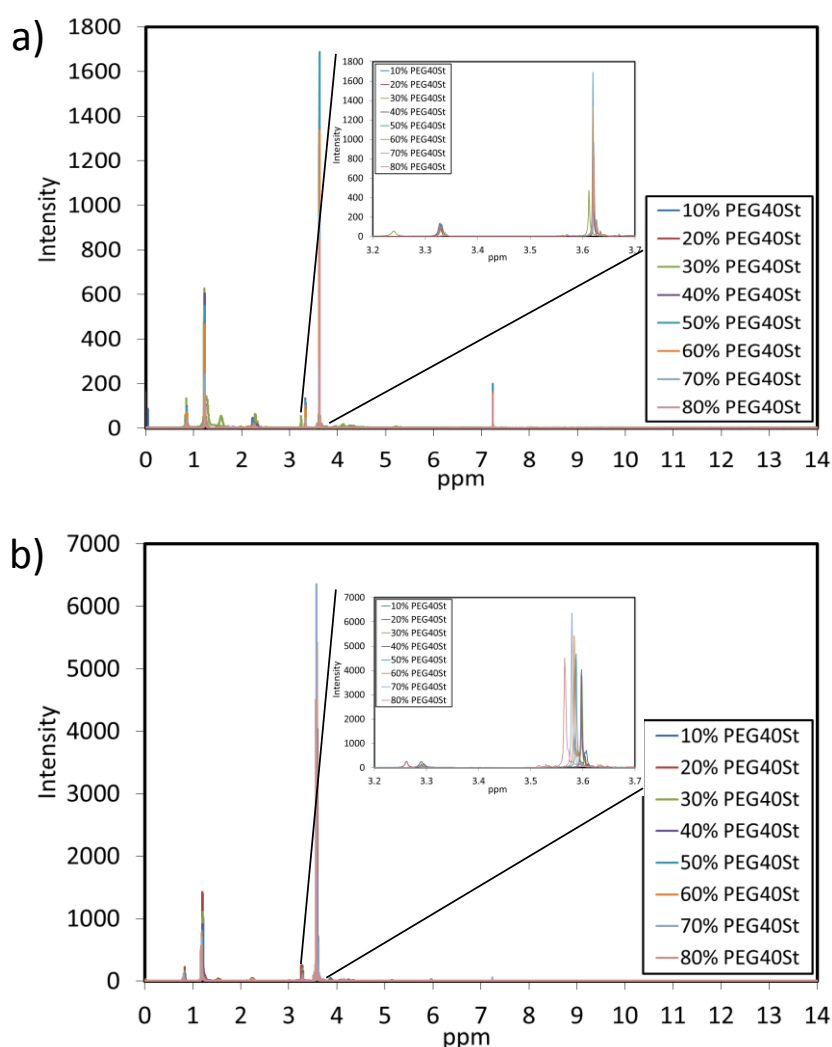


Figure 4.9. <sup>1</sup>H NMR spectra of microbubble shells (a) and subphases (b) at different PEG<sub>40</sub>St contents from 10% to 80%.

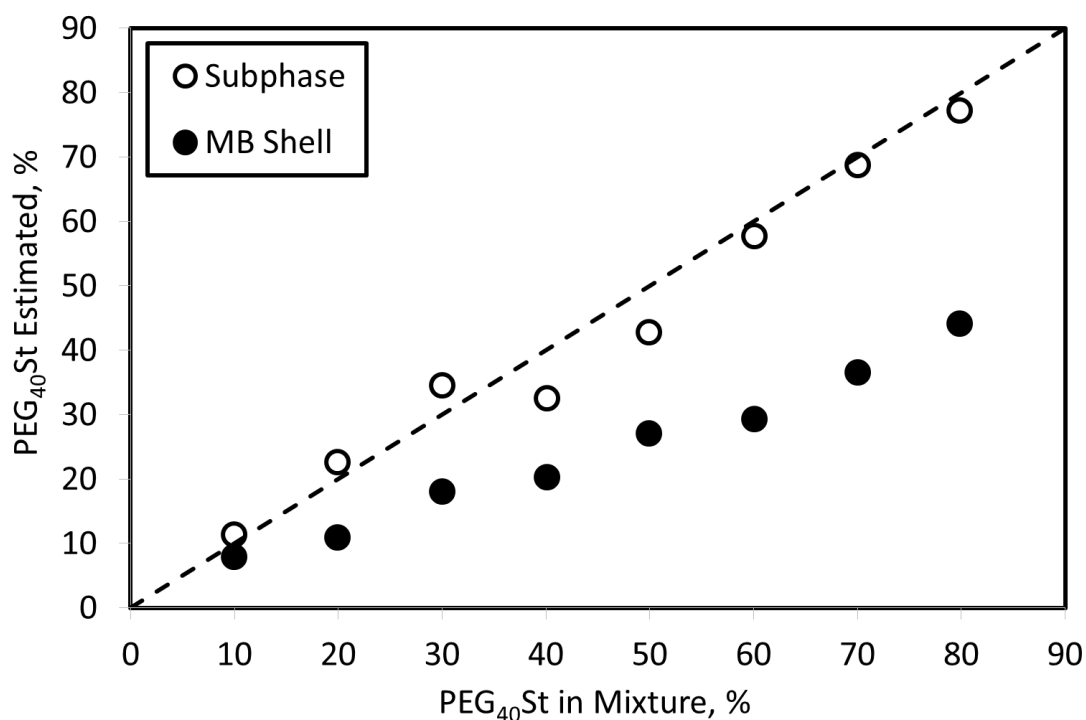


Figure 4.10. Molar percentage of PEG<sub>40</sub>St in the shells of DSPC/PEG<sub>40</sub>St-coated microbubbles as a function of PEG<sub>40</sub>St content in the DSPC/PEG<sub>40</sub>St mixture prior to microbubble formation. The line is theoretical result of equivalent shell and mixture fractions.

### 4.3. The Amount of Microbubble Shell and Subphase in the Microbubble Suspension

The amount of the microbubble shell and subphase components in the microbubble suspensions prepared from DSPC:PEG<sub>40</sub>St mixtures of varying molar ratios was estimated. Figure 4.11 illustrates the percentages of microbubble shells and subphases in the microbubble suspensions as a function of DSPC/PEG<sub>40</sub>St molar ratios of 9:1, 7:3, 5:5 and 3:7. It was found that the microbubble shells formed only 4-6% of the microbubble suspension while the majority of the microbubble suspension was its subphase or excess lipid which did not form the part of the microbubble shells.

It was concluded that the microbubble shell had a negligible amount of lipid and emulsifier with respect to the subphase of the microbubble suspension.

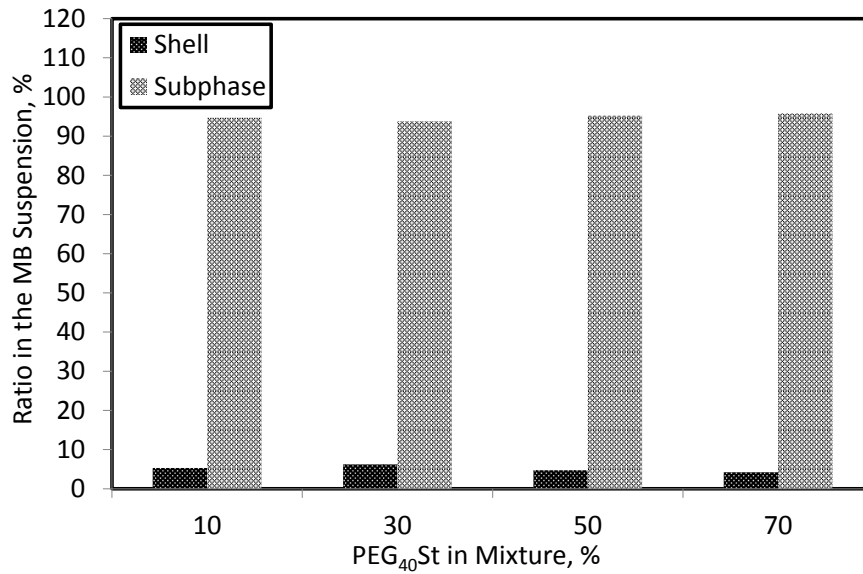


Figure 4.11. Percentages of microbubble shells and subphases in the microbubble suspensions as a function of PEG<sub>40</sub>St content in the mixtures.

#### 4.4. *In-vitro* Characterization of Microbubbles under Ultrasound Activation

In this study, in-house made microbubbles were characterized under ultrasound using the ultrasonic echoscope GAMPT-Scan. For this purpose, calibration studies were performed at different transmitter output powers for different transducer frequencies to assess quantitatively the microbubble concentration in the A-scan mode and B-mode of the ultrasound system. It was also aimed to determine the limiting concentration to eliminate the attenuation for accurate measurements.

##### 4.4.1. Determination of Focus Zones

The ultrasound system was characterized to determine the focus zones of three ultrasonic transducers (1 MHz, 2 MHz and 4 MHz) at the transmitter output power of 10 dB. Figure 4.12 shows the measured amplitudes for each probe. The focal distances which correspond to measured maximum amplitudes for the 1 MHz, 2 MHz and 4 MHz probes were found to be about 40 mm, 100 mm and 125 mm, respectively. Further experiments were conducted at those distances with related probes.

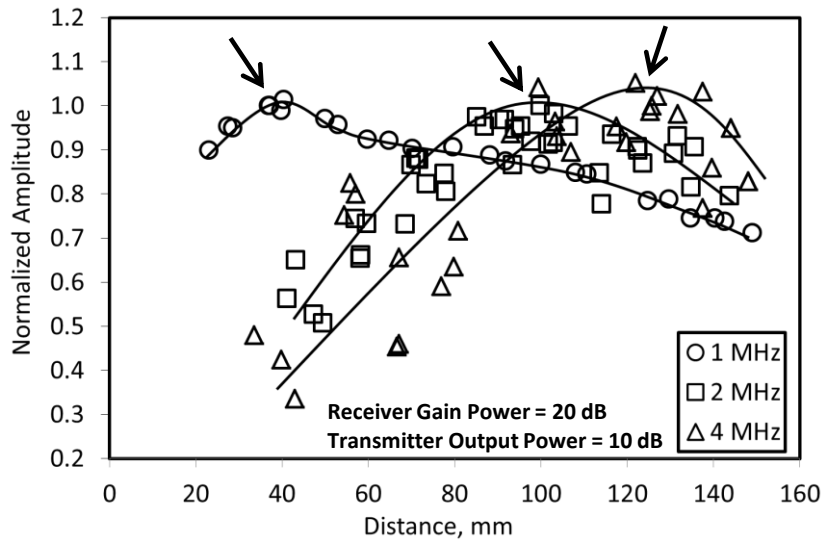


Figure 4.12. Focus zones for different probe frequencies.

#### 4.4.2. Characterization of the Ultrasonic Echoscope

An experimental set-up (Figure 3.2) was designed to characterize the ultrasonic echoscope. Figure 4.13a shows the amplitude profile of a plastic tube containing PBS in the A-scan mode. Diameter of the plastic tube was 2 mm and the wall thickness was 0.5 mm. In the A-scan mode, front wall, rear wall and inside of the plastic tube presented three peaks separately, as seen in Figure 4.13a. We could determine the distance between the front wall and the rear wall of the tube from the A-scan mode. Here, the front wall of the tube was selected as reference point for the ratio of the amplitude of ultrasonic echo reflected from buffer to that of the front wall. As seen in Figure 4.13b, the peak amplitudes of the front wall and buffer in the tube were both increased exponentially as the receiver gain power increased at constant transmitter output power (10 dB). On the other hand, the ratio of the peak amplitude of buffer to the peak amplitude of front wall stayed constant. This result showed that a reference point such as the front wall of the tube could be used in characterizing the ultrasound system even the receiver gain power was changed.

The peak amplitudes of buffer in the plastic tube and the front wall of the tube were measured at different receiver gain powers for each transmitter output power (10 dB, 20 dB, 30 dB). Figure 4.13c shows the peak amplitudes of buffer at each transmitter output power. The peak amplitude increased exponentially when the receiver gain

power increased at each output power. The ratio of buffer amplitude to the front wall amplitude stayed also constant at about 0.8 for different output powers. This result exhibited that the ratio stayed almost constant even if the gain power was changed at the constant output power indicating that the front wall of the tube could be a reference point for any sample measured.

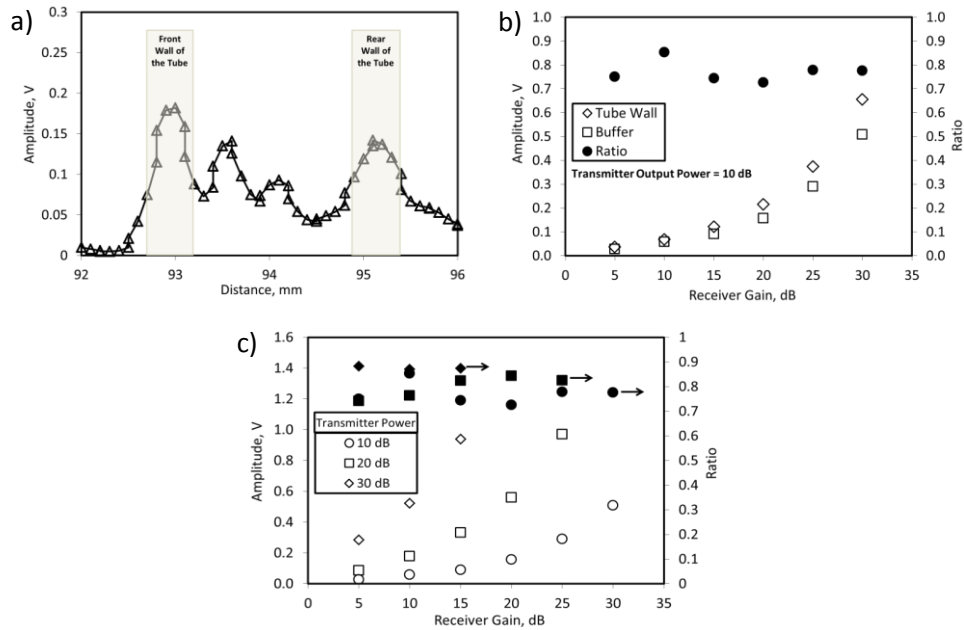


Figure 4.13. (a) Amplitude profile of the plastic tube containing PBS. (b) Peak amplitudes of PBS and front wall of the tube for different receiver gain powers at a 10 dB of output power and the ratios. (c) Maximum amplitude values for PBS.

#### 4.4.3. Characterization of Microbubbles under Ultrasound Excitation

Characterization of the ultrasound system with microbubbles was conducted in both A-scan mode and B-mode. Figure 4.14a shows the peak amplitude values of air, buffer solution and the microbubbles in buffer solution in a plastic tube with a thickness of 0.5 mm in the A-scan mode at a transmitter output power of 10 dB and a frequency of 2 MHz. As seen in the figure, the peaks belonging to the front wall and rear wall of the plastic tube and the inside of the tube can be observed clearly. Air has the highest amplitude when the inside of the plastic tube filled with no buffer solution. This is due to the acoustic impedance producing the highest contrast in the presence of phase

change. When the plastic tube was filled with buffered solution, the amplitude decreased to its minimum value. As a result, in the reflection mode, sound waves were poorly reflected from the inside of the tube in the presence of liquid phase due to low acoustic impedance producing no contrast. In the presence of microbubbles, the amplitude value increased to a certain level lower than that of air itself. This indicated that microbubbles had an acoustic response to the ultrasonic propagation. Figure 4.14b shows the images of air, buffer solution and microbubbles in the plastic tube in the B-mode of ultrasonic echoscope. The B-mode images were produced by stacking the successive frames in every second. The brightness of B-mode images varied due to the acoustic response of each medium. Accordingly, it is clearly seen that the amplitude value is proportional to the image brightness.

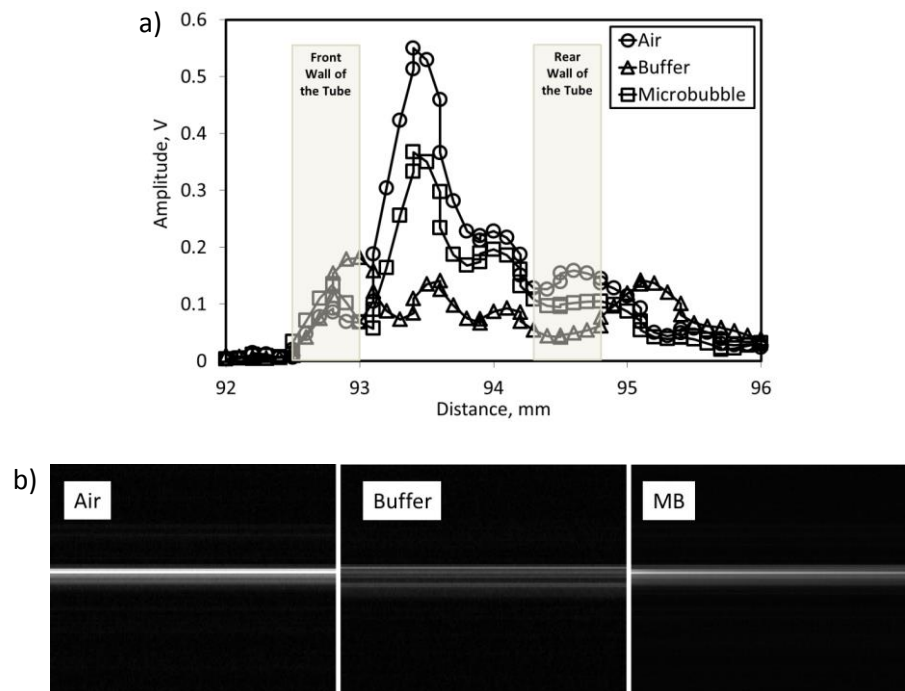


Figure 4.14. (a) Characterization of microbubbles in the A-scan mode under ultrasound, (b) imaging the air, buffer solution and microbubbles in the B-mode.

#### 4.4.4. Calibration Study for Microbubbles in the A-scan Mode and in the B-mode

An experimental set-up shown in Figure 3.3 was used to determine the relationship between the microbubble concentration and the amplitude in A-scan mode

and B-mode intensity. The stock concentration of microbubbles was calculated through the Coulter counter apparatus and the stock solution was diluted to various concentrations. In the A-scan mode, the peak amplitude of microbubble suspension in the plastic tube was measured at different concentrations. B-mode intensity of each microbubble suspension was also estimated from the B-mode images of microbubble suspensions in the tube. The transmitter output power was set at 10 dB and the probe frequency was 2 MHz. Figure 4.15 illustrates the amplitude profile of microbubbles at different concentrations within a plastic tube in the A-scan mode. We could observe from the figure that the front wall of the tube was at a distance of about 100 mm from the probe and that the rear wall of the tube was at a distance of 102 mm from the probe. Therefore, the microbubbles within the tube created ultrasonic signals between these two points. It was observed from the figure that there were two peaks created by the microbubbles. For the analysis, the maximum peak amplitude from the two peaks was evaluated. The amplitude of buffer solution was the minimum value. As the microbubble concentration was increased, the signal amplitude increased.

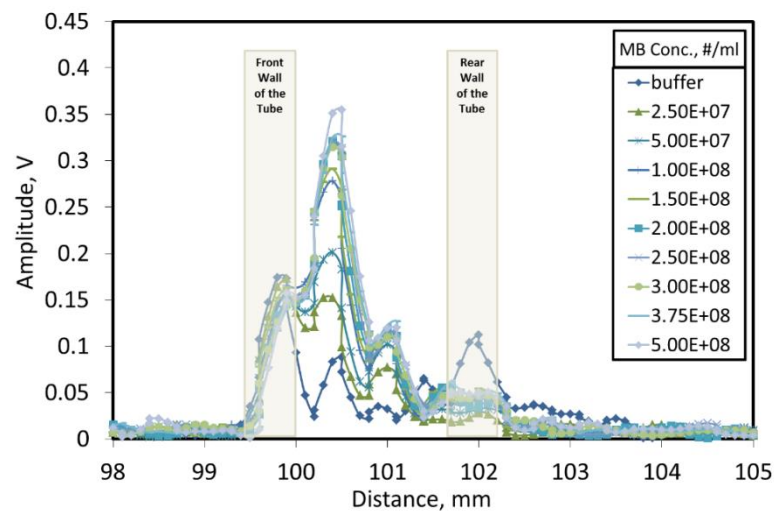


Figure 4.15. Amplitude profile of microbubbles at different concentrations within a plastic tube in the A-scan mode.

Figure 4.16 shows amplitude change as a function of concentration for microbubbles and the change of the signals reflected from the tube wall in the A-scan mode and the B-mode. The front wall was identified as a reference point and the signal from the front wall was also plotted against the microbubble concentration. As seen in

the figure, there is a logarithmic relationship between microbubble concentration and amplitude or B-mode intensity. The signal amplitude or the B-mode intensity of the front wall was stayed constant as the microbubble concentration was increased. Microbubble concentration range used was from  $2.5E+07$  #/ml to  $5E+08$  #/ml. Both the amplitude value and B-mode intensity tended to decrease at high microbubble concentrations. At high microbubble concentrations, the sound waves were absorbed by the microbubbles at the surface of the front wall of plastic tube. This caused attenuation, and thus the most of the sound waves could not pass through microbubble suspension and were reflected from the front wall of the tube. At low concentrations, there was a more linearity between the microbubble concentration and amplitude or intensity. It was concluded that the limiting concentration was  $5E+08$  #/ml for ultrasound contrast agents in ultrasound studies and that low concentrations should be used for accurate calculations. Since there was a logarithmic relationship between the microbubble concentration and amplitude or B-mode intensity, the amplitude and B-mode intensity were plotted against the logarithm of microbubble concentration, as seen in Figure 4.16b. It was shown that there was a linear trend between the logarithm of microbubble concentration and the amplitude or B-mode intensity up to certain concentrations.

The ratio of both amplitude and B-mode intensity of microbubbles to that of the front wall of tube as a reference point were plotted versus the microbubble concentration, as seen in Figure 4.16c. As seen in the figure, there is a logarithmic relationship between the amplitude ratio or the B-mode intensity ratio and the microbubble concentration. Amplitude ratio and the B-mode intensity ratio was also plotted against the logarithm of microbubble concentration, as seen in Figure 4.16d. In both modes, a linear trend was found between the amplitude ratio or B-mode intensity ratio and the logarithm of microbubble concentration. However, the linear curves of two modes gave equations with significantly different coefficients. Therefore, it was concluded that using the front wall of the plastic tube as a reference point could not give accurate results for the calibration studies. Instead, the normalized amplitude and the normalized B-mode intensity with respect to buffer solution were evaluated to find accurate results for the calibration studies in both modes.

Figure 4.16e shows the normalized amplitudes and B-mode intensities of the microbubble suspensions were plotted against the microbubble concentration. As seen in the figure, there is a logarithmic relationship between microbubble concentration and

amplitude or B-mode intensity. According to this result, amplitude and B-mode intensity values were plotted versus the logarithm of microbubble concentration, as seen in Figure 4.16f. There is a linear trend between the logarithm of microbubble concentration and the normalized amplitude or normalized B-mode intensity. The estimated slope values of the curves were very similar indicating that the A-scan mode amplitude and the B-mode intensity were correlated with each other. Concentration of microbubbles could be estimated from the calibration equations according to normalized values in both modes by using the ultrasonic echoscope GAMPT-Scan.

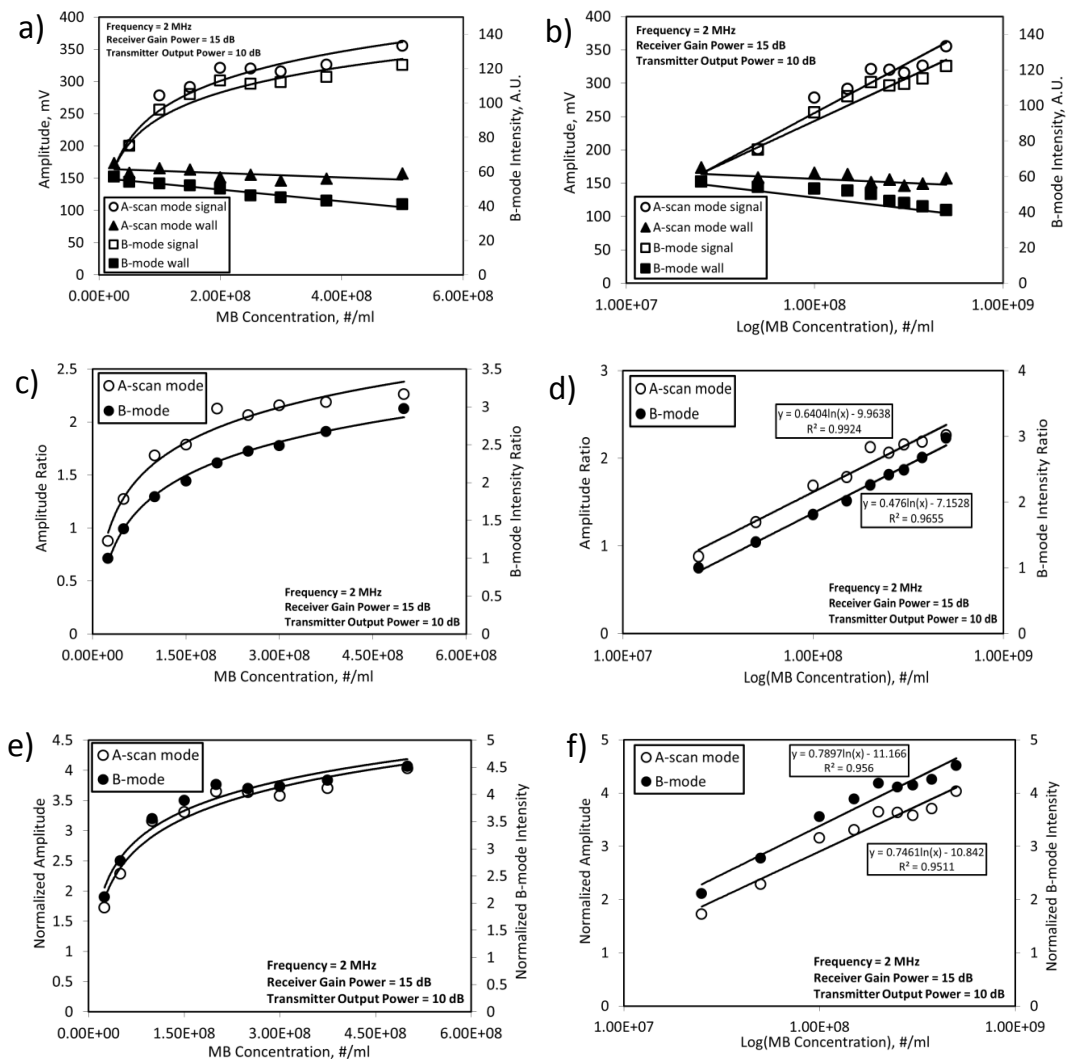


Figure 4.16. Amplitude change as a function of microbubble concentration and the change of the signal reflected from the tube wall in the A-scan mode and the B-mode.

#### 4.4.5. Characterization of Microbubbles at Different Transmitter Powers and Different Transducer Frequencies

Experimental set-up shown in Figure 3.3 was utilized for the calibration study of microbubbles at different transmitter powers (0 dB, 10 dB, 20 dB and 30 dB) and different transducer frequencies (1 MHz, 2 MHz and 4 MHz) in the A-scan mode. Figure 4.17 shows the amplitude profiles of microbubbles within a plastic tube at different concentrations for 1 MHz, 2 MHz and 4 MHz probes in the A-scan mode. It was observed that the front wall of the tube could be seen at 1 MHz. This could be attributed to the frequency effect. The ultrasonic sensitivity of the probe decreased at low frequencies.

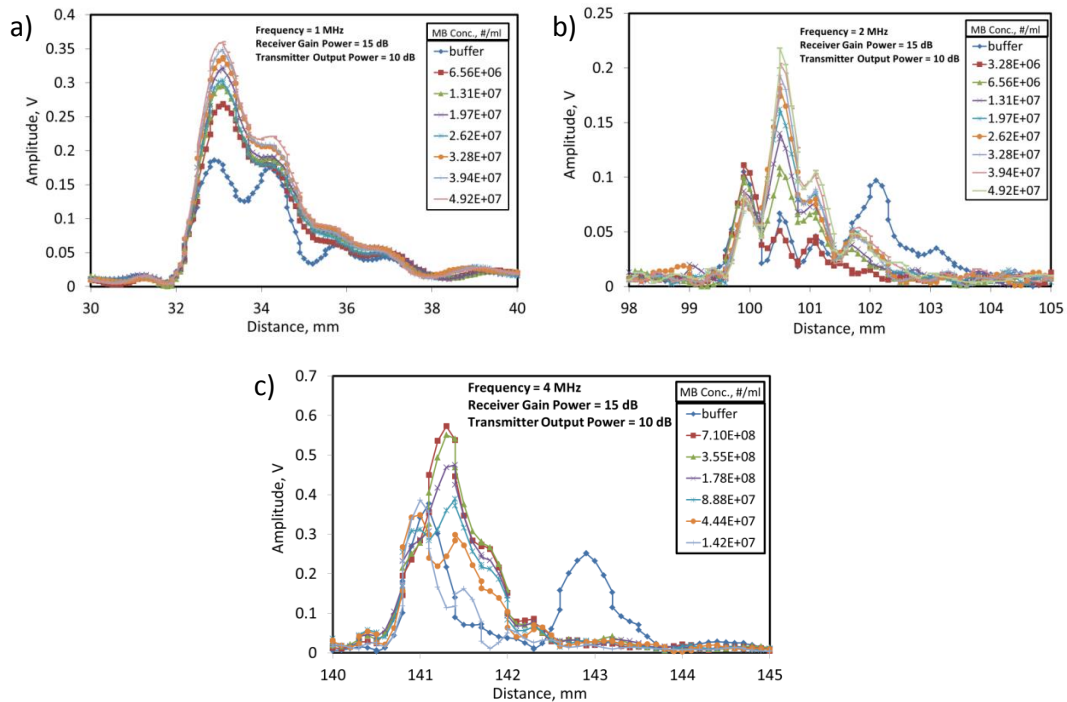


Figure 4.17. Amplitude profiles of microbubbles within a plastic tube at different concentrations for (a) 1 MHz, (b) 2 MHz and (c) 4 MHz in the A-scan mode.

Normalized amplitudes according to buffer solution were assessed for different microbubble concentrations from the amplitude profiles. Figure 4.18a illustrates the normalized amplitudes versus microbubble concentrations for different transducer frequencies at the transmitter power of 10 dB. It can be seen that there is a logarithmic

relationship between the normalized amplitude and the microbubble concentration at three different frequencies. At high concentrations, the amplitude tends to decrease due to attenuation effect. It was also observed from the figure that there was an effect of the frequency on the amplitude of ultrasonic echoes. As the probe frequency was increased, the amplitude increased at the same concentration. Figure 4.18b shows the graph of normalized amplitude with respect to the logarithm of microbubble concentration at different frequencies. It is seen that there is a linear trend between the logarithm of microbubble concentration and the amplitude of ultrasonic echo. Slope values of the curves increased with increasing probe frequencies at the constant transmitter power.

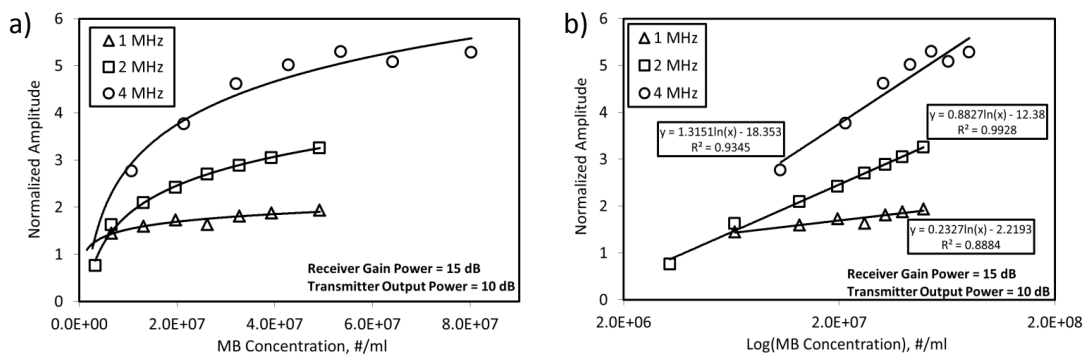


Figure 4.18. (a) Change in amplitude of ultrasonic echo versus microbubble concentration for different transducer frequencies at the transmitter power of 10 dB in the A-scan mode, (b) linear relationship between the logarithm of microbubble concentration and the amplitude for different transducer frequencies.

Calibration study of microbubbles under ultrasound was also performed for different ultrasound powers and probe frequencies in the A-scan mode. Figure 4.19 shows the amplitude profiles of microbubbles of different concentrations within a plastic tube at different transmitter output powers for the 1 MHz probe. Buffer solution had the minimum amplitude value, and the amplitude increased with increasing microbubble concentration.

Figure 4.20a shows the normalized amplitudes with respect to different microbubble concentrations at different transmitter powers for the 1 MHz probe in the A-scan mode. A logarithmic relationship was seen between the amplitude value and microbubble concentration for different transmitter powers.

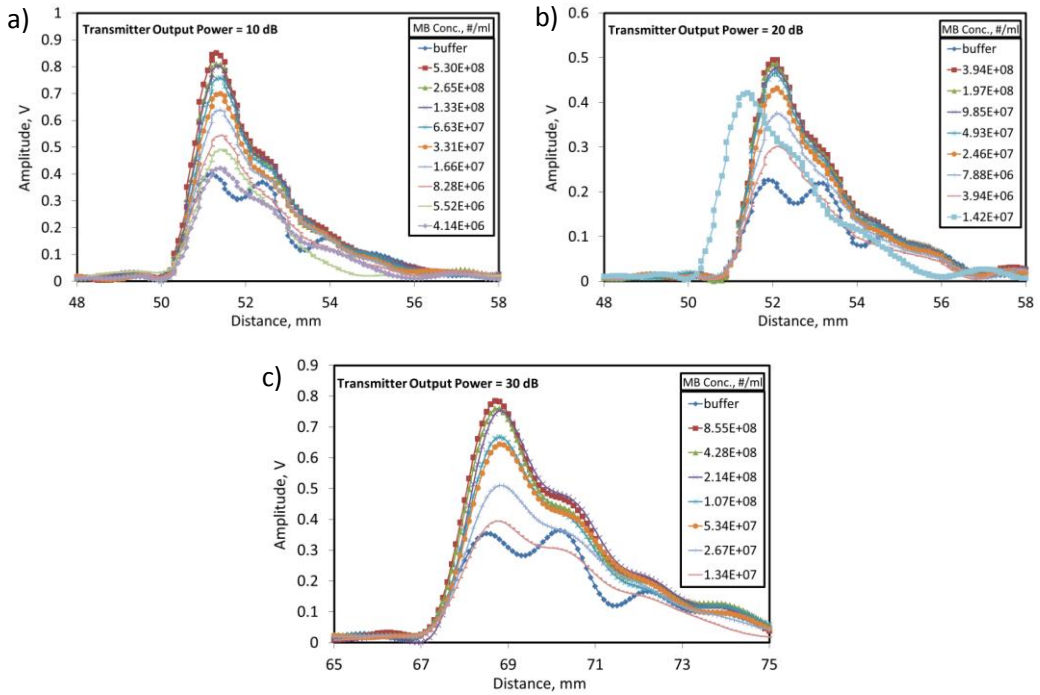


Figure 4.19. Amplitude profiles of microbubbles of different concentrations within a plastic tube at different transmitter powers, (a) 10 dB, (b) 20 dB, (c) 30 dB, for the 1 MHz probe in the A-scan mode.

When we plot the normalized amplitude values versus the logarithm of microbubble concentration, linear trend could be seen for lower concentrations at different transmitter powers (Figure 4.20b). Linear relationship between the logarithm of microbubble concentration and the normalized amplitude could be seen up to a concentration of  $5E+07$  #/ml at all transmitter powers.

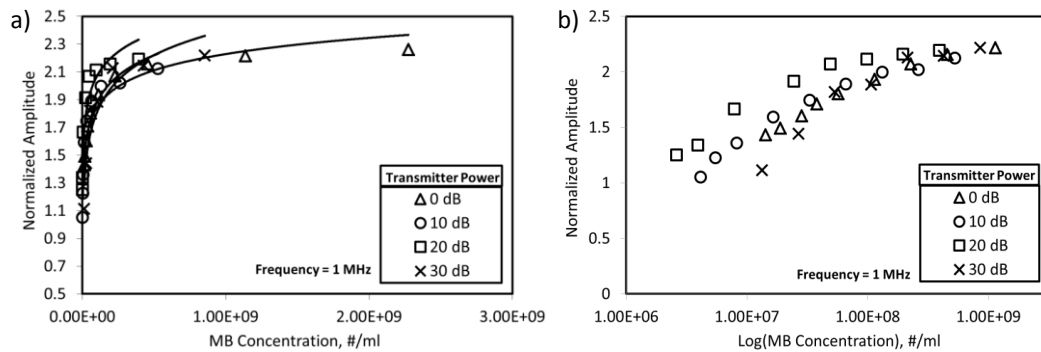


Figure 4.20. Change in amplitude with respect to microbubble concentration at different transmitter powers for the 1 MHz probe in the A-scan mode.

Figure 4.21 shows the amplitude profiles of microbubbles of different concentrations within a plastic tube at different transmitter output powers for the 2 MHz probe. Buffer solution had the minimum amplitude value and the amplitude increased with increasing microbubble concentration.

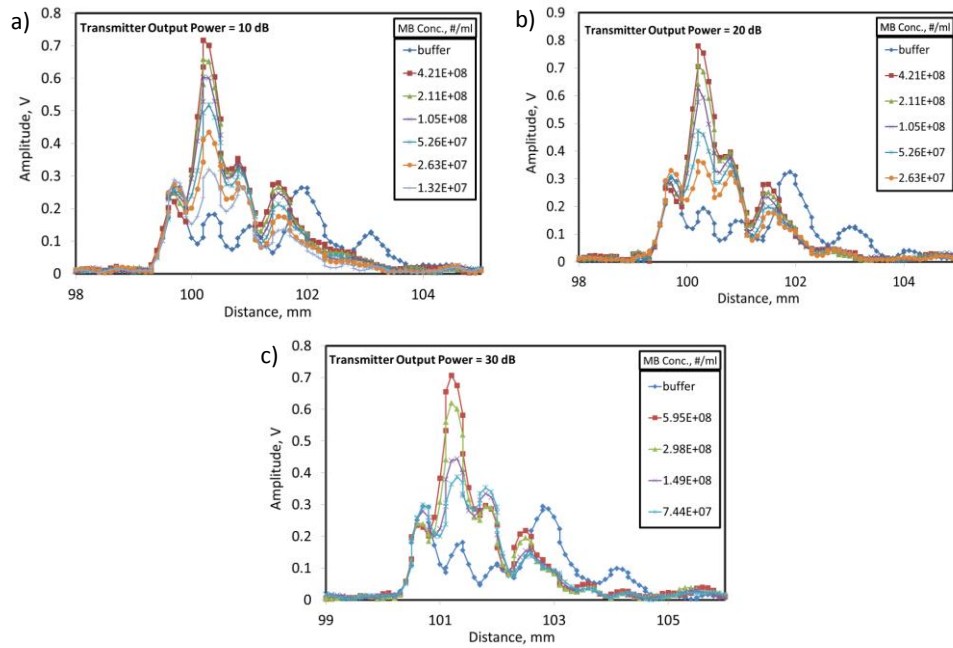


Figure 4.21. Amplitude profiles of microbubbles of different concentrations within a plastic tube at different transmitter powers, (a) 10 dB, (b) 20 dB, (c) 30 dB, for the 2 MHz probe in the A-scan mode.

Figure 4.22a shows the normalized amplitudes with respect to different microbubble concentrations at different transmitter powers for the 2 MHz probe in the A-scan mode. A logarithmic relationship was seen between the amplitude value and microbubble concentration for different transmitter powers. Linear relationship between the logarithm of microbubble concentration and the normalized amplitude could be seen up to a concentration of  $5E+08$  #/ml at all transmitter powers (Figure 4.22b). It was also found that the slope of the curve increased as the transmitter power increased.

Figure 4.23 shows the amplitude profiles of microbubbles of different concentrations within a plastic tube at different transmitter output powers for the 4 MHz probe. Buffer solution had the minimum amplitude value, and the amplitude increased with increasing microbubble concentration.

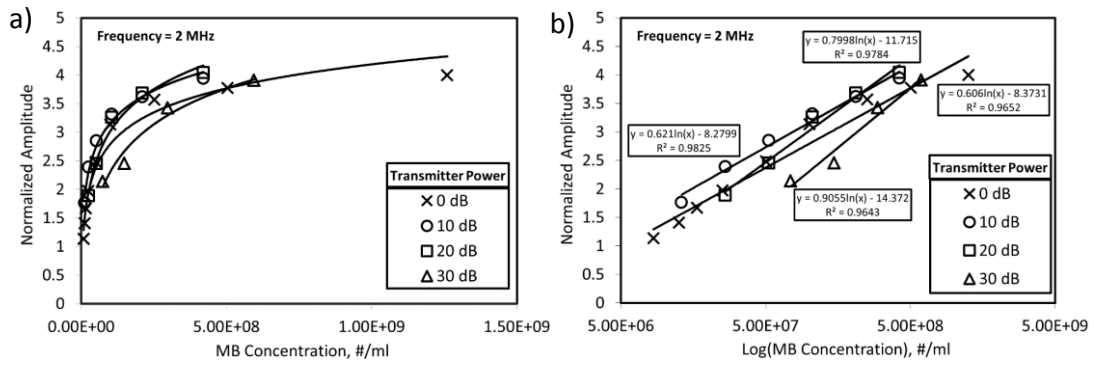


Figure 4.22. Change in amplitude with respect to microbubble concentration at different transmitter powers for the 2 MHz probe in the A-scan mode. (a) Normalized amplitude vs. concentration for different transmitter powers, (b) linear relationship between the logarithm of microbubble concentration and the amplitude of ultrasonic echo for different transmitter powers.

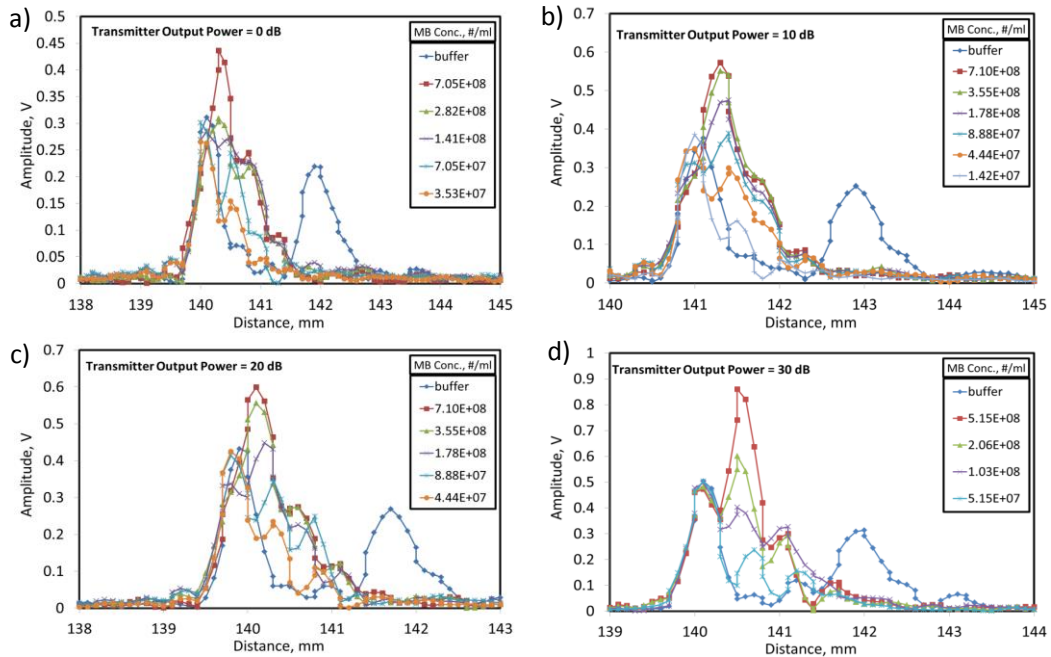


Figure 4.23. Amplitude profiles of microbubbles of different microbubbles within a plastic tube at different transmitter powers, (a) 0 dB, (b) 10 dB, (c) 20 dB, (d) 30 dB, for the 4 MHz probe in the A-scan mode.

Figure 4.24a shows the normalized amplitudes with respect to different microbubble concentrations at different transmitter powers for the 2 MHz probe in the A-scan mode. A logarithmic relationship was seen between the amplitude value and microbubble concentration for different transmitter powers. Linear trend between the logarithm of microbubble concentration and the normalized amplitude could be seen up

to a concentration of  $7E+08$  #/ml at all transmitter powers (Figure 4.24b). It was also found that the slope of the curve increased as the transmitter power increased.

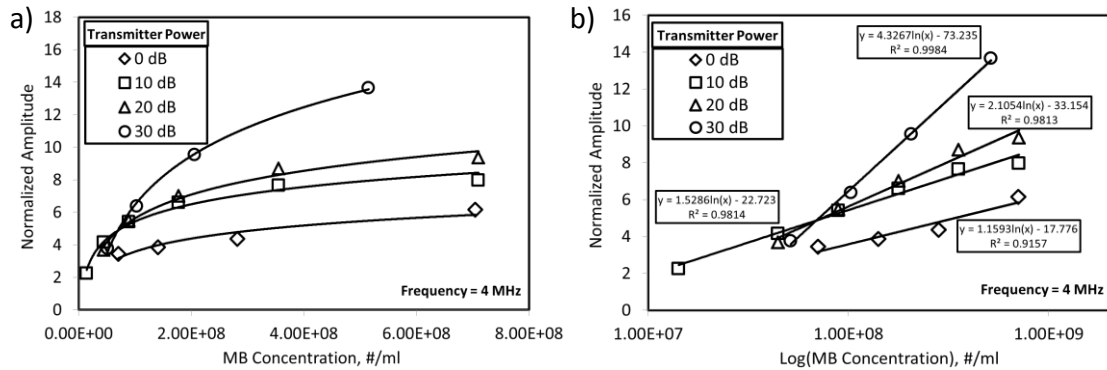


Figure 4.24. Change in amplitude with respect to microbubble concentration at different transmitter powers for the 4 MHz probe in the A-scan mode. (a) Normalized amplitude vs. concentration for different transmitter powers, (b) linear relationship between the logarithm of microbubble concentration and the amplitude of ultrasonic echo for different transmitter powers.

In subsequent experiments, it was observed that the ultrasound sound waves were absorbed by the dense microbubble layer on the surface of the tube when microbubbles were used at high concentrations. Thus, it was found that a large part of the sound wave was actually returned from the surface, not reaching the microbubbles in the targeted area. As a result, ultrasound studies showed that there was a limiting concentration for ultrasound contrast agents, and it should be necessary to study at low concentrations.

In calibration equations derived from the calibration curves, 'x' and 'y' refer to the microbubble concentration and the normalized amplitude, respectively. In the subsequent stability studies, the concentration values were calculated by substituting the obtained amplitude values for the 'y' in the equations.

#### 4.5. Investigation of the Stability of Microbubbles under Ultrasound Excitation through the Peristaltic Pump

*In-vitro* stability of the microbubbles was investigated using the experimental setup shown in Figure 3.4. Microbubbles were circulated by a peristaltic pump.

### 4.5.1. Investigation of Shear Effect on Microbubbles under Ultrasound Excitation

In this study, the effect of flow rate on the stability of microbubbles was investigated under ultrasound activation in a closed system. Stability of microbubbles was measured for different flow rates at 2 MHz and 10 dB output power. Figure 4.25 shows the change of normalized amplitude with time for different flow rates. At low flow rates, microbubbles passed slowly through the tube in the circulation and this caused the microbubbles going upward due to the buoyancy force rather than driving force. As a result, microbubbles attached to the tube wall and most of the microbubble population could not reach to the acoustic zone, therefore low acoustic signals were seen in A-scan mode. As the flow rate was increased, microbubbles started to stay in the circulation in longer period of times such as 5 hours. This is a very long time for our study. On the other hand, the decrease in the number of microbubbles was accelerated due to both the shear stress effect at high flow rates and the increase in the rotation of the rotating parts of the peristaltic pump. As shown in the figure, it is understood that the optimum flow was at the flow rate of 10.089 ml/min.

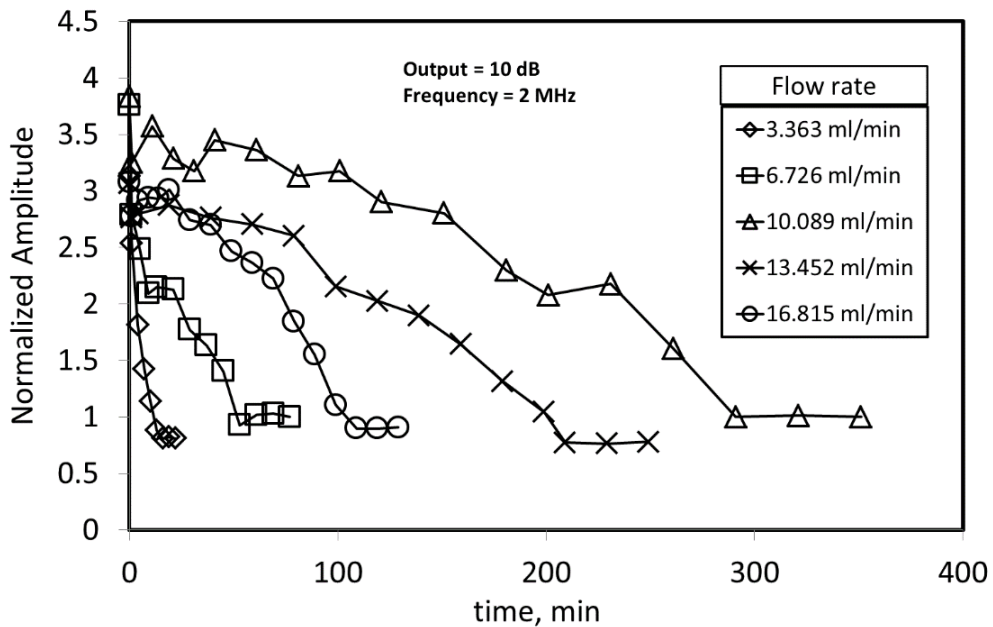


Figure 4.25. The effect of shear rate on the stability of microbubbles under ultrasound activation.

## 4.5.2. Effect of Ultrasound Power and Transmitter Frequency on the Stability of Microbubbles

In the first experiment, stability of microbubbles was assessed over time at the frequencies of 1 MHz, 2 MHz, and 4 MHz, at a constant flow rate of 8.127 ml/min, at 0 dB output power, and at the same initial microbubble concentration of  $\sim 6E+07$  #/ml.

Figure 4.26 shows the time-concentration graphs created using the normalized amplitude values and calibration equations obtained by dividing the measured amplitude value for the microbubble suspensions to that of the phosphate buffer solution. As shown in Figure 4.26, microbubbles exhibited greater stability at low frequencies, while microbubbles lost their stability in shorter times at 4 MHz.

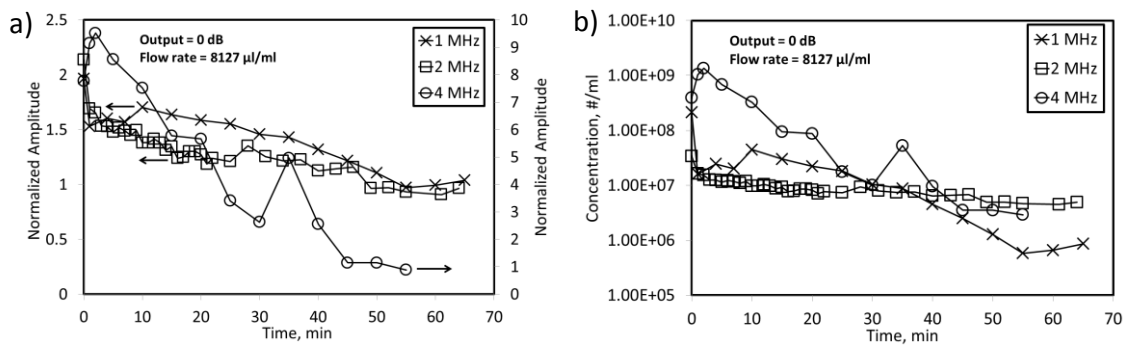


Figure 4.26. The effect of different transducer frequencies on the stability of microbubbles.

In the second assay, stability of microbubbles was investigated at a constant flow rate (8.127 ml/min), at a frequency of 2 MHz and at the same initial concentration ( $\sim 6E+07$  #/ml) over time. Figure 4.27 shows the time-normalized amplitude graph and the time-concentration graph derived from calibration equations.

As seen in the figure, as the output dB increased, the stability of the microbubbles decreased and the microbubbles quickly dissolved at 30 dB. At 0 dB, the ultrasound effect on the microbubbles was minimized. As seen in the figure, as the output dB increased, the stability of the microbubbles decreased.

Microbubbles lost their stability in less than 5 min at 10 dB, in about 30 min at 20 dB and in about 10 min at 30 dB. These findings are expected. It has been demonstrated in previous studies that the microbubbles, normally at room temperature,

remain stable for more than 1 hour (without circulation). However, even though the ultrasound effect is almost non-existent (0 dB), it is seen that there is a slight decrease in the concentration of microbubbles.

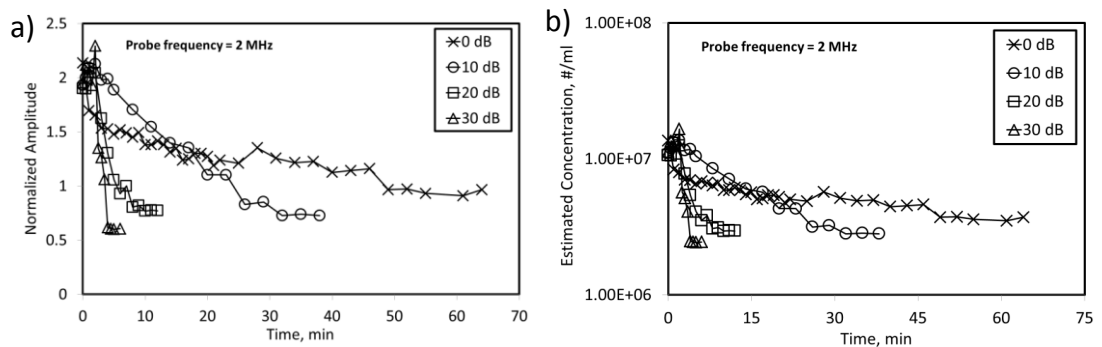


Figure 4.27. Effect of different dBs on stability.

In the stability study with the peristaltic pump, we might suggest two reasons that were effective in leading to dissolution of microbubbles. The first reason was that the microbubbles burst as a result of the compressing of the tube by the peristaltic pump roller in the peristaltic pump chamber, where the tube was located. This effect became like a hammer effect at high flow rates and, in a much more sensible manner, affected the microbubble stability.

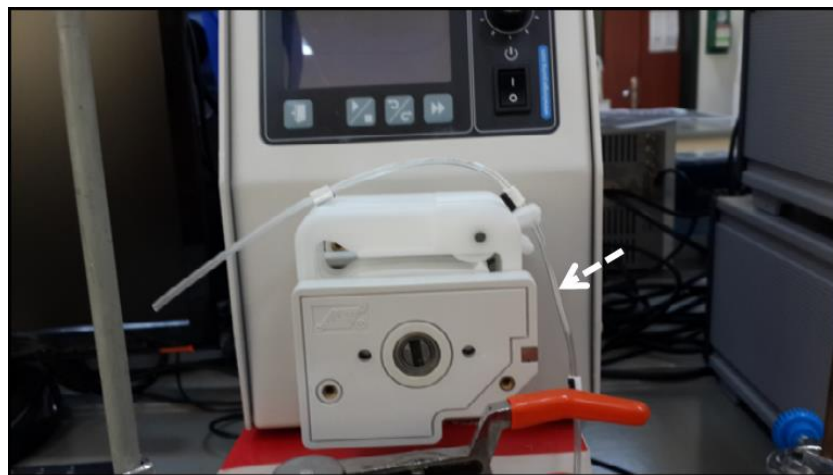


Figure 4.28. Photo indicating that the peristaltic pump rotating parts used in the experiment crushed the microbubbles. White arrow shows the remaining lipid aggregates from the destroyed microbubbles.

The second factor was that microbubbles lose their stability as a result of circulation at a certain shear stress in the fluid. In the first approach, it was understood from the examination of the tube used for the experiment that the peristaltic pump crushed the tube wall and the microbubbles lost their stability during flowing.

Figure 4.28 shows the wall of the silicon tube used in the peristaltic pump rotating parts. In the region indicated by the white arrow, the lipid aggregates accumulated in the silicon tube wall are seen as a result of the dissolution of microbubbles. This is an indication of the role of crushing microbubbles in the stability decrease over time. In the following studies, it was aimed to use devices other than the peristaltic pump to eliminate this negative effect.

## **4.6. Investigation of the Stability of Microbubbles with Different Shell Compositions under Ultrasound Activation**

An experimental set-up was designed to analyze the *in-vitro* stability of microbubbles with different shell compositions as shown in Figure 3.5.

### **4.6.1. Calibration Study for Microbubbles**

Calibrations were performed for the microbubble concentration with the new experimental design. For this purpose, 1, 2 and 4 MHz probes were used at the output power of 10 dB. First, the reference amplitudes of the rear wall of the container were saved in the presence of buffered solution containing no microbubbles for each frequency. After the magnetic stirrer was operated, 1  $\mu$ l volume of microbubbles from the stock suspension was added into the buffered solution in order to get the lowest concentration of  $1E+02$  #/ml in the container. Shortly after, the amplitude of the rear wall was saved as a reference point. Volumes of microbubble suspension from the stock concentration were added into the container increasingly. After every addition, the peak amplitudes of the rear wall were recorded. The acoustic signal dropped as the microbubbles were added into the solution. Figure 4.29 shows the amplitudes for every microbubble suspension volume and the calibration graph. As seen in Figure 4.29a, the highest signal was obtained when there was no microbubble in the medium. The attenuation coefficients were calculated for each microbubble concentration in the

solution using the Eq. (3.1). As seen in Figure 4.29b, there is a linear relationship between the microbubble concentration and the attenuation values in a certain concentration range. This range corresponds to  $1\text{E}+03 - 5\text{E}+06 \text{ \#/ml}$ .

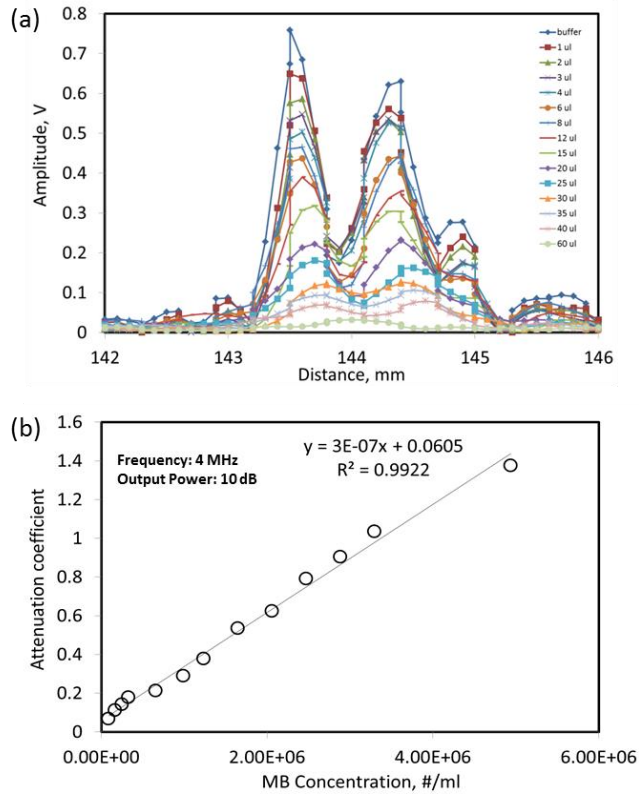


Figure 4.29. a) The peak signals reflected from the rear wall of the container at different microbubble concentrations, (b) calibration graph for microbubble concentration.

Previous calibration experiment was performed for the 4 MHz probe. Two calibration experiments were also performed for 1 MHz and 2 MHz. As seen in Figure 4.30, there is an inverse relationship between concentration-amplitude and concentration-attenuation values. Figure 4.30a shows that at low concentrations maximum amplitude values were obtained due to completely transmission of sound waves through the microbubble suspension. As the concentration increased, after a certain concentration point the amplitude started to drop to zero. However, as seen in Figure 4.30b, at low concentrations, attenuation values were found to be zero from the Eq. (3.1). As a result, amplitude and attenuation calibrations of microbubbles were conducted in a certain concentration range for each probe frequency in order to measure the stability of microbubbles under ultrasound.

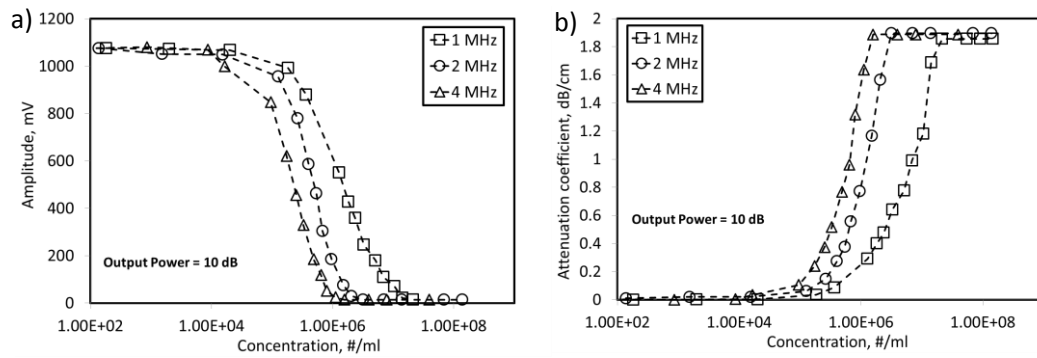


Figure 4.30. Microbubble calibration graphs at different frequencies, (a) concentration values vs. amplitude values, (b) concentration values vs. attenuation values.

#### 4.6.2. Stability of Microbubbles at Different Transducer Frequencies

The effect of ultrasound frequency on the stability of microbubbles under stirring at the highest output power was investigated using the experimental set-up shown in Figure 3.5. Figure 4.31a and Figure 4.31b show the concentration and attenuation change at different frequencies, respectively. Concentration of microbubbles was also measured under stirring over time without ultrasound application. When no ultrasound was applied on microbubbles, it was observed that there was a slight decrease in microbubble concentration over time. This could be attributed to the shear effect due to the stirring condition. However, this decrease occurred over a relatively long time as about 200 min. It might be suggested that the 5:5 microbubbles were stable under stirring conditions for *in-vivo* studies. Microbubbles exhibited greater stability at low frequencies, while microbubbles lost their stability in shorter times at high frequencies, as seen in the figure. Both the concentration and the attenuation of microbubbles decreased in shorter times as the frequency was increased. Microbubbles lost their stability in 100 min at 4 MHz. They lost their stability in 150 min for the 2 MHz frequency and in 300 min for the 1 MHz frequency. The frequency effect could be attributed to the resonance frequency of microbubbles. It has shown that the resonance frequency of a bubble is inversely proportional to its diameter (De Jong, Ten Cate et al. 1991). The 5:5 microbubbles have a mean size of 2.5-3  $\mu\text{m}$  and a resonance frequency of 3-4 MHz. Therefore, at 4 MHz, 5:5 microbubbles are expected to have higher oscillations compared to lower frequencies. They could undergo destruction more

rapidly at the highest transmit power due to the higher interaction with ultrasound at the resonant frequency.

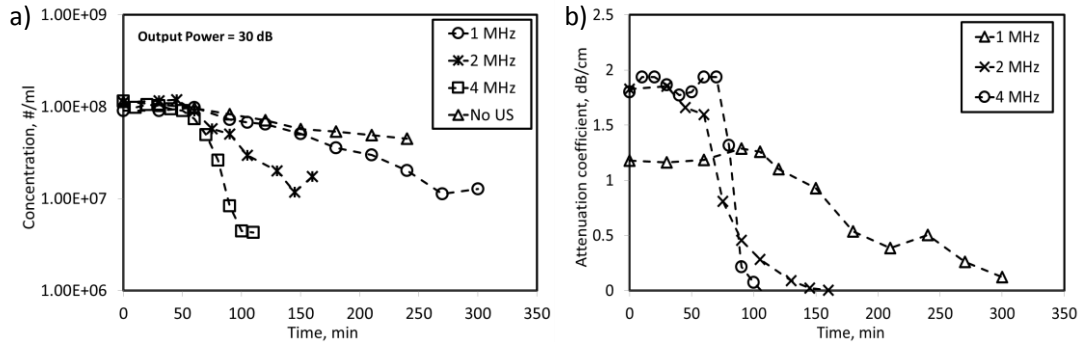


Figure 4.31. Stability of microbubbles at different probe frequencies in terms of concentration and attenuation.

### 4.6.3. Stability Test for the Microbubbles with Different Shell Compositions under Ultrasound Excitation

*In vitro* stability of microbubbles filled with perfluorocarbon was investigated at different PEG<sub>40</sub>St contents under ultrasound. Each type of microbubble suspension was exposed to ultrasound at high frequency (4 MHz) and at the highest output power (30 dB) at ambient conditions. Experiments were also repeated at least 5 times for each type of microbubble suspension. The initial concentration was kept constant for each assay. Concentration of the microbubble suspension in the container was measured through the Coulter-Counter apparatus over time. Figure 4.32 shows the change in concentration and attenuation coefficient for microbubbles at DSPC/PEG<sub>40</sub>St molar ratios of 9:1, 8:2, 7:3, 6:4 and 5:5. For the 10% PEG<sub>40</sub>St, the attenuation coefficient was not decreased for a long period of time and stayed at high values. This could be attributed to the presence of daughter microbubbles or micelles, liposomes and lipid aggregates formed after the destruction of microbubbles in the suspension at high powers, thus preventing the reflection of sound waves from the rear wall of the container. Inertial cavitation can lead to fragmentation during the bubble collapse, thus the splitting of microbubbles into smaller bubbles (Dayton, Morgan et al. 1999, Chomas, Dayton et al. 2001, Chomas, Dayton et al. 2001, Postema, Van Wamel et al. 2004). As seen in the figure, experiments were repeated 5 times for the 9:1 shell composition. Attenuation decrease

could be measured from 80 to 200 min. For the 8:1 shell composition, microbubble concentration did not change in the first 20 min, and then the concentration decrease was seen due to the ultrasonic exposure. Attenuation decrease could be measured after 40 minutes and the microbubbles lost their stability in 80 minutes totally. For the 7:3 shell composition, after 25 min microbubble concentration started to decline and proceeded to decrease. Attenuation decrease could be measured after 50 minutes and attenuation was zero in about 200 min. The least stable microbubble type was found to be 6:4 shell composition. These microbubbles lost their stability totally in 40 minutes in terms of both concentration and attenuation. Finally, for the 5:5 shell composition, microbubble concentration almost showed no decrease in the first 20 min, after then all the microbubbles in the suspension were destructed with a sharp decline in concentration in 75 min. Attenuation decrease could be measured after 30 min and the attenuation was zero in about 80 min for the 5:5 shell composition.

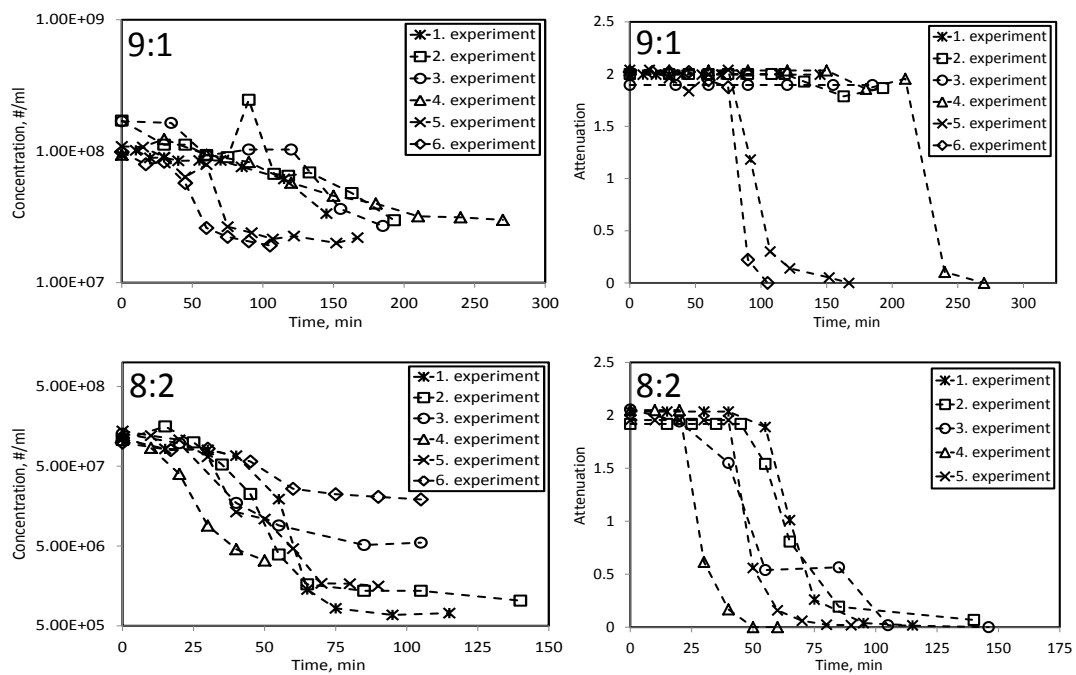


Figure 4.32. Stability of microbubbles with different shell compositions under ultrasound activation with respect to concentration and attenuation.

(Cont. on next page)

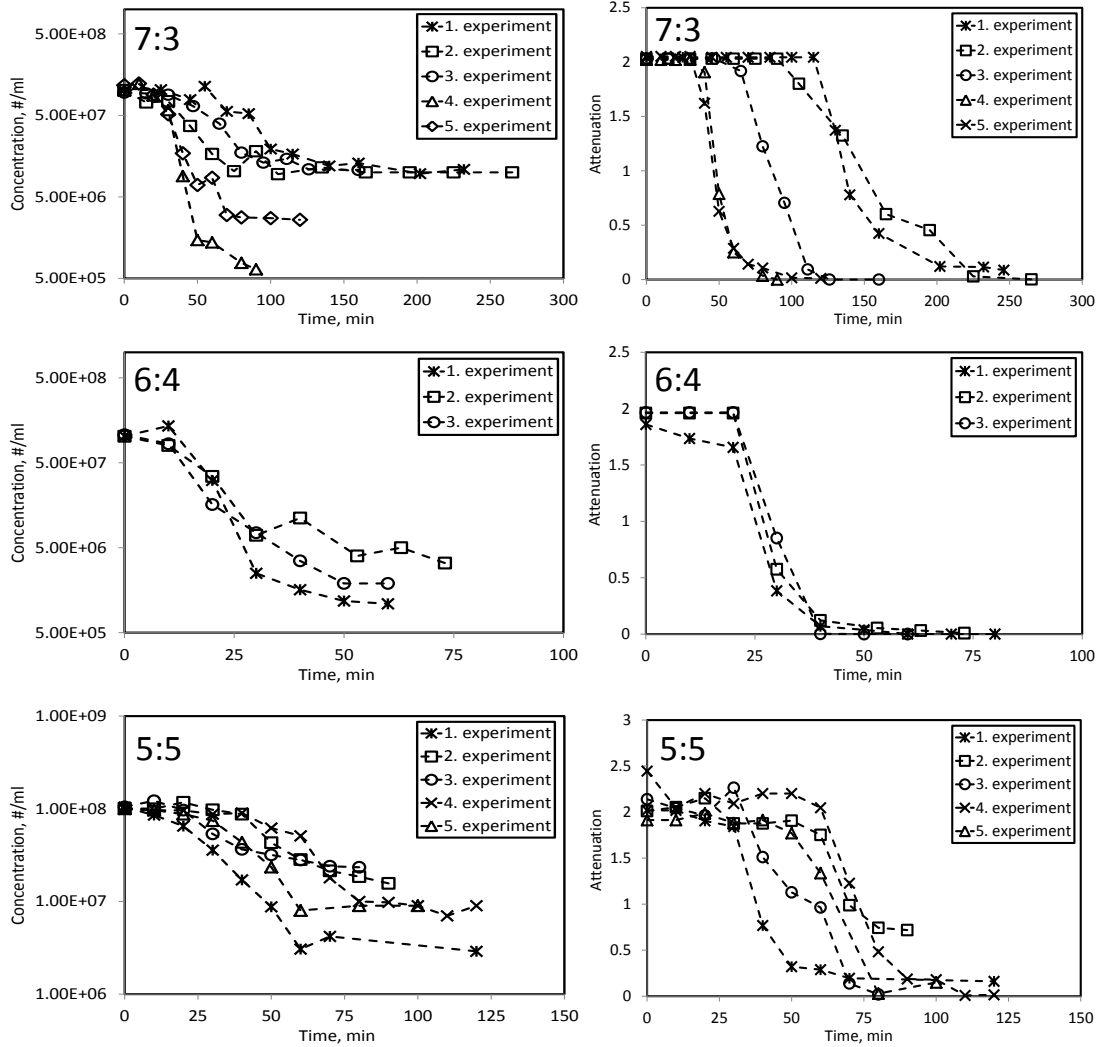


Figure 4.32. (cont.)

Size distributions of the microbubble populations were also measured during the acoustic propagation using the Coulter Counter apparatus. Figure 4.33 shows the change of size distributions for the microbubble populations with different PEG<sub>40</sub>St molar ratios over time. For all compositions, the total volume of microbubbles was decreased over time.

Figure 4.34 shows the mean diameter change with time for microbubbles at DSPC/PEG<sub>40</sub>St molar ratios of 9:1, 8:2, 7:3, 6:4, 5:5 under ultrasound. For the 9:1 composition, mean size of the population stayed almost constant at around 5  $\mu\text{m}$  over time. For the compositions from 8:2 to 5:5, it was observed that the mean size increased for a certain period of time. This could be attributed to the fusion of the smaller daughter bubbles fragmented from the parent bubbles in the suspension. This fusion

might increase the mean size of the population while the number of the microbubbles decreased.

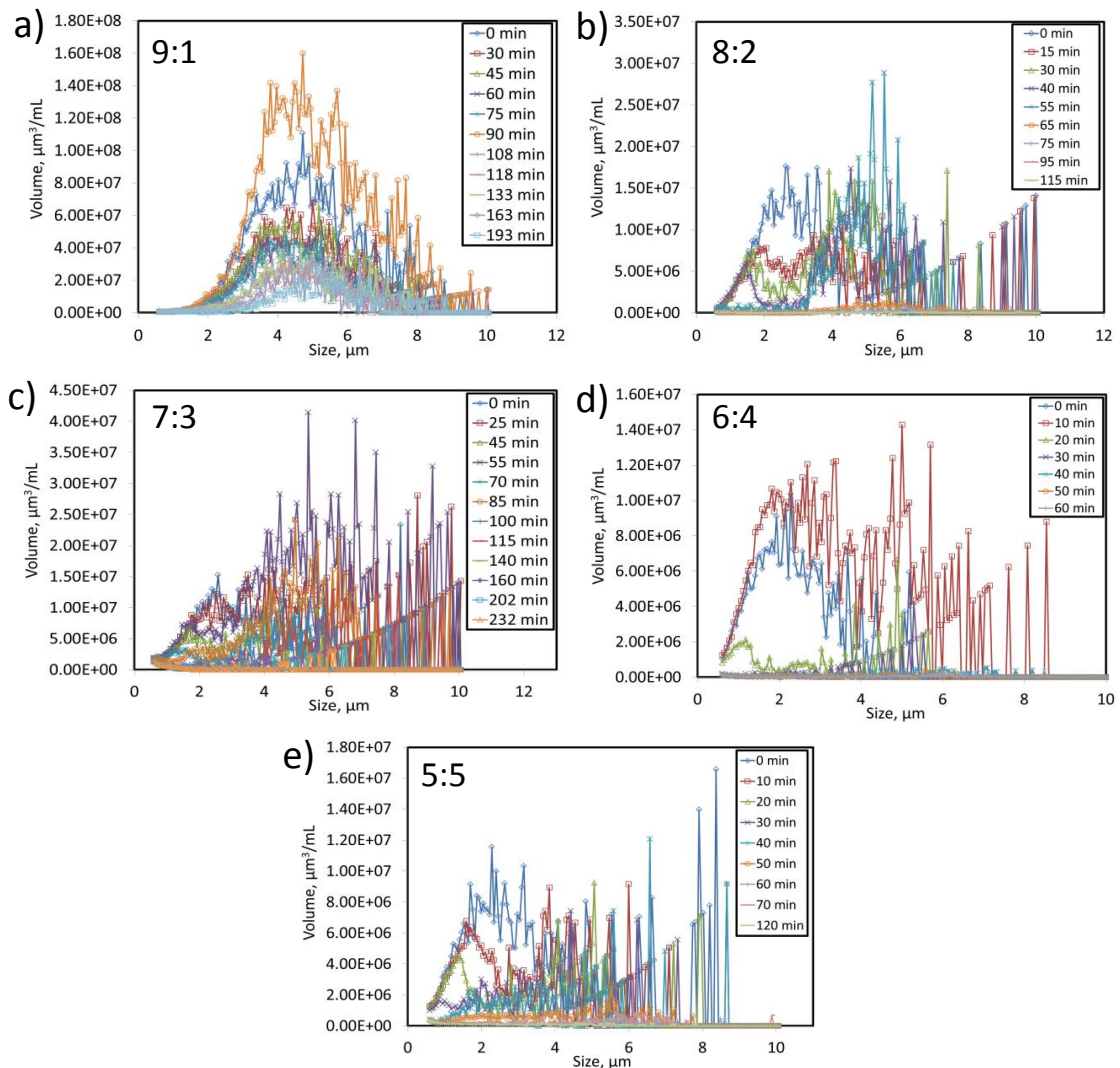


Figure 4.33. The change of volume-weighted size distribution with time for microbubbles at DSPC/PEG<sub>40</sub>St molar ratios of (a) 9:1, (b) 8:2, (c) 7:3, (d) 6:4, and (e) 5:5 under ultrasound excitation.

Comparison of microbubble stabilities as a function of PEG<sub>40</sub>St concentration in the shell of microbubbles for the attenuation and concentration is shown in Figure 4.35 indicating that above 7.5% PEG<sub>40</sub>St content, lifetime of microbubbles decreased significantly under ultrasound in terms of attenuation or concentration. However, higher mole fractions of PEG<sub>40</sub>St did not appear to significantly impact the lifetime of microbubbles.

Bubble destruction at higher ultrasonic pressures is mostly related to the lipid shell physicochemical properties (Borden, Kruse et al. 2005, Wrenn, Mleczko et al. 2009). The emulsifier PEG molecules in the microbubble monolayer shell may be in the brush or mushroom regimes (Wrenn, Dicker et al. 2012, Dicker, Mleczko et al. 2013, Abou-Saleh, Swain et al. 2014). Above 10% PEG concentration, the shells of microbubbles have a dense brush regime due to higher packing density of PEG. Recent experimental investigations by Hosny et al. (Hosny, Mohamedi et al. 2013) have demonstrated that both the shell viscosity and elastic modulus of microbubbles significantly decreased with increasing PEG<sub>40</sub>St concentration from 10% to 50% indicating that the shell stiffness decreases as the PEG concentration increases. We could attribute the higher stability of 9:1 microbubbles under ultrasound to its higher stiffness. It could be concluded that the microbubble stiffness decreased as the PEG concentration increased, thus leading to higher bubble destructions under ultrasound.

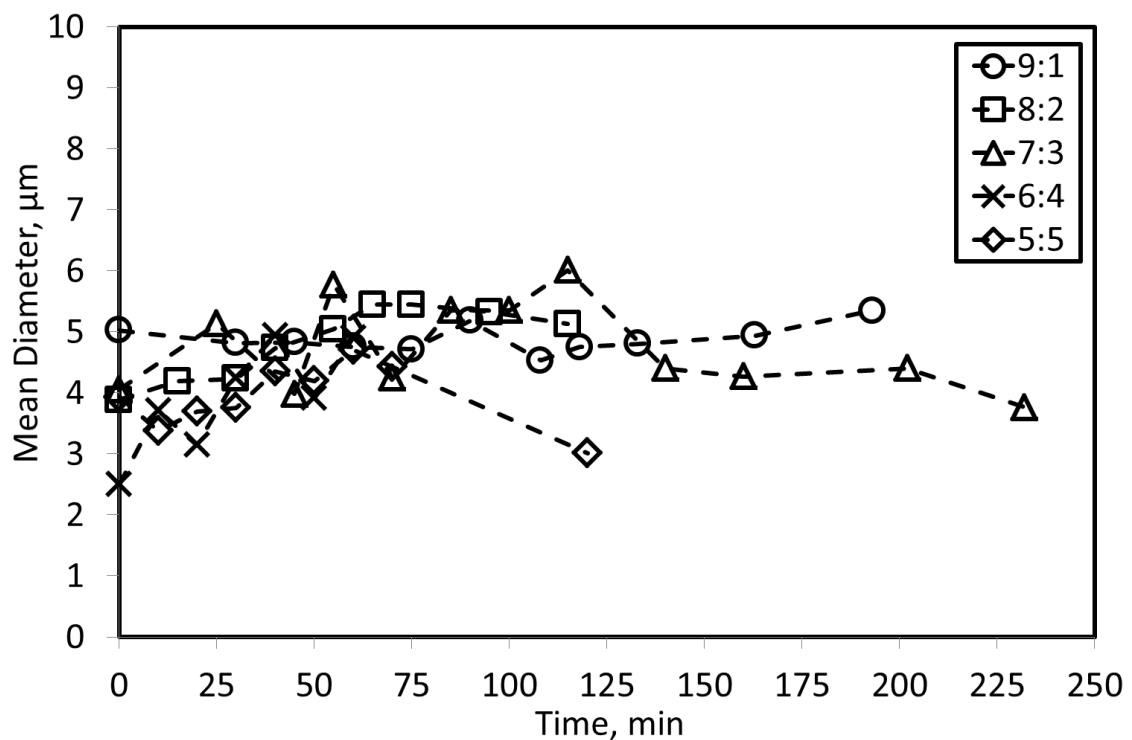


Figure 4.34. The mean diameter changes with time for microbubbles at DSPC/PEG<sub>40</sub>St molar ratios of 9:1, 8:2, 7:3, 6:4, 5:5 under high-power ultrasound excitation.

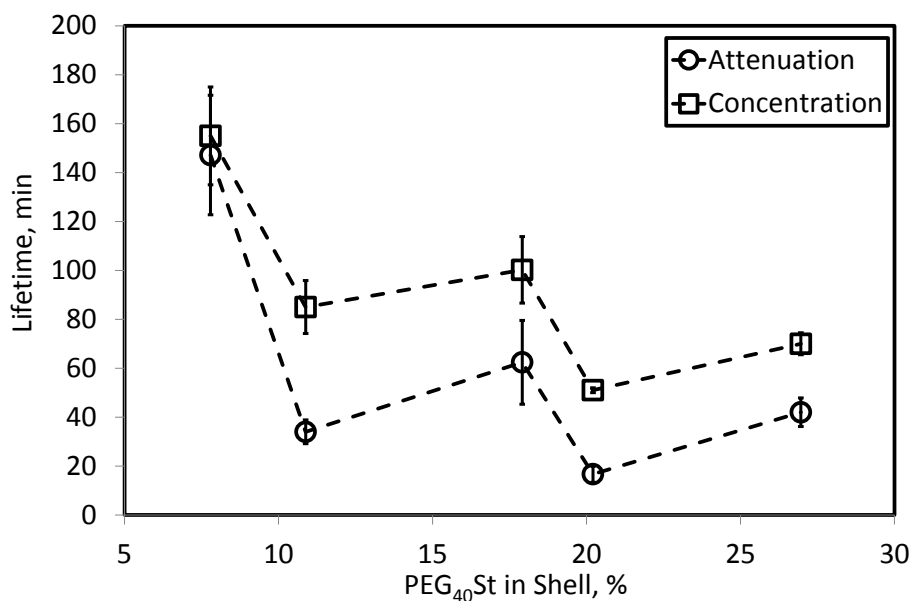


Figure 4.35. Lifetime of microbubbles as a function of PEG concentration at high ultrasound powers.

#### 4.7. Characterization of the Oscillation of Microbubbles under Ultrasound Activation with High-Speed Imaging

In order to understand the behavior of microbubbles in acoustic field and to create new approaches within the scope of this study, a high-speed imaging system (UPMC Cam) found in Dr. Flordeliza Villanueva's laboratory at the University of Pittsburgh-Medical School was used to acquire movies of oscillating microbubbles. The images were analyzed using these movies. An image of the lipid microbubbles in the video is shown in Figure 4.36.

The oscillations of different sizes of microbubbles were examined for each image frame forming the movie. Four single microbubbles were chosen from the movie of microbubble population and tracked to investigate their behavior under acoustic field. Figure 4.37 presents optical image sequence of two selected microbubbles, MB-1 and MB-2. Their initial diameters were 2.6  $\mu\text{m}$  and 1.5  $\mu\text{m}$ , respectively. As seen in the figure, the MB-1, which is large in size, starts to oscillate with increasing size under ultrasound excitation. It fuses with another adjacent microbubble at a similar size, and then acts as a single microbubble. Again, the oscillation continued as if it was a single microbubble after it fused with a new combined structure consisting of two adjacent

microbubbles. From the surface morphology, it seems that each microbubble did not fuse to form a homogeneous surface, but a combined structure of different microbubbles. However, at the later stages of the oscillation, the microbubble behaved like a single microbubble with a homogeneous surface and the size gradually increased over time. This behavior might also explain why microbubble concentration decreased, thus the decrement in echogenicity under ultrasound excitation.

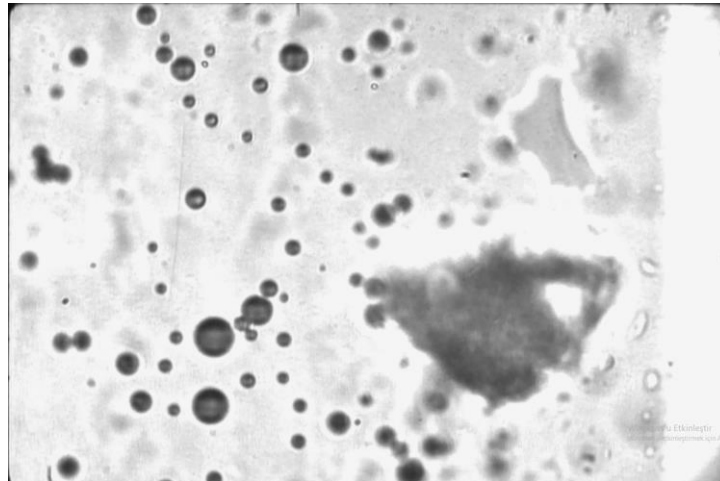


Figure 4.36. Video image recorded with “Ultra High Speed Camera System” at the University of Pittsburgh Medical Center (UPMC).

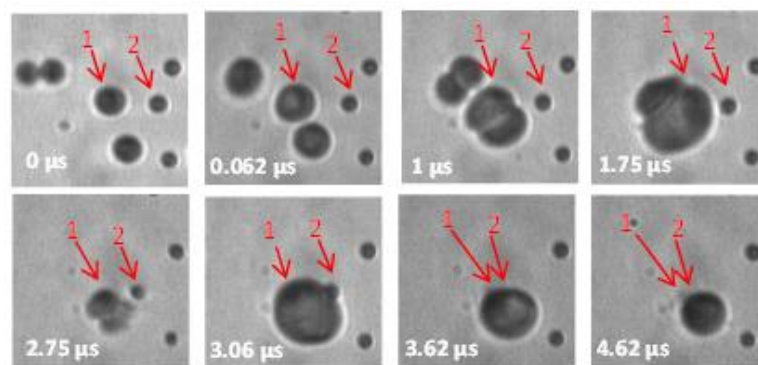


Figure 4.37. Sequence of 8 image frames of two selected microbubbles, MB-1 and MB-2, under ultrasound excitation.

Figure 4.38 illustrates optical image sequence of a selected single microbubble (MB-3) with an initial diameter of  $4.2 \mu\text{m}$ . MB-3 showed non-linear oscillations with a greater bubble expansion than contraction causing different non-spherical shapes (de Jong, Emmer et al. 2009). It did not fuse with any microbubbles around it, but it

touched another microbubble with nearly the same diameter in the later stages of the oscillation. This led to a flexible collision, which is called the damping effect between two microbubbles. During the oscillation, it is seen that the surface of the microbubble changed and the jetting formation occurred. Another important finding here is that although microbubbles were in contact with one another, they could maintain their boundaries due to the surface tension and protect their structure without diffusing to each other.

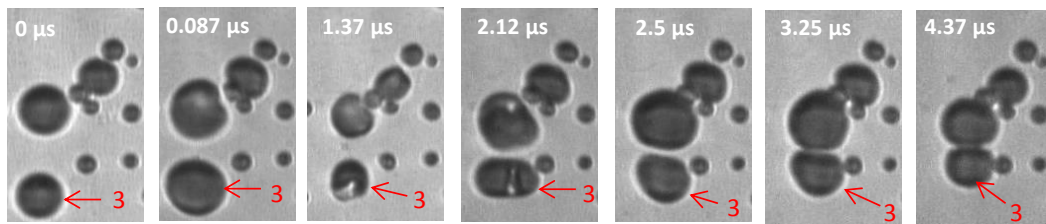


Figure 4.38. Sequence of 7 image frames of a single microbubble (MB-3) with an initial diameter of  $4.2 \mu\text{m}$  under ultrasound excitation.

Figure 4.39 shows optical image sequence of a selected single microbubble (MB-4) with an initial diameter of  $2.9 \mu\text{m}$ . When the MB-4 was in contact with the adjacent microbubble, the oscillation started. As the MB-4 oscillated aggressively, it fused with four adjacent bubbles. Therefore, its diameter reached a maximum diameter of  $6.35 \mu\text{m}$ . When the size decreased, the distance between the two microbubbles was increased, but then the two microbubbles have coalesced, when the size increased more than the first. It seems that this fusion did not result in a single microbubble at first, but they still behaved like two different microbubbles. It was observed that at the later stages of the oscillation fusion with the adjacent microbubbles occurred, and that the gas in the microbubble was transferred from one microbubble to another and the shell structure of this microbubble was disrupted while another microbubble proceeded to oscillate as a single microbubble. Here, it was understood that the microbubbles that were in contact with each other during the oscillation undergo fusion, disappeared, and decreased in number.

Normalized diameter of selected microbubbles in each image frame was also determined. The change of microbubble diameters with time is shown in Figure 4.40. As can be seen in the figure, at the beginning of the oscillation of MB-1, there was a

shrinkage and expansion in its size. When interacting with adjacent microbubble at a similar size, the oscillation that occurred at the microbubble size was switched from a periodic oscillation to a non-periodic oscillation with the damping effect. By fusion of two microbubbles, microbubble size increased. After dissolution of the combined microbubble over time in milliseconds, there was a shrinkage in the size of the microbubble and a drop in the intensity of the oscillation.

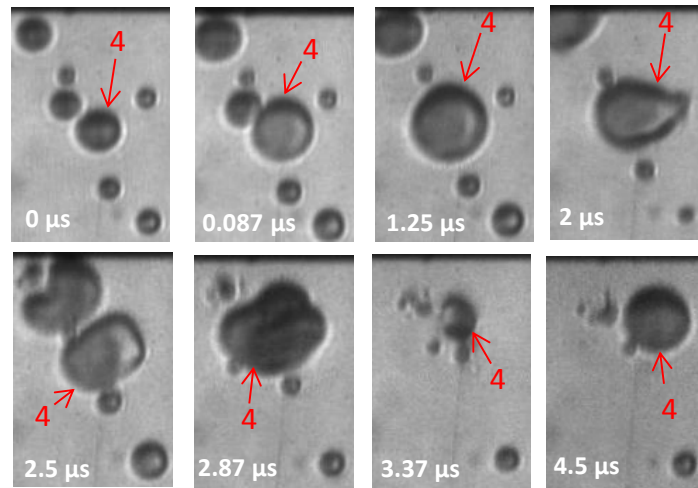


Figure 4.39. Sequence of 8 image frames of a single microbubble (MB-4) with an initial diameter of 2.9  $\mu\text{m}$  under ultrasound excitation.

The MB-2 with a size of 1.6  $\mu\text{m}$  exhibited compression-only behavior (de Jong, Emmer et al. 2009, Sijl, Overvelde et al. 2011). This behaviour is observed when the bubbles compress efficiently, but hardly expand. In principle, “normal” nonlinear bubble oscillation shows an infinite expansion in contrast to compression. It has been suggested that the compression-only behavior results from a rapid change of the shell elasticity with bubble radius (Sijl, Overvelde et al. 2011). There was no apparent increase in size of this small sized microbubble until it fused with another microbubble. It could be concluded that the oscillation of the microbubbles under ultrasound excitation depended on the size of the microbubbles. On the other hand, it could also be suggested that the signal intensity of small-sized microbubbles might be low when considering the fact that the signal intensity is proportional to the sixth power of the microbubble size in ultrasound imaging (Kabalnov, Klein et al. 1998).

The MB-3 began to oscillate upon the ultrasonic propagation, and its diameter decreased with time due to contact with another microbubble. Here, it can be seen that

the two microbubbles did not fuse with each other, but they could maintain their shell structures, even though their size changed during the oscillation. As can be seen, when the microbubble was alone, the oscillation intensity decreased due to the damping effect through elastic collision. The MB-4 did not oscillate periodically due to contact with adjacent microbubble when starting oscillation with the ultrasonic propagation. The intensity of the oscillation increased due to fusion with the adjacent microbubble. However, towards the end, the decrement in their size and periodic oscillations indicated that the microbubble shrank and moved alone.

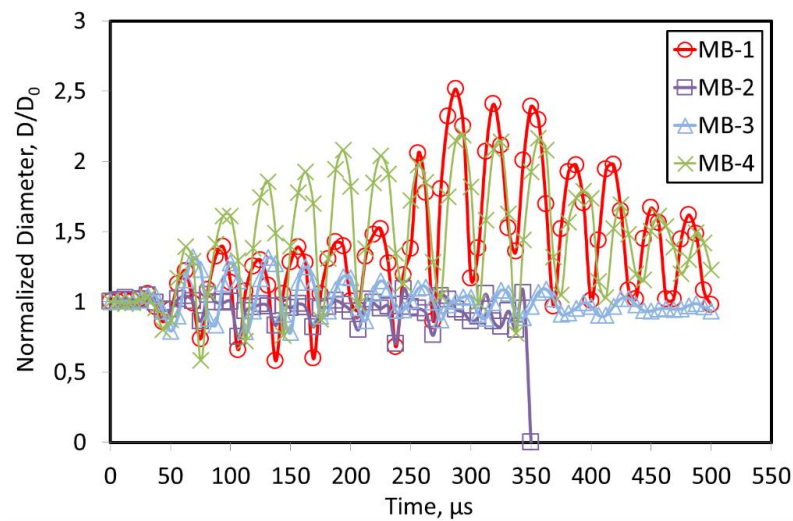


Figure 4.40. Normalized diameter-time curves for four selected microbubbles.

#### 4.8. Stability of Microbubbles under Hydrostatic Pressure

The hydrostatic constant pressure system shown in Figure 3.13 was designed to understand the dimensional changes of the microbubbles under ultrasound and the possible changes in the shell structure. Upon the hydrostatic constant pressure system, firstly, as seen in Figure 4.41a, the changes in the sizes of the bare bubbles in different sizes with the pressure were examined. The figure shows an oval image in the middle of the bare bubbles. As the pressure increased, the size of the bare bubbles decreased. When the pressure was reduced again, it is seen that small bare bubbles were completely dissolved and the size of the large bare bubble was increased and went back to its initial size.

Variations in the size of bare bubbles at different pressures are shown in Figure 4.41b. As shown in the figure, as the pressure increased, the size of the bubbles decreased. In the meantime, small bubbles were completely dissolved. The largest bubble was reduced in size as the pressure increased, but when the pressure was lowered again, the size of this bubble almost reached its original size. It is evident that as the surface tension of the bare bubble increased with increasing pressure, the air in the gas phase was not dissolved in the liquid, and when the pressure was lowered, it could return to its initial size. On the other hand, when small bare bubbles became smaller than a certain critical diameter with increasing pressure, they dissolved completely in the medium. The smallest bubble dissolved faster and it seems that it took longer to dissolve as the size increased. This shows that the dissolution rate of a bubble is inversely proportional to its diameter (Kabalnov, Klein et al. 1998). Moreover, even after the pressure was increased and stabilized, the size of all three bubbles decreased at certain levels.

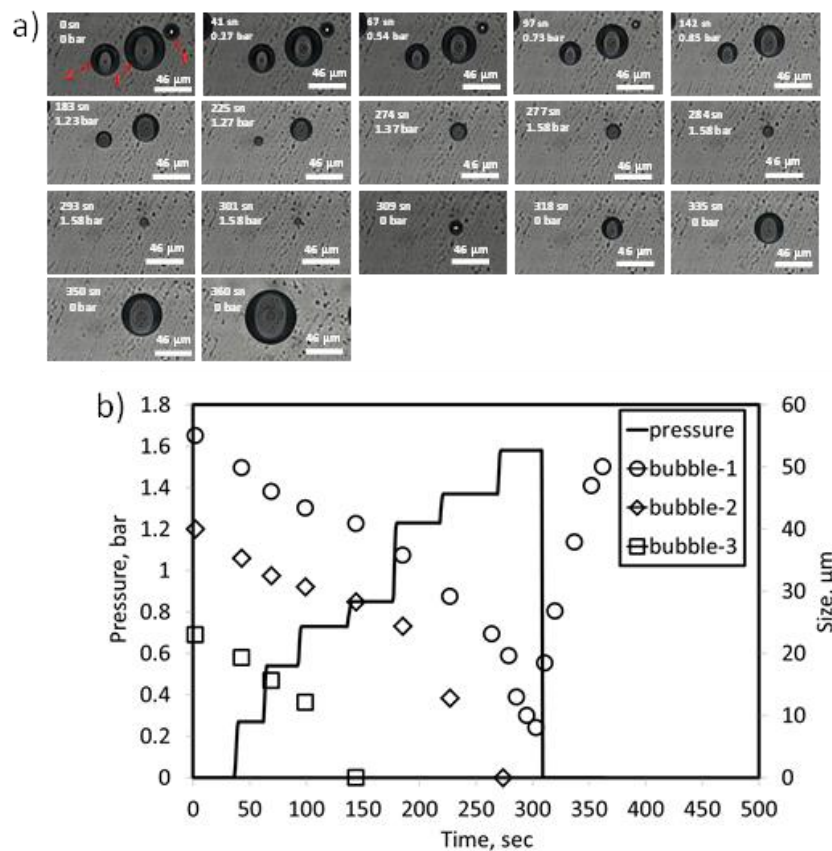


Figure 4.41. (a) Microscope images of changes in the sizes of bare bubbles with pressure, (b) changes in the sizes of bare bubbles at different pressures.

In another assay, changes in the size of bare bubbles of different sizes were examined with respect to pressure. As can be seen in Figure 4.42, the sizes of the bare bubbles were initially constant. When the pressure was gradually increased, the bare bubbles became smaller in size. Smaller bubbles dissolved in the medium when their size decreased to a critical value. The size of the largest bubble (bubble-1) decreased with the pressure increase, and when the pressure was gradually reduced, the bubble was observed to grow proportionally. When the pressure was reduced to the atmospheric pressure, the bubble-1 grew close to its initial size.

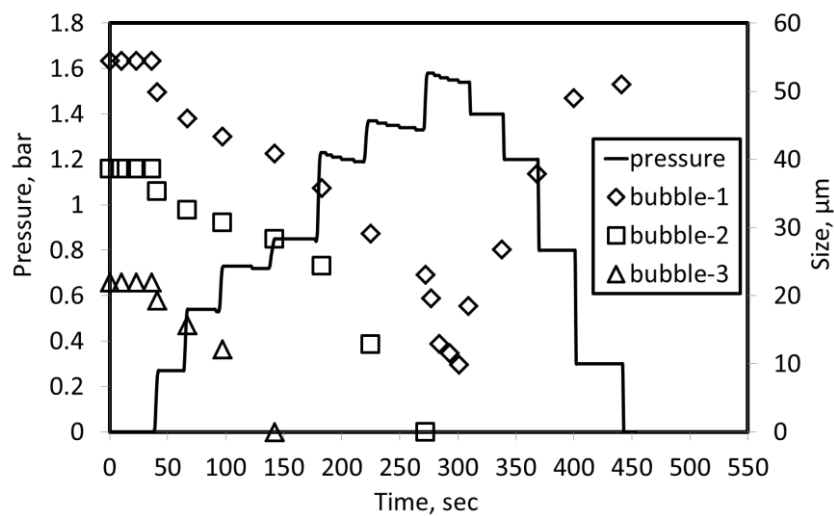


Figure 4.42. Change in the size of bare bubbles with time by increasing and decreasing pressure gradually.

As shown in Figure 4.43, when the bare bubbles were left under pressure for a long period of time, their size decreased. When a bare bubble was left at atmospheric pressure (0 bars) for a long period of time, there was no change in size. Another bare bubble in similar size appeared to shrink at a pressure of 2.91 bars and finally dissolved in the medium. A similar behavior was observed in theoretical modeling by Kabalnov (Kabalnov, Klein et al. 1998). Similarly, when two bare bubbles in different sizes were left under a pressure of 4.38 bars, the size of both bare bubbles decreased and finally dissolved and they disappeared at the same pressure. The higher the pressure, the faster the dissolution. As the diameter of the bare bubble decreased, an increase trend was observed in the dissolution rate.

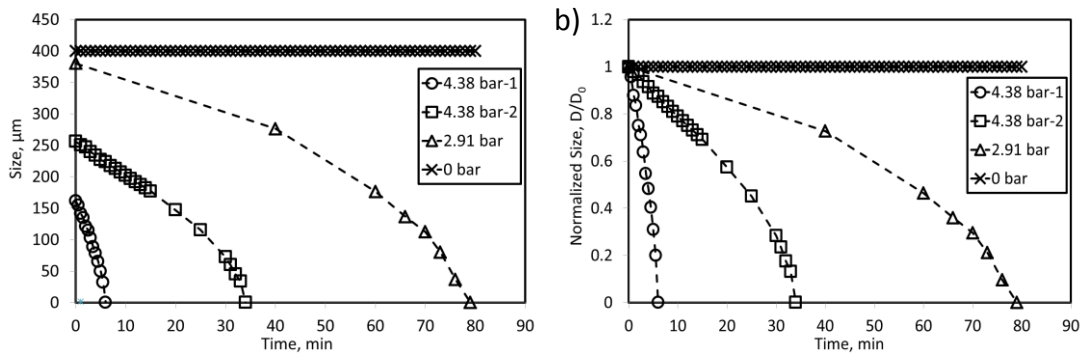


Figure 4.43. Change in the dimensions of bare bubbles in different initial sizes with different pressures over time.

Change in the size of a lipid microbubble with pressure is seen in Figure 4.44. When the pressure was too high, the lipid microbubbles dissolved very rapidly and disappeared in the medium. The lipid microbubbles have a spherical smooth shell structure at atmospheric pressures. When the pressure was increased, a change in the shell structure occurred, the microbubble buckled, and some protrusions occurred in different regions of the shell. When the pressure was reduced again, the microbubbles returned to their spherical structure. When the pressure was increased and reduced repeatedly, the microbubbles were diminished in size, dissolved and even split into smaller microbubbles, and eventually disappeared.

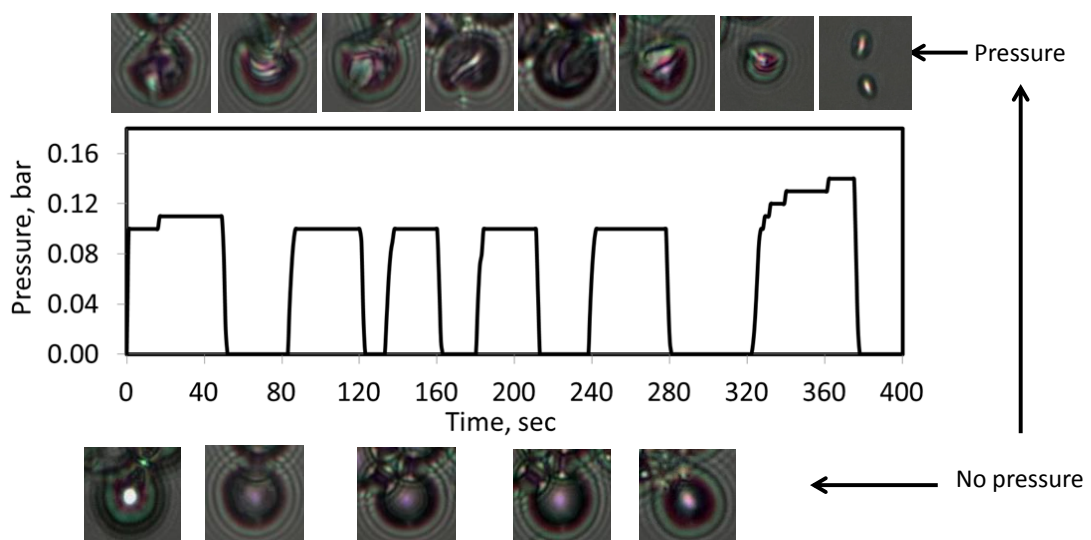


Figure 4.44. Behavior of lipid microbubbles under pressure.

Hydrostatic pressure experiments were carried out in order to investigate the change in the microbubble size and surface morphologies. 5:5 air-filled microbubbles were used for the investigation. Constant pressure values could be obtained at the desired level with constant pressure experimental setup. Behavior of the lipid microbubbles under 0.11 bar pressure is shown in Figure 4.45a. Light microscopy, fluorescence and the merged images are also shown in Figure 4.45b. As can be seen from the figure, when the pressure of 0.11 bars was applied to the microbubbles, it is clear that the buckling was formed on the surface of the microbubbles upon external pressure. This buckling, however, appeared as a line in a portion of the microbubble surface. Finally, some microbubbles disappeared and were dissolved, and some returned back to their spherical form.

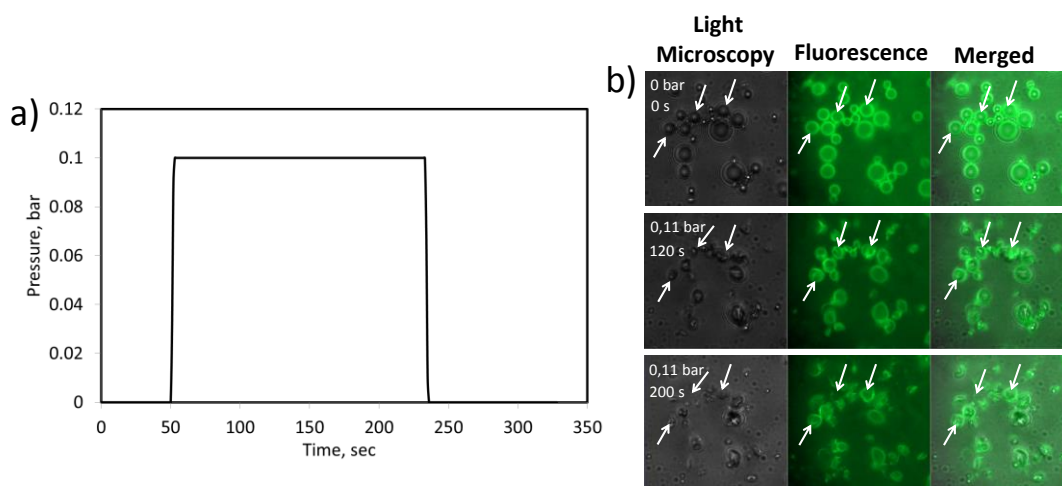


Figure 4.45. Behavior of 5:5 air-filled microbubbles at a pressure of 0.11 bar.

As shown in Figure 4.46, when the pressure was increased to 0.19 bar, microbubbles were dissolved and disappeared in about 2 minutes. A rapid decrease in microbubble size was observed with the increase of the pressure, while the number of microbubbles decreased rapidly. The microbubble that disappeared in the medium adhered to the upper glass of the pressure cell. The aggregations due to the buckling and folding of the lipids are evident in the fluorescence images shown in Figure 4.46c. Therefore, these aggregations, which were not seen in the light microscope, could be easily observed in the fluorescence image.

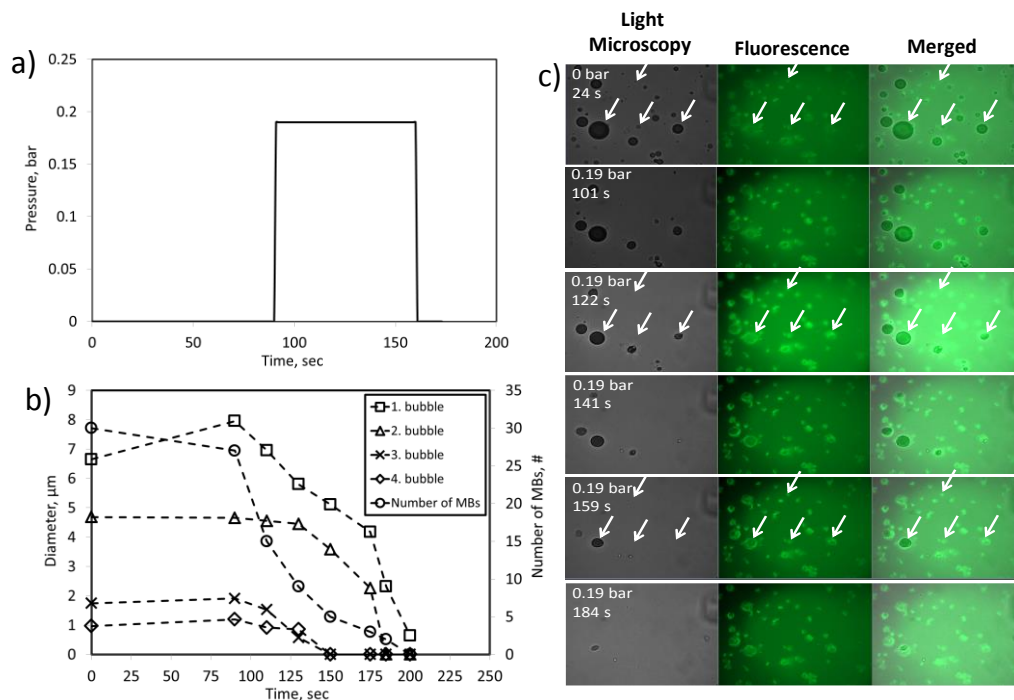


Figure 4.46. Behavior of lipid microbubbles under the pressure of 0.19 bar; (a) pressure, (b) the change in the number and size of the microbubbles over time, and (c) the light, fluorescence, and the merged microscope images of the microbubbles.

In order to understand the oscillation of microbubbles under ultrasound, changes in the size, number, and morphology of microbubbles with different pressure pulses were investigated. As shown in Figure 4.47a, the pressure was applied to the microbubbles as short pulses. First, a pressure of 0.04 bars was applied, and as can be seen in Figure 4.47b, no change was observed in the size or number of microbubbles. Thereafter, the pressure was increased to 0.16 bars and returned to initial conditions. In the meantime, the size of the microbubbles decreased. When the pressure was increased to 0.36 bars for a very short period of time and immediately lowered to the normal level, the decrease in the microbubble size was accelerated, and many small sized microbubbles disappeared in the medium. In the second pressure shock, microbubbles were completely dissolved and disappeared. The lipids present in the remaining microbubble shell structures adhered to the glass surface were monitored by fluorescence microscope, as can be seen in Figure 4.47c.

As shown in the pressure studies, the microbubbles under pressure shrank in volume by compressing the gas inside, thus folding and buckling on their surfaces.

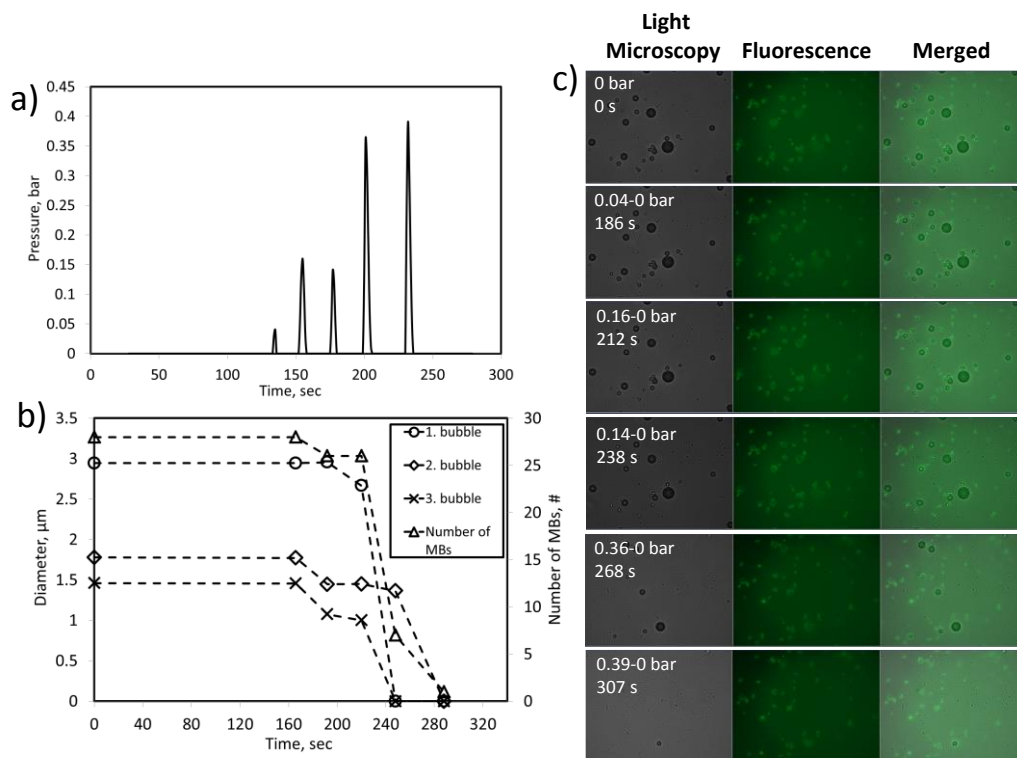


Figure 4.47. The behavior of microbubbles in short-term pressure pulses; (a) change in pressure, (b) change in the number and size of microbubbles over time, and (c) light, fluorescence, and merged microscope images of microbubbles.

It was suggested that by increasing the pressure of the liquid in which the microbubbles were suspended, the concentration of saturated gas that the liquid could dissolve increased, thus leading to the transmission of gas to the liquid from the microbubbles and causing a reduction in the volume of the microbubbles. In the meantime, when folding and buckling on the surface of the microbubbles returned back to the normal state, the microbubbles recovered their spherical structure. However, at high pressures, the microbubbles disappeared in a very short time by the effect of both external pressure and dissolution.

As a result of the experiment, it was concluded that microbubbles lost their stability under hydrostatic pressure. The decrease in stability in the presence of hydrostatic pressure might explain the instability of microbubbles when injected into body *in-vivo*. The increase of pressure in the syringe during the injection of microbubbles through the tail vein with a very small diameter of the 27G needle might result in decrease in the number of microbubbles.

## 4.9. Effect of Ultrasound Power on the Stability of Microbubbles

Low stability of the microbubbles limits their use for prolonged period of time in medical applications. It is therefore required to investigate the possible physical mechanisms of instability of contrast agents related to insonation parameters (e.g., acoustic intensity, duration of exposure) experimentally under the acoustic field.

There are mainly three mechanisms proposed for the destruction of microbubbles under ultrasound excitation: static diffusion, acoustically-driven diffusion, and rapid fragmentation (Dayton, Morgan et al. 1999, Chomas, Dayton et al. 2001, Chomas, Dayton et al. 2001, Porter, Smith et al. 2006, Qin, Caskey et al. 2009, Sirsi and Borden 2009). At very low amplitudes, bubble dissolution can occur thanks to the gas diffusion into the medium in the absence of ultrasound effect. This process is attributed to the static diffusion. In acoustically-driven diffusion, gas diffusion out of the bubble is affected by insonation due to variation of acoustic pressure over time while microbubbles have soft oscillations. Rapid fragmentation occurs when microbubbles undergo non-linear oscillations at high amplitudes, which make microbubbles unstable and, finally, fragmented into smaller bubbles.

*In vitro* ultrasound destructibility of microbubbles with varying acoustic pressures was examined in several reports (Vandenberg and Melton 1994, Ota, Hillman et al. 1997, Villarraga, Foley et al. 1997, Chatterjee, Jain et al. 2005, Porter, Smith et al. 2006, Yeh and Su 2008). In these studies, it has been reported that the transmit power severely affects the persistence of contrast agents. It has been shown that ultrasonic backscatter decreases significantly after an acoustic pressure threshold. Exponential models were proposed to predict the pressure threshold for microbubble destruction from the fitted exponential curve.

It is clear that higher intensity of ultrasound excitation causes microbubble destruction. However, mathematical models proposed in the literature do not explicitly explain the energy thresholds and possible mechanisms for the microbubble destruction. Here, we investigated the decrease in B-mode ultrasound intensity obtained from a population of microbubbles and, for the first time, developed a model to relate the intensity to effective bubble concentration. We calculated an acoustic energy threshold for the destruction of microbubbles and explained a possible mechanism for the destruction of microbubbles under ultrasound.

### 4.9.1. Stability of Microbubbles under Doppler Ultrasonography

The effect of increasing acoustic power on the stability of microbubbles was investigated using the experimental set-up shown in Figure 3.6. Figure 4.48 shows the change in B-mode intensities of the insonified microbubbles over time at certain time intervals for the 20% and 100% transmit powers. As evidenced from the figure, at the 40% transmit power, the image brightness of the microbubbles in the acoustic window area was slightly reduced within 20 seconds. However, at the 90% transmit power, the brightness of the microbubbles in the acoustic window area showed a rapid decline in a shorter time, indicating that microbubbles undergo destruction much more rapidly at high ultrasound powers (Ota, Hillman et al. 1997, Moran, Anderson et al. 2000, Porter, Smith et al. 2006). The red color seen in the 100% power images is based on the color-intensity scale in the color Doppler ultrasound system (Mann, Zipes et al. 2014). It shows the high backscattered intensity of microbubbles when the high transmit power was applied.

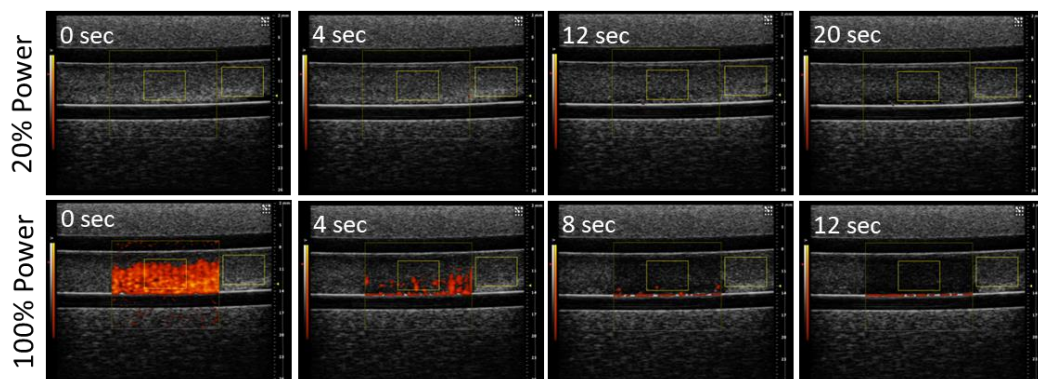


Figure 4.48. B-mode images of microbubbles in the tubing of flow phantom at certain time intervals for the 20% and 100% transmit powers.

Figure 4.49 displays the normalized time-intensity curves for ROI1 (a) and ROI2 (b) at different transmit powers. As can be seen in Figure 4.49a, there was a similar trend at powers less than 40%. A 30-40% of echogenicity loss was observed within 25 seconds in this range, which is in good agreement with the literature for low acoustic pressures (Porter, Smith et al. 2006). For such cases, the primary mode of destruction is gas dissolution with forced oscillation (Klibanov, Ferrara et al. 1998, Dayton, Morgan et al. 1999, Chomas, Dayton et al. 2000, Chatterjee, Jain et al. 2005). Increasing the

transmit power beyond 20% resulted in a faster decrease of B-mode intensity indicating a faster rate of destruction. Microbubbles lost 50-60% of their B-mode intensity at moderate powers (40-60%). A sharp decrement in intensity was seen in shorter times at high powers, suggesting a mechanism of rapid fragmentation (Chomas, Dayton et al. 2001, Chen, Matula et al. 2003, Porter, Smith et al. 2006). At the 100% transit power, intensity was decreased to its half value in 3 seconds. As seen in Figure 4.49a, a steep decrease was observed at powers of greater than 60%, indicating that there is a critical power level above which rapid fragmentation takes place. The critical power level for the rapid fragmentation is 60% considered here. As evidenced from the figure, the normalized B-mode intensity stayed constant after 20 seconds of ultrasonic propagation at high powers. This can be attributed to the presence of several smaller microbubbles as a result of fragmentation of the original bubbles (Dayton, Morgan et al. 1999, Chomas, Dayton et al. 2001). Microbubbles have a resonance frequency at which the amplitude of acoustic response is maximal. The resonant frequency is inversely proportional to the radius of a microbubble. (De Jong, Bouakaz et al. 2002, Doinikov, Haac et al. 2009). Because sizes of the microbubbles decrease, these smaller bubbles will oscillate at resonant frequencies higher than the transmitted frequency. On the other hand, it has demonstrated that resonance frequencies of lipid-coated microbubbles decrease with increasing acoustic pressure (Doinikov, Haac et al. 2009). Therefore, we can relate the flattening of the curve to oscillating smaller microbubbles that are not destroyed or created by fragmentation of larger microbubbles. As shown in Figure 4.49b, microbubbles in the out of focal zone were almost stable at low powers and slightly lost their B-mode intensities at high powers, indicating that ultrasound effect is very low in this area.

During the acoustic propagation, we have observed that the insonified microbubbles are drifted downwards within the vessel of flow phantom with time. This phenomenon could be attributed to the acoustic radiation force under the acoustic field (Lee and Wang 1993, Dayton, Klibanov et al. 1999, Doinikov 2003). Microbubbles can displace in the direction of the wave field or toward each other due to primary and secondary acoustic radiation forces. Dayton et al. have shown that radiation force can lead to translation of microbubbles within a flowing stream when the ultrasound is transmitted with a low acoustic pressure and high pulse repetition frequency (Dayton, Morgan et al. 1997).

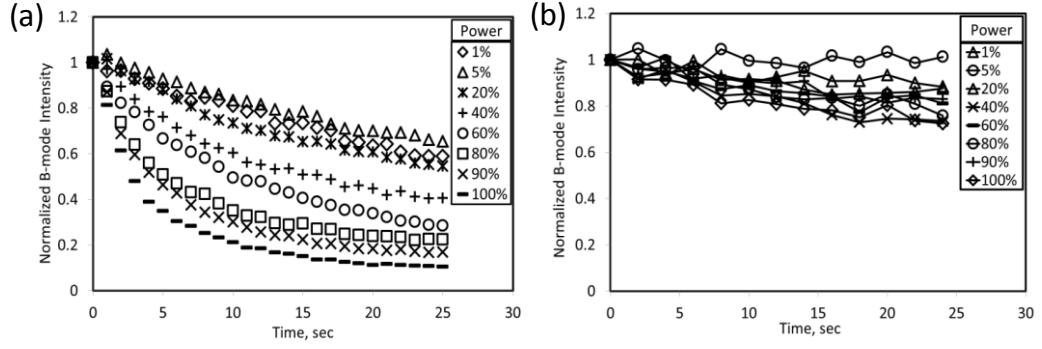


Figure 4.49. Time-intensity curves for ROI1 (a) and ROI2 (b) at different transmit powers.

#### 4.9.2. Model for Calculating the Acoustic Energy Thresholds

A new mathematical model was employed to relate the B-mode intensity to effective bubble concentration. The derived model equations were utilized to calculate the acoustic energy thresholds for the destruction mechanisms of microbubbles.

The change of microbubble concentration related to B-mode intensity over time can be expressed by the following equation:

$$\frac{dC}{dt} = -kC^n \quad (4.7)$$

where  $k$  is the decay constant in  $s^{-1}$  and  $C$  is the effective microbubble concentration raised to some power  $n$ .  $n$  gives the order of the equation. If  $n = 0$ , the equation is zero-order; if  $n = 1$ , the equation first-order; if  $n = 2$  the equation is second order; and so on. Here, we mainly propose two mechanisms for the destruction of microbubbles: soft oscillation/acoustically driven dissolution and fusion/rapid fragmentation (Figure 4.50). We can relate these mechanisms to the order of equations,  $n$ . In case of  $n = 0$ , there is a microbubble destruction due to static diffusion without ultrasonic effect. In case of  $n = 1$ , self-oscillating single bubbles undergo soft oscillations resulting in acoustically-driven dissolution with time. This mechanism applies at relatively low acoustic pressures. It should be noted that the shell dynamics and the initial microbubble diameter may also play critical roles in the acoustically dissolution rate (Chomas, Dayton et al. 2001). In case of  $n > 1$ , if the medium is not too dilute, two or more adjacent microbubbles fuse with an aggressive oscillation due to high external acoustic

energy. It has shown that bubbles have a stability criterion which states that if the bubble radius in the compressional phase decreases to less than one-tenth of the maximum expanded phase radius, the bubble becomes unstable (Chomas, Dayton et al. 2001). The extent of non-spherical distortions becomes larger than the bubble diameter. Considering that the size of a microbubble can reach up to four times its initial size under ultrasound excitation (May, Allen et al. 2002, Qin, Caskey et al. 2009), fused bubble above a critical size may implode upon compression and break into fragments when the ultrasound pressure is greater than the critical pressure threshold.

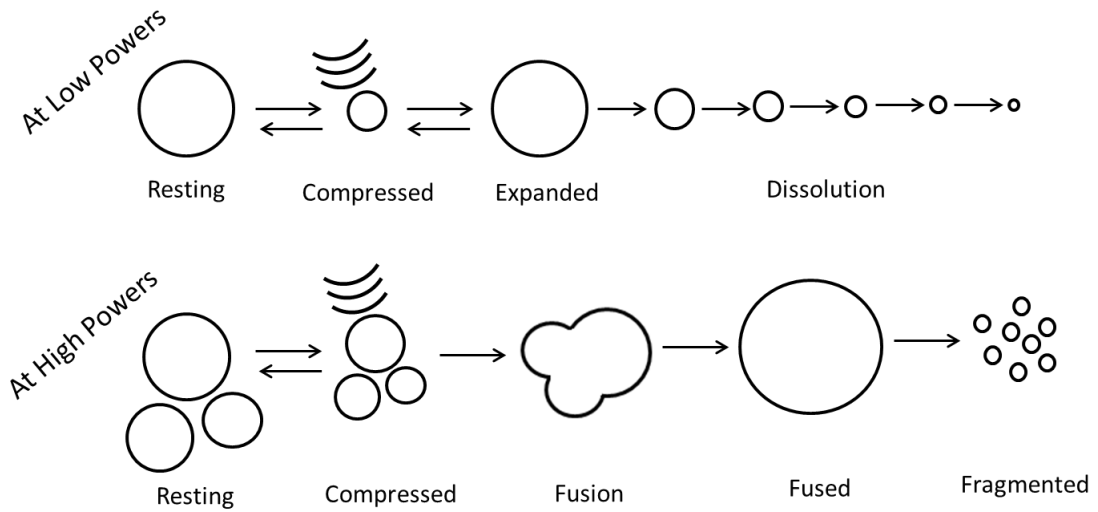


Figure 4.50. Schematic representation illustrating the possible physical mechanisms for the destruction of microbubbles under insonification.

The decay constant can be given by

$$k = k_0 e^{\left(\frac{1}{E_T}\right)P_A} \quad (4.8)$$

where  $k_0$  is pre-exponential factor and  $E_T$  is the energy threshold in  $\text{mW}/\text{cm}^2$ . Taking the natural logarithm of Eq. (4.8) yields:

$$\ln(k) = \ln(k_0) + \left(\frac{1}{E_T}\right)P_A \quad (4.9)$$

If we plot  $\ln k$  versus  $P_A$  slope of the linear curve will be  $E_T^{-1}$ .

We can determine the acoustic energy thresholds from Eq. (4.9). Now we can derive the time-intensity equations for two cases ( $n = 1$  and  $n > 1$ ).

If  $n = 1$ , a solution to Eq. (4.7) gives:

$$\frac{dC}{dt} = -kC \quad (4.10)$$

$$\ln C = -kt + c \quad (4.11)$$

$$\ln C = \ln C_0 - kt \quad (4.12)$$

where  $C_0$  is the initial microbubble concentration. It has shown that there is a logarithmic relationship between microbubble concentration and backscattered intensity (Xie and Meltzer 1988, Vandenberg and Melton 1994, Ota, Hillman et al. 1997, Lampaskis and Averkiou 2010). According to this, plotting the natural logarithm of microbubble concentration versus B-mode intensity ( $I$ ) gives a slope which can be denoted as  $\alpha$ . Multiplying Eq. (4.12) with the  $\alpha$  parameter gives:

$$\alpha \ln C = \alpha \ln C_0 - k\alpha t \quad (4.13)$$

$$I = I_0 - k\alpha t \quad (4.14)$$

where  $I_0$  is the initial B-mode intensity. Eq. (4.14) gives the first order equation for the self-oscillating microbubbles. According to Eq. (4.14), the B-mode intensity decreases linearly as a function of time. If we plot  $I$  versus time, slope of the curve will be  $k\alpha$  (Figure 4.51). Therefore, we obtained the slopes of the time-intensity curves, taking only the linearly descending portion of the curves.

Inserting  $k\alpha$  into Eq. (4.9) gives:

$$\ln(k\alpha) = \ln(k_0\alpha) + \left(\frac{1}{E_T}\right) P_A \quad (4.15)$$

Eq. (4.15) gives the acoustic energy threshold for the soft oscillation of microbubbles. If we plot  $\ln(k\alpha)$  against  $P_A$ , slope of the curve will be  $1/E_T$ . The  $\ln(k\alpha)$  values were plotted versus  $P_A$ , as seen in Figure 4.52. As seen in the figure, there is

linearity between  $\ln(k\alpha)$  and  $P_A$ , and the slope of the curve is 0.0804. Therefore, the acoustic energy threshold for the soft oscillation of single microbubbles was found to be 12.43 mW/cm<sup>2</sup>. 12.43 mW/cm<sup>2</sup> corresponds to ~43% transmit power. It could be suggested that single microbubbles showed soft oscillation below this energy threshold, and that they underwent destruction through rapid fragmentation with increasing acoustic energies beyond this threshold.

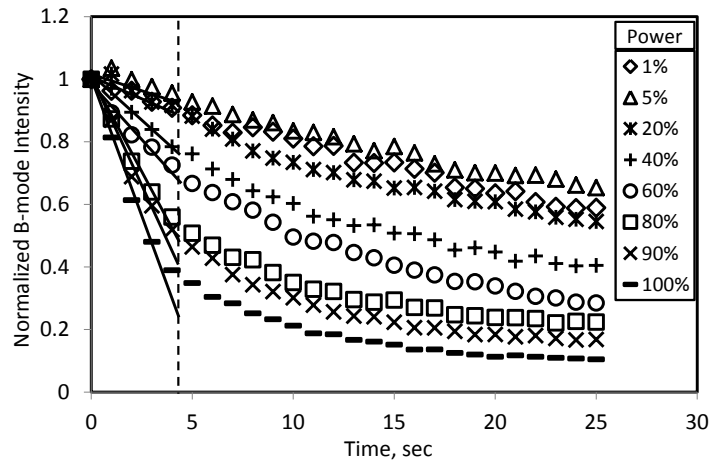


Figure 4.51. The initial slopes for the first order equation.

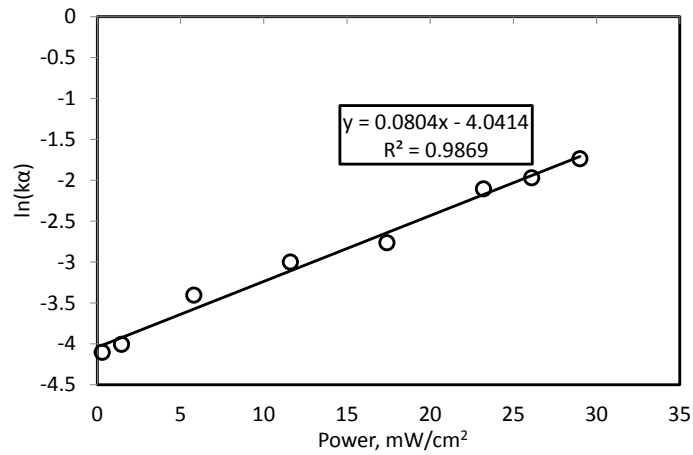


Figure 4.52.  $\ln(k\alpha)$  versus  $P_A$ . Slope of the curve gives  $1/E_T$ .

If  $n > 1$ , Eq. (4.7) becomes:

$$C^{-n} dC = -kdt \tag{4.16}$$

Eq. (4.17) gives intensity as a function of time after required mathematical operations:

$$I = I_0 - \frac{\alpha}{n-1} \ln[1 + k(n-1)C_0^{n-1}t] \quad (4.17)$$

If  $k(n-1)C_0^{n-1}t \gg 1$ , then Eq. (4.17) becomes:

$$I = -\frac{\alpha}{n-1} \ln[k(n-1)] - \frac{\alpha}{n-1} \ln t \quad (4.18)$$

Eq. (4.18) gives the  $n^{\text{th}}$  order equation for the fusion of microbubbles at high acoustic powers. If we plot  $I$  versus  $\ln t$ , the intercept and the slope will be  $-\frac{\alpha}{n-1} \ln[k(n-1)]$  and  $-\frac{\alpha}{n-1}$ , respectively (Figure 4.53). As seen in the figure, the B-mode intensity decreases linearly in the last portion of the curve. Accordingly, we obtained the intercepts and the slopes of the curves, taking only the linearly descending part of the curves.

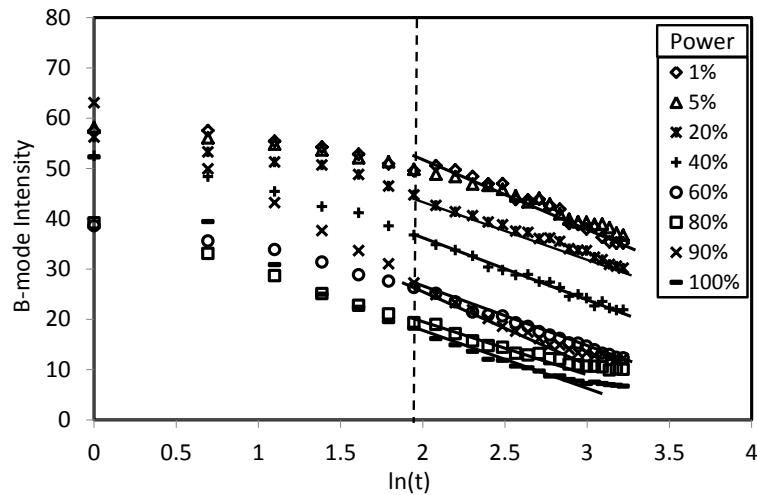


Figure 4.53. Different slopes taken for the  $n^{\text{th}}$  order equation.

Dividing the intercept by the slope gives

$$\frac{\text{Intercept}}{\text{Slope}} = \ln[k(n-1)] \quad (4.19)$$

Inserting  $\ln[k(n-1)]$  into Eq. (4.9) gives

$$\frac{\text{Intercept}}{\text{Slope}} = \ln[k_0(n-1)] + \left(\frac{1}{E_T}\right) P_A \quad (4.20)$$

Eq. (4.20) gives the acoustic energy threshold for the fusion/rapid fragmentation of microbubbles. If we plot intercept/slope against  $P_A$ , slope of the curve will be 0.1327, as seen in Figure 4.54. Therefore, the acoustic energy threshold for the fusion of microbubbles was found to be 7.53 mW/cm<sup>2</sup>. 7.53 mW/cm<sup>2</sup> corresponds to ~26% transmit power. The acoustic energy threshold for the fusion of microbubbles was found to be lower than that for the soft oscillation/acoustically driven dissolution of single microbubbles. This could be attributed to the size effect due to fusion of microbubbles. As the bubble size increased as a result of fusion, the acoustic energy needed for the motion of bubbles toward each other decreased. Acoustic response of a microbubble to ultrasound excitation is strongly influenced by its initial size. It has shown that the scattering intensity by microbubbles is proportional to the sixth power of the radius of the bubble (MorAvi, Robinson et al. 1997, Schutt, Klein et al. 2003). Such an increase in bubble size could reduce the energy threshold for the fused bubbles.

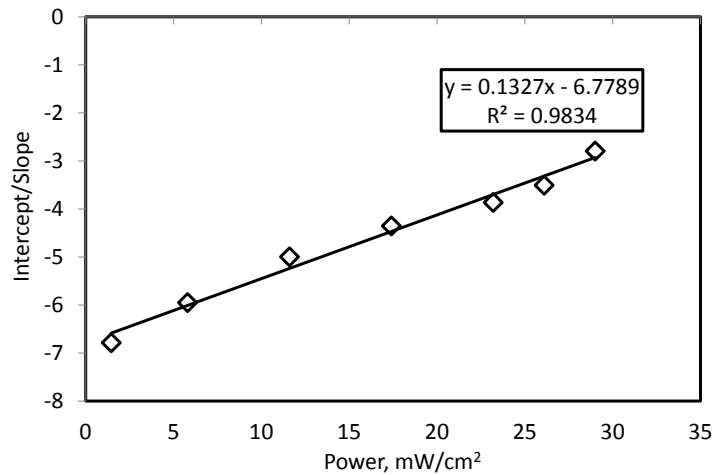


Figure 4.54. Intercept/slope versus  $P_A$ . Slope of the curve gives  $1/E_T$ .

The decay constants can be calculated from Eq. (4.19) for each acoustic power. In case of  $n = 2$ , Eq. (4.19) becomes:

$$\frac{\text{Intercept}}{\text{Slope}} = \ln k \quad (4.21)$$

$$k = e^{\left(\frac{\text{Intercept}}{\text{Slope}}\right)} \quad (4.22)$$

As shown in Figure 4.55, there is an exponential relationship between the decay constant and the acoustic energy, indicating that the disruption of microbubbles is accelerated as the acoustic energy increases. The decay constants illustrated in Figure 4.55 were comparable to results reported by Sboros et al. (Sboros, Moran et al. 2000). The decay constant for the fusion of microbubbles was found to be  $\sim 3\text{E-}03 \text{ s}^{-1}$  from the exponential equation shown in the figure. Our data indicated that this mechanism was characterized by a decay constant of  $\sim 3\text{E-}03 \text{ s}^{-1}$ .

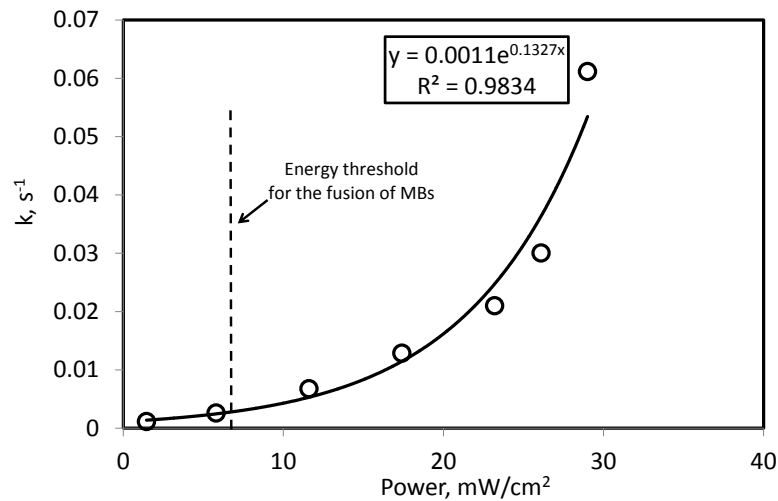


Figure 4.55. Decay constants plotted against  $P_A$ .

As a conclusion, we anticipated that microbubbles show soft oscillation resulting in acoustically driven dissolution at relatively low powers. At higher powers, two or more microbubbles undergo fusion resulting in rapid fragmentation. The results also demonstrated that it is possible to define acoustic energy thresholds for better design of stable microbubbles in diagnostic ultrasound applications.

#### 4.10. Investigation of the Echogenicities of Microbubbles with Different Shell Compositions

Microbubbles formed in varying phospholipid and emulsifier compositions were investigated under ultrasound excitation to estimate their echogenicity. Bolus

injection of microbubbles was performed at various flow rates, concentrations and volumes. In this study, a new concentration estimation method was also developed for the bolus injection technique.

#### 4.10.1. Developing Concentration Estimation Method for the Bolus Injection Technique

The model setup used in the estimation method for the bolus injection technique is shown in Figure 4.56a. The time-intensity curves (TICs) that can be obtained in such an experimental setup, as shown in Figure 4.56b, first display an increasing and then a decreasing trend. In this method, also referred to as the indicator dilution model, after the bolus injection, the indicator is diluted along the flow plane and followed by an increase and then a decrease in the concentration.

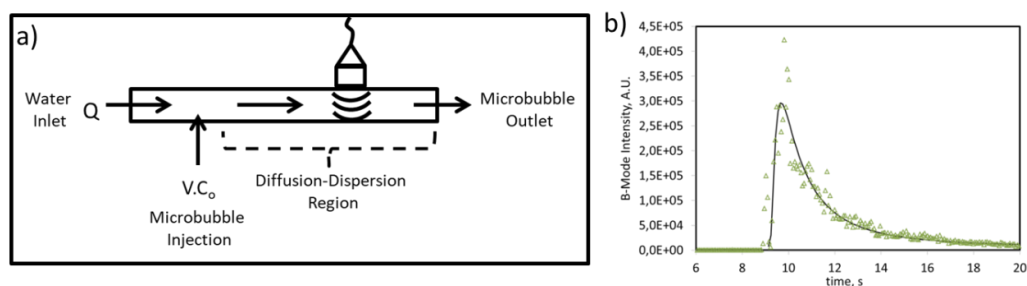


Figure 4.56. Development of the estimation method for the bolus injection technique. (a) The model setup and (b) the resulting experimental TIC.

In the bolus injection method, the indicator molecules (microbubbles) that are injected into a flow medium are diluted in the flow medium by dispersion, Brownian motion, laminar flow, or turbulence (Strouthos, Lampaskis et al. 2010). Thus, after the bolus injection, the microbubbles pass at different times to ROI and produce a dilution curve. The indicator dilution curve can be defined by the probability density function of the transit times of microbubbles. This is proportional to the amount of microbubbles that pass through the ROI. If the amount of microbubbles in the bolus injection is known and the microbubble concentration as a function of time can be measured in the ROI, the volumetric flow rate ( $Q$ ) and blood volume ( $V$ ) can be calculated by the following equations in terms of the area under the curve (AUC):

$$Q = m * (AUC)^{-1} \quad (4.23)$$

$$V = Q * MTT \quad (4.24)$$

where  $m$  is the amount of microbubbles,  $MTT$  is the mean transit time. In the ultrasound system, the acoustic wave intensity  $I(t)$  is measured instead of the microbubble concentration, therefore it is not possible to measure  $Q$  and  $V$  values directly. However, at low microbubble concentrations the backscattered intensity is linearly proportional to the concentration. This allows us to measure the amount that is proportional to  $Q$  and  $V$ . At high blood flow velocities, the microbubbles move quickly into the ROI and the time to the peak intensity ( $t_p$ ) becomes shorter.

Dilution in concentration in the bolus injection may be given by (Strouthos, Lampaskis et al. 2010)

$$\frac{\partial C(x, t)}{\partial t} = D \frac{\partial^2 C(x, t)}{\partial x^2} - v \frac{\partial C(x, t)}{\partial x} \quad (4.25)$$

where  $C(x, t)$  is the indicator concentration at position  $x$  and time  $t$ ,  $D$  is the effective longitudinal diffusion coefficient, and  $v$  is the fluid velocity. This is one of the well-known diffusion-dispersion equations in chemical engineering. It is assumed that there is a direct proportion between the acoustic intensity and the concentration, which is valid at low concentrations. The first passage time (FPT) model is proposed for a solution of the diffusion with drift equation (Eq. (4.25)). In this case, the solution for the acoustic signal is given by Eq. (4.26) (Strouthos, Lampaskis et al. 2010), since the concentration-time curve to be obtained for the microbubble concentration is similar to the acoustic signal-time curve:

$$I(t) = AUC \left( \frac{e^\lambda}{\mu} \right) \sqrt{\frac{\lambda}{2\mu}} \left( \frac{\mu}{(t - t_0)} \right)^{3/2} \exp \left[ -\frac{1}{2} \lambda \left( \frac{\mu}{(t - t_0)} + \frac{(t - t_0)}{\mu} \right) \right] + I_0 \quad (4.26)$$

Here, the parameter  $\mu \equiv x_0/v$  ( $x_0$  is the distance between the entry and exit sites of the ROI) is the mean transit time required for a microbubble to travel the distance  $x_0$ . The parameter  $\lambda$  is defined as  $\lambda \equiv \mu v^2/2D$ , and the skewness of the curve is equal to  $\lambda^{-1}$ . The Peclet number (Pe) is defined as  $Pe = \tau_D/\tau_c$ , where  $\tau_D = x_0^2/D$  is the diffusive time of

microbubbles and  $\tau_c = \mu$  is the convective time. Therefore,  $Pe = 2\lambda$ . This indicates the direct physiological significance of  $\lambda$  (Strouthos, Lampaskis et al. 2010). For example, if the flow rate is too high, a narrower TIC is observed, since dispersion is neglected due to diffusion; if the flow rate is low, then the TIC show a wider profile. In a constant flow, when the bolus volume  $V$  from the microbubbles with a concentration of  $\beta C_0$  is injected into the system, the sum of concentration-time curve read by the sensor of this amount can be given as in Eq. (4.27). Here,  $\beta$  is used as a coefficient for the microbubble amount that is not precisely known:

$$V. \beta C_0 = \int_0^{\infty} Q. C(t) dt \quad (4.27)$$

At low microbubble concentrations, there is a linear relationship between acoustic intensity and concentration. Therefore, the calibration curve equation can be given by

$$I(t) = \alpha. C(t) + \varphi \quad (4.28)$$

where  $\alpha$  is the slope of the calibration curve, and  $\varphi$  is the intercept of the y-axis. In this case, Eq. (4.28) can be written as

$$V. \beta C_0 = Q. \int_0^{\infty} \frac{I(t) - \varphi}{\alpha} dt \quad (4.29)$$

When the equation is simplified, Eq. (4.30) is obtained. If we take the integral of Eq. (4.30),

$$\frac{V. \alpha. \beta C_0}{Q} = \int_0^{\infty} I(t) dt - \int_0^{\infty} \varphi dt \quad (4.30)$$

The first integral is the area under the TIC, known as the AUC. The second integral is a constant. Thus, Eq. (4.31) is obtained:

$$\frac{V. \alpha. \beta C_0}{Q} = AUC - \varphi_0 \quad (4.31)$$

Eq. (4.32) is obtained by re-organizing the Eq. (4.31):

$$AUC = (\alpha \cdot \beta \cdot C_0) \left( \frac{V}{Q} \right) + \varphi_0 \quad (4.32)$$

Here, AUC is different from that shown in Eq. (4.23). A constant is present in the equation, and it functions as a significant parameter in the evaluation of the obtained data. Eq. (4.33) is used to calculate the mean transit time (MTT) value:

$$MTT = \frac{\int_0^{\infty} t \cdot I(t) dt}{\int_0^{\infty} I(t) dt} \quad (4.33)$$

The result obtained for MTT is given by

$$MTT = \mu = \frac{x_0}{v} \quad (4.34)$$

Since the average flow rate  $v = Q/A$ , the mean transit time  $MTT = x_0 \cdot A/Q$ , and the ROI volume  $= x_0 \cdot A$ , the relationship between MTT and ROI volume can be given by

$$MTT = ROI \cdot \left( \frac{1}{Q} \right) + \psi_0 \quad (4.35)$$

Thus, the necessary calculations can be made from the curve-fitting values obtained by the TICs.

#### **4.10.2. Estimation of Microbubble Concentration by Bolus Injection Method**

The intensity-time values measured by the bolus injection method at different bolus volumes, different flow rates, different concentrations and different microbubble formulations and their compatibility with the model equation are shown in Figure 4.57. As seen in Figure 4.57a, the microbubble serum set of the same type and at the same concentration was injected in different bolus volumes into the fluid flowing through the

tube at a constant flow rate. Obtained TICs are seen in the figure. Experiments with the Vevo2100 ultrasound device were much more controlled and more reliable results were obtained due to the repeatable data. The software program of the Vevo2100 device analyzes the data using the log-normal model equation. However, since the device is programmed rather for *in-vivo* experiments, we experienced problems in evaluating the data obtained with the very short transit time of microbubbles. As a solution to this problem, we performed analysis of the obtained data manually according to the FPT model. As seen Figure 4.57a, the curve-fitting data is in very good agreement with the FPT model.

In another study, TICs obtained at different fluid flow rates were studied. In this study, same volumes of bolus injections from the same type of microbubble and stock solution were injected into the fluid stream at different flow rates. The fitting-curves obtained according to the TICs and the FPT models are shown in Figure 4.57b. As can be seen, the experimental data and the FTP model are in very good agreement.

The TICs obtained for the same type of microbubbles at different concentrations are shown in Figure 4.57c. The obtained experimental data and the FTP model are in very good agreement.

In another study, the time-intensity data were obtained at the same volume of bolus injections and at the same fluid flow rates for the microbubbles prepared in different formulations. The evaluation of the obtained data according to the FTP model is shown in Figure 4.57d. As can be seen, the experimental data and the model are in a very good agreement.

AUC and MTT values for the bolus injection under different conditions are shown in Figure 4.58. The AUC is inversely proportional to the flow rate, linearly proportional to the bolus volume and concentration, as seen in Eq. (4.32). MTT is inversely proportional to the flow rate, as seen in Eq. (4.35). As shown in Figure 4.58a, the AUC and MTT values for different bolus volumes vary linearly. The fact that there is a y-axis intercept for the curve means that this value cannot be neglected. As seen in Figure 4.58b, when the AUC and MTT are compared with the inverse of the flow rate, it is seen that there is also a linear trend. However, here, it is suggested that there may be some deviations due to prolonged time it takes for the pump to reach the equilibrium value during the experiment. As seen in Figure 4.58c, there is no direct correlation between MTT values and concentration, although there is a linear relationship between

AUC values and concentration. Finally, the AUC and MTT values obtained for microbubbles with different shell compositions are shown in Figure 4.58d. As can be seen, the MTT values are not significantly changed for each type of microbubble, while the AUC values differ. This may show that the concentration of microbubbles differ from the accepted value.

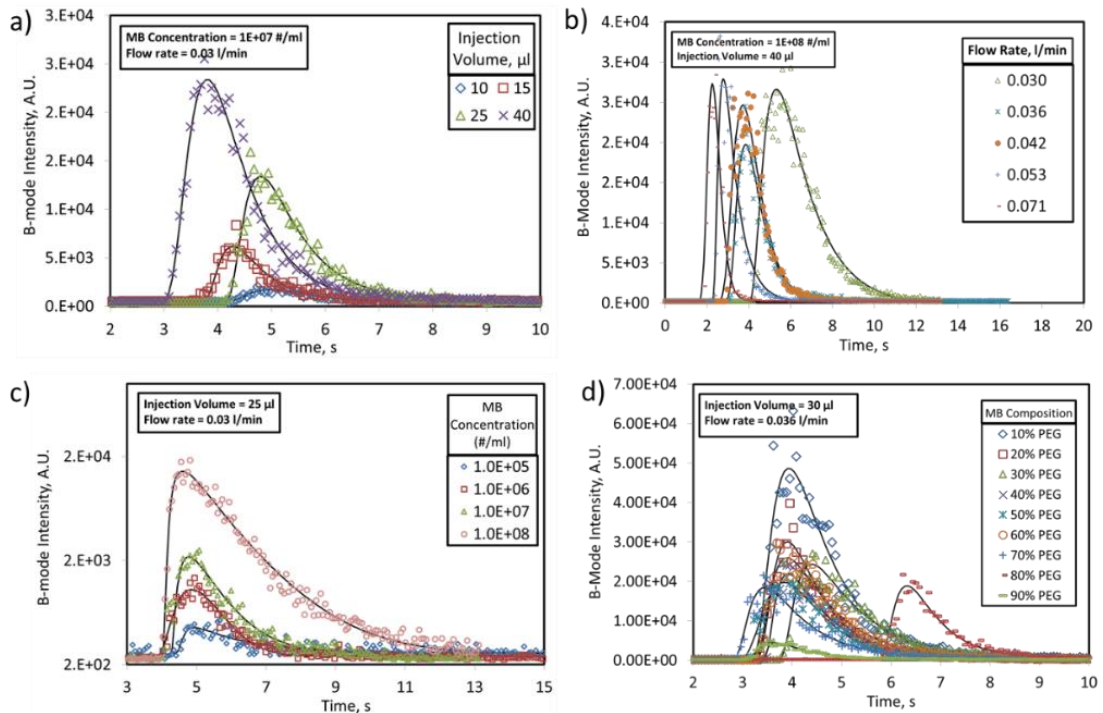


Figure 4.57. (a) TICs obtained with Vevo2100 in different bolus injection volumes, (b) TICs obtained for bolus injection at different flow rates, (c) TICs obtained for bolus injection at different concentrations, (d) TICs obtained for bolus injection in different microbubble compositions. The curves shown by straight lines are model equation curves.

The AUC and MTT values were evaluated for all measured parameters, as shown in Figure 4.59. As seen in Figure 4.59a, the AUC value appears to be in a linear relationship with the  $V \cdot C_0 / Q$  values. However, it is understood that two to three of the microbubbles in different compositions show significant deviations. In this case, the  $\beta$  parameter is expressed in Eq. (4.32) to find the actual values. On the other hand, as shown in Figure 4.59b, when the MTT values were evaluated with  $1/Q$  values, a linear relationship was found, where the concentration of microbubbles in different shell compositions did not affect the MTT values as expected.

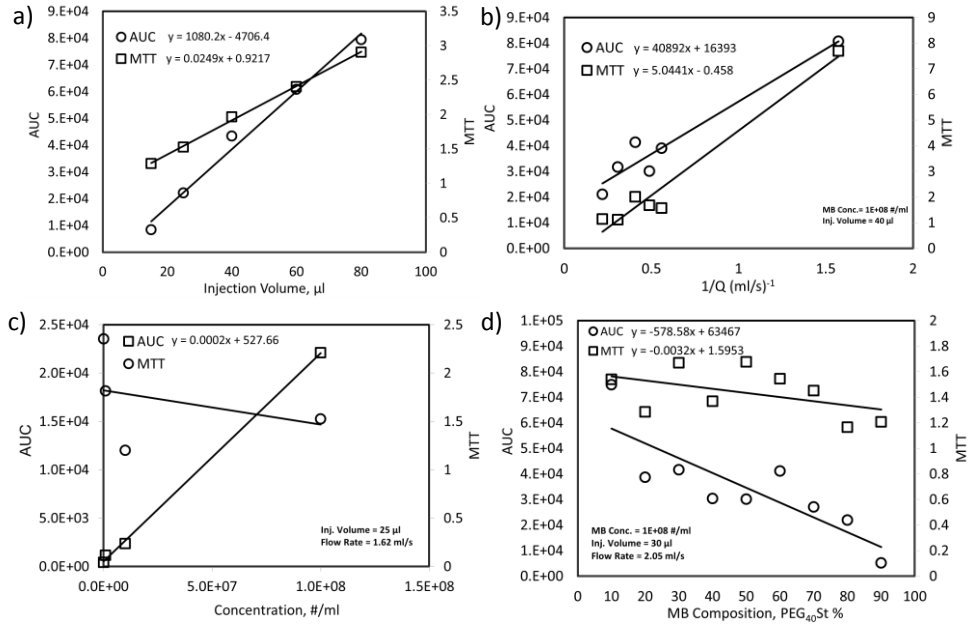


Figure 4.58. Evaluation of the AUC and MTT parameters obtained with the bolus injection for (a) different bolus injection volumes, (b) different flow rates, (c) different concentrations, and (d) different microbubble compositions.

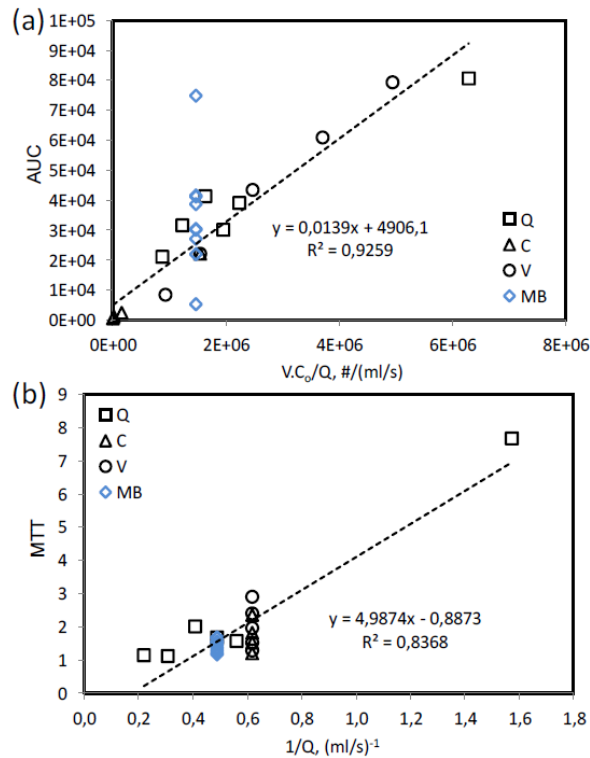


Figure 4.59. Evaluation of (a) AUC and (b) MTT values for all measured parameters.

A method has been developed to determine the concentration of microbubbles with ultrasound. In this method, AUC values were calculated for different bolus volumes and different flow rates at different concentrations for the same type of microbubbles. These calculated values were plotted versus the  $V/Q$  value, and the slope values were obtained for each concentration. In Figure 4.60, the AUC values are given for different concentrations of 9:1 microbubbles at different injection volumes and flow rates.

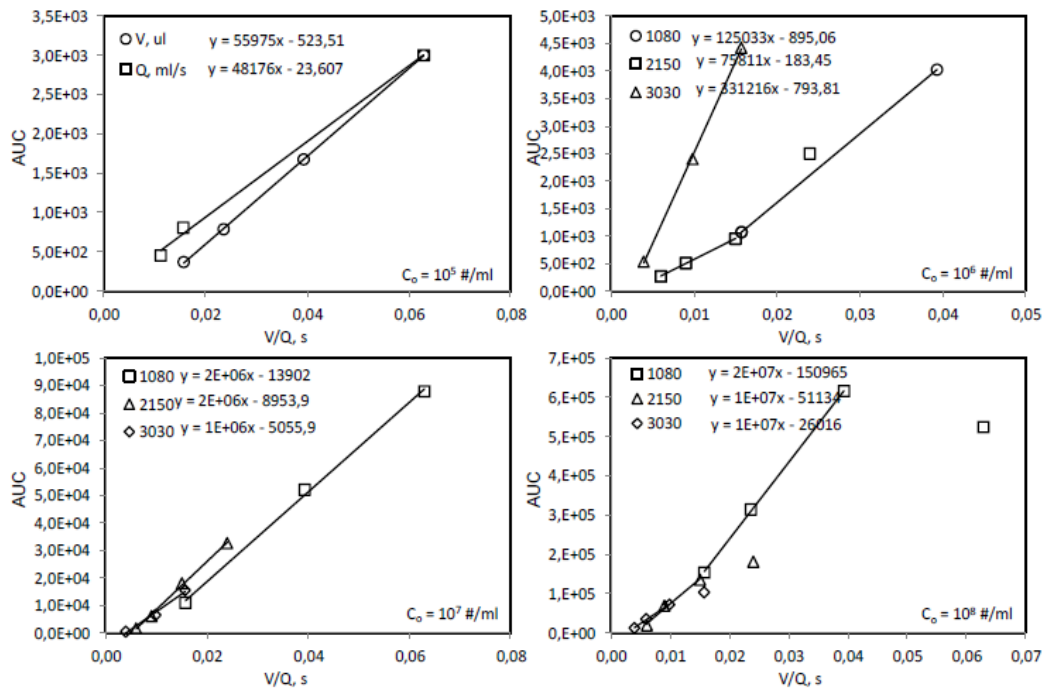


Figure 4.60. Different bolus volumes for different concentrations of 9:1 microbubbles and AUC values for different flow rates.

The slope values obtained in Figure 4.60 for the 9:1 microbubbles at different concentrations are shown in Figure 4.61a. As can be seen in the figure, the value of  $\alpha$  indicating the relationship between microbubble concentration and acoustic intensity and the coefficient  $\beta$  of microbubbles with unknown concentration could be found from the slope of this curve. This value was found to be 0.159 for the 9:1 microbubbles.

In Figure 4.61b, the slope value for the same microbubble at different concentrations at a flow rate of 0.64 ml/s and in a injection volume of 25  $\mu$ l was found to be 0.0062. Here, using Eq. (4.32) the value of  $\alpha \cdot \beta$  was calculated to be 0.159. The value of  $\alpha$  was calculated to be 0.0135 for a known microbubble concentration.

Accordingly, the concentration of microbubbles in different shell compositions could be estimated under ultrasound excitation.

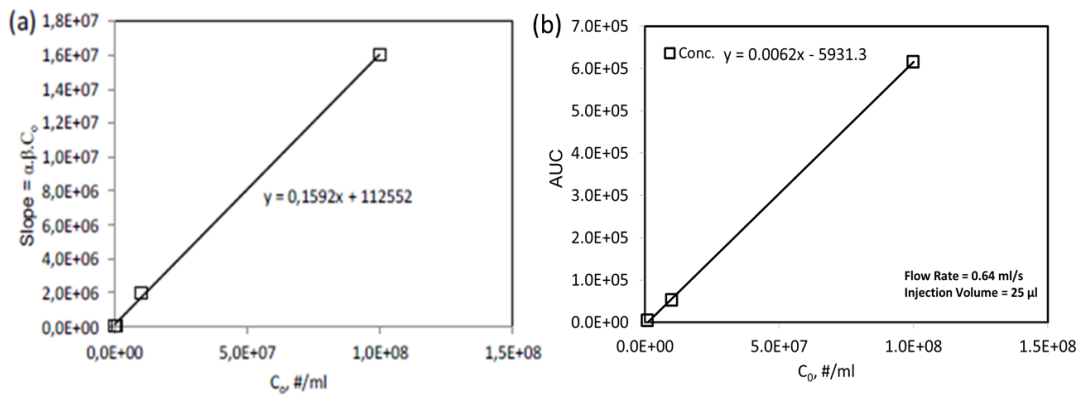


Figure 4.61. (a) The slope values obtained for the 9:1 microbubbles at different concentrations and (b) the slope value measured for the same microbubble.

The calculated microbubble concentration versus the measured microbubble concentration is shown in Figure 4.62a. As can be seen in the figure, the microbubble concentrations calculated by the ultrasound method and the measured microbubble concentrations are in good agreement except for two to three microbubble types. Figure 4.62b compares the measured microbubble concentrations for each microbubble composition and the microbubble concentrations calculated by the ultrasound method. Which type of microbubble is different in concentration is seen in the figure. In general, the concentration of microbubbles is either directly calculated from microscope images, or is measured via the Coulter Counter apparatus. However, each method has its own advantages and disadvantages. Sensitivities of these devices are also contradictory. The measured intensities are linearly proportional to the microbubble concentration. Figure 4.62c shows the microbubble concentrations calculated by the newly developed method with the AUC obtained for the ultrasound contrast agent microbubbles prepared in different formulations. As can be seen, it is understood that the calculated microbubble concentrations and the measured AUC values are generally in good agreement. Given the sensitivity of determining the concentration of microbubbles and the ultrasound measurements are linear with the concentration, it may be possible to determine the concentration of microbubbles by ultrasound. It has been found that the different microbubbles give different intensity values since the microbubbles are at different

concentrations. In this case, it is understood that the concentration factor should not be ignored in order to be able to detect the echogenicity of the different microbubbles.

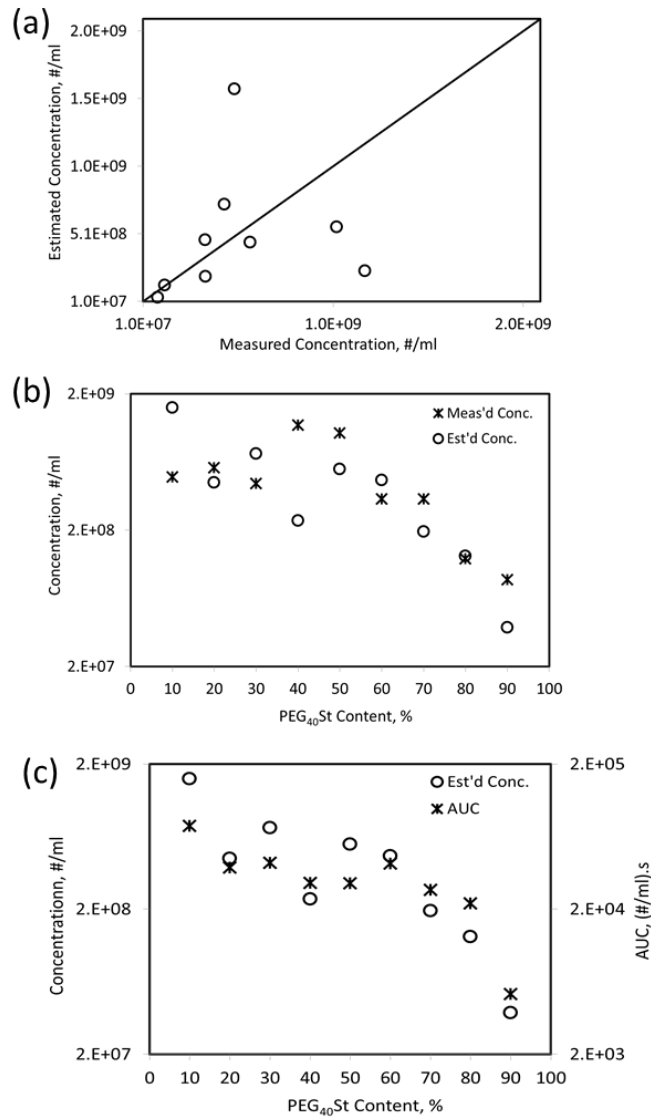


Figure 4.62. (a) The measured microbubble concentration versus the microbubble concentration calculated by the ultrasound method, (b) the measured microbubble concentration and the calculated microbubble concentration as a function of PEG<sub>40</sub>St, and (c) the microbubble concentrations calculated by the AUC obtained for the ultrasound contrast agent microbubbles prepared in different formulations.

Figure 4.63 shows that there is linear relationship between the logarithm of the microbubble concentration and AUC. B-mode images under ultrasound are actually reported as the logarithmic value of image intensity. This result was not surprising since

the intensity values obtained from the B-mode images taken with the Vevo2100 ultrasound device were used. As can be seen in the figure, three points showed deviation and other points were on the line with linear correlation.

There are three main methods for determining the number of microbubbles. These are light (optical) microscope, Coulter Multisizer, and light scattering (DLS) method (Sennoga, Yeh et al. 2012). Each method has its own advantages and disadvantages. The optical microscope method is more suitable for measuring the size of microbubbles; it is reported that the Coulter Multisizer method gives better results in determining the number of microbubbles (Sennoga, Yeh et al. 2012). As a fourth method developed and used for the first time in this study, the ultrasound method could be used to estimate the microbubble concentration.

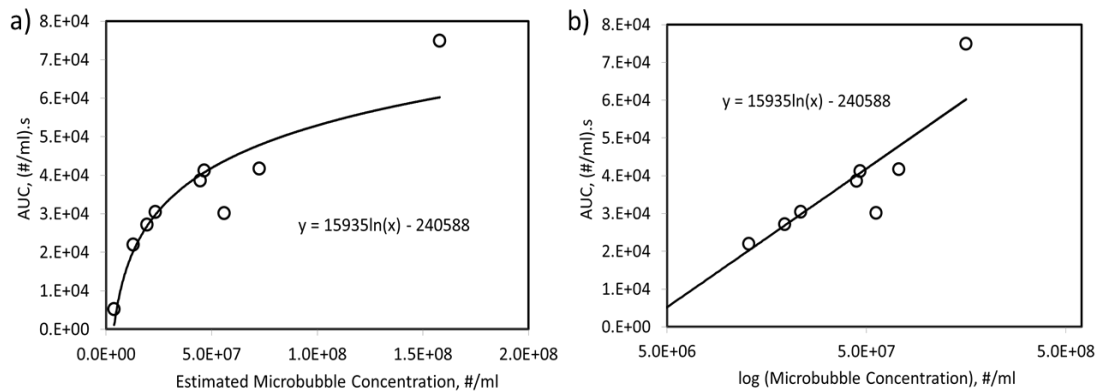


Figure 4.63. The logarithm of the microbubble concentration is linearly proportional to the AUC.

### 4.10.3. Echogenicities of Microbubbles with Different Shell Compositions

The Peak Enhancement values or the AUC values can be useful in determining the echogenicity of the microbubbles. However, in the relation given by Eq. (4.32), it is seen that the AUC values are linearly proportional to the concentration. Again, from the same equation, it is expected that the experimental parameters such as bolus injection volume and fluid flow rate, for each microbubble type should be the same. It was obtained that these parameters were the same for our microbubbles. The size distribution of microbubbles is also important in determining the ultrasound

echogenicity of microbubbles. The resonance frequencies of microbubbles differ from the applied frequency and depend on their sizes. While microbubbles with sizes below resonance frequencies do not oscillate, the microbubbles above the critical size can start to oscillate. In this case, the echogenicity of the microbubbles with different shell compositions is regarded as the AUC divided by microbubble concentration, as seen in Figure 4.64. As can be seen in the figure, the echogenicity increased with increasing PEG<sub>40</sub>St concentration in the shells of microbubbles. In a study by Hosny et al. (Hosny, Mohamedi et al. 2013), it was experimentally shown that the shell stiffness of microbubbles significantly decreased with increasing PEG<sub>40</sub>St concentration up to 50%. The lower the shell stiffness, the higher the acoustic response. Therefore, the echogenicity increase could be attributed to the decreased shell stiffness as the percentage of PEG<sub>40</sub>St content in the microbubble shell was increased.

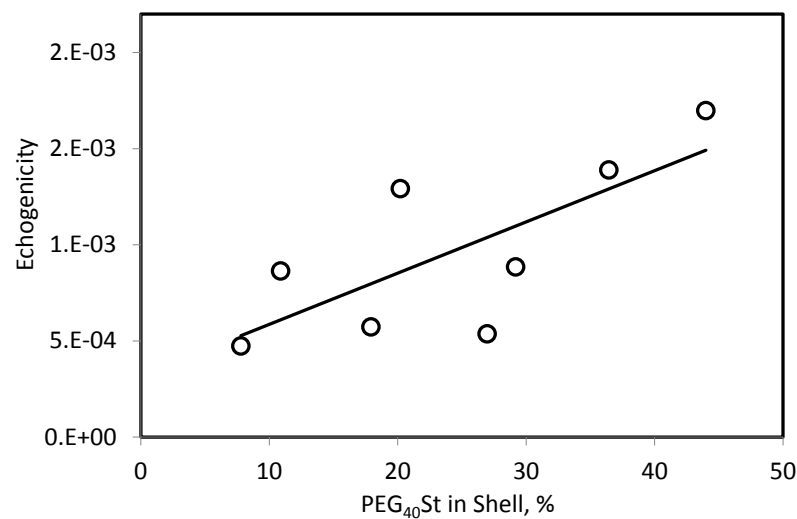


Figure 4.64. Echogenicity of microbubbles with different shell compositions.

In conclusion, a method was developed to estimate the microbubble concentration under ultrasound excitation. The analysis of time-intensity values obtained via the bolus injection method revealed that the AUC value was dependent on the experimental conditions such as the bolus volume and the microbubble concentration, and that the background intensity values acquired during the measurement could not be ignored in the calculations. It was also found that the microbubble echogenicity increased with increasing PEG<sub>40</sub>St concentration in the shell of microbubbles.

#### 4.11. Investigation of the Echogenicity of Microbubbles Loaded with Different Masses

In this study, the effect of loadings of different masses on the echogenicity of microbubbles was investigated. An experimental set-up was designed for this purpose, as shown in Figure 3.11. The system was first characterized. Figure 4.65 shows the B-mode image of the inside of the tube. When the tube was filled with buffer solution, brightness was low with respect to the front wall of the tube. After injecting the microbubbles, the brightness increases in the presence of microbubbles due to the sound wave reflected from the microbubbles. After passing through the acoustic field, the brightness of microbubbles decreased to the level of buffer solution.

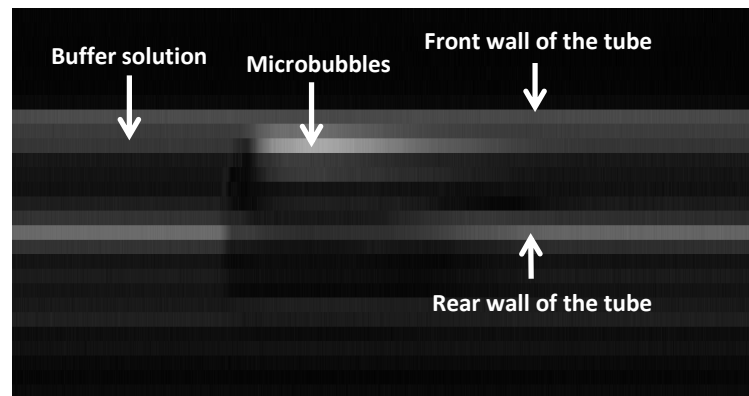


Figure 4.65. B-mode image of the inside of the tube filled with buffer solution as microbubbles pass through the tube after injected.

Microbubbles were injected in a bolus volume of 100  $\mu\text{l}$  into the liquid flowing at a constant velocity of 0.7 l/min through a centrifugal pump. After injecting the microbubble suspensions at different concentrations, each image obtained in the B-mode was analyzed in the ImageJ program. Here, the intensity of the pixels in the image, called the gray scale value, was plotted against time. Thus, time-intensity curves were generated depending on the increase in intensity in the region of interest where the microbubbles passed through. Figure 4.66 shows time-intensity curves at different microbubble concentrations for loaded microbubble populations. These gray scale values here correspond to the pixel intensities of the B-mode images. In the SigmaPlot program, the intensity values for each microbubble concentration for different types of

microbubbles were fitted to the First Passage Time model (Strouthos, Lampaskis et al. 2010). It is apparent from the figures that the experimental data fit well with the model equation. AUC, one of the parameters fitted to the experimental data, was used in our subsequent calculations (Eq. (4.32)). Since the values of injection volume and flow rate were known, value of the coefficient,  $\alpha$ , could be calculated from the slope of the curves to be obtained from the AUC values measured at different microbubble concentrations.

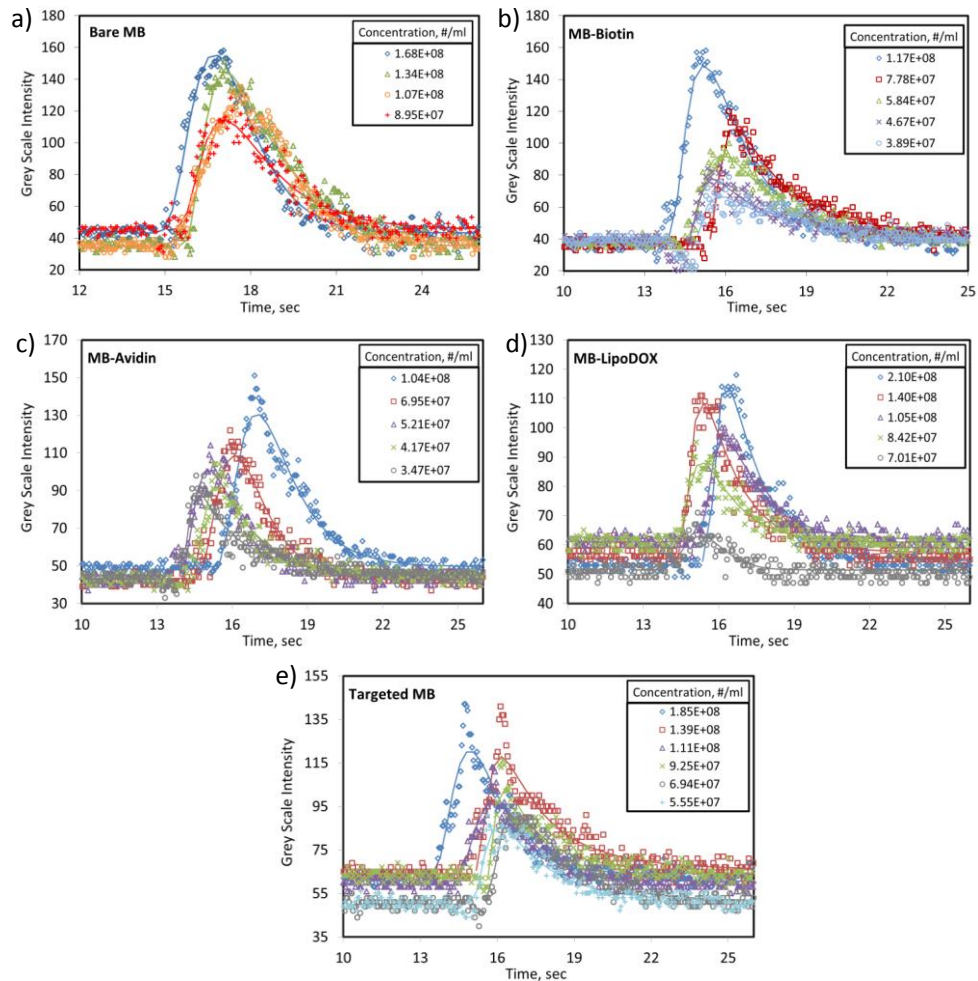


Figure 4.66. Time-intensity curves fitted to the model equation at different microbubble concentrations for different types of microbubbles: (a) bare MB, (b) MB-Biotin, (c) MB-Avidin, (d) MB-LipoDOX, and (e) Targeted MB.

The AUC values were plotted with respect to microbubble concentration for different types of microbubbles, as shown in Figure 4.67. As can be seen from the figure that there is a linear relationship between the AUC value and concentration up to a concentration of 1E+08 #/ml. This indicates

that accurate estimates for the microbubble concentration could be obtained by the quantification of AUC values from the time-intensity curves fitted to the indicator dilution model.

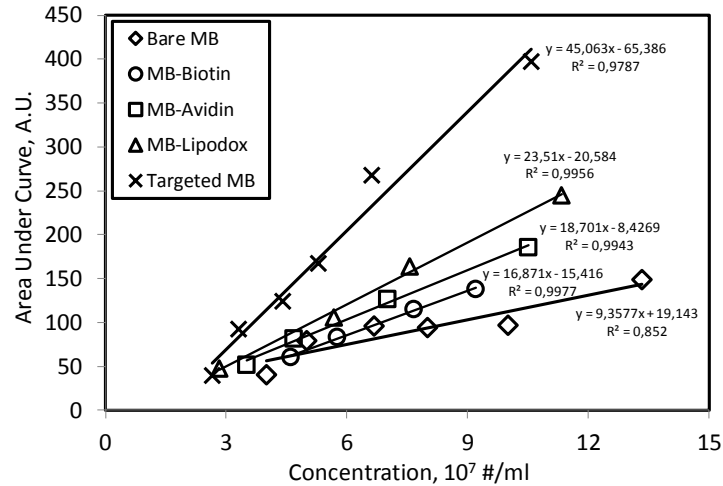


Figure 4.67. AUC-Concentration curves for the loaded microbubbles.

The echogenicity, which is regarded as AUC divided by concentration, of microbubbles loaded with different masses is given in Figure 4.68. Experiments were repeated at least 3 times. As seen in the figure, the echogenicity of microbubbles increases with increasing loading mass on the microbubble. In a study by Luan et al. (Luan, Faez et al. 2012), it was experimentally showed that liposome-loaded bubbles had a lower oscillation amplitude compared with unloaded bubbles. They also found that loaded bubbles had higher shell viscosity than unloaded bubbles. They suggested that the higher shell viscosity was the cause of lower echogenicity due to the higher “internal friction” during oscillations of loaded bubbles. This finding seems to be opposed to our findings. However, they investigated single bubbles for the acoustic pressure experiments in the time scale of microseconds with an ultra-high-speed camera. In our case, a microbubble population was injected into tubing and the image intensities of the suspensions were determined within about five seconds as the acoustic propagation was applied. In a microbubble population, significant interactions between microbubbles under external acoustic field must be taken into account. McLaughlan studied the acoustic response of drug filled liposome-loaded and unloaded bubble populations (McLaughlan, Ingram et al. 2013). They found that liposome loading on

microbubbles increased the average pixel brightness compared with unloaded bubbles under subharmonic imaging (15 MHz). As a conclusion, our result could be attributed to the fact that microbubbles might perform further expanding and contraction motion by the effect of the repulsive oscillation force created by the extra mass on the microbubbles. The amplitude of oscillation increased with increasing loading on the microbubble surface. Therefore, the higher the oscillation motion, the greater the acoustic response of the microbubble.

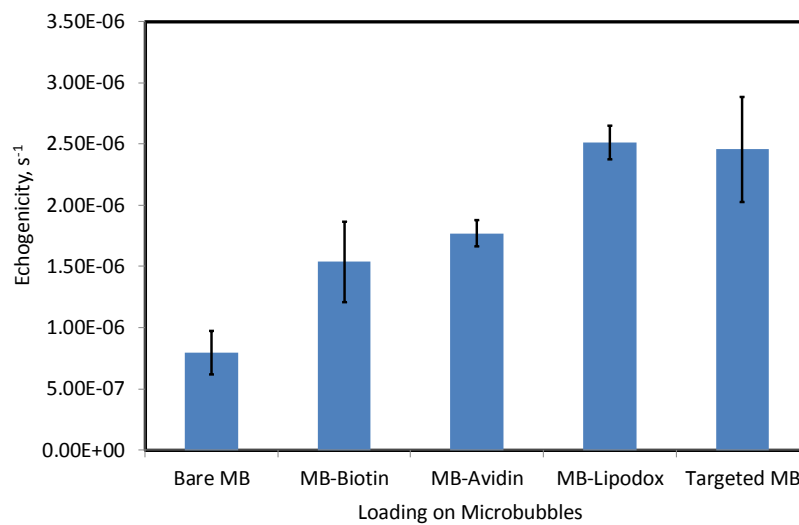


Figure 4.68. Echogenicity of microbubbles loaded with different masses.

#### 4.12. Stability of Loaded Microbubbles under Ultrasound Activation

The experimental set-up shown in Figure 3.5 was developed to examine the stability of microbubbles loaded with different masses (Biotin, Biotin-Avidin, Biotin-Avidin-Lipo-DOX, Biotin-Avidin-Lipo-DOX-Avidin, and Biotin-Avidin-Lipo-DOX-Avidin-EGF) under ultrasound through the concentration and attenuation measurements. At the high frequency (4 MHz) and output power (30 dB), each microbubble type was subjected to ultrasound under the same conditions. In the experimental set-up shown in Figure 3.5, the amplitude values of the backscattered acoustic signals from the rear wall of the cuvette, in which microbubbles were placed, are shown in Figure 4.69. As seen in the figure, there are two peak signals that are backscattered from the rear wall. The first signal, which is about 144 mm away from the

ultrasonic probe, comes from the front surface of the rear wall, and the second signal at a distance of 145 mm is backscattered from the rear surface of the wall. There is a distance of about 1 mm between the front surface and the rear surface. The amplitude of the signal from the front surface was evaluated for the analysis. Before adding the microbubble suspension into the buffer solution, the cuvette containing the buffer solution was placed in the water bath to obtain the maximum peak amplitude from the rear wall. As can be seen in Figure 4.69, after the microbubble suspension was added into the medium, the acoustic signal completely disappeared at 0 minute because the sound wave could not reach the rear wall due to microbubbles in the medium. Ultrasonic waves began to reach the rear wall of the cuvette as the microbubbles underwent destruction at high output power. Hence, the acoustic signal increased over time and reached the maximum value that the buffer solution corresponds to.

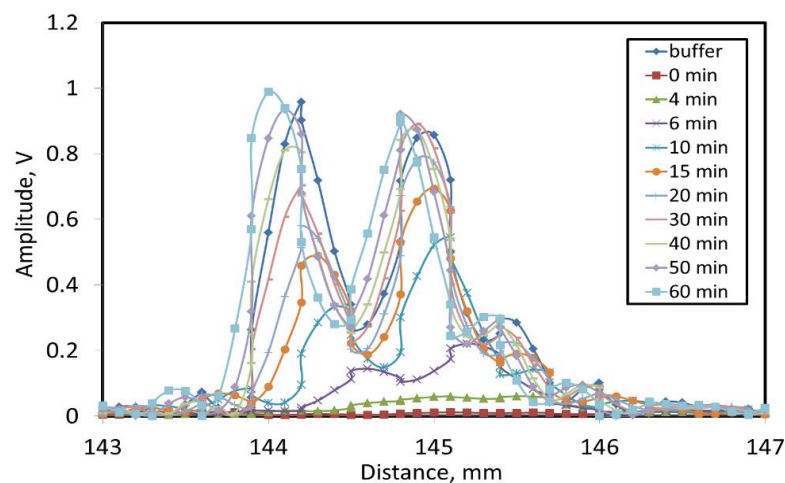


Figure 4.69. Change of amplitudes of acoustic signals reflected from the rear wall of the cuvette with respect to time.

The change in attenuation and concentration for microbubbles loaded with different masses over time under ultrasound excitation is shown in Figure 4.70. Experiments were repeated 3 times for each microbubble type with the same initial concentrations. In case of unloaded microbubbles, the attenuation decreased within the first 10 minutes, and subsequently decreased by 50%. For the change in bubble concentration over time, it was observed that the unloaded microbubbles completely lost their stability within 30 minutes. Biotinylated microbubbles and avidin-bound microbubbles started to decline in attenuation after 20 and 30 minutes, respectively.

50% loss in attenuation for biotinylated microbubbles was observed within about 25-30 minutes and for avidin-bound microbubbles within about 50 minutes. For the lipo-DOX loaded microbubbles, the attenuation was not decreased and remained almost constant. This is probably due to the formation of larger numbers of free particles such as micelles, liposomes or lipid aggregates in the medium compared to other loaded microbubbles during the destruction of the microbubble-lipo-DOX complex under ultrasound excitation. It was seen that these structures formed in the medium caused the sound waves to be backscattered without passing through the cuvette to the rear wall, and no signal therefore could be received from the rear wall. Hence, in the case of lipo-DOX loaded microbubbles, the inability to observe changes in attenuation did not indicate that they were stable. Because it was found that their concentration decreased with time. For the change in the concentration of loaded microbubbles over time, it was observed that biotinylated microbubbles lost their stability completely in about the first 25 minutes, and both the avidin-bound microbubbles and lipo-DOX loaded microbubbles lost their stability in about 50 minutes. When we evaluate all these findings as a whole, it could be concluded that as the loadings on the microbubbles were increased, they retained their stability under ultrasound excitation for a longer time.

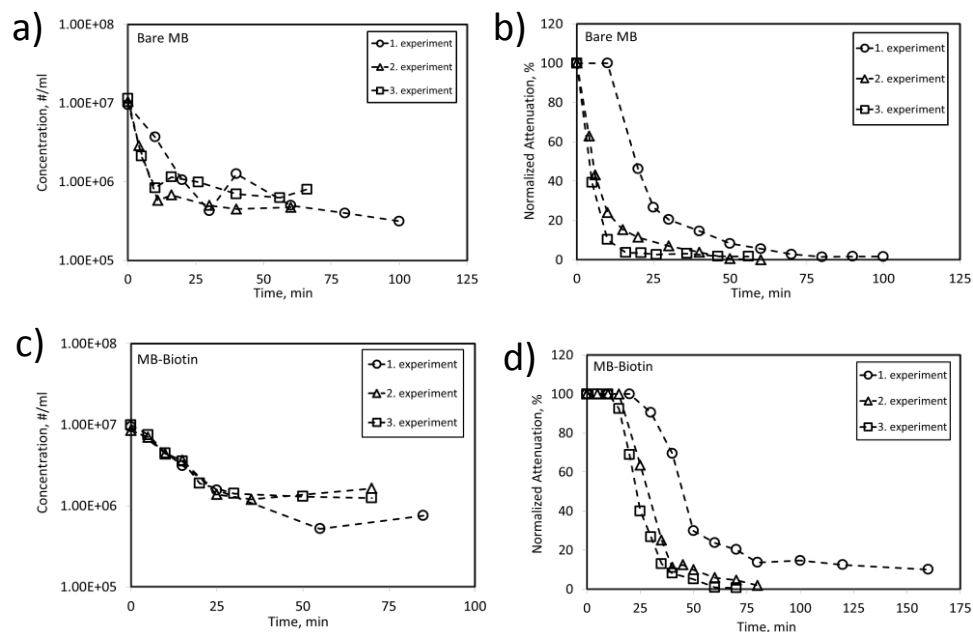


Figure 4.70. Change in concentration and attenuation over time for the unloaded microbubble and microbubbles loaded with different mass under ultrasound excitation.

(Cont. on next page)

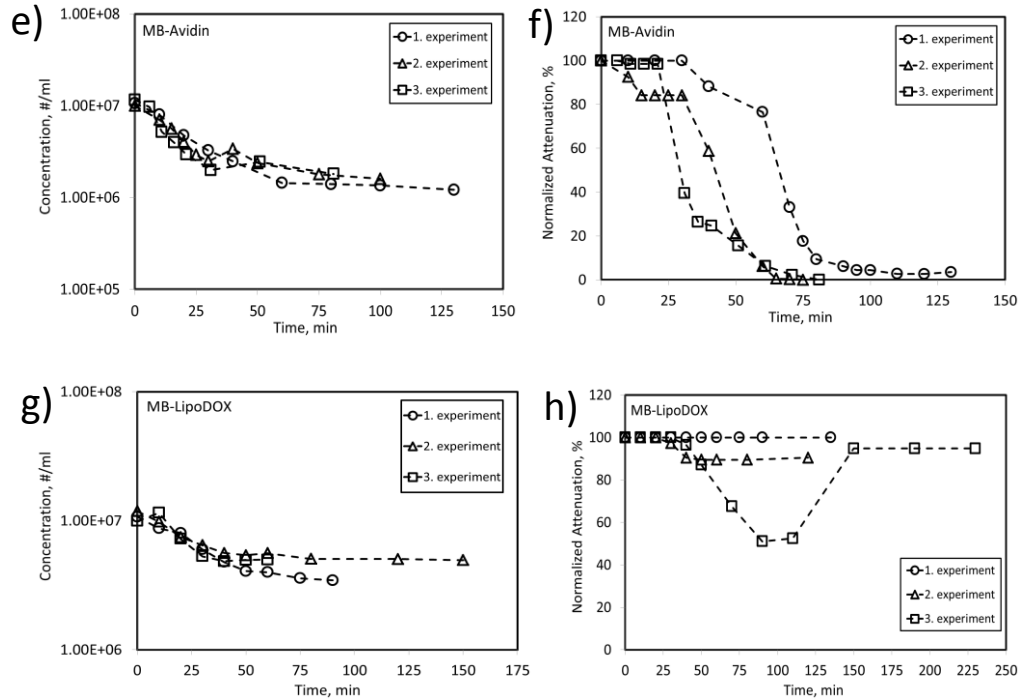


Figure 4.70. (cont.)

The stability of microbubbles loaded with different masses under ultrasound excitation in terms of both attenuation and concentration is shown in Figure 4.71. As can be seen from the figure, there is an enhancement in microbubble stability under ultrasound excitation as the loading on the microbubble is increased. The acoustic behavior of microbubbles under ultrasound depends on the mechanical properties of the shell, in particular the microbubble stiffness. Recently, atomic force microscopy has been used to measure the mechanical response of lipid encapsulated microbubbles with an extra coating layer, streptavidin (Abou-Saleh, Peyman et al. 2013). Addition of streptavidin significantly increased the stiffness of the microbubbles. It was hypothesized that the increase in stiffness was due to the presence of streptavidin that might induce a rigid polycrystalline shell forming a stiffer external layer. In our study, the loading on the microbubble surface was increased step by step through the formation of lipoDOX-loaded microbubbles. Therefore, we could attribute the increase in stability under ultrasound to the stiffening of the microbubble shell with increasing loading on the microbubble surface. We might hypothesize that the acoustic propagation had less destructive effects on the microbubbles with stiffer shells.

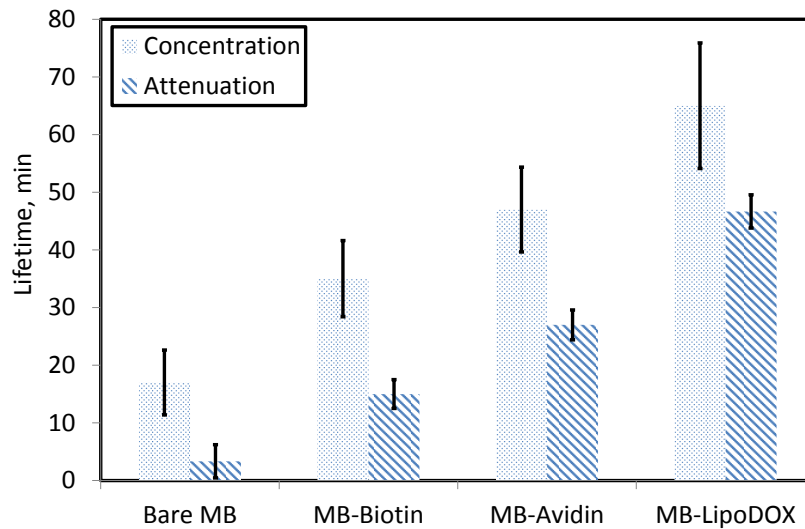


Figure 4.71. Stability of microbubbles with increasing loadings under ultrasound excitation.

#### 4.13. Characterization of Microbubbles in the Doppler Flow Phantom

In the studies performed with the peripheral vascular Doppler flow phantom, it was aimed to characterize the flow pattern and behavior of ultrasound contrast agent microbubbles in the luminal structure with stenosis. At different flow velocities and concentrations, microbubbles were injected into the tubing and the flow profiles were evaluated with the ultrasonic probe placed on the stenosis region. Experiments were performed on three separate veins with 25%, 50% and 75% stenosis. Measurements and evaluations were made in the same ROI before and after stenosis. Pre-stenosis segment ROI was defined as “ROI 1”, and post-stenosis ROI as “ROI 2”. In this model, in the post-stenosis area, microbubbles flowing with a velocity increase in the center flow profile were observed, and immediately after the stenosis in the periphery, microbubbles circulating with a turbulent flow were observed. These findings supported the laminar flow pattern in the stenosis model.

With this experiment, microbubbles were also shown to exhibit a pattern of behavior according to the laminar flow profile, such as shaped blood elements, e.g. erythrocyte, platelets, etc. This situation is of great importance because of the identification of behavior in live animal injection in accordance with the physiological flow. Microbubbles did not accumulate on the surface of the vessel lumen or did not collapse on the bottom of the lumen. They did not form aggregates in the stenosis

region. The laminar flow model showed a homogenous distribution, and the flow was rapid in the central and was slow in the periphery. In the periphery, slow flowing microbubbles did not coalesce, aggregate and form stasis. As a result of this experiment, it has been shown that microbubbles can be safely applied to animal model in accordance with the physiological flow and are suitable for the circulation system *in vivo*.

#### **4.14. *In-Vivo* Studies with Microbubbles**

*In vivo* studies were performed with the rat and rabbit animal models to evaluate the behavior of 5:5 microbubbles and their possible toxic effects in the living systems. The aim of this study was to investigate the bioavailability of the administration method, the problems that may be encountered in the field of administration, whether the pulmonary capillary barrier could be overcome and the level of access to the target tissue. Determination of the optimal dose of a contrast agent is crucial, more particularly when quantitative perfusion parameters are needed. Thus, determination of the diagnostic optimum dose was performed for the microbubbles in rats. In addition to these, we aimed to compare the first domestic microbubbles produced in our laboratory with the commercial standard contrast agents in terms of echogenicity. Two separate animal models have been studied for the *in-vivo* experiments. Rat was used as a small animal model and rabbit as the larger animal model.

Ultrasonographic images were recorded after the microbubble injection through the tail vein of the rat. The images were evaluated by using VevoCQ software program which was dedicated for the data evaluation. The microbubble distribution in the vessels was plotted as a time-echogenicity curve with the ROI placed in the vena cava inferior (VIC), abdominal aorta and vena portae (Figure 4.72). A significant increase in echogenicity was observed in 3 ROIs placed in VCI, abdominal aorta and vena portae. The echogenicity increase observed in these areas was first seen in VCI, which was in accordance with the physiological distribution model (purple line in the graph). The echogenicity increase due to the filling of the aorta by the microbubbles returning from the heart and lungs was also evident in the abdominal aorta (yellow line in the graph). The microbubbles distributed throughout the body via the aorta reached the vena portae, which was the collector of the spleen and the intestinal tract and thus increased the

echogenicity in the vena portae (green line in the graph). Microbubbles distributed in the portae branches and liver parenchyma via vena portae resulted in a general echogenicity increase.



Figure 4.72. In the time-echogenicity curve, echogenicity was significantly increased in ROIs after the microbubble injection.

This study has shown that our microbubbles can remain in the circulatory system of the rat without destruction, that they can pass through the lung capillary barrier, and that they can disperse at the physiological flow parameters without accumulation or obstruction. In addition, our microbubbles could provide sufficient echogenicity for the imaging. In the light of these findings, the next step which was the injection of microbubbles for the *in-vivo* subject groups was performed.

#### 4.14.1. Determination of Diagnostic Microbubble Dose for the Rats

The diagnostic dose for rats was determined using the liver and kidney models. The procedure was described in the methods section. Microbubbles prepared at different concentrations and different bolus injection volumes were administered through the tail vein of the rat. Simultaneously, ultrasonography images were recorded. In each bolus injection, image recording was performed for 20 minutes, and it was kept until the time when microbubbles did not produce significant measurable echogenicity.

Images were evaluated by using the VevoCQ software program. The microbubble dispersion in the vessels was plotted as a time-echogenicity curve using the VevoCQ software with ROI placed in the VCI, aorta and vena portae.

In the first experiment, six rats were used for the bolus injection of microbubbles with different concentrations at an injection volume of 0.05 ml. Figure 4.73 shows the change in the contrast mean power at different ROIs with time after bolus injection of microbubbles at different concentrations through the tail vein under ultrasound. Data obtained in all trials was also fitted using the VevoCQ program. Significant echogenicity was observed in 3 ROIs placed in the VCI, abdominal aorta and vena portae. The echogenicity increase observed in these areas was first determined in VCI, which was in accordance with the physiological distribution model. Then, the echogenicity increased in the abdominal aorta due to the filling of the aorta by the microbubbles returning from the heart and lungs. Microbubbles distributed throughout the body via the aorta reached the vena portae where the blood from the spleen and intestinal tract is collected, and increased the echogenicity in the vena portae. Microbubbles distributed in portae branches and liver parenchyma via vena portae caused an echogenicity increase. This liver model was similar in all 6 rats. 1 rat was excluded because its vascular access could not be opened.

Figure 4.74 shows the peak enhancement (PE) at different regions in the rat liver with respect to microbubble concentration. It was found that the concentration of microbubbles at a dose of  $2.5E+8$  #/ml was determined as a diagnostic dose for the VCI that gave the highest echogenicity creating no attenuation. For higher doses, signal measured in the VCI was lower because of shadowing. In the abdominal aorta, no significant peak enhancement was observed. In the vena portae, there was a low peak enhancement at concentrations of  $2.5E+08$  and  $5E+08$  #/ml when compared to the VCI; at lower concentrations no significant peak enhancement was seen. PE values could not reach the desired level lower than this concentration. However, repeatable data was needed to ensure the optimum dose obtained.

This experiment has shown us that microbubbles can remain in the circulatory system of the rat without destruction, they can pass the lung through the capillary barrier, and they can be distributed without accumulation or without obstruction regarding the physiological flow parameters. In addition, microbubbles could provide sufficient echogenicity for the imaging.

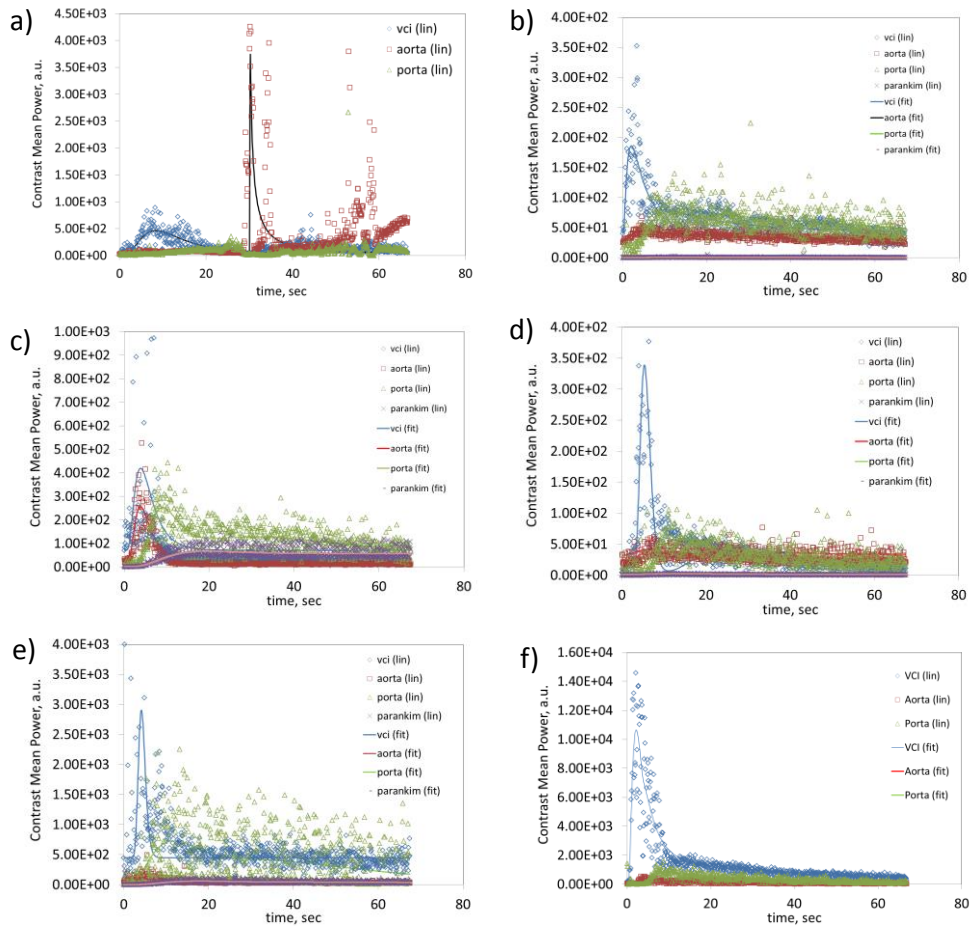


Figure 4.73. Change in the contrast mean power at different ROIs with time after bolus injection of microbubbles at different concentrations through the tail vein under ultrasound: (a)  $1\text{E}+08$  #/ml, (b)  $1\text{E}+08$  #/ml, (c)  $1\text{E}+09$  #/ml, (d)  $1\text{E}+07$  #/ml, (e)  $5\text{E}+08$  #/ml, and (f)  $2.5\text{E}+08$  #/ml.

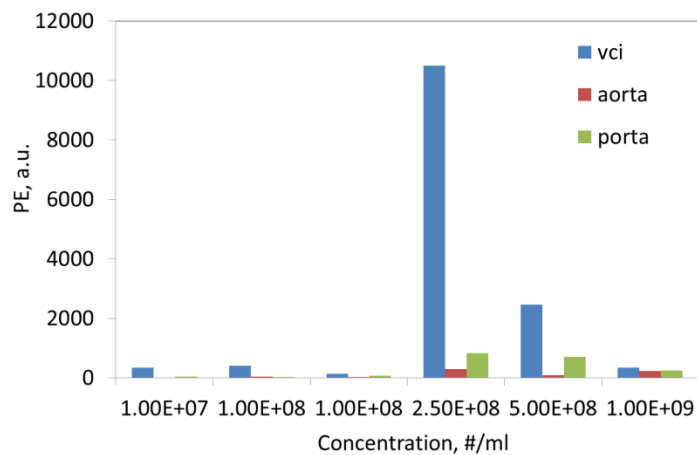


Figure 4.74. Echogenicity of microbubbles at different concentrations. Concentration of  $2.5\text{E}+08$  #/ml gives the highest peak enhancement for the VCI.

In the second experiment, diagnostic dose study was repeated to produce the repeatability of the data. Reproducibility may be assessed by performing successive injections of microbubbles over the same imaging session in the same animal (Hyvelin, Tardy et al. 2013). First, single injection was performed at different concentrations ( $1E+08$ ,  $2.5E+08$  and  $5E+08$  #/ml) with a bolus volume of 0.15 ml for different rats. Secondly, multiple injections were performed at different concentrations and injection volumes within the same animal for the parametric analysis. Figure 4.75 illustrates the change in the contrast mean power at different ROIs at different microbubble concentrations as a function of time after single bolus injection of microbubbles. The data was also fitted using the VevoCQ program.

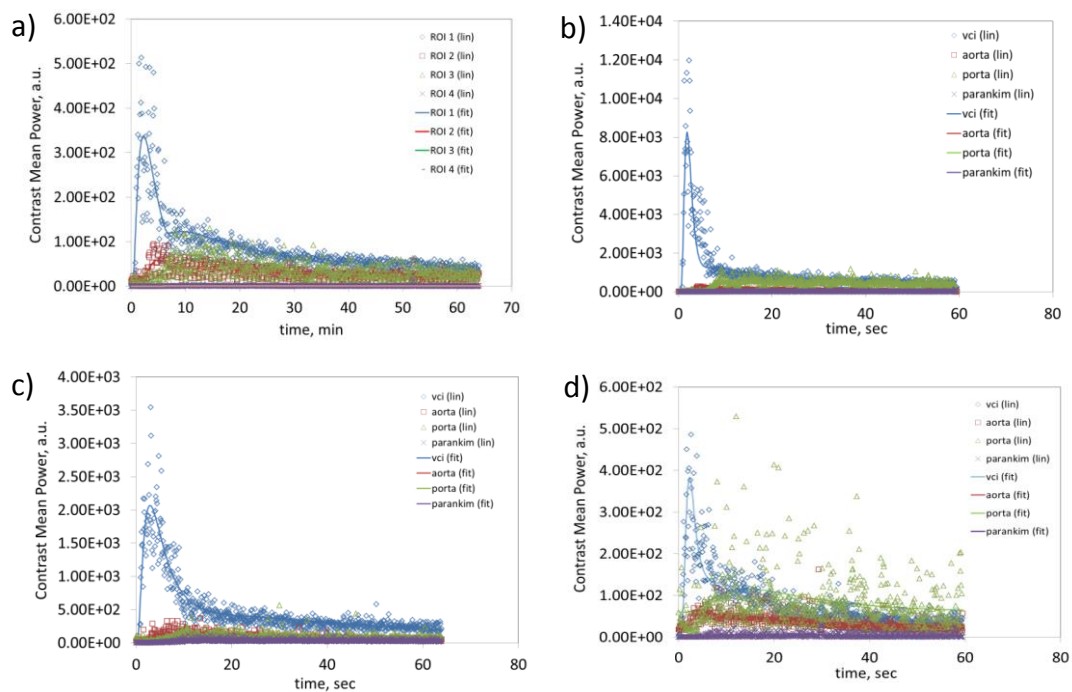


Figure 4.75. Change in the contrast mean power at different ROIs with time after single bolus injection of microbubbles at different concentrations through the tail vein under ultrasound: (a)  $1E+08$  #/ml, (b)  $5E+08$  #/ml, (c)  $2.5E+08$  #/ml and (d)  $2.5E+08$  #/ml.

Figure 4.76 shows the peak enhancement at different regions in the rat liver as a function of microbubble concentration. As seen in the figure, the highest echo power was seen at the concentration of  $5E+08$  #/ml for the VCI. The echogenicity was lower at  $2.5E+08$  #/ml. However, in the previous experiment, the highest value was at  $2.5E+08$  #/ml. This was a contradictory result in terms of the reproducibility.

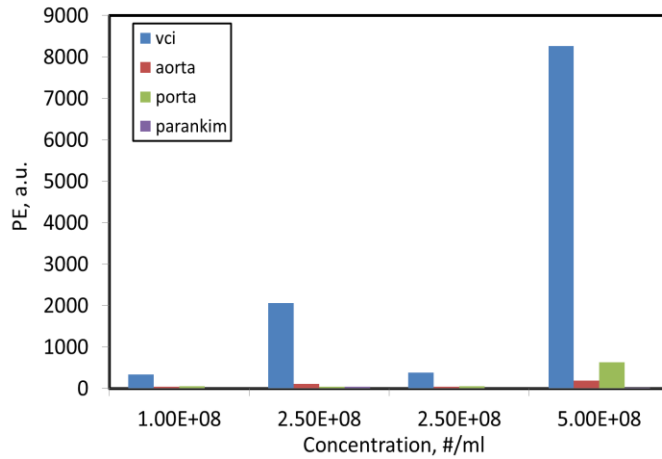


Figure 4.76. Echo power of microbubbles at different concentrations. Concentration of  $5E+08$  #/ml gives the highest peak enhancement for the VCI.

For the multiple injections, in the first trial, microbubble suspensions of different bolus volumes at a concentration of  $3.4E+08$  #/ml were administered successively. In the second trial, microbubble suspensions of different concentrations at a bolus volume of 0.15 ml were administered successively. Figure 4.77 illustrates the change in the contrast mean power at different ROIs at different bolus volumes as a function of time via multiple injections.

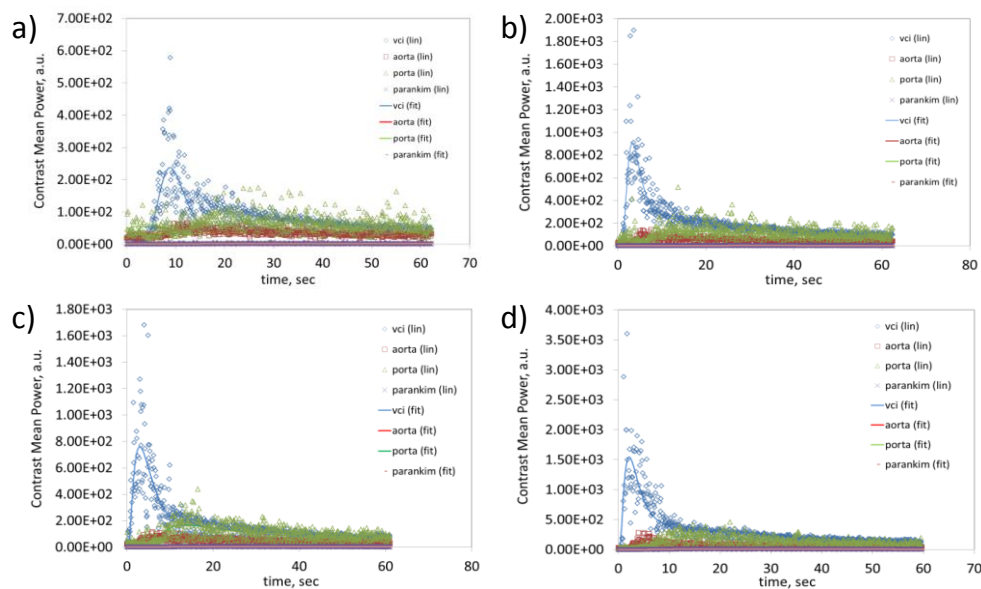


Figure 4.77. Change in the contrast mean power at different ROIs with time at different bolus injection volumes: (a) 0.03 ml, (b) 0.05 ml, (c) 0.1 ml and (d) 0.15 ml.

Figure 4.78 illustrates the peak enhancement at different regions with the multiple injections in the same rat as a function of bolus injection volume. As the bolus volume was increased, the echo power increased in all regions at the same concentration. However, the echo power was lower at 0.1 ml bolus both in the VCI and the aorta, unexpectedly. This could be attributed to the change in the physiological conditions of the rat during injection session. Microbubbles seemed not to create sufficient contrast enhancement at this volume in these regions. As a result, the highest peak enhancement was observed at a bolus injection volume of 0.15 ml.

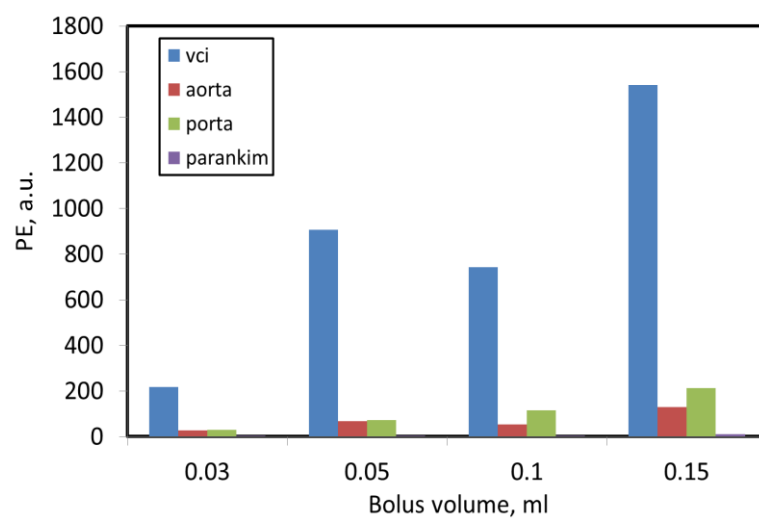


Figure 4.78. Echo power of microbubbles at different bolus volumes in a multiple injection. 0.15 ml bolus volume gives the highest peak enhancement for all regions.

Figure 4.79 depicts the change in the contrast mean power at different ROIs at different concentrations as a function of time via multiple injections. As seen in the figure, no significant peak was observed in any region. This could be due to the physiological resistance of the same rat during injection.

The rat liver model used in our study did not yield repeatable results to obtain the diagnostic dose of microbubbles for *in-vivo* imaging. There was an inconsistency between the findings reported previously. The lack of echogenicity in some of the rat injections and differences in the VCI, abdominal aorta and vena portae diameters of the animals could make it difficult to compare the measurements. In addition, possible misleading situations such as the late arrival of contrast agents to VCI due to

thrombosis, stenosis or anatomical variations in the tail vein could not be completely ignored in this model.

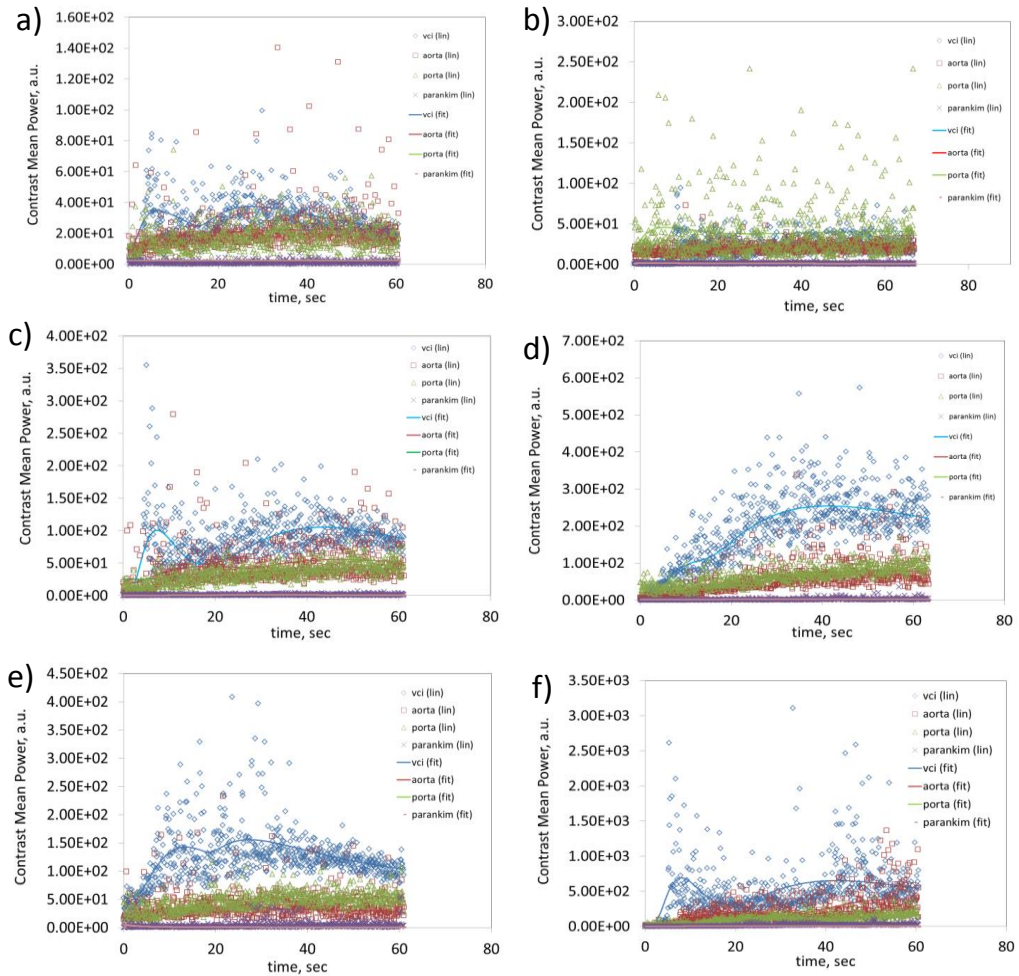


Figure 4.79. Change in the contrast mean power at different ROIs with time at different microbubble concentrations: (a) 8.5E+06 #/ml, (b) 1.7E+07 #/ml, (c) 1.7E+08 #/ml, (d) 2E+08 #/ml, (e) 5E+08 #/ml and (f) 1.7E+09 #/ml.

As a conclusion, it was decided that the circulation and hepatic system model would not be suitable and the test model should be changed in order to determine the optimum dose for the 5:5 microbubbles. In order to be able to make more consistent measurements and to evaluate the microbubbles in a more similar hemodynamic environment, a new experiment was performed for the kidney model.

The kidney is a well-vascularized organ and easy to visualize with ultrasound (Needles, Arditi et al. 2010). The kidney model experimental setup allows us to evaluate the microbubbles in a more homogeneous environment, which shows

parenchymal distribution at the capillary level and increases the parenchymal echogenicity. In the previous model, vascular diameter differences that may affect the homogenization in the measurement have been eliminated, and additionally, increasing the parenchymal echogenicity with microbubbles was also tested. In the rat kidney model, two regions of interest were manually drawn around the anterior (deeper) cortex and the posterior (superficial) cortex. As shown in Figure 4.80, after the insertion of the ROIs similar to the anterior and posterior cortex areas of the kidney, renal perfusion of microbubbles through renal artery was performed. In this way, the increase in parenchymal echogenicity values of the microbubbles could be compared with each other through the more standardized measurements. In this model, multiple injections were performed in the same animal.



Figure 4.80. ROIs placed at the level of the cortex of the kidney parenchyma were monitored. Contrast signal was measured in 2 ROIs, drawn in the anterior cortex and the posterior cortex of rat kidney.

In the first experiment, microbubble suspensions at different volumes at a concentration of  $1.96 \times 10^8$  #/ml were injected via tail vein of the rat. Figure 4.81 shows the change in the contrast mean power at the anterior and posterior cortex at different volumes as a function of time with the curve fit. As seen in the figure, in the rat kidney model, curves comprised two distinct sections: one initial peak associated with the initial wash-in of the contrast agent, and a subsequent less pronounced peak attributed

to recirculation of the contrast bolus in the rat during its slow elimination from the animal (Needles, Arditi et al. 2010).

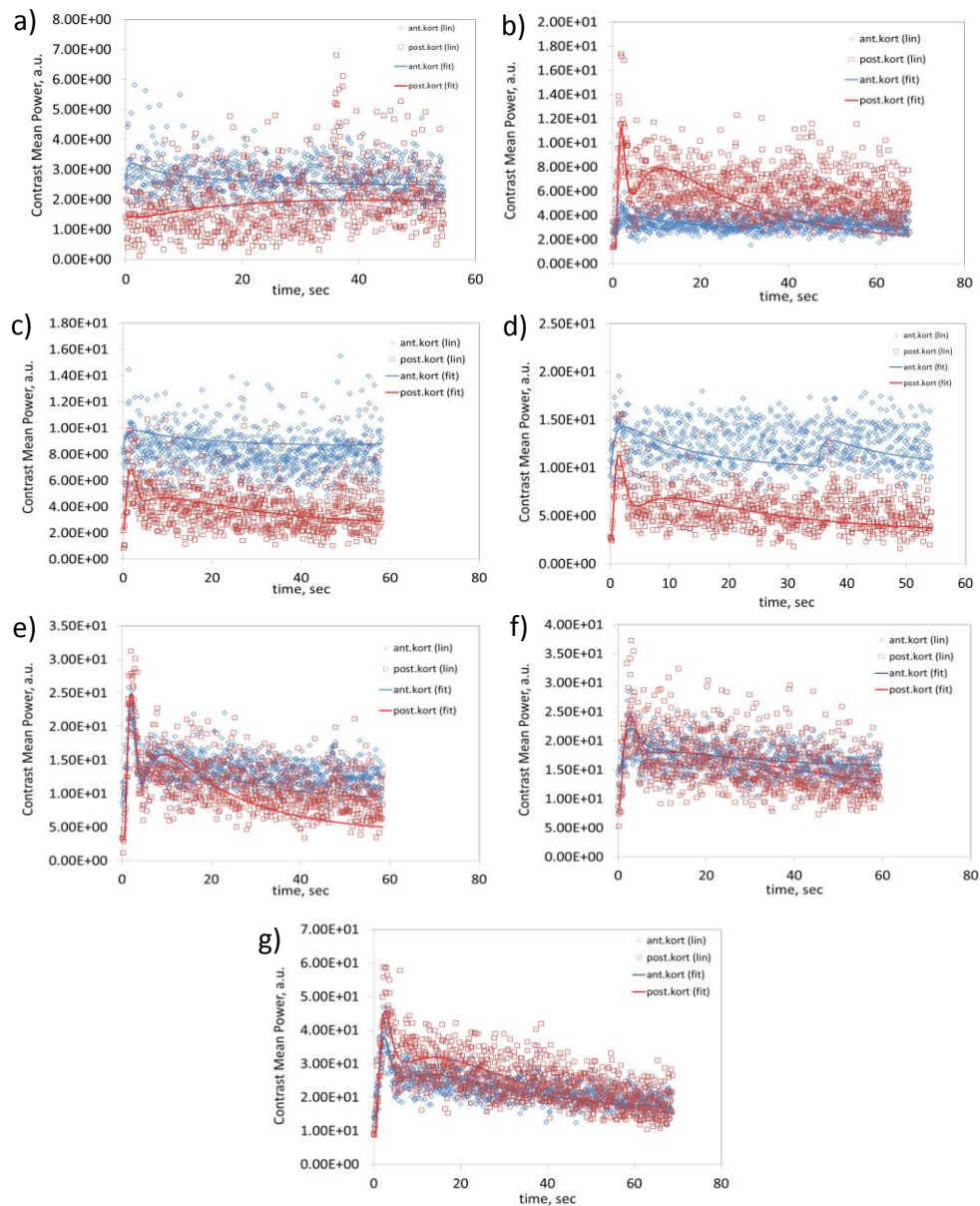


Figure 4.81. Change in the contrast mean power at the anterior and posterior cortex with time at different bolus injection volumes: (a) 0.01 ml, (b) 0.03 ml, (c) 0.06 ml, (d) 0.08 ml, (e) 0.1 ml, (f) 0.15 ml and (g) 0.23 ml.

Figure 4.82 shows the peak enhancements at different bolus volumes in both RIOs. The echogenicity showed an increasing trend with increasing bolus volume for both ROIs. Peak enhancement was higher in the posterior cortex than that of the anterior cortex. This could be attributed to the shadowing effect emanating from the posterior

cortex. The anterior cortex was the deeper cortex and the sound waves reflected from the anterior cortex could be attenuated due to the posterior cortex. The highest peak enhancement was seen at the bolus volume of 0.23 ml.

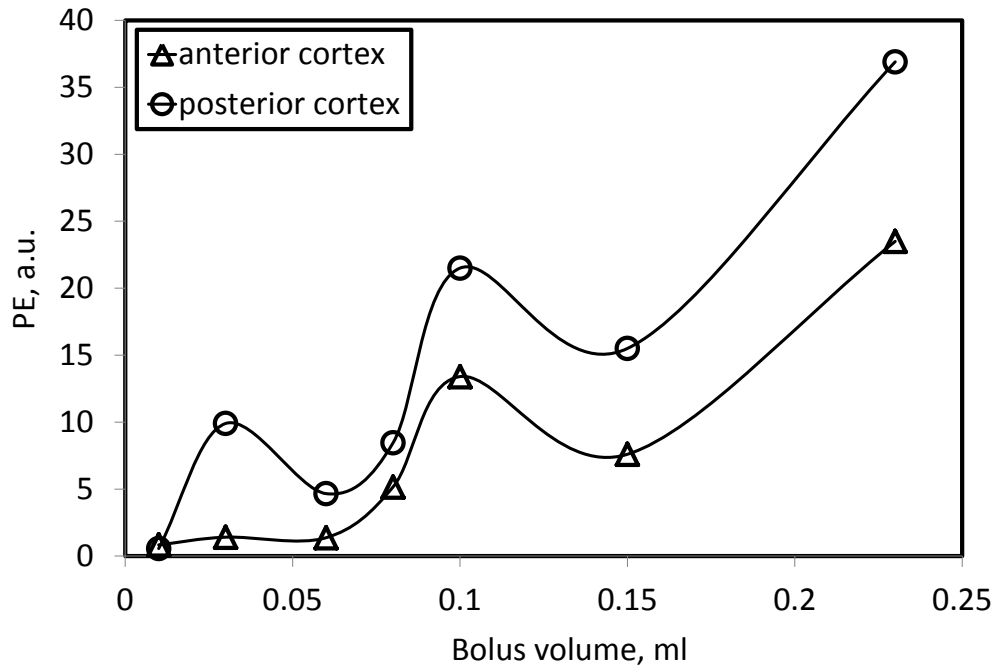


Figure 4.82. Peak enhancement at different bolus volumes in the anterior and posterior cortex regions. 0.23 ml bolus volume gives the highest peak enhancement for the two regions.

In the second assay, microbubble suspensions at different concentrations in a bolus volume of 0.15 ml were injected via tail vein of the rat. Figure 4.83 shows the change in the contrast mean power at the anterior and posterior cortex at different concentrations as a function of time with the curve fit. As seen in the figure, the curve was not well fit to the data for the anterior cortex at concentrations higher than  $1\text{E}+08$  #/ml. This was probably due to the shadowing effect emanating from the posterior cortex. Because the results obtained for the anterior cortex were not reliable, only the results obtained for the posterior cortex were assessed.

Figure 4.84 shows the peak enhancements at different microbubble concentrations in a bolus volume of 0.15 ml in the posterior cortex. As seen in the figure, the echogenicity increased up to the concentration of  $2.5\text{E}+08$  #/ml, and then declined at higher doses. According to these findings, the optimum diagnostic dose was found to be  $2.5\text{E}+08$  #/ml using the rat kidney model.

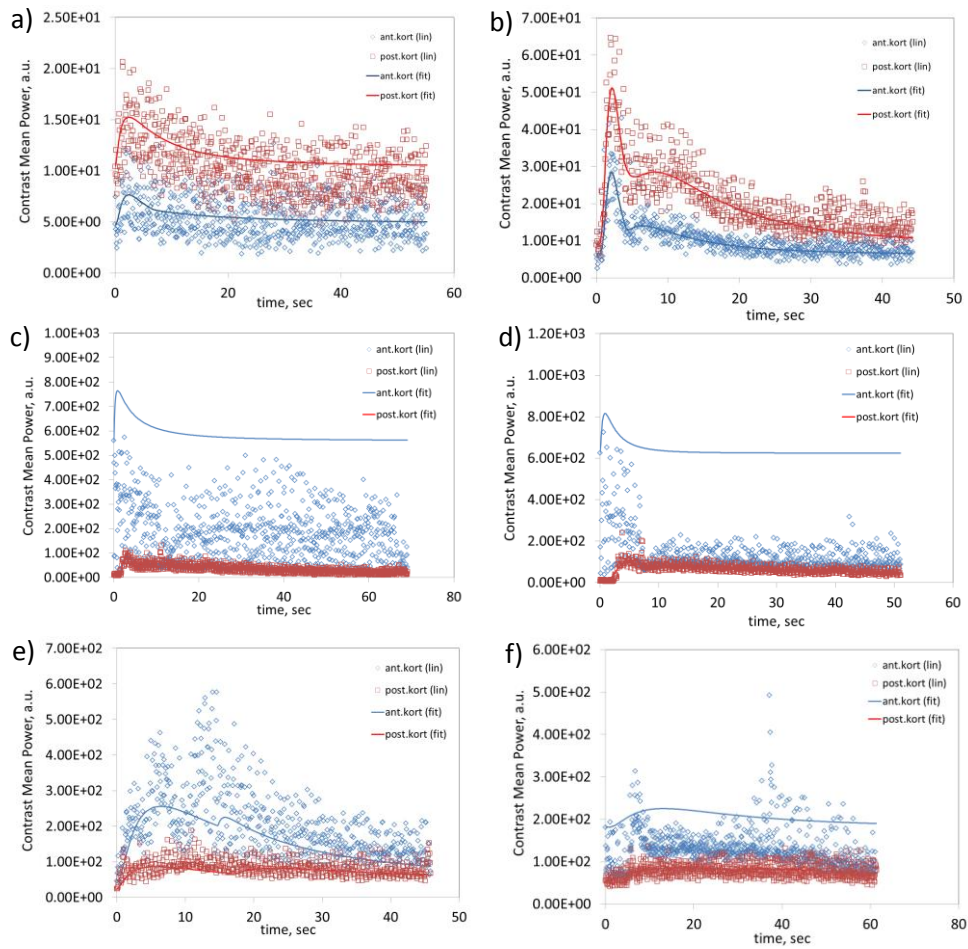


Figure 4.83. Change in the contrast mean power at the anterior and posterior cortex with time at different concentrations: (a)  $1.9 \times 10^7$  #/ml, (b)  $1 \times 10^8$  #/ml, (c)  $2.5 \times 10^8$  #/ml, (d)  $5 \times 10^8$  #/ml, (e)  $8 \times 10^8$  #/ml and (f)  $1 \times 10^9$  #/ml.

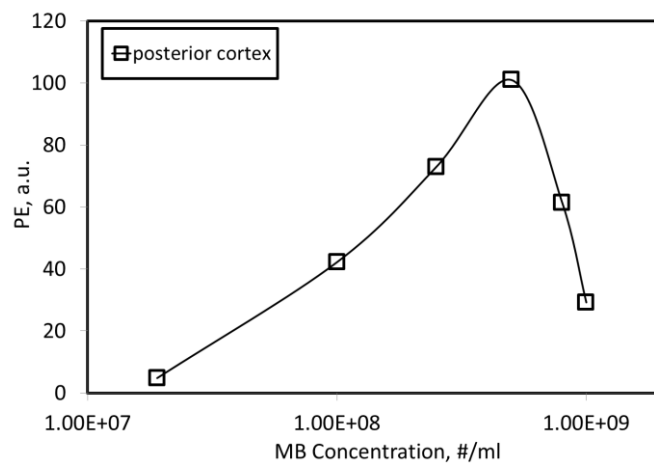


Figure 4.84. Peak enhancements at different microbubble concentrations in the posterior cortex region.  $2.5 \times 10^8$  #/ml gives the highest peak enhancement for the posterior cortex.

#### 4.14.2. Comparison of 5:5 Microbubbles with the Commercial Standard Vevo MicroMarker<sup>®</sup>

After the study of diagnostic dose determination for the 5:5 microbubbles, Vevo MicroMarker<sup>®</sup> was selected as the commercial standard contrast agent for the comparison with 5:5 microbubbles. The recommended diagnostic dose was  $2E+08$  #/ml for the Vevo MicroMarker<sup>®</sup> contrast agent according to the VisualSonics Application Protocol. 3 rats were used for the Vevo MicroMarker<sup>®</sup> injections and 4 rats were used for the 5:5 microbubble injections for the repeatability. ROIs were determined as VCI, abdominal aorta and vena portae within the rat liver. Injection volume (0.05 ml) was the same in all assays. Figure 4.85 shows the change in the contrast mean power in different ROIs for the commercial contrast agent and the 5:5 microbubbles with single injection.

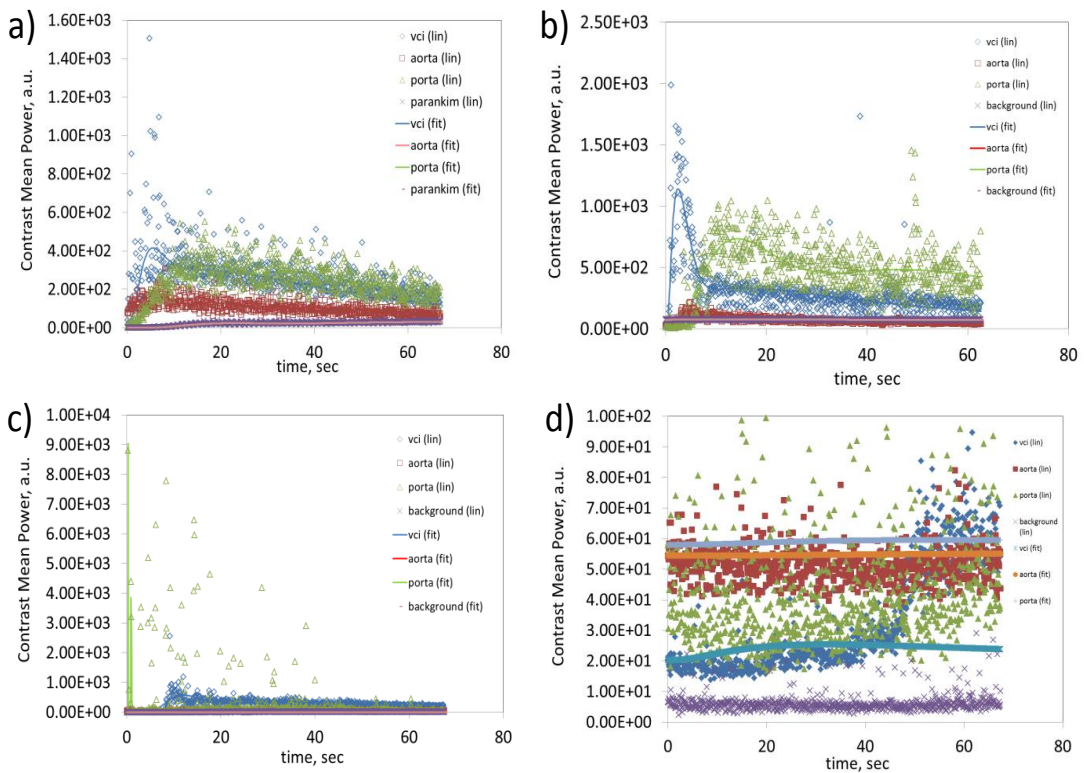


Figure 4.85. Change in the contrast mean power in different ROIs with time for the commercial contrast agent and the 5:5 microbubbles. (a), (b) and (c) represent the commercial standard. (d), (e), (f) and (g) represent the 5:5 microbubbles.

(Cont. on next page)

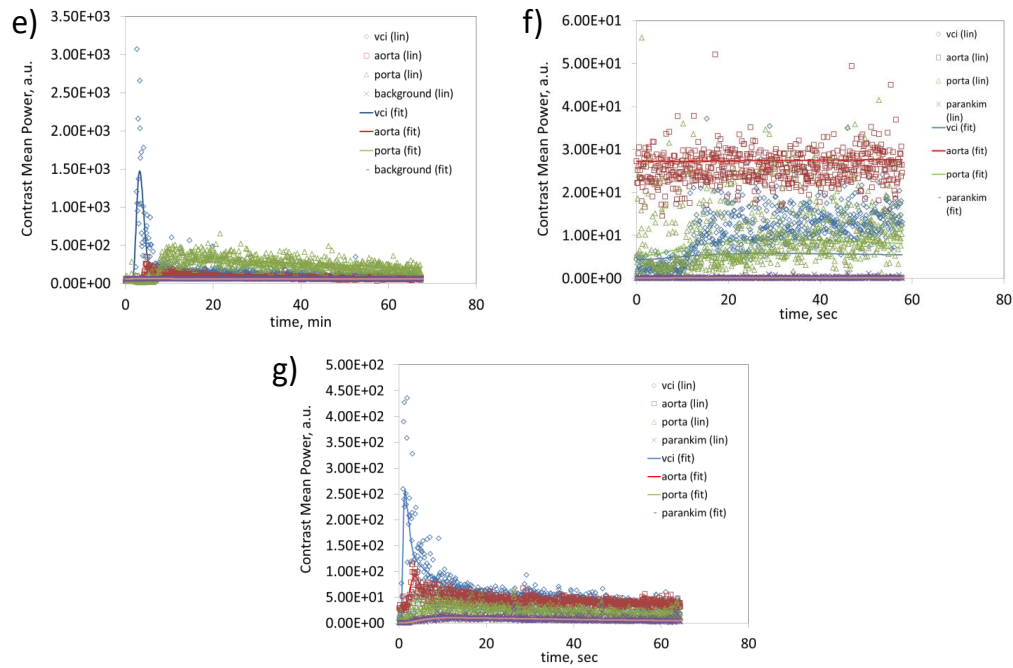


Figure 4.85. (cont.)

Figure 4.86 shows the peak enhancements in different ROIs for the Vevo MicroMarker<sup>®</sup> contrast agent and 5:5 microbubbles. As seen in the figure, the measured echogenicity values of the 2 rats (Rat 5 and Rat 7) in which the 5:5 microbubbles were applied were comparable to that of the rats in which the Vevo MicroMarker<sup>®</sup> contrast agents were applied. The echogenicity in the Rat 5 in which the 5:5 microbubbles were applied was higher than that of all rats in which the Vevo MicroMarker<sup>®</sup> contrast agents were applied. Significant peak enhancement was not seen in the other 2 rats (Rat 4 and Rat 6). In these two rats, echogenicity was observed as late as 40 sec. It was thought to be related to an anatomical problem (venous anomaly) or place of application. Also the peak enhancements in different rats for the Vevo MicroMarker<sup>®</sup> were not repeatable. As a conclusion, this experiment could not produce repeatable results. Rat kidney model was suggested and applied to solve this problem.

In the second assay, comparison study with the commercial product was performed in the kidney model experimental group. 3 rats were used for each group (5:5 microbubbles and Vevo MicroMarker<sup>®</sup> contrast agents). All injections were measured by VevoCQ and manual methods. Doses were 5E+08 #/ml and 2.5E+08 #/ml for the 5:5 microbubbles and Vevo MicroMarker<sup>®</sup> contrast agents, respectively. It was found that the PE values of each group were variable in the measurement performed by both

methods. Figure 4.87 shows the peak enhancement in echo-power for the groups of 5:5 microbubbles and the commercial standard. The highest echogenicity in rats was found to be 17.19 a.u. for the 5:5 microbubble group and 15.02 a.u. for the Vevo MicroMarker® group, respectively. As a result of this experiment, it was shown that in-house made 5:5 microbubbles and the commercial standard Vevo MicroMarker® contrast agents could reach equivalent PE values, indicating that acoustic response of 5:5 microbubbles was comparable to that of Vevo MicroMarker® contrast agents. However, the differences in the PE values among the experimental groups including the commercial standard were still less than that of the previous liver model.

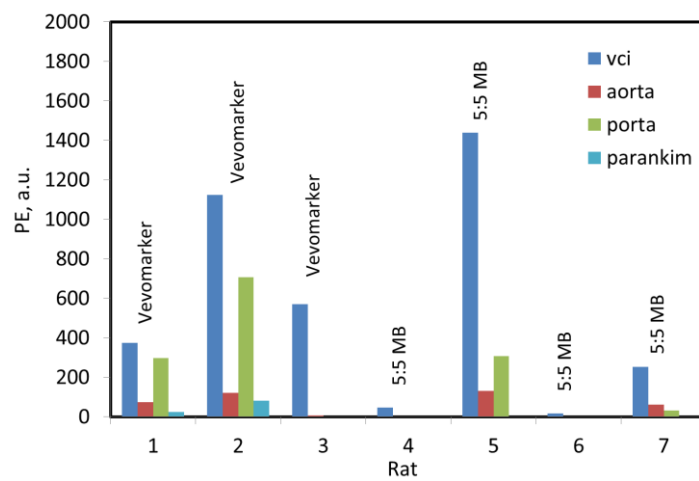


Figure 4.86. Peak enhancements in ROIs of the rat liver after single bolus injection of Vevo MicroMarker® contrast agents and 5:5 microbubbles.

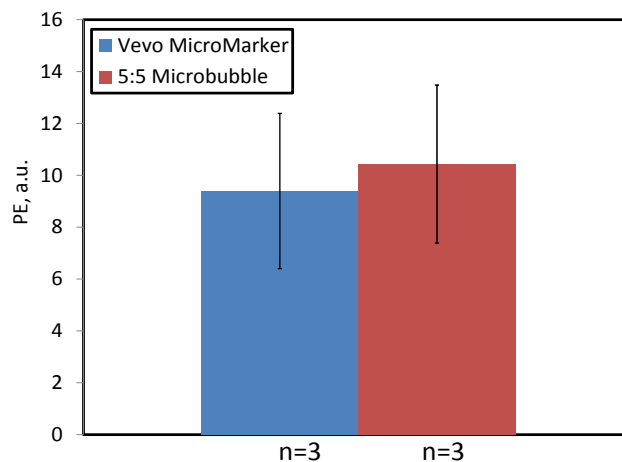


Figure 4.87. Echogenicities of 5:5 microbubbles and Vevo MicroMarker® contrast agents in the rat kidney model.

### **4.14.3. Toxicity Studies**

In the toxicity studies, biochemical and pathological analysis were conducted for the rats and the rabbits exposed to microbubble injection at toxic doses. First, the rats included in the toxic dose study were prepared as described in the previous experiments and imaged with the same data recording steps. In the imaging, attenuation was observed as seen similarly at high doses under ultrasonography. Subsequently, the rats were taken to the metabolism cages for the acute toxic effects. For late toxic effects, the rats were followed for 14 days and sacrificed at the end of this process.

In order to evaluate the toxic dose in a larger model than the rat, a high dose of microbubble injection for the rabbits was conducted. During administration, ultrasonographic evaluation was performed. The purpose of the ultrasonographic evaluation in this experiment was to ensure that the contrast agents reached the system and resulted in attenuation, suggesting that it was in high doses as expected. As a result of this experiment, rabbits were followed for 24 hours and their tissues were sent to the pathology unit.

#### **4.14.3.1. Biochemistry and Complete Blood Count (CBC) Results in Toxicities of Microbubbles**

All data that could be sampled from all rats included in the study were grouped as control group and microbubbles at different doses. Biochemical values and CBC values for the rats are given in Table 4.2 and Table 4.3, respectively. As can be seen from the tables, the urine creatinine and urea values of the rats did not show a statistically significant difference between the groups. No statistically significant difference was found between the blood values of creatinine, urea, ALT, AST, ALP, albumin, direct, indirect and total bilirubin (Table 4.2). There was no statistically significant difference between the CBC values (Table 4.3).

The identified findings suggested that the microbubbles had no toxicity in rats that could be demonstrated by biochemical or CBC values. For the toxicity tests in rabbits, the control group and the experimental group were used. In rabbits, statistical differences were found between the experimental group and the control group for the blood values before and after microbubble application. Because the values were

different from the control group, Wilcoxon test was applied for the values before and after microbubble administration in the experimental group, and the parameters that differed before and after the procedure were investigated. The results are summarized in Table 4.4.

Table 4.2. Biochemical values for rats.

	Microbubble Injected Rats (All Groups) (n=37)		Control (n=4)		<i>p</i>
	Mean	Std Dev.	Mean	Std Dev.	
Urine Creatinine (Before)	81.12	19.14	83.25	12.29	0.82
Urine Creatinine (After)	81.17	20.55	86.99	8.58	0.25
Urine Urea (Before)	6880.72	1173.67	6418.09	833.93	0.35
Urine Urea (After)	5962.46	1015.23	6312.99	482.08	0.29
Blood Creatinine (Before)	0.23	0.04	0.26	0.01	0.19
Blood Creatinine (After)	0.32	0.07	0.36	0.04	0.29
Blood Urea (Before)	21.05	2.4	21.55	0.95	0.56
Blood Urea (After)	18.84	2.24	18.67	3.59	0.91
AST (Before)	130.37	22.83	143.5	24.24	0.34
AST (After)	108.18	20.09	105.75	10.14	0.99
ALT (Before)	51.58	12.87	46.75	12.26	0.89
ALT (After)	45.21	10.86	47.25	12.12	0.32
ALP (Before)	262.66	77.55	262.25	131.67	0.75
ALP (After)	189.08	73.86	178.25	109.45	0.79
Albumin (Before)	2.96	0.17	3.1	0.15	0.14
Albumin (After)	2.87	0.2	2.95	0.06	0.4
Total Bilirubin (Before)	0.31	0.23	0.47	0.04	0.62
Total Bilirubin (After)	0.2	0.04	0.18	0.02	0.27
Indirect Bilirubin (Before)	0.28	0.23	0.44	0.04	0.72
Indirect Bilirubin (After)	0.17	0.04	0.12	0.05	0.06
Direct Bilirubin (Before)	0.02	0.01	0.02	0.009	0.98
Direct Bilirubin (After)	0.02	0.01	0.05	0.06	0.83

Table 4.3. CBC values for rats.

	Microbubble Injected Rats (All Groups) (n=37)		Control (n=4)		<i>p</i>
	Mean	Std Dev.	Mean	Std Dev.	
RBC	7.62	0.56	7.72	0.6	0.78
Hemoglobin	13.87	0.92	14.33	0.79	0.38
Hematocrit	41.92	3.09	43.28	3.1	0.43
MCV	55.31	2.72	56.28	2.42	0.4
MCHC	33.12	0.83	33.15	0.62	0.98
RDW	16.22	1.85	15.13	2.86	0.19
Platelet	963.61	143.19	886.25	99.85	0.27
MPV	5.88	0.52	5.73	0.72	0.59
PCT	0.56	0.08	0.51	0.08	0.67
Leucocyte	7.09	3.66	8.28	7.1	0.98
Neutrophil (%)	11.92	10.27	6.4	4.75	0.27
Lymphocyte (%)	83.68	9.86	91.5	9.73	0.08
Monocyte (%)	0.56	0.85	0.88	0.69	0.14
Basophil (%)	3.2	6.06	0.8	0.7	0.78
Eosinophil (%)	0.64	0.5	0.43	0.26	0.46

The biochemistry parameters which show statistically significant difference between the control group and the experimental group in rabbits revealed that the blood urea, ALP, total bilirubin and indirect bilirubin values were decreased following microbubble injection, and that the AST and ALT values were increased. The decrease in the blood urea amount, the decline in the control group and the lack of correlation between the values and creatinine suggested that the urea increase was not clinically relevant. The decrease in total and indirect bilirubin and ALP values was not clinically significant. Increase in the values of AST and ALT, which were liver function tests, was a significant finding. However, the reliability of the sample was questionable because the standard deviation of the values in the experimental group was high due to the

narrow experimental group. Repeating the assay for the AST and ALT values with large groups could be a solution. Despite these changes in the enzyme, as described in the pathology section below, the absence of significant liver damage in the rabbits by autopsy revealed no significant liver toxicity in the rabbits.

Table 4.4. Rabbit Biochemistry Values.

	Microbubble Injected Rabbits (All Groups) (n=6)		Control (n=3)		Control group variation	Experimental group before after variation
	Mean	Std Dev.	Mean	Std Dev.	<i>p</i>	<i>p</i>
Blood Creatinine (Before)	0.9	0.12	0.81	0.05	0.25	0.05
Blood Creatinine (After)	1.03	0.13	0.7	0.1	0.02	
Blood Urea (Before)	16.86	2.67	15.06	2	0.43	0.07
Blood Urea (After)	15.3	1.38	12.43	1.09	0.02	
AST (Before)	25.83	7.05	28.66	4.72	0.6	0.02
AST (After)	56.83	16.82	30.66	4.5	0.02	
ALT (Before)	62.33	18.57	54	20.8	0.43	0.02
ALT (After)	82	22.3	54.66	21.54	0.12	
ALP (Before)	75	21.54	204.33	37.2	0.02	0.04
ALP (After)	61.83	22.58	187	42.32	0.02	
Albumin (Before)	3.99	0.23	3.92	0.35	0.89	0.34
Albumin (After)	4.11	0.37	3.97	0.25	0.12	
Total Bilirubin (Before)	0.32	0.1	0.28	0.02	0.59	0.02
Total Bilirubin (After)	0.18	0.008	0.27	0.04	0.01	
Indirect Bilirubin (Before)	0.3	0.1	0.27	0.02	0.79	0.02
Indirect Bilirubin (After)	0.16	0.05	0.26	0.05	0.01	
Direct Bilirubin (Before)	0.02	0.008	0.01	0.006	0.05	0.31
Direct Bilirubin (After)	0.02	0.004	0.01	0.005	0.15	

Rabbit CBC values are listed in Table 4.5. As can be seen in the table, microbubbles did not show a statistically significant change in rabbit CBC values. It was found that the eosinophil values increased after the microbubble injection. The

increase was not found to be statistically significant. However, it is appropriate to consider that this parameter which is an allergy indicator in the experiments should be repeated in larger groups together.

Table 4.5. Rabbit CBC Values.

	Microbubble Injected Rats (All Groups) (n=6)		Control (n=3)		Control group variation	Experimental group before after variation <i>p</i>
	Mean	Std Dev.	Mean	Std Dev.	<i>p</i>	
RBC (Before)	5.19	2.55	6.76	0.61	0.12	0.91
RBC (After)	5.3	2.62	6.65	0.72	0.31	
Hemoglobin (Before)	10.91	5.35	13.8	0.43	0.07	0.67
Hemoglobin (After)	11.15	5.48	13.2	0.98	0.86	
Hematocrit (Before)	32.68	16.04	41.56	1.36	0.06	0.46
Hematocrit (After)	34.31	16.92	40	2.96	0.73	
MCV (Before)	52.48	25.79	61.76	3.76	0.79	0.34
MCV (After)	54.05	26.63	60.25	2.19	0.31	
MCHC (Before)	27.85	13.64	33.2	0.1	0.79	0.24
MCHC (After)	27.11	13.28	33	0	0.31	
RDW (Before)	11.56	5.71	14.96	1.02	0.07	0.35
RDW (After)	12.2	6.02	14.85	1.06	0.73	
Platelet (Before)	268.66	136.63	375.33	123.34	0.12	0.46
Platelet (After)	304.83	196.73	362.5	68.58	0.99	
MPV (Before)	5.1	2.58	6.23	0.15	0.15	0.49
MPV (After)	5.68	3.03	5.95	0.07	0.61	
PCT (Before)	0.16	0.08	0.23	0.03	0.12	0.46
PCT (After)	0.19	0.12	0.21	0.1	0.99	
Leucocyte (Before)	7.55	4.96	6.66	0.8	0.43	0.24
Leucocyte (After)	5.53	3.01	8.1	0	0.18	
Neutrophil % (Before)	10.81	8.56	11.7	9.54	0.79	0.6
Neutrophil % (After)	13.08	10.55	12.85	10.96	0.99	
Lymphocyte % (Before)	65.8	32.42	75.3	27.04	0.79	0.24
Lymphocyte % (After)	52.13	27.11	83.25	10.39	0.09	
Monocyte % (Before)	1.76	0.98	2.73	0.64	0.12	0.75
Monocyte % (After)	1.81	1.76	2.4	1.41	0.73	
Basophil % (Before)	1.46	1.98	3.86	5.37	0.69	0.89
Basophil % (After)	1.78	2.88	0.2	2.55	0.39	
Eosinophil % (Before)	3.48	7.31	6.4	8.05	0.36	0.08
Eosinophil % (After)	14.51	15.8	1.3	0.56	0.73	

#### **4.14.3.2. Pathology Results**

Pathological evaluation included lung, liver, kidney and brain tissues of the rats and the rabbits.

##### **4.14.3.2.1. Microbubble-1 (RAT – 5E+08 #/ml)**

As a result of the examination of the pathological specimen sections of the lung, alveolar ventilation in the lung was observed as normal. Chronic inflammation was observed in one of the main bronchioles. Bronchiolitis was observed. There was no pleural thickening. Aerating was in the usual appearance.

As a result of examination of the pathological specimen sections of the liver, portal areas were observed in the sections of the liver. Reticular roof was observed as normal. There was no bleeding in the parenchyma. No lubrication was observed. The capsule had the usual appearance. No inflammation or bleeding was observed in the portal area.

As a result of examination of kidney specimens, kidney glomeruli were observed in the usual shape and size. Basal layer thickening was not observed. Afferent arterioles were common in appearance. Slight congestion was observed in the glomerular capillary bed. No acute tubular necrosis was detected. No accumulation of tubular material was observed.

As a result of examination of the pathological specimen sections of the brain, cerebellum was observed as normal. Ventricular was normal. Meningitis was not observed. Brain membranes were normal. The normal alignment was observed. Neither bleeding nor necrosis was observed.

##### **4.14.3.2.2. Microbubble-2 (RAT – 5E+08 #/ml)**

As a result of the examination of the pathological specimen sections of the lung, alveolar ventilation in the lung was observed. There was no pleural thickening. Aerating was in its usual appearance.

As a result of examination of the pathological specimens of the liver, portal areas were common in the sections of the liver. Reticular roof was observed as normal.

There was no bleeding in the parenchyma. No lubrication was observed. The capsule had the usual appearance. No inflammation or bleeding was observed in the portal area.

As a result of examination of kidney specimens, kidney glomeruli were observed in the usual shape and size. Basal layer thickening was not observed. Afferent arterioles were common in appearance. No acute tubular necrosis was detected. No accumulation of tubular material was observed. As a result of examination of the pathological sample sections of the brain, cerebellum was observed as normal. Ventricular was normal. Meningitis was not observed. Brain membranes were normal. The normal alignment was observed. Neither bleeding nor necrosis was observed.

#### **4.14.3.2.3. Microbubble-3 (RAT – 2.5E+08 #/ml)**

No suitable tissue of the lung to be evaluated pathologically was observed.

As a result of examination of the pathological specimen sections of the liver, portal areas were observed in the sections of the liver. Reticular roof was observed as normal. There was no bleeding in the parenchyma. No lubrication was observed. The capsule had the usual appearance. No inflammation or bleeding was observed in the portal area.

As a result of examination of the pathological specimen sections of the kidney, kidney glomeruli were of the usual shape and size. Basal layer thickening was not observed. Afferent arterioles were common in appearance. Mild tubular congestion was observed. No acute tubular necrosis was detected. No accumulation of tubular material was observed.

As a result of examination of the pathological sample sections of the brain, cerebellum was observed as normal. Ventricular was normal. Meningitis was not observed. Brain membranes were common. The normal alignment was observed. Neither bleeding nor necrosis was observed.

#### **4.14.3.2.4. Microbubble-4 (RAT – 5E+08 #/ml)**

As a result of the examination of the pathological specimen sections of the lung, alveolar ventilation in the lung was normal. There was no pleural thickening. Aerating was normal.

As a result of the examination of the pathological specimens of the liver, portal areas were observed in liver sections. Reticular roof was observed as normal. There was no bleeding in the parenchyma. No lubrication was observed. The capsule had the usual appearance. Inflammation and bleeding were not observed in the portal area.

As a result of the examination of the pathological specimens of the kidney, renal glomeruli were of normal shape and size. Basal layer thickening was not observed. Afferent arterioles were normal in appearance. Acute tubular necrosis was not detected. No intra-tubular accumulation was observed.

As a result of the examination of the pathological specimen sections of the brain, cerebellum was observed as normal. Ventricular was normal. Meningitis was not observed. The brain membranes were normal. Neither bleeding nor necrosis was observed.

#### **4.14.3.2.5. Microbubble-5 (RAT – 5E+08 #/ml)**

As a result of the examination of the pathological specimen sections of the lung, alveolar roof ventilation in the lung was observed as normal. There was no pleural thickening. Aerating was normal.

As a result of the examination of the pathological specimens of the liver; Portal areas are common in liver sections. Reticular roof was observed as normal. There was no bleeding in the parenchyma. No lubrication was observed. The capsule had the usual appearance. Inflammation and bleeding were not observed in the portal area.

As a result of the examination of the pathological specimens of the kidney, mild congestion was observed in renal glomerular. Basal layer thickening was not observed. Afferent arterioles were normal in appearance. Acute tubular necrosis was not detected. No intra-tubular accumulation was observed.

As a result of the examination of the pathological specimen sections of the brain, cerebellum was observed as normal. Ventricular was normal. Meningitis was not observed. Brain membranes were normal. Normal alignment was observed. Neither bleeding nor necrosis was observed.

#### **4.14.3.2.6. Microbubble-6 (RAT - 2.5E+08 #/ml)**

As a result of the examination of the pathological specimen sections of the lung, bronchiolitis was observed. Mononuclear cell infiltration was observed in the bronchial walls. Focal congestion was observed. Focal bronchopneumonia was observed.

As a result of the examination of the pathological specimens of the liver, portal areas were observed in liver sections. Reticular roof was observed as normal. There was no bleeding in the parenchyma. No lubrication was observed. The capsule had the usual appearance. Inflammation and bleeding were not observed in the portal area.

As a result of the examination of the pathological specimens of the kidney, renal glomeruli were of normal shape and size. Basal layer thickening was not observed. Afferent arterioles were normal in appearance. Acute tubular necrosis was not detected. No intra-tubular accumulation was observed.

As a result of the examination of the pathological specimen sections of the brain, cerebellum was observed as normal. Ventricular was normal. Meningitis was not observed. Brain membranes were normal. Normal alignment was observed. No bleeding, necrosis was observed.

#### **4.14.3.2.7. Microbubble-7 (RAT - 2.5E+08 #/ml)**

As a result of the examination of the pathological specimen sections of the lung, alveolar roof ventilation in the lung was observed as normal. There was no pleural thickening. Aerating was normal.

As a result of the examination of the pathological specimens of the liver, portal areas were observed in liver sections. Reticular roof was observed as normal. There was no bleeding in the parenchyma. No lubrication was observed. The capsule had the usual appearance. Inflammation and bleeding were not observed in the portal area.

As a result of the examination of the pathological specimens of the kidney, renal glomeruli were of normal shape and size. Basal layer thickening was not observed. Afferent arterioles were normal in appearance. Acute tubular necrosis was not detected. No intra-tubular accumulation was observed.

As a result of the examination of the pathological specimen sections of the brain, cerebellum was observed as normal. Ventricular was normal. Meningitis was not

observed. Brain membranes were normal. Normal alignment was observed. Neither bleeding nor necrosis was observed.

#### **4.14.3.2.8. Microbubble-8 (RAT - 2.5E+08 #/ml)**

As a result of the examination of the pathological specimen sections of the lung, alveolar ventilation in the lung was observed as normal. Focal bronchopneumonia was observed.

As a result of the examination of the pathological specimens of the liver, portal areas were observed in liver sections. Reticular roof was observed as normal. There was no bleeding in the parenchyma. No lubrication was observed. The capsule had the usual appearance. Inflammation and bleeding were not observed in the portal area.

As a result of the examination of the pathological specimens of the kidney, renal glomeruli were of normal shape and size. Basal layer thickening was not observed. Afferent arterioles were normal in appearance. Acute tubular necrosis was not detected. No intra-tubular accumulation was observed.

As a result of the examination of the pathological specimen sections of the brain, cerebellum was observed as normal. Ventricular was normal. Meningitis was not observed. Brain membranes were normal. Normal alignment was observed. Neither bleeding nor necrosis was observed.

#### **4.14.3.2.9. Microbubble-9 (RAT – 3.2E+09 #/ml)**

As a result of the examination of the pathological specimen sections of the lung, alveolar ventilation in the lung was observed as normal. There was no pleural thickening. Aerating was normal.

As a result of the examination of the pathological specimens of the liver, portal areas were observed in liver sections. Reticular roof was observed as normal. There was no bleeding in the parenchyma. No lubrication was observed. The capsule had the usual appearance. Inflammation and bleeding were not observed in the portal area.

As a result of the examination of the pathological specimens of the kidney, renal glomeruli were of normal shape and size. Basal layer thickening was not observed.

Afferent arterioles were normal in appearance. Acute tubular necrosis was not detected. No intra-tubular accumulation was observed. Slight congestion was observed.

As a result of the examination of the pathological specimen sections of the brain, cerebellum was observed as normal. Ventricular was normal. Meningitis was not observed. Brain membranes were normal. Normal alignment was observed. Neither bleeding nor necrosis was observed.

#### **4.14.3.2.10. Microbubble-10 (RABBIT – 3.2E+09 #/ml)**

As a result of the examination of the pathological specimen sections of the lung, focal emphysema was observed. Focal bleeding and congestion were observed. The presence of hemosiderin loaded macrophages was detected.

As a result of the examination of the pathological specimens of the liver, portal areas were observed in liver sections. Reticular roof was observed as normal. There was no bleeding in the parenchyma. No lubrication was observed. The capsule had the usual appearance. Congestion was observed in central veins. Inflammation and bleeding were not observed in the portal area. As a result of the examination of the pathological specimens of the kidney, renal glomeruli were of normal shape and size. Basal layer thickening was not observed. Afferent arterioles were normal in appearance. Acute tubular necrosis was not detected. No intra-tubular accumulation was observed.

As a result of the examination of the pathological specimen sections of the brain, cerebellum was observed as normal. Ventricular was normal. Meningitis was not observed. Brain membranes were normal. Normal alignment was observed. Neither bleeding nor necrosis was observed.

#### **4.14.3.2.11. Microbubble-11 (RABBIT – 3.2E+09 #/ml)**

As a result of the examination of the pathological specimen sections of the lung, liver and kidney, slight congestions were observed in all of them.

As a result of the examination of the pathological specimen sections of the brain, cerebellum was observed as normal. Ventricular was normal. Meningitis was not observed. Brain membranes were normal. Normal alignment was observed. Neither bleeding nor necrosis was observed.

#### **4.14.3.2.12. Microbubble-12 (RABBIT – 3.2E+09 #/ml)**

As a result of the examination of the pathological specimen sections of the lung, alveolar ventilation in the lung was normal. There was no pleural thickening. Aerating was normal.

As a result of the examination of the pathological specimens of the liver, portal areas were normal in liver sections. Reticular roof was observed as normal. There was no bleeding in the parenchyma. No lubrication was observed. The capsule had the usual appearance. Inflammation and bleeding were not observed in the portal area.

As a result of the examination of the pathological specimens of the kidney, significant congestion was observed.

As a result of the examination of the pathological specimen sections of the brain, cerebellum was normal. Ventricular was normal. Meningitis was not observed. Brain membranes were normal. Normal alignment was observed. Neither bleeding nor necrosis was observed.

#### **4.14.3.2.13. Microbubble-13 (RABBIT – 3.2E+09 #/ml)**

As a result of the examination of the pathological specimens of the lung, focal emphysema was observed. Alveolar ventilation in the lung was normal. There was no pleural thickening. Aerating was normal.

As a result of the examination of the pathological specimens of the liver, portal areas were normal in liver sections. Reticular roof was observed as normal. There was no bleeding in the parenchyma. No lubrication was observed. The capsule had the usual appearance. Inflammation and bleeding were not observed in the portal area.

As a result of the examination of the pathological specimens of the kidney, renal glomeruli were of normal shape and size. Basal layer thickening was not observed. Afferent arterioles were normal in appearance. Acute tubular necrosis was not detected. No intra-tubular accumulation was observed.

As a result of the examination of pathological specimen sections of the brain, cerebellum was observed as normal. Ventricular was normal. Meningitis was not observed. Brain membranes were normal. Normal alignment was observed. Neither bleeding nor necrosis was observed.

#### **4.14.3.2.14. Microbubble-14 (RABBIT – 3.2E+09 #/ml)**

As a result of the examination of the pathological specimen sections of the lung, alveolar ventilation in the lung was normal. There was no pleural thickening. Aerating was normal.

As a result of the examination of the pathological specimens of the liver, portal areas were normal in liver sections. Reticular roof was observed as normal. There was no bleeding in the parenchyma. No lubrication was observed. The capsule had the usual appearance. Inflammation and bleeding were not observed in the portal area.

As a result of the examination of the pathological specimens of the kidney, renal glomeruli were of normal shape and size. Basal layer thickening was not observed. Afferent arterioles were normal in appearance. Acute tubular necrosis was not detected. No intra-tubular accumulation was observed.

As a result of the examination of the pathological specimen sections of the brain, cerebellum was normal. Ventricular was normal. Meningitis was not observed. Brain membranes were normal. Normal alignment was observed. Neither bleeding nor necrosis was observed.

#### **4.14.3.2.15. Vevo MicroMarker<sup>®</sup>-15 (RAT – 5E+08 #/ml)**

As a result of the examination of the pathological specimens of the lung, alveolar ventilation in the lung was normal. There was no pleural thickening. Aerating was normal.

As a result of the examination of the pathological specimens of the liver, portal areas were normal in liver sections. Reticular roof was observed as normal. There was no bleeding in the parenchyma. No lubrication was observed. The capsule had the usual appearance. Inflammation and bleeding were not observed in the portal area.

As a result of the examination of the pathological specimens of the kidney, renal glomeruli were of normal shape and size. Basal layer thickening was not observed. Afferent arterioles were normal in appearance. Acute tubular necrosis was not detected. No intra-tubular accumulation was observed.

As a result of the examination of pathological specimen sections of the brain, cerebellum was observed as normal. Ventricular was normal. Meningitis was not

observed. Brain membranes were normal. Normal alignment was observed. Neither bleeding nor necrosis was observed.

#### **4.14.3.2.16. Vevo MicroMarker<sup>®</sup>-16 (RAT – 5E+08 #/ml)**

As a result of the examination of the pathological specimen sections of the lung, focal pneumonia was observed.

As a result of the examination of the pathological specimens of the liver, portal areas were common in liver sections. Reticular roof was observed as normal. There was no bleeding in the parenchyma. No lubrication was observed. The capsule had the usual appearance. Inflammation and bleeding were not observed in the portal area.

As a result of the examination of the pathological specimens of the kidney, renal glomeruli were of normal shape and size. Basal layer thickening was not observed. Afferent arterioles were normal in appearance. Acute tubular necrosis was not detected. No intra-tubular accumulation was observed.

As a result of the examination of the pathological specimen sections of the brain, cerebellum was observed as normal. Ventricular was normal. Meningitis was not observed. Brain membranes were normal. Normal alignment was observed. Neither bleeding nor necrosis was observed.

## CHAPTER 5

### CONCLUSIONS

The overall aims of this dissertation were to conduct *in-vitro* characterization of the microbubble contrast agents produced in our lab and increase their stability under ultrasound.

This chapter gives the conclusions drawn from the studies described in the previous chapters and identifies areas for future work.

#### 5.1. Contributions

The stability of the microbubbles with different shell compositions was investigated under ultrasound. It was found that the stability of the microbubbles decreased under ultrasound when the PEG<sub>40</sub>St concentration was increased in the microbubble shells. Previous experimental studies have shown that the shell stiffness decreases as the PEG<sub>40</sub>St concentration increases (Hosny, Mohamedi et al. 2013). It was hypothesized that the decreased stability of microbubbles could be attributed to decreasing shell stiffness at higher PEG concentrations.

An experimental study was conducted to determine the echogenicity of microbubbles with different shell compositions. An increase in echogenicity was observed with the increase in the amount of PEG<sub>40</sub>St added to the microbubble formulation. It was hypothesized that the echogenicity increase could be attributed to the decreased shell stiffness as the percentage of PEG<sub>40</sub>St content in the microbubble shell is increased.

A new method was developed to estimate the microbubble concentrations with ultrasound. The analysis of time-intensity curves obtained with the bolus injection method revealed that the AUC values was dependent on the experimental conditions such as the injection volume and the microbubble concentration, and that the background intensity values acquired during the measurement could not be ignored in the calculations.

The stability of microbubbles was investigated under hydrostatic pressure. First, the change in size of the plain air bubbles was observed under pressure. In terms of gas

solubility, gas bubbles could not dissolve in a saturated liquid; however, with the increase in pressure, as the saturation level of the liquid decreased as well as the bubble volume, the gas in the bubble began to dissolve, and the bubbles shrank until they disappeared in the medium during the experiment. When the pressure was reduced back to its initial value, the shrunken bubble returned to its original state; the size has increased even more. This demonstrates the importance of the saturation degree of the liquid in which the microbubbles are suspended. When the degree of gas saturation of the medium changes due to temperature or the presence of ions and other molecules, gas exchange through the microbubbles affect the surface morphologies of microbubbles, thus their stability. Hydrostatic pressure studies also showed that the microbubbles recovered their spherical structures at low pressure pulses, in contrast, disappeared in a very short time at high pressure pulses.

B-mode ultrasound intensity of microbubbles was investigated at different ultrasound powers under Doppler ultrasonography, and for the first time, a model was developed to relate the intensity to effective bubble concentration. We calculated acoustic energy thresholds for the destruction of microbubbles and explained a possible destruction mechanism under ultrasound. The acoustic energy thresholds for the soft oscillation of single microbubbles and for the fusion of microbubbles were found to be  $12.43 \text{ mW/cm}^2$  and  $7.53 \text{ mW/cm}^2$ , respectively. The decay constant for the fusion of microbubbles was also found to be  $\sim 3\text{E-}03 \text{ s}^{-1}$ . We anticipated that microbubbles show soft oscillation resulting in acoustically driven dissolution at relatively low powers. At higher powers, two or more microbubbles undergo fusion resulting in rapid fragmentation.

The effect of shell loadings with different masses on the acoustic response and stability of microbubbles was investigated under ultrasound. It was found that both the echogenicity and stability of microbubbles increased with increasing loading on their shells. The increase in echogenicity could be attributed to the fact that microbubbles may perform further expanding and contraction motion by the effect of the repulsive oscillation force created by the extra mass on the microbubbles. Therefore, the greater the extra loading, the higher the acoustic response of the microbubble. A recent study has been shown that the addition of an external layer, streptavidin, significantly increased the stiffness of the microbubbles (Abou-Saleh, Peyman et al. 2013). For our results, it was hypothesized that the increase in stability of microbubbles under

ultrasound could be attributed to the stiffening of the microbubble shell with increasing loading on the microbubble surface. It was concluded that the acoustic propagation has less destructive effects on the microbubbles with stiffer shells at high powers.

In *in-vivo* studies of rat and rabbit models, the microbubbles, when injected into systemic circulation, were shown to pass pulmonary barrier, create echogenicity in the aorta when pumped into the arterial systemic circulation by the heart, and filled all areas of the vascular bed. *In-vivo* studies showed that the acoustic performance of developed microbubbles was comparable to that of commercial standard Vevo MicroMarker<sup>®</sup> contrast agents. No significant toxic effect of 5:5 microbubbles was also observed for the rats and rabbits used in the toxicity studies according to biochemical and pathological analysis.

## **5.2. Future Work**

For a future projection, the mechanical response of the surfaces of microbubbles at different PEG<sub>40</sub>St concentrations can be characterized using atomic force microscopy. The information about the shell stiffness of microbubbles can better explain the decreased stability with increasing PEG<sub>40</sub>St concentration observed in ultrasound tests. Shell morphology of these microbubbles can be visualized under fluorescence microscopy and also through the ultra-high speed imaging system under ultrasound to observe the effect of shell composition on the acoustic response and stability.

Loading on the surface of microbubbles both increased the stability and acoustic response of microbubbles. Novel nanoparticle loaded microbubbles can be engineered for the *in-vivo* applications in which stable microbubbles are needed for a longer period of times. Also, new *in-vivo* models can be developed for the enhanced targeted cancer therapy using the novel nanoparticle loaded microbubbles.

## REFERENCES

- A. Sofferan, R. (2012). *Physics and Principles of Ultrasound*: 9-19.
- Abou-Saleh, R. H., S. A. Peyman, K. Critchley, S. D. Evans and N. H. Thomson (2013). "Nanomechanics of lipid encapsulated microbubbles with functional coatings." Langmuir **29**(12): 4096-4103.
- Abou-Saleh, R. H., M. Swain, S. D. Evans and N. H. Thomson (2014). "Poly(ethylene glycol) Lipid-Shelled Microbubbles: Abundance, Stability, and Mechanical Properties." Langmuir **30**(19): 5557-5563.
- Ali, S. and R. Bittman (1988). "Facile Diacylation of Glycidyl Tosylate - Chiral Synthesis of Symmetric-Chain Glycerophospholipids." Journal of Organic Chemistry **53**(23): 5547-5549.
- Allen, C., N. Dos Santos, R. Gallagher, G. N. C. Chiu, Y. Shu, W. M. Li, S. A. Johnstone, A. S. Janoff, L. D. Mayer, M. S. Webb and M. B. Bally (2002). "Controlling the physical behavior and biological performance of liposome formulations through use of surface grafted poly(ethylene glycol)." Bioscience Reports **22**(2): 225-250.
- Alzaraa, A., G. Gravante, W. Y. Chung, D. Al-Leswas, M. Bruno, A. R. Dennison and D. M. Lloyd (2012). "Targeted microbubbles in the experimental and clinical setting." The American Journal of Surgery **204**(3): 355-366.
- Azhari, H. (2010). Basics of biomedical ultrasound for engineers, John Wiley & Sons.
- Azmin, M. (2016). Engineering Ultrasound Contrast Agents for Increased Stability and Nonlinearity, UCL (University College London).
- Bloch, S. H., M. Wan, P. A. Dayton and K. W. Ferrara (2004). "Optical observation of lipid- and polymer-shelled ultrasound microbubble contrast agents." Applied Physics Letters **84**(4): 631-633.
- Bohmer, M. R., A. L. Klibanov, K. Tiemann, C. S. Hall, H. Gruell and O. C. Steinbach (2009). "Ultrasound triggered image-guided drug delivery." European Journal of Radiology **70**(2): 242-253.
- Borden, M. (2009). "Nanostructural features on stable microbubbles." Soft Matter **5**(4): 716-720.
- Borden, M. A., C. F. Caskey, E. Little, R. J. Gillies and K. W. Ferrara (2007). "DNA and polylysine adsorption and multilayer construction onto cationic lipid-coated microbubbles." Langmuir **23**(18): 9401-9408.
- Borden, M. A., P. Dayton, S. K. Zhao and K. W. Ferrara (2004). "Physico-chemical properties of the microbubble lipid shell - Composition, microstructure & properties of targeted ultrasound contrast agents." 2004 IEEE Ultrasonics Symposium, Vols 1-3: 20-23.

- Borden, M. A., D. E. Kruse, C. F. Caskey, S. K. Zhao, P. A. Dayton and K. W. Ferrara (2005). "Influence of lipid shell physicochemical properties on ultrasound-induced microbubble destruction." Ieee Transactions on Ultrasonics Ferroelectrics and Frequency Control **52**(11): 1992-2002.
- Borden, M. A. and M. L. Longo (2001). "Effect of lipid type on stability of air-filled microbubbles." Abstracts of Papers of the American Chemical Society **221**: U339-U339.
- Borden, M. A. and M. L. Longo (2002). "The dependence of lipid-coated microbubble dissolution behavior on acyl chain length." Biophysical Journal **82**(1): 35a-35a.
- Borden, M. A. and M. L. Longo (2002). "Dissolution behavior of lipid monolayer-coated, air-filled microbubbles: Effect of lipid hydrophobic chain length." Langmuir **18**(24): 9225-9233.
- Borden, M. A. and M. L. Longo (2004). "Oxygen permeability of fully condensed lipid monolayers." Journal of Physical Chemistry B **108**(19): 6009-6016.
- Borden, M. A., G. V. Martinez, J. Ricker, N. Tsvetkova, M. Longo, R. J. Gillies, P. A. Dayton and K. W. Ferrara (2006). "Lateral phase separation in lipid-coated microbubbles." Langmuir **22**(9): 4291-4297.
- Borden, M. A., G. Pu, M. L. Longo, P. A. Dayton and K. W. Ferrara (2005). "Phase behavior and transport properties of the lipid-monolayer shell of a microbubble." Abstracts of Papers of the American Chemical Society **230**: U1072-U1073.
- Borden, M. A., G. Pu, G. Runner and M. L. Longo (2003). "Transport properties and surface morphology of the microbubble lipid shell." Biophysical Journal **84**(2): 294a-294a.
- Borden, M. A., G. Pu, G. J. Runner and M. L. Longo (2004). "Surface phase behavior and microstructure of lipid/PEG-emulsifier monolayer-coated microbubbles." Colloids and Surfaces B-Biointerfaces **35**(3-4): 209-223.
- Brussler, J., E. Marxer, A. Becker, R. Schubert, J. Schummelfeder, C. Nimsky and U. Bakowsky (2014). "Correlation of structure and echogenicity of nanoscaled ultrasound contrast agents in vitro." Colloids and Surfaces B-Biointerfaces **117**: 206-215.
- Burns, P. N., J. E. Powers, D. H. Simpson, A. Brezina, A. Kolin, C. T. Chin, V. Uhlendorf and T. Fritsch (1994). "Harmonic Power Mode Doppler Using Microbubble Contrast Agents - an Improved Method for Small Vessel Flow Imaging." 1994 Ieee Ultrasonics Symposium Proceedings, Vols 1-3: 1547-1550.
- Chaline, J., N. Jimenez, A. Mehrem, A. Bouakaz, S. Dos Santos and V. J. Sanchez-Morcillo (2015). "Macroscopic acousto-mechanical analogy of a microbubble." Journal of the Acoustical Society of America **138**(6): 3600-3606.
- Chatterjee, D., P. Jain and K. Sarkar (2005). "Ultrasound-mediated destruction of contrast microbubbles used for medical imaging and drug delivery." Physics of Fluids **17**(10).

- Chen, C. C. and M. A. Borden (2011). "The role of poly(ethylene glycol) brush architecture in complement activation on targeted microbubble surfaces." Biomaterials **32**(27): 6579-6587.
- Chen, W.-S., T. J. Matula, A. A. Brayman and L. A. Crum (2003). "A comparison of the fragmentation thresholds and inertial cavitation doses of different ultrasound contrast agents." The Journal of the Acoustical Society of America **113**(1): 643-651.
- Chomas, J. E., P. Dayton, J. Allen, K. Morgan and K. W. Ferrara (2001). "Mechanisms of contrast agent destruction." Ieee Transactions on Ultrasonics Ferroelectrics and Frequency Control **48**(1): 232-248.
- Chomas, J. E., P. Dayton, J. Allen, K. Morgan and K. W. Ferrara (2001). "Mechanisms of contrast agent destruction." IEEE transactions on ultrasonics, ferroelectrics, and frequency control **48**(1): 232-248.
- Chomas, J. E., P. Dayton, D. May and K. Ferrara (2001). "Threshold of fragmentation for ultrasonic contrast agents." Journal of Biomedical Optics **6**(2): 141-150.
- Chomas, J. E., P. A. Dayton, D. May, J. Allen, A. Klibanov and K. Ferrara (2000). "Optical observation of contrast agent destruction." Applied Physics Letters **77**(7): 1056-1058.
- Church, C. C. (1988). "Prediction of Rectified Diffusion during Nonlinear Bubble Pulsations at Biomedical Frequencies." Journal of the Acoustical Society of America **83**(6): 2210-2217.
- Correas, J. M., L. Bridal, A. Lesavre, A. Mejean, M. Claudon and O. Helenon (2001). "Ultrasound contrast agents: properties, principles of action, tolerance, and artifacts." European Radiology **11**(8): 1316-1328.
- Cox, D. J. and J. L. Thomas (2010). "Ultrasound-Induced Dissolution of Lipid-Coated and Uncoated Gas Bubbles." Langmuir **26**(18): 14774-14781.
- Crum, L. (1984). "Acoustic cavitation series: part five rectified diffusion." Ultrasonics **22**(5): 215-223.
- Curcio, M., B. Blanco-Fernandez, L. Diaz-Gomez, A. Concheiro and C. Alvarez-Lorenzo (2015). "Hydrophobically Modified Keratin Vesicles for GSH-Responsive Intracellular Drug Release." Bioconjugate Chemistry **26**(9): 1900-1907.
- Dan, N. (1994). "Brush Adsorption from Polydisperse Solutions." Macromolecules **27**(8): 2310-2312.
- Dayton, P., A. Klibanov, G. Brandenburger and K. Ferrara (1999). "Acoustic radiation force in vivo: A mechanism to assist targeting of microbubbles." Ultrasound in Medicine and Biology **25**(8): 1195-1201.
- Dayton, P. A. and K. W. Ferrara (2002). "Targeted imaging using ultrasound." Journal of Magnetic Resonance Imaging **16**(4): 362-377.

Dayton, P. A., K. E. Morgan, A. L. Klibanov, G. Brandenburger, K. R. Nightingale and K. W. Ferrara (1997). "A preliminary evaluation of the effects of primary and secondary radiation forces on acoustic contrast agents." IEEE transactions on ultrasonics, ferroelectrics, and frequency control **44**(6): 1264-1277.

Dayton, P. A., K. E. Morgan, A. L. Klibanov, G. H. Brandenburger and K. W. Ferrara (1999). "Optical and acoustical observations of the effects of ultrasound on contrast agents." Ieee Transactions on Ultrasonics Ferroelectrics and Frequency Control **46**(1): 220-232.

De Jong, N., A. Bouakaz and P. Frinking (2002). "Basic acoustic properties of microbubbles." Echocardiography **19**(3): 229-240.

de Jong, N., M. Emmer, A. van Wamel and M. Versluis (2009). "Ultrasonic characterization of ultrasound contrast agents." Medical & Biological Engineering & Computing **47**(8): 861-873.

de Jong, N., L. Hoff, T. Skotland and N. Bom (1992). "Absorption and scatter of encapsulated gas filled microspheres: theoretical considerations and some measurements." Ultrasonics **30**(2): 95-103.

De Jong, N., F. Ten Cate, C. Lancee, J. Roelandt and N. Bom (1991). "Principles and recent developments in ultrasound contrast agents." Ultrasonics **29**(4): 324-330.

Degennes, P. G. (1987). "Polymers at an Interface - a Simplified View." Advances in Colloid and Interface Science **27**(3-4): 189-209.

Dejong, N. and L. Hoff (1993). "Ultrasound Scattering Properties of Alburnex Microspheres." Ultrasonics **31**(3): 175-181.

Dejong, N., L. Hoff, T. Skotland and N. Bom (1992). "Absorption and Scatter of Encapsulated Gas Filled Microspheres - Theoretical Considerations and Some Measurements." Ultrasonics **30**(2): 95-103.

Dejong, N., F. J. Tencate, C. T. Lancee, J. R. T. C. Roelandt and N. Bom (1991). "Principles and Recent Developments in Ultrasound Contrast Agents." Ultrasonics **29**(4): 324-330.

Dicker, S., M. Mleczko, G. Schmitz and S. Wrenn (2010). "Determination of microbubble cavitation threshold pressure as function of shell chemistry." Bubble Science, Engineering & Technology **2**(2): 55-64.

Dicker, S., M. Mleczko, M. Siepmann, N. Wallace, Y. Sunny, C. R. Bawiec, G. Schmitz, P. Lewin and S. P. Wrenn (2013). "Influence of Shell Composition on the Resonance Frequency of Microbubble Contrast Agents." Ultrasound in Medicine and Biology **39**(7): 1292-1302.

Doinikov, A. A. (2003). "Acoustic radiation forces: Classical theory and recent advances." Recent Res Devel Acoustics **1**: 39-67.

- Doinikov, A. A., J. F. Haac and P. A. Dayton (2009). "Resonance frequencies of lipid-shelled microbubbles in the regime of nonlinear oscillations." Ultrasonics **49**(2): 263-268.
- Dollet, B., S. M. Van Der Meer, V. Garbin, N. De Jong, D. Lohse and M. Versluis (2008). "Nonspherical oscillations of ultrasound contrast agent microbubbles." Ultrasound in medicine & biology **34**(9): 1465-1473.
- ElBayoumi, T. A., V. P. Torchilin and V. Weissig (2010). "Liposomes: methods and protocols, volume 1: pharmaceutical nanocarriers."
- Epstein, P. S. and M. S. Plesset (1950). "On the stability of gas bubbles in liquid- gas solutions." The Journal of Chemical Physics **18**(11): 1505-1509.
- Escoffre, J. M., C. Mannaris, B. Geers, A. Novell, I. Lentacker, M. Averkiou and A. Bouakaz (2013). "Doxorubicin Liposome-Loaded Microbubbles for Contrast Imaging and Ultrasound-Triggered Drug Delivery." Ieee Transactions on Ultrasonics Ferroelectrics and Frequency Control **60**(1): 78-87.
- Feinstein, S. B., M. W. Keller, R. E. Kerber, B. Vandenberg, J. Hoyte, C. Kutruff, J. Bingle, T. D. Fraker, R. Chappell and A. H. Welsh (1989). "Sonicated echocardiographic contrast agents: reproducibility studies." Journal of the American Society of Echocardiography **2**(2): 125-131.
- Feinstein, S. B., P. M. Shah, R. J. Bing, S. Meerbaum, E. Corday, B. L. Chang, G. Santillan and Y. Fujibayashi (1984). "Microbubble Dynamics Visualized in the Intact Capillary Circulation." Journal of the American College of Cardiology **4**(3): 595-600.
- Ferrara, K., R. Pollard and M. Borden (2007). "Ultrasound microbubble contrast agents: Fundamentals and application to gene and drug delivery." Annual Review of Biomedical Engineering **9**: 415-447.
- Ferrara, K. W., M. A. Borden and H. Zhang (2009). "Lipid-Shelled Vehicles: Engineering for Ultrasound Molecular Imaging and Drug Delivery." Accounts of Chemical Research **42**(7): 881-892.
- Feshitan, J. A., C. C. Chen, J. J. Kwan and M. A. Borden (2009). "Microbubble size isolation by differential centrifugation." Journal of Colloid and Interface Science **329**(2): 316-324.
- Freeman, S. (2017). Biological science, Pearson Education.
- Frinking, P. J. A. and N. de Jong (1998). "Acoustic modeling of shell-encapsulated gas bubbles." Ultrasound in Medicine and Biology **24**(4): 523-533.
- Fyrillas, M. M. and A. J. Szeri (1995). "Dissolution or Growth of Soluble Spherical Oscillating Bubbles - the Effect of Surfactants." Journal of Fluid Mechanics **289**: 295-314.

- Garg, S., A. A. Thomas and M. A. Borden (2013). "The effect of lipid monolayer in-plane rigidity on in vivo microbubble circulation persistence." Biomaterials **34**(28): 6862-6870.
- Gerber, F., M. P. Krafft, G. Waton and T. F. Vandamme (2006). "Microbubbles with exceptionally long life - synergy between shell and internal phase components." New Journal of Chemistry **30**(4): 524-527.
- Gramiak, R. and P. Shah (1968). "Echocardiography of the Aortic Root." Investigative Radiology **3**: 356-366.
- Guidi, F., H. J. Vos, R. Mori, N. De Jong and P. Tortoli (2009). "Microbubble characterization through acoustically induced deflation." IEEE transactions on ultrasonics, ferroelectrics, and frequency control **57**(1): 193-202.
- Guo, X. S., Q. Li, Z. Zhang, D. Zhang and J. Tu (2013). "Investigation on the inertial cavitation threshold and shell properties of commercialized ultrasound contrast agent microbubbles." Journal of the Acoustical Society of America **134**(2): 1622-1631.
- Hauff, P., M. Reinhardt and S. Foster (2008). "Ultrasound Basics." Handbook of experimental pharmacology **185**: 91-107.
- Helfield, B., X. C. Chen, B. Qin and F. S. Villanueva (2016). "Individual lipid encapsulated microbubble radial oscillations: Effects of fluid viscosity." Journal of the Acoustical Society of America **139**(1): 204-214.
- Hernot, S. and A. L. Klibanov (2008). "Microbubbles in ultrasound-triggered drug and gene delivery." Advanced drug delivery reviews **60**(10): 1153-1166.
- Hilman, J., R.-R. Hoffmann, W. Muetzel and I. Zimmermann (1984). Carrier liquid solutions for the production of gas microbubbles, preparation thereof, and use thereof as contrast medium for ultrasonic diagnostics, Google Patents.
- Hoff, L., P. C. Sontum and B. Hoff (1996). "Acoustic properties of shell-encapsulated, gas-filled ultrasound contrast agents." 1996 Ieee Ultrasonics Symposium, Proceedings, Vols 1 and 2: 1441-1444.
- Hosny, N. A., G. Mohamedi, P. Rademeyer, J. Owen, Y. Wu, M.-X. Tang, R. J. Eckersley, E. Stride and M. K. Kuimova (2013). "Mapping microbubble viscosity using fluorescence lifetime imaging of molecular rotors." Proceedings of the National Academy of Sciences **110**(23): 9225-9230.
- Hosny, N. A., G. Mohamedi, P. Rademeyer, J. Owen, Y. L. Wu, M. X. Tang, R. J. Eckersley, E. Stride and M. K. Kuimova (2013). "Mapping microbubble viscosity using fluorescence lifetime imaging of molecular rotors." Proceedings of the National Academy of Sciences of the United States of America **110**(23): 9225-9230.
- Hyvelin, J. M., I. Tardy, C. Arbogast, M. Costa, P. Emmel, A. Helbert, M. Theraulaz, A. D. Nunn and F. Tranquart (2013). "Use of Ultrasound Contrast Agent Microbubbles in Preclinical Research Recommendations for Small Animal Imaging." Investigative Radiology **48**(8): 570-583.

- Immordino, M. L., F. Dosio and L. Cattel (2006). "Stealth liposomes: review of the basic science, rationale, and clinical applications, existing and potential." International Journal of Nanomedicine **1**(3): 297-315.
- Israelachvili, J. N., D. J. Mitchell and B. W. Ninham (1976). "Theory of Self-Assembly of Hydrocarbon Amphiphiles into Micelles and Bilayers." Journal of the Chemical Society-Faraday Transactions II **72**: 1525-1568.
- Kabalnov, A., J. Bradley, S. Flaim, D. Klein, T. Pelura, B. Peters, S. Otto, J. Reynolds, E. Schutt and J. Weers (1998). "Dissolution of multicomponent microbubbles in the bloodstream: 2. Experiment." Ultrasound in Medicine and Biology **24**(5): 751-760.
- Kabalnov, A., D. Klein, T. Pelura, E. Schutt and J. Weers (1998). "Dissolution of multicomponent microbubbles in the bloodstream: 1. Theory." Ultrasound in medicine & biology **24**(5): 739-749.
- Kabalnov, A., D. Klein, T. Pelura, E. Schutt and J. Weers (1998). "Dissolution of multicomponent microbubbles in the bloodstream: 1. Theory." Ultrasound in Medicine and Biology **24**(5): 739-749.
- Kane, S. A., N. Donaldson and B. Gelman (2009). Introduction to physics in modern medicine, CRC Press.
- Kasprzak, J. D. and F. J. Ten Cate (1998). "New ultrasound contrast agents for left ventricular and myocardial opacification." Herz **23**(8): 474-482.
- Kenworthy, A. K., K. Hristova, D. Needham and T. J. McIntosh (1995). "Range and Magnitude of the Steric Pressure between Bilayers Containing Phospholipids with Covalently Attached Poly(Ethylene Glycol)." Biophysical Journal **68**(5): 1921-1936.
- Kenworthy, A. K., S. A. Simon and T. J. McIntosh (1995). "Structure and Phase-Behavior of Lipid Suspensions Containing Phospholipids with Covalently Attached Poly(Ethylene Glycol)." Biophysical Journal **68**(5): 1903-1920.
- Kheirrolomoom, A., P. A. Dayton, A. F. Lum, E. Little, E. E. Paoli, H. Zheng and K. W. Ferrara (2007). "Acoustically-active microbubbles conjugated to liposomes: characterization of a proposed drug delivery vehicle." Journal of Controlled Release **118**(3): 275-284.
- Kheirrolomoom, A., P. A. Dayton, A. F. H. Lum, E. Little, E. E. Paoli, H. R. Zheng and K. W. Ferrara (2007). "Acoustically-active microbubbles conjugated to liposomes: Characterization of a proposed drug delivery vehicle." Journal of Controlled Release **118**(3): 275-284.
- Kilic, S. and E. S. Bolukcu (2018). "Phase behavior of DSPC/PEG40St mixtures at higher emulsifier contents." Colloids and Surfaces B: Biointerfaces **171**: 368-376.
- Kilic, S. and E. S. Bolukcu (2018). "Phase behavior of DSPC/PEG(40)St mixtures at higher emulsifier contents." Colloids and Surfaces B-Biointerfaces **171**: 368-376.

- Kilic, S., E. D. Lu, E. Tom, J. Gretton, W. R. Wagner and F. S. Villanueva (2005). "Modifications of lipid microbubble shell composition affect intravascular kinetics." Journal of the American College of Cardiology **45**(3): 271a-272a.
- Kim, D. H., M. J. Costello, P. B. Duncan and D. Needham (2003). "Mechanical properties and microstructure of polycrystalline phospholipid monolayer shells: Novel solid microparticles." Langmuir **19**(20): 8455-8466.
- Kim, K., C. Kim and Y. Byun (2004). "Biostability and biocompatibility of a surface-grafted phospholipid monolayer on a solid substrate." Biomaterials **25**(1): 33-41.
- Klibanov, A. L. (1999). "Targeted delivery of gas-filled microspheres, contrast agents for ultrasound imaging." Advanced Drug Delivery Reviews **37**(1-3): 139-157.
- Klibanov, A. L. (2002). "Ultrasound contrast agents: Development of the field and current status." Contrast Agents II **222**: 73-106.
- Klibanov, A. L., K. W. Ferrara, M. S. Hughes, J. H. Wible Jr, J. K. Wojdyla, P. A. Dayton, K. E. Morgan and G. H. Brandenburger (1998). "Direct video-microscopic observation of the dynamic effects of medical ultrasound on ultrasound contrast microspheres." Investigative radiology **33**(12): 863-870.
- Klibanov, A. L., M. S. Hughes, J. K. Wojdyla, J. H. Wible and G. H. Brandenburger (2002). "Destruction of contrast agent microbubbles in the ultrasound field: The fate of the microbubble shell and the importance of the bubble gas content." Academic Radiology **9**: S41-S45.
- Kozlov, M. M., D. Lichtenberg and D. Andelman (1997). "Shape of phospholipid/surfactant mixed micelles: Cylinders or disks? Theoretical analysis." Journal of Physical Chemistry B **101**(33): 6600-6606.
- Kudo, N., K. Okada and K. Yamamoto (2009). "Sonoporation by Single-Shot Pulsed Ultrasound with Microbubbles Adjacent to Cells." Biophysical Journal **96**(12): 4866-4876.
- Kwan, J. J. and M. A. Borden (2010). "Microbubble Dissolution in a Multigas Environment." Langmuir **26**(9): 6542-6548.
- Kwan, J. J. and M. A. Borden (2012). "Lipid monolayer collapse and microbubble stability." Advances in Colloid and Interface Science **183**: 82-99.
- Lampaskis, M. and M. Averkiou (2010). "Investigation of the Relationship of Nonlinear Backscattered Ultrasound Intensity with Microbubble Concentration at Low Mi." Ultrasound in Medicine and Biology **36**(2): 306-312.
- Lee, C. P. and T. G. Wang (1993). "Acoustic Radiation Force on a Bubble." Journal of the Acoustical Society of America **93**(3): 1637-1640.
- Lentacker, I., S. C. De Smedt and N. N. Sanders (2009). "Drug loaded microbubble design for ultrasound triggered delivery." Soft Matter **5**(11): 2161-2170.

- Leong-Poi, H., J. Song, S. J. Rim, J. Christiansen, S. Kaul and J. R. Lindner (2002). "Influence of microbubble shell properties on ultrasound signal: Implications for low-power perfusion imaging." Journal of the American Society of Echocardiography **15**(10): 1269-1276.
- Lozano, M. M. and M. L. Longo (2009). "Microbubbles Coated with Disaturated Lipids and DSPE-PEG2000: Phase Behavior, Collapse Transitions, and Permeability." Langmuir **25**(6): 3705-3712.
- Luan, Y., T. Faez, E. Gelderblom, I. Skachkov, B. Geers, I. Lentacker, T. van der Steen, M. Versluis and N. de Jong (2012). "Acoustical Properties of Individual Liposome-Loaded Microbubbles." Ultrasound in Medicine and Biology **38**(12): 2174-2185.
- Luan, Y., T. Faez, E. Gelderblom, I. Skachkov, B. Geers, I. Lentacker, T. van der Steen, M. Versluis and N. de Jong (2012). "Acoustical properties of individual liposome-loaded microbubbles." Ultrasound in medicine & biology **38**(12): 2174-2185.
- Mann, D. L., D. P. Zipes, P. Libby and R. O. Bonow (2014). Braunwald's heart disease e-book: a textbook of cardiovascular medicine, Elsevier Health Sciences.
- Marmottant, P., S. van der Meer, M. Emmer, M. Versluis, N. de Jong, S. Hilgenfeldt and D. Lohse (2005). "A model for large amplitude oscillations of coated bubbles accounting for buckling and rupture." Journal of the Acoustical Society of America **118**(6): 3499-3505.
- May, D. J., J. S. Allen and K. W. Ferrara (2002). "Dynamics and fragmentation of thick-shelled microbubbles." IEEE transactions on ultrasonics, ferroelectrics, and frequency control **49**(10): 1400-1410.
- May, D. J., J. S. Allen and K. W. Ferrara (2002). "Dynamics and fragmentation of thick-shelled microbubbles." Ieee Transactions on Ultrasonics Ferroelectrics and Frequency Control **49**(10): 1400-1410.
- Mayer, S. and P. A. Grayburn (2001). "Myocardial contrast agents: Recent advances and future directions." Progress in Cardiovascular Diseases **44**(1): 33-44.
- McLaughlan, J., N. Ingram, R. Abou-Saleh, S. Harput, T. Evans, S. Evans, L. Coletta and S. Freear (2013). "High-Frequency Subharmonic Imaging of Liposome-Loaded Microbubbles." 2013 Ieee International Ultrasonics Symposium (Ius): 1493-1496.
- McLaughlan, J., N. Ingram, R. Abou-Saleh, S. Harput, T. Evans, S. Evans, L. Coletta and S. Freear (2013). High-frequency subharmonic imaging of liposome-loaded microbubbles. 2013 IEEE International Ultrasonics Symposium (IUS), IEEE.
- Meltzer, R. S., O. E. H. Sartorius, C. T. Lancee, P. W. Serruys, P. D. Verdouw, C. E. Essed and J. Roelandt (1981). "Transmission of Ultrasonic Contrast through the Lungs." Ultrasound in Medicine and Biology **7**(4): 377-384.
- Mleczo, M., S. M. Dicker, S. P. Wrenn and G. Schmitz (2012). "Influence of Microbubble Shell Chemistry on the Destruction Threshold of Ultrasound Contrast Agent Microbubbles." Acoustical Imaging, Vol 31 **31**: 91-101.

- Mohamedi, G. (2014). Engineering the surface properties of microbubbles for biomedical applications.
- Mohamedi, G., P. Rademeyer, M. Azmin, M. Edirisinghe, J. Perez-Juste, I. Pastoriza-Santos, L. Liz-Marzan and E. Stride (2013). "Investigating the acoustic response of gold nanoparticle coated microbubbles." Abstracts of Papers of the American Chemical Society **245**.
- Monteiro, N., A. Martins, R. L. Reis and N. M. Neves (2014). "Liposomes in tissue engineering and regenerative medicine." Journal of the Royal Society Interface **11**(101).
- Moran, C. M., T. Anderson, S. D. Pye, V. Sboros and W. N. McDicken (2000). "Quantification of microbubble destruction of three fluorocarbon-filled ultrasonic contrast agents." Ultrasound in Medicine and Biology **26**(4): 629-639.
- MorAvi, V., K. A. Robinson, S. G. Shroff and R. M. Lang (1997). "Effects of temperature on Alunex and FS069 echocardiographic contrast agents: In vitro investigation using ultrasonic irradiation." Echocardiography-a Journal of Cardiovascular Ultrasound and Allied Techniques **14**(1): 39-49.
- Moriyasu, F. and K. Itoh (2009). "Efficacy of Perflubutane Microbubble-Enhanced Ultrasound in the Characterization and Detection of Focal Liver Lesions: Phase 3 Multicenter Clinical Trial." American Journal of Roentgenology **193**(1): 86-95.
- Morris, J., E. P. Ingenito, L. Mark, R. D. Kamm and M. Johnson (2001). "Dynamic behavior of lung surfactant." Journal of Biomechanical Engineering-Transactions of the Asme **123**(1): 106-113.
- Mulvana, H., E. Stride, J. V. Hajnal and R. J. Eckersley (2010). "Temperature Dependent Behavior of Ultrasound Contrast Agents." Ultrasound in Medicine and Biology **36**(6): 925-934.
- Mulvana, H., E. Stride, M. X. Tang, J. V. Hajnal and R. Eckersley (2011). "Temperature-Dependent Differences in the Nonlinear Acoustic Behavior of Ultrasound Contrast Agents Revealed by High-Speed Imaging and Bulk Acoustics." Ultrasound in Medicine and Biology **37**(9): 1509-1517.
- Nanda, N. C., P. M. Shah and R. Gramiak (1976). "Echocardiographic Evaluation of Tricuspid-Valve Incompetence by Contrast Injections." Clinical Research **24**(3): A233-A233.
- Needles, A., M. Arditi, N. G. Rognin, J. Mehi, T. Coulthard, C. Bilan-Tracey, E. Gaud, P. Frinking, D. Hirson and F. S. Foster (2010). "Nonlinear Contrast Imaging with an Array-Based Micro-Ultrasound System." Ultrasound in Medicine and Biology **36**(12): 2097-2106.
- O'Brien, J. P., N. Ovenden and E. Stride (2011). "Accounting for the stability of microbubbles to multi-pulse excitation using a lipid-shedding model." Journal of the Acoustical Society of America **130**(4): E1180-E1185.

- Ophir, J. and K. J. Parker (1989). "Contrast Agents in Diagnostic Ultrasound." Ultrasound in Medicine and Biology **15**(4): 319-333.
- Ota, T., N. D. Hillman, D. Craig, J. Kisslo and P. K. Smith (1997). "Contrast echocardiography: Influence of ultrasonic machine settings, mixing conditions, and pressurization on pixel intensity and microsphere size of Albunex solutions in vitro." Journal of the American Society of Echocardiography **10**(1): 31-40.
- Overvelde, M., V. Garbin, J. Sijl, B. Dollet, N. de Jong, D. Lohse and M. Versluis (2010). "Nonlinear Shell Behavior of Phospholipid-Coated Microbubbles." Ultrasound in Medicine and Biology **36**(12): 2080-2092.
- Owen, J., S. Kamila, S. Shrivastava, D. Carugo, J. Bernardino de la Serna, C. Mannaris, V. Pereno, R. Browning, E. Beguin and A. P. McHale (2018). "The Role of PEG-40-stearate in the Production, Morphology, and Stability of Microbubbles." Langmuir.
- Parrales, M. A., J. M. Fernandez, M. Perez-Saborid, J. A. Kopechek and T. M. Porter (2014). "Acoustic characterization of monodisperse lipid-coated microbubbles: Relationship between size and shell viscoelastic properties." Journal of the Acoustical Society of America **136**(3): 1077-1084.
- Plesset, M. S. (1949). "The dynamics of cavitation bubbles." Journal of applied mechanics **16**: 277-282.
- Porter, T. M., D. A. Smith and C. K. Holland (2006). "Acoustic techniques for assessing the Optison destruction threshold." Journal of ultrasound in medicine **25**(12): 1519-1529.
- Porter, T. M., D. A. B. Smith and C. K. Holland (2006). "Acoustic techniques for assessing the Optison destruction threshold." Journal of Ultrasound in Medicine **25**(12): 1519-1529.
- Postema, M., A. Bouakaz, F. J. ten Cate, G. Schmitz, N. De Jong and A. van Wamel (2006). "Nitric oxide delivery by ultrasonic cracking: Some limitations." Ultrasonics **44**: E109-E113.
- Postema, M., A. Van Wamel, C. T. Lancee and N. De Jong (2004). "Ultrasound-induced encapsulated microbubble phenomena." Ultrasound in Medicine and Biology **30**(6): 827-840.
- Pu, G., M. A. Borden and M. L. Longo (2006). "Collapse and shedding transitions in binary lipid monolayers coating microbubbles." Langmuir **22**(7): 2993-2999.
- Pu, G., M. L. Longo and M. A. Borden (2005). "Effect of microstructure on molecular oxygen permeation through condensed phospholipid monolayers." Journal of the American Chemical Society **127**(18): 6524-6525.
- Qin, S., C. F. Caskey and K. W. Ferrara (2009). "Ultrasound contrast microbubbles in imaging and therapy: physical principles and engineering." Physics in medicine & biology **54**(6): R27.

- Qin, S. P., C. F. Caskey and K. W. Ferrara (2009). "Ultrasound contrast microbubbles in imaging and therapy: physical principles and engineering." Physics in Medicine and Biology **54**(6): R27-R57.
- Rayleigh, L. (1917). On the pressure developed in a liquid during the collapse of a spherical cavity: Philosophical Magazine Series 6, 34, 94–98.
- Sboros, V., C. M. Moran, T. Anderson, S. D. Pye, I. C. Macleod, A. M. Millar and W. N. McDicken (2000). "Evaluation of an experimental system for the in vitro assessment of ultrasonic contrast agents." Ultrasound in Medicine and Biology **26**(1): 105-111.
- Schutt, C. E., S. D. Ibsen, M. J. Benchimol, M. J. Hsu and S. C. Esener (2014). "Manipulating Nanoscale Features on the Surface of Dye-Loaded Microbubbles to Increase Their Ultrasound-Modulated Fluorescence Output." Small **10**(16): 3316-3324.
- Schutt, E. G., D. H. Klein, R. M. Mattrey and J. G. Riess (2003). "Injectable microbubbles as contrast agents for diagnostic ultrasound imaging: the key role of perfluorochemicals." Angewandte Chemie International Edition **42**(28): 3218-3235.
- Schutt, E. G., D. H. Klein, R. M. Mattrey and J. G. Riess (2003). "Injectable microbubbles as contrast agents for diagnostic ultrasound imaging: The key role of perfluorochemicals." Angewandte Chemie-International Edition **42**(28): 3218-3235.
- Segers, T., L. De Rond, N. de Jong, M. Borden and M. Versluis (2016). "Stability of monodisperse phospholipid-coated microbubbles formed by flow-focusing at high production rates." Langmuir **32**(16): 3937-3944.
- Sen, T., O. Tufekcioglu and Y. Koza (2015). "Mechanical index." Anatolian Journal of Cardiology **15**(4): 334-336.
- Sennoga, C. A., J. S. M. Yeh, J. Alter, E. Stride, P. Nihoyannopoulos, J. M. Seddon, D. O. Haskard, J. V. Hajnal, M. X. Tang and R. J. Eckersley (2012). "Evaluation of Methods for Sizing and Counting of Ultrasound Contrast Agents." Ultrasound in Medicine and Biology **38**(5): 834-845.
- Sharma, A. and U. S. Sharma (1997). "Liposomes in drug delivery: progress and limitations." International Journal of Pharmaceutics **154**(2): 123-140.
- Shen, Y. Y., R. L. Powell and M. L. Longo (2008). "Influence of the dissolution rate on the collapse and shedding behavior of monostearin/monopalmitin-rich coated microbubbles." Langmuir **24**(18): 10035-10040.
- Sijl, J., M. Overvelde, B. Dollet, V. Garbin, N. de Jong, D. Lohse and M. Versluis (2011). "'Compression-only' behavior: A second-order nonlinear response of ultrasound contrast agent microbubbles." Journal of the Acoustical Society of America **129**(4): 1729-1739.
- Sijl, J., M. Overvelde, B. Dollet, V. Garbin, N. de Jong, D. Lohse and M. Versluis (2011). "'Compression-only' behavior: A second-order nonlinear response of ultrasound contrast agent microbubbles." The Journal of the Acoustical Society of America **129**(4): 1729-1739.

- Sirsi, S. and M. Borden (2009). "Microbubble compositions, properties and biomedical applications." Bubble Science, Engineering & Technology **1**(1-2): 3-17.
- Sirsi, S. R. and M. A. Borden (2014). "State-of-the-art materials for ultrasound-triggered drug delivery." Advanced drug delivery reviews **72**: 3-14.
- Stride, E. and M. Edirisinghe (2008). "Novel microbubble preparation technologies." Soft matter **4**(12): 2350-2359.
- Stride, E. and N. Saffari (2003). "Microbubble ultrasound contrast agents: a review." Proceedings of the Institution of Mechanical Engineers Part H-Journal of Engineering in Medicine **217**(H6): 429-447.
- Stride, E. P. and C. C. Coussios (2010). "Cavitation and contrast: the use of bubbles in ultrasound imaging and therapy." Proceedings of the Institution of Mechanical Engineers Part H-Journal of Engineering in Medicine **224**(H2): 171-191.
- Strouthos, C., M. Lampaskis, V. Sboros, A. McNeilly and M. Averkiou (2010). "Indicator Dilution Models for the Quantification of Microvascular Blood Flow With Bolus Administration of Ultrasound Contrast Agents." Ieee Transactions on Ultrasonics Ferroelectrics and Frequency Control **57**(6): 1296-1310.
- Strouthos, C., M. Lampaskis, V. Sboros, A. McNeilly and M. Averkiou (2010). "Indicator dilution models for the quantification of microvascular blood flow with bolus administration of ultrasound contrast agents." IEEE transactions on ultrasonics, ferroelectrics, and frequency control **57**(6).
- Suzuki, R., Y. Oda, N. Utoguchi and K. Maruyama (2011). "Progress in the development of ultrasound-mediated gene delivery systems utilizing nano- and microbubbles." Journal of Controlled Release **149**(1): 36-41.
- Swanson, E. J., V. Mohan, J. Kheir and M. A. Borden (2010). "Phospholipid-Stabilized Microbubble Foam for Injectable Oxygen Delivery." Langmuir **26**(20): 15726-15729.
- Szjijarto, C., S. Rossi, G. Waton and M. P. Krafft (2012). "Effects of Perfluorocarbon Gases on the Size and Stability Characteristics of Phospholipid-Coated Microbubbles: Osmotic Effect versus Interfacial Film Stabilization." Langmuir **28**(2): 1182-1189.
- Talu, E., K. Hettiarachchi, R. L. Powell, A. P. Lee, P. A. Dayton and M. L. Longo (2008). "Maintaining monodispersity in a microbubble population formed by flow-focusing." Langmuir **24**(5): 1745-1749.
- Tang, M. X., H. Mulvana, T. Gauthier, A. K. P. Lim, D. O. Cosgrove, R. J. Eckersley and E. Stride (2011). "Quantitative contrast-enhanced ultrasound imaging: a review of sources of variability." Interface Focus **1**(4): 520-539.
- Tinkov, S., R. Bekeradjian, G. Winter and C. Coester (2009). "Microbubbles as Ultrasound Triggered Drug Carriers." Journal of Pharmaceutical Sciences **98**(6): 1935-1961.

- Tinkov, S., G. Winter, C. Coester and R. Bekeredjian (2010). "New doxorubicin-loaded phospholipid microbubbles for targeted tumor therapy: Part I—Formulation development and in-vitro characterization." Journal of Controlled Release **143**(1): 143-150.
- Tu, J., J. F. Guan, Y. Y. Qiu and T. J. Matula (2009). "Estimating the shell parameters of SonoVue (R) microbubbles using light scattering." Journal of the Acoustical Society of America **126**(6): 2954-2962.
- Unger, E. C., T. Porter, W. Culp, R. Labell, T. Matsunaga and R. Zutshi (2004). "Therapeutic applications of lipid-coated microbubbles." Advanced Drug Delivery Reviews **56**(9): 1291-1314.
- van Wamel, A., K. Kooiman, M. Hartevelde, M. Emmer, F. J. ten Cate, M. Versluis and N. de Jong (2006). "Vibrating microbubbles poking individual cells: Drug transfer into cells via sonoporation." Journal of Controlled Release **112**(2): 149-155.
- Vandenberg, B. F. and H. E. Melton (1994). "Acoustic lability of albumin microspheres." Journal of the American Society of Echocardiography **7**(6): 582-589.
- Vanliew, H. D. and M. E. Burkard (1995). "Behavior of Bubbles of Slowly Permeating Gas Used for Ultrasonic-Imaging Contrast." Investigative Radiology **30**(5): 315-321.
- Vannan, M. A., P. N. Burns, D. Hope-Simpson, M. Averkiou and J. E. Powers (1998). "Pulse Inversion Detection, an improved method for myocardial contrast echocardiography: Experimental studies and preliminary clinical experience." Circulation **98**(17): 503-503.
- Villanueva, F. S., E. X. Lu, S. Bowry, S. Kilic, E. Tom, J. J. Wang, J. Gretton, J. J. Pacella and W. R. Wagner (2007). "Myocardial ischemic memory imaging with molecular echocardiography." Circulation **115**(3): 345-352.
- Villarraga, H. R., D. A. Foley, B. C. Aeschbacher, K. W. Klarich and S. L. Mulvagh (1997). "Destruction of contrast microbubbles during ultrasound imaging at conventional power output." Journal of the American Society of Echocardiography **10**(8): 783-791.
- Wang, J. F., C. J. Wu, C. M. Zhang, Q. Y. Qiu and M. A. Zheng (2009). "Ultrasound-mediated microbubble destruction facilitates gene transfection in rat C6 glioma cells." Molecular Biology Reports **36**(6): 1263-1267.
- Wang, T. Y., K. E. Wilson, S. Machtaler and J. K. Willmann (2013). "Ultrasound and Microbubble Guided Drug Delivery: Mechanistic Understanding and Clinical Implications." Current Pharmaceutical Biotechnology **14**(8): 743-752.
- Wilhjelm, J. E., M. K. Andreas Illum and O. Trier (2013). "Medical diagnostic ultrasound-physical principles and imaging." Biomedical Engineering, DTU Elektro Technical University of Denmark.
- Williams, R., J. M. Hudson, B. A. Lloyd, A. R. Sureshkumar, G. Lueck, L. Milot, M. Atri, G. A. Bjarnason and P. N. Burns (2011). "Dynamic Microbubble Contrast-

enhanced US to Measure Tumor Response to Targeted Therapy: A Proposed Clinical Protocol with Results from Renal Cell Carcinoma Patients Receiving Antiangiogenic Therapy." Radiology **260**(2): 581-590.

Wrenn, S. P., S. M. Dicker, E. F. Small, N. R. Dan, M. Mleczko, G. Schmitz and P. A. Lewin (2012). "Bursting Bubbles and Bilayers." Theranostics **2**(12): 1140-1159.

Wrenn, S. P., M. Mleczko and G. Schmitz (2009). "Phospholipid-stabilized microbubbles: Influence of shell chemistry on cavitation threshold and binding to giant uni-lamellar vesicles." Applied Acoustics **70**(10): 1313-1322.

Wu, J. R. and J. Tong (1998). "Experimental study of stability of a contrast agent in an ultrasound field." Ultrasound in Medicine and Biology **24**(2): 257-265.

Xie, F. and R. Meltzer (1988). "Determination of ejection fraction from contrast echocardiography using videodensitometry in an in vitro model." Journal of ultrasound in medicine **7**(10): 581-587.

Yeh, C. K. and S. Y. Su (2008). "Effects of acoustic insonation parameters on ultrasound contrast agent destruction." Ultrasound in Medicine and Biology **34**(8): 1281-1291.

Yu, H., Z. S. Lin, L. Xu, D. L. Liu and Y. Y. Shen (2015). "Theoretical study of microbubble dynamics in sonoporation." Ultrasonics **61**: 136-144.

Zhou, M. F., F. Cavalieri and M. Ashokkumar (2011). "Tailoring the properties of ultrasonically synthesised microbubbles." Soft Matter **7**(2): 623-630.

# VITA

**Date and Place of Birth:** 1987, İskenderun/TURKEY

## Education

Ph.D., Bioengineering (GPA: 3.56/4.00) | Izmir Institute of Technology | Izmir –Turkey, 2019. Thesis Title: “Increasing Stability of Microbubbles under Ultrasound”

M.Sc., Biotechnology (GPA: 3.00/4.00) | Izmir Institute of Technology | İzmir –Turkey, 2014. Thesis Title: “Biocatalytic Performance of Carbonic Anhydrase Immobilized within Polyurethane Foam in Water-Miscible Organic Solvents”

B.Sc., Bioengineering (GPA: 2.60/4.00) | Ege University | Izmir – Turkey, 2011

## Work Experience

Internship | DEPA İlaç Aktif Maddeleri Sanayi ve Pazarlama A.Ş. | Izmit – Turkey | 07/2008 – 08/2008

## Grants

Project scholarship | The Scientific and Technological Research Council of Turkey (TÜBİTAK) 113M270 | 2013-2016.

Project scholarship | The Scientific and Technological Research Council of Turkey (TÜBİTAK) 213M668 | 2016-2017.

## Proceedings

Ayaz, U., Baris, M., Ozdemir, S.K., and Ozdemir, E., “Stability of Microbubbles under Ultrasound”, 3<sup>rd</sup> International Porous and Powder Materials Symposium and Exhibition (PPM 2017), Kusadasi-Izmir, September 12-15, 2017. (Poster)

Ayaz, U., Baris, M., Secil, M., Ozdemir, S.K., and Ozdemir, E., “Effect of Ultrasound Power on Microbubbles”, 4<sup>th</sup> International Porous and Powder Materials Symposium and Exhibition (PPM 2019), Marmaris-Izmir, October 09-11, 2019. (Oral Presentation)